Emission of electron-electron and electron-positron pairs from solid surfaces due to electron or positron impact

Vom Fachbereich Physik
der Universität Duisburg-Essen
(Campus Duisburg)

zur Erlangung des akademischen Grades eines
Doktors der Naturwissenschaften (Dr. rer. nat.)
genehmigte Dissertation von

Franz-Josef Giebels
aus Kleve

Referent: Prof. Dr. rer. nat. Roland Feder
Korreferent: Prof. Dr. rer. nat. Jürgen Kirschner
Tag der mündlichen Prüfung: 9. Juni 2015

Abstract

The present theoretical work deals with the emission of correlated electron-electron and electron-positron pairs from crystalline surfaces induced by the collision of a low-energy primary electron or positron with a valence electron. For short, these two processes are referred to as $(e, 2e)$ and (p, ep), respectively.

In generalization of earlier theory, an $(e, 2e)$ formalism has been developed, which incorporates spin-orbit coupling and exchange in ferromagnets on an equal footing. The basic ingredients are single-particle states, which are solutions of a Dirac equation with an effective magnetic field. From these states, two-electron states are obtained, which are correlated by exchange and Coulomb interaction. The spin-dependent $(e, 2e)$ reaction cross section is then expressed as the transition probability between an initial and a final two-electron state. While of course already applicable to $(e, 2e)$ from nonmagnetic systems as a special case, the theory has been extended to handle positron-induced electron-positron emission (p, ep).

The formalism was implemented in a computer code and numerical results were obtained for several selected crystalline surface systems. The quasiparticle potential input required for these computations was obtained by firstly performing, within density functional theory, an *ab initio* calculation of the ground state of the system and secondly augmenting the resulting real potential by a complex self-energy correction. This quasiparticle potential was also used to calculate spin- and layer-resolved densities of states (spectral functions), which are very valuable for the interpretation of the calculated pair emission spectra.

A comparative study of $(e, 2e)$ and (p, ep) was carried out for the Cu(111) surface. As a consequence of the opposite sign of the Coulomb interaction, the most outstanding difference appears in angular distributions of the two emitted particles with equal energies. While for $(e, 2e)$ there is a central depletion zone (exchange-correlation hole), the (p, ep) distributions exhibit a central accumulation zone (correlation hill). At larger angles sharp features arise from single-particle surface resonances.

In conjunction with experimental work at the Max-Planck-Institut für Mikrostrukturphysik in Halle, spin-dependent $(e, 2e)$ angular and energy distributions were calculated for the ferromagnetic Fe(001) surface. They are analyzed with the aid of the spin-, momentum-, symmetry- and layer-resolved valence electron density of states. The observed spectra are found to arise almost completely from only three surface-parallel atomic layers. Momentum distributions for parallel spins of the emitted electrons exhibit an exchange-correlation hole, which is larger than the correlation hole in the antiparallel spin case. By comparing experimental antiparallel-spin pair spectra with their theoretical counterparts an effective screening strength of the Coulomb interaction in the surface region is determined.

A similar separation of Coulomb correlation and exchange effects in $(e, 2e)$ is possible, if the valence electron is in a recently discovered spin-polarized surface state on the nonmagnetic W(110) surface. Further, $(e, 2e)$ can achieve a spin-resolved mapping of the dispersion of this state with surface-parallel momentum.

As a prototype case, for which spin-orbit coupling effects are comparable in size to magnetic exchange effects, the ferromagnetic surface system Co/W(110) has been chosen. $(e, 2e)$ spectra are presented together with the underlying spin- and layer-resolved valence electron spectral density. More detailed insight is provided by calculations, in which spin-orbit coupling was selectively switched off for the valence electron and for the primary and emitted electrons. The theoretical results are in overall agreement with experimental data. Furthermore, sizable magnetic dichroism is predicted.

Zusammenfassung

Die vorliegende theoretische Arbeit behandelt die Emission von korrelierten Elektron-Elektron und Elektron-Positron Paaren aus kristallinen Oberflächen induziert durch den Stoß eines niederenergetischen primären Elektrons oder Positrons mit einem Valenzelektron. Diese beiden Prozesse werden kurz als $(e, 2e)$-Prozess bzw. (p, ep)-Prozess bezeichnet.

In Verallgemeinerung einer früheren Theorie wurde ein $(e, 2e)$-Formalismus entwickelt, der Spin-Bahn-Kopplung und Austausch in Ferromagneten auf gleicher Stufe behandelt. Die grundlegenden Bestandteile sind Einteilchenzustände, die Lösungen einer Dirac-Gleichung mit effektivem Magnetfeld sind. Aus diesen Zuständen werden Zweiteilchenzustände gewonnen, die durch Austausch und Coulomb-Wechselwirkung korreliert sind. Der spinabhängige $(e, 2e)$-Wirkungsquerschnitt wird dann ausgedrückt als Übergangswahrscheinlichkeit zwischen einem Zweiteilchen-Anfangszustand und einem Zweiteilchen-Endzustand. Neben der Anwendbarkeit auf $(e, 2e)$ von nichtmagnetischen Systemen als Spezialfall, wurde die Theorie so erweitert, dass auch die Positronen-induzierte Elektron-Positron Emission (p, ep) behandelt werden kann.

Der Formalismus wurde in ein Computer-Programm umgesetzt und numerische Ergebnisse für einige ausgewählte kristalline Oberflächensysteme erzeugt. Das für die Rechnungen benötigte Quasiteilchen-Potential erhält man im Rahmen der Dichtefunktional-Theorie aus ab-initio Berechnungen des Grundzustands des untersuchten Systems, ergänzt durch eine komplexe Selbstenergiekorrektur.

Eine vergleichende Untersuchung von $(e, 2e)$ und (p, ep) wurde für eine Cu(111)-Oberfläche durchgeführt. Wegen des entgegengesetzten Vorzeichens der Coulomb-Wechselwirkung zeigt sich der auffallendste Unterschied in Winkelverteilungen für auslaufende Teilchen mit gleichen Energien. Während es für $(e, 2e)$ einen zentralen Bereich verminderter Intensität gibt (Austausch-Korrelations-Loch), zeigt die (p, ep)-Verteilung einen zentralen Bereich erhöhter Intensität (Korrelations-Hügel). Für größere Winkel zeigen sich aufgrund von Oberflächenresonanzen scharfe Strukturen.

Im Zusammenhang mit Experimenten am Max-Planck-Institut für Mikrostrukturphysik in Halle wurden spinabhängige Winkel- und Energieverteilungen der $(e, 2e)$-Spektren für die ferromagnetische Fe(001) Oberfläche berechnet. Diese wurden analysiert mit Hilfe von spin-, impuls-, symmetrie- und lagenaufgelösten Valenzelektronen-Zustandsdichten. Es stellt sich heraus, dass die gefundenen Intensitätsverteilungen fast vollständig durch die Emission aus den drei obersten oberflächenparallelen Atomlagen festgelegt sind. Impulsverteilungen für parallele Spins der auslaufenden Elektronen zeigen ein Austausch-Korrelations-Loch, welches größer ist als das Korrelations-Loch für den Fall antiparalleler Spins. Durch Vergleich der experimentellen Intensitätsverteilungen für antiparallele Spins mit den theoretischen Ergebnissen wurde eine effektive Abschirmlänge der Coulombwechselwirkung im Oberflächenbereich bestimmt.

Der Einfluss von Coulomb-Korrelation und Austausch-Wechselwirkung auf die $(e, 2e)$-Spektren wurde desweiteren an einem kürzlich entdeckten spin-polarisierten Oberflächenzustand in der nichtmagnetischen W(110)-Oberfläche untersucht. Zusätzlich konnte aus den berechneten $(e, 2e)$-Spektren die Dispersion $E(k^{\parallel})$ des Oberflächenzustands gewonnen werden.

Als System, für das magnetischer Austausch und Spin-Bahn-Kopplung von gleicher Größenordnung sind, wurde Co/W(110), d.h. Kobalt, adsorbiert in wenigen Monolagen auf eine W(110) Oberfläche, ausgewählt. Hierfür werden $(e, 2e)$-Intensitätsverteilungen zusammen mit den zugrundeliegenden spin- und lagenaufgelösten Zustandsdichten gezeigt. Detailliertere Einsicht wird durch Rechnungen gewonnen, bei denen die Spin-Bahn-Kopplung selektiv bei dem Valenzelektron, bei dem einfallenden Elektron und bei den auslaufenden Elektronen abgeschaltet wird. Die theoretischen Ergebnisse sind allgemein in guter Übereinstimmung mit den experimentellen Daten. Darüberhinaus lässt sich ein beträchtlicher magnetischer Dichroismus voraussagen.

Contents

Chapter 1

Introduction

The present work deals with the emission of two correlated electrons from crystalline surfaces following the collision of a primary low-energy electron with a valence electron. For short referred to as $(e, 2e)$, such coincidence spectroscopy has a long history of intense experimental and theoretical study in atomic physics (cf. e.g. [1–3] and ample references therein). In solid state physics, $(e, 2e)$ has over the past two decades evolved into a very powerful tool for studying collision dynamics, pair diffraction, correlation effects and electronic structure at solid surfaces (cf. [4–19] and ample references therein).[1]

The basic principles of correlation spectroscopy and some experimental aspects are described in Chapter 2. Chapter 3 contains a theoretical formalism for calculating fully spin-resolved $(e, 2e)$ intensities from ferromagnetic surfaces including spin-orbit coupling (SOC). SOC and magnetic exchange are treated on an equal footing by means of a Dirac equation with an effective magnetic field.

Replacing the incident electron beam by a beam of positrons, valuable complementary information can be obtained by observing the electron-positron pairs, which are emitted from the surface (cf. [20–23] and references therein). The essential theoretical aspects of positron-induced electron positron emission, referred to as (p, ep), are presented in Chapter 4 while Chapter 5 deals with a comparison of typical $(e, 2e)$ and (p, ep) results obtained for a Cu(111) surface.

Of major importance in $(e, 2e)$ spectroscopy are spin effects due to spin-orbit coupling and to ferromagnetism, which are observable by using polarized primary electrons. In Chapter 6 calculated $(e, 2e)$ spectra obtained for a ferromagnetic Fe(001) surface are presented and compared with recent experimental results. In this case spin-orbit coupling effects are rather weak. On the other hand, for compounds of a ferromagnetic material with a material of large atomic number, SOC and magnetic exchange interaction can be of similar magnitude and thus have both to be taken into account in calculations. As a typical example of such a system we have chosen ferromagnetic Co layers on a W(110) surface in Chapter 7.

Parts of this thesis have already been published as original articles in international physics journals (Refs. [9, 10, 16–18, 22][2]). These results are presented together with further material in a coherent and more detailed way.

In this work, atomic units (Hartree units) are used if not stated otherwise.

[1] The above part of the introduction has been published in Ref. [18].

[2] Refs. [9] and [10] are joint theory-experiment papers. The theoretical results were obtained as part of the present thesis work, whereas the experimental results are due to J. Kirschner, F. O. Schumann, and C. Winkler at the Max-Planck-Institut für Mikrostrukturphysik in Halle.

Chapter 2

Principles and experimental aspects of pair correlation spectroscopy

An electron or positron which impinges on a solid surface can induce different processes in the solid. In some of these the incoming particle is elastically scattered as, e.g., in Low Energy Electron Diffraction (LEED), Reflection High Energy Electron Diffraction (RHEED), or in Low Energy Positron Diffraction (LEPD). In other cases the energy of the primary particle is used to expel crystal electrons from the surface, as in the electron-induced electron-electron emission $(e, 2e)$ and the positron-induced electron-positron emission (p, ep). In inverse photoemission, on the other hand, the energy of the primary electron is partly used to emit photons out of the crystal surface. Spectroscopies based on these processes are widely used to determine the structural and electronic properties of solids. Furthermore, the incoming electron can induce excitations in the electronic or phononic system (described as quasiparticle excitations, pairs of quasiparticle excitations, collective excitations, or combinations of these). Even though each of these processes deals with the interaction of many-particle states, it is often sufficient to use a one-particle picture for its description as, e.g., for LEED or photoemission. In the case of $(e, 2e)$ or (p, ep) spectroscopy, however, one has to include two-particle effects for an appropriate description. Here, the interaction between the excited particles in the presence of the solid is of particular interest. How is their movement affected by exchange and Coulomb correlation, and under which particular conditions is it possible to study both effects independently from each other? A sketch of the $(e, 2e)$ process in real space is shown in Fig. 2.1(a).

As already mentioned, in the $(e, 2e)$ process (and also in the (p, ep) process) the incoming (primary) particle (state $|1\rangle$) can transfer a sufficient part of its kinetic energy to one valence electron (state $|2\rangle$) and consequently set it free (state $|4\rangle$). If the primary particle, now with its remaining energy E_3, is also emitted into the vacuum (state $|3\rangle$) it may be detected in coincidence with the particle in state $|4\rangle$. In the $(e, 2e)$ case, in addition to this direct process, one can observe the exchange process where state $|1\rangle$ is transferred into state $|4\rangle$ and state $|2\rangle$ into state $|3\rangle$. Both processes form the so called $(e, 2e)$ transition. Since, as symbolically shown in Fig. 2.1(b), the energy lost by the primary particle is totally absorbed by only one of the valence electrons, the $(e, 2e)$ process is characterized by conservation of energy in the form

$$E_1 + E_2 = E_3 + E_4 \,, \tag{2.1}$$

where E_1 and E_2 are the energies of the primary electron and the valence electron, respectively, and E_3 and E_4 are the energies of the two emitted electrons. Furthermore, for crystalline surfaces the sum of the surface-parallel momenta is conserved (modulo a reciprocal surface lattice vector)

$$\mathbf{k}_1^{\parallel} + \mathbf{k}_2^{\parallel} = \mathbf{k}_3^{\parallel} + \mathbf{k}_4^{\parallel} + \mathbf{g}^{\parallel} \,, \tag{2.2}$$

which is a consequence of the periodicity of the target parallel to the surface. This means that additional elastic scattering events of the involved electrons at the crystal lattice have no influence on their parallel momenta.

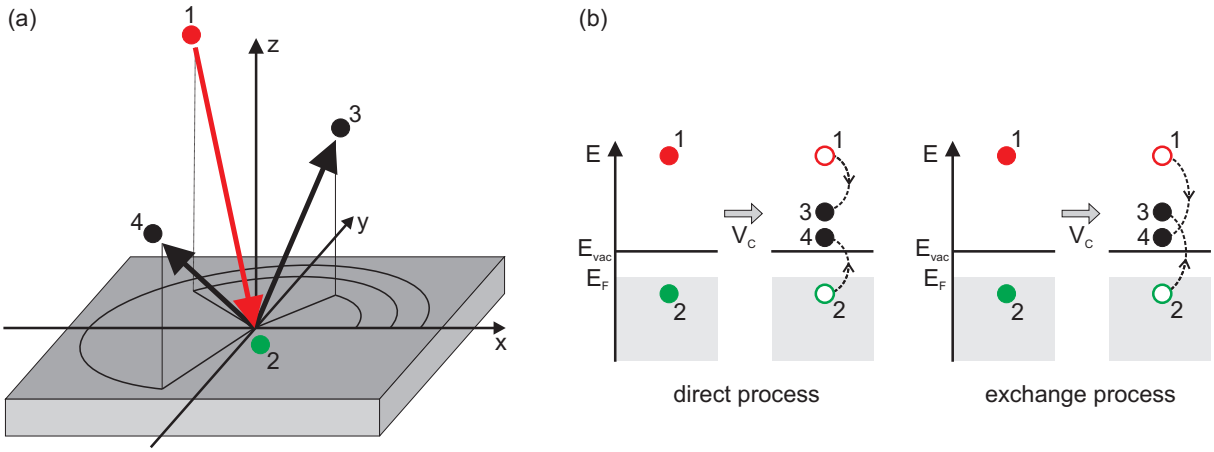

Fig. 2.1: Sketch of the $(e, 2e)$ process. The primary electron (1) collides with a valence electron (2) leading by Coulomb interaction to a correlated electron pair (3, 4) emitted from the surface. In the case of positron-induced pair emission (p, ep) the primary particle and one of the emitted particles is a positron. (a) real space, (b) energy diagram.

The central quantity to characterize the $(e, 2e)$ process (and similarly in the (p, ep) case) in theory and experiment is the reaction cross section $I^{\sigma_1}_{\sigma_3,\sigma_4}(E_1, \vartheta_1, \varphi_1; E_3, \vartheta_3, \varphi_3, E_4, \vartheta_4, \varphi_4)$, which contains all information about the transition probability that a primary beam (characterized by energy E_1, angles ϑ_1, φ_1 and spin σ_1) is scattered into states $|3\rangle$ and $|4\rangle$ of the outgoing particles (characterized by $(E_3, \vartheta_3, \varphi_3, \sigma_3)$ and $(E_4, \vartheta_4, \varphi_4, \sigma_4)$).

As mentioned, it is of particular interest how the obtained intensities are affected by two-particle interactions (i.e., exchange and Coulomb correlation) between the outgoing particles. Valuable information concerning this question can be obtained by a well selected choice of the spin polarizations σ_1 (of the primary electron), σ_3, σ_4, and, in addition, of the energy of the valence electron. If, for instance, we choose E_2 within a region where the spin-up density of states is zero and $\sigma_1 = +$ (up), then we will mainly observe the $I^{\sigma_1}_{\sigma_3,\sigma_4} = I^{+}_{+-}$ contribution[1] which is only affected by Coulomb correlation. For a primary spin-down electron ($\sigma_1 = -$), on the other hand, we will mainly observe the I^{-}_{--} contribution which will be dominantly affected by the exchange interaction.

If the parameters of the primary beam are fixed, the parameter space of the outgoing particles is six dimensional ($E_i, \vartheta_i, \varphi_i$, $i = 3, 4$, if spin is not included). For an easier interpretation of the results it is therefore often necessary to choose certain geometries, e.g., a coplanar setup. In a theoretical description of the $(e, 2e)$ process it is relatively easy to fix certain characteristic parameters of the particles involved and calculate reaction cross sections only for this restricted set.

The situation is different in the experiment. Due to the low counting rates it is not useful to specify parameters (energies E_i and angles ϑ_i, φ_i, $i = 3, 4$) of the outgoing electrons a priori

[1] Due to spin-orbit coupling, however, there is also a small additional I^{+}_{++} contribution.

and count only the events which fit these parameters. By contrast, one first collects the data of as many coincidence events as possible. Depending on the physical properties one wants to investigate a suitable selection from all those data has to be done. For instance, one takes into account all events with sum energies $E_{\mathrm{sum}} = E_3 + E_4$ which lie in a selected energy window. Because of the small counting rates in $(e, 2e)$, especially for metal surfaces, one has to use finite angular windows instead of fixed polar and azimuthal angles of the ejected particles.

A typical experimental setup (cf. Ref. [10]) is shown in Fig. 2.2. The electron gun shoots an electron beam at the target. The resulting current I of the beam is so low that on average less than one electron hits the surface within a suitably chosen time window τ. If one electron is registered by detector 1 and another one by detector 2 within a second time window $\tilde{\tau}$ (which has to be properly chosen with respect to the experimental setup), one $(e, 2e)$ event is counted. From the coordinates at which the two electrons hit the detectors and from their times of flight, one can determine their energies E_3 and E_4 and their surface parallel momenta $\mathbf{k}_3^{\parallel}$ and $\mathbf{k}_4^{\parallel}$. For the study of ferromagnetic surfaces and of spin-orbit coupling effects on nonmagnetic surfaces an electron gun is used which produces a spin-polarized beam.

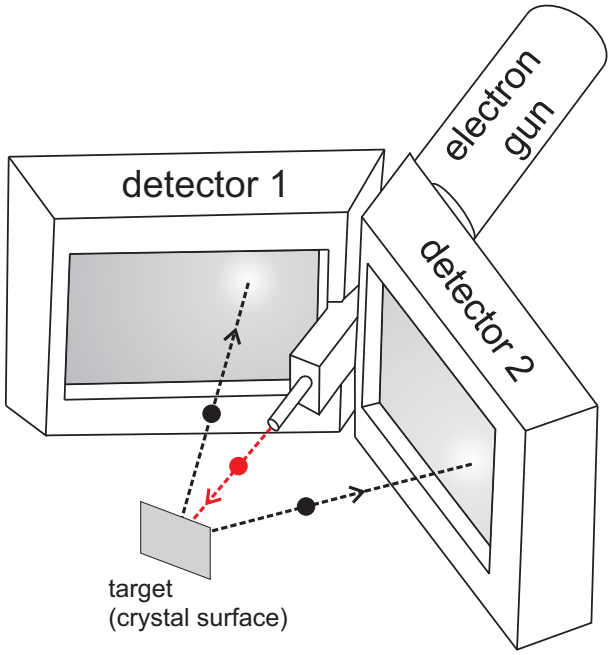

Fig. 2.2: Schematic view of an experimental $(e, 2e)$ setup. An electron released by the electron gun hits a crystal surface. The two emitted correlated electrons hit the position sensitive detectors which in combination with a time of flight analysis determine their energies and parallel momenta. (This figure is adapted from Ref. [9], Fig. 1.)

In Fig. 2.3 the results of a typical $(e, 2e)$ experiment for a coplanar setup are shown. Displayed is the intensity distribution as a function of the energies E_3 and E_4 of the two detected electrons. The dashed diagonal line marks those transitions where the valence electron, which is set free by the $(e, 2e)$ process, comes directly from the Fermi level. In this case we have $E_3 + E_4 = E_1 + E_F =: E_{\mathrm{sum}}^{\mathrm{max}}$. For $E_3 + E_4 > E_{\mathrm{sum}}^{\mathrm{max}}$, $(e, 2e)$ transitions are not possible. The low counting rates in this region, indicated by the blue color in Fig. 2.3, are due to random coincidences.

For $E_{\mathrm{sum}} \leqq 8$ eV the observed intensity is significantly increased. The reason for this is that in addition to proper $(e, 2e)$ processes there are additional processes which contribute. These involve in particular multiple inelastic scattering processes and Auger processes. In an experiment it is not possible to distinguish between proper $(e, 2e)$ events and processes formed by two or more steps, as for instance an $(e, 2e)$ process followed by an Auger process.

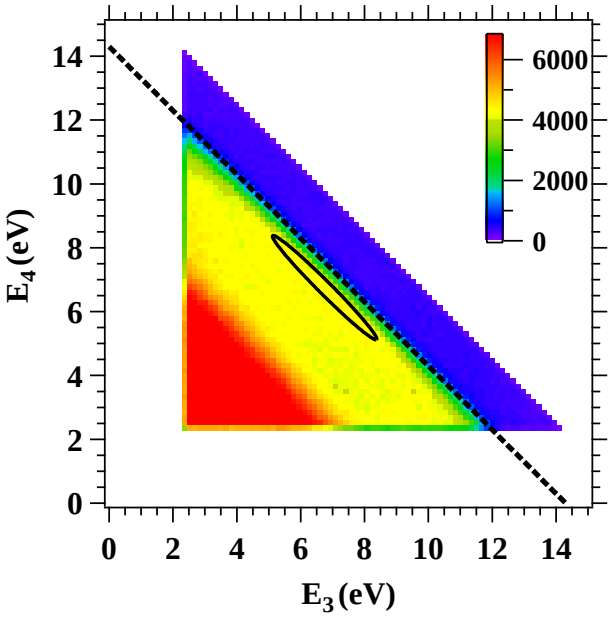

Fig. 2.3: Typical $(e, 2e)$ energy distribution from an experiment obtained with primary energy $E_1 = 19$ eV. The dashed diagonal line marks the maximum of the sum energy $E_{\mathrm{sum}}^{\mathrm{max}} = 14.3$ eV (which corresponds to a valence electron energy $E_2 = E_F$) that the pair can have. (This figure is adapted from Fig. 2 in Ref. [10].)

Chapter 3

Theory of electron-induced electron-electron emission $[(e, 2e)]$

In this chapter the formalism to calculate electron-induced electron-electron emission intensities ($(e, 2e)$ intensities) for ferromagnetic surface systems is presented. This formalism incorporates ferromagnetic exchange interaction and spin-orbit coupling (SOC) on an equal footing and is of course also applicable to nonmagnetic systems, for which it is equivalent to an earlier formalism [24–26]. In general, one has to deal here with an $(N + 1)$-particle problem which can, however, be approximated by an expression for the transition probability that contains only effective one- and two-particle states and a two-particle interaction potential. In this chapter we will elaborate how to calculate

- the effective one-particle states describing the incident electron and the two outgoing electrons including all multiple scattering effects,
- the radial parts of these states by solving the one-particle Dirac equation with a ferromagnetic effective potential,
- the correlated two-particle state representing the outgoing electron pair,
- the valence electron Green function for ferromagnetic systems, including spin-orbit coupling, which is a central part in the expression for the transition probability.

From the spin-dependent $(e, 2e)$ intensities one can construct three asymmetry quantities, which are particularly useful for analyzing $(e, 2e)$ spectra. These are presented at the end of this chapter.

3.1 General framework

As symbolically sketched in Fig. 3.1, the $(e, 2e)$ process describes one possible transition

$$|N + 1\rangle_i \rightarrow |N + 1\rangle_f \tag{3.1}$$

where the initial $(N + 1)$-particle state $|N + 1\rangle_i \approx |N\rangle|1\rangle$ is formed by N crystal electrons and an additional electron shot at the crystal. The final state $|N + 1\rangle_f$ contains the two outgoing electrons and the remaining $N - 1$ particles in the crystal.

A unique feature of the $(e, 2e)$ process is that, even though there is Coulomb interaction between all $N + 1$ electrons, only two of them exchange energy (and momentum): the incoming electron loses part of its energy which is completely absorbed by one of the valence electrons. If the energy transfer is large enough, this electron can — together with the back-reflected primary electron — leave the crystal and both electrons may be detected in coincidence.

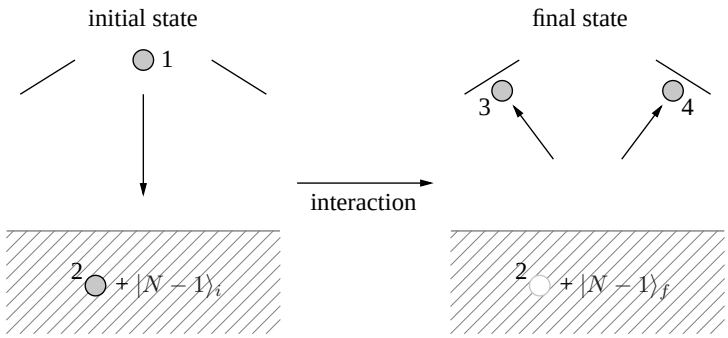

Fig. 3.1: Many-particle states involved in an $(e, 2e)$ process: Initial state $|N+1\rangle_i$ and final state $|N+1\rangle_f$ are $(N+1)$-particle states where $|N+1\rangle_i$ is a combination of the one-particle state $|1\rangle$ of the incoming electron and the N-particle state $|N\rangle$ of the (unperturbed) crystal and $|N+1\rangle_f$ consists of the two-particle state $|3,4\rangle$ of the outgoing electrons and the $(N-1)$-particle state $|N-1\rangle_f$ of the perturbed crystal.

The other $N-1$ electrons, which are not directly affected by the transition, feel only a slight indirect disturbance. Their influence on the two active electrons is taken into account in an effective one-electron potential and in the screening of the interaction between the two electrons. The $(e, 2e)$ process is thence governed by a two-electron Hamilton operator of the form

$$\mathcal{H} = H_1 + H_2 + U = \mathcal{H}_0 + U, \tag{3.2}$$

where H_1 and H_2 are one-particle operators, U describes the two-particle interaction, and $\mathcal{H}_0 = H_1 + H_2$ is the two-particle operator without the pair-interaction. H_1 and H_2 include the interaction with the semi-infinite crystal through complex one-particle quasiparticle potentials the imaginary parts of which account for life-time effects. U is the Coulomb interaction screened by the dielectric function of the semi-infinite system. The observable $(e, 2e)$ reaction cross section is the transition probability from an initial to a final two-electron state, as will be described in the following.

Asymptotically the two-particle initial state is the antisymmetrized product of the state φ_1 of an incoming electron (eigenstate of H_1) with a selected valence electron state φ_2 (eigenstate of H_2), and the two-particle final state is the antisymmetrized product of the states φ_3 and φ_4 of outgoing electrons (eigenstates of H_1 and H_2)

$$\varphi_{\text{initial}} = \frac{1}{\sqrt{2}}(\varphi_1 \otimes \varphi_2 - \varphi_2 \otimes \varphi_1)\,, \tag{3.3}$$

$$\varphi_{\text{final}} = \frac{1}{\sqrt{2}}(\varphi_3 \otimes \varphi_4 - \varphi_4 \otimes \varphi_3)\,. \tag{3.4}$$

φ_{initial} and φ_{final} are eigenstates of the two-particle operator $\mathcal{H}_0$ (without the pair-interaction).

Considering the interaction U as a perturbation, i.e., the unperturbed Hamiltonian is $\mathcal{H}_0$, it is useful to define the following two-particle Green operators $\mathcal{G}$ and $\mathcal{G}_0$:

$$\mathcal{G}(z) = (z - \mathcal{H})^{-1}, \tag{3.5}$$

$$\mathcal{G}_0(z) = (z - \mathcal{H}_0)^{-1}. \tag{3.6}$$

Here, the variable z stands for a complex energy (e.g., $z = E \pm i\epsilon$). With

$$\begin{aligned}
\mathcal{G}(z) &= \mathcal{G}_0(z)(z - \mathcal{H}_0)\mathcal{G}(z) \\
&= \mathcal{G}_0(z)(z - \mathcal{H}_0 - U + U)\mathcal{G}(z) \\
&= \mathcal{G}_0(z) + \mathcal{G}_0(z)U\mathcal{G}(z) \\
&= \mathcal{G}_0(z) + \mathcal{G}_0(z)U\mathcal{G}_0(z) + \mathcal{G}_0(z)U\mathcal{G}_0(z)U\mathcal{G}_0(z) + \ldots \\
&= \mathcal{G}_0(z) + \mathcal{G}_0(z) \underbrace{(U + U\mathcal{G}_0(z)U + \ldots)}_{=:\mathcal{T}(z)} \mathcal{G}_0(z),
\end{aligned} \tag{3.7}$$

where the transition operator $\mathcal{T}$ can be written as

$$\begin{aligned}
\mathcal{T}(z) &= U + U\mathcal{G}_0(z)U + U\mathcal{G}_0(z)U\mathcal{G}_0(z)U + \ldots \\
&= [1 + U\mathcal{G}_0(z) + U\mathcal{G}_0(z)U\mathcal{G}_0(z) + \ldots]U \\
&= [1 + U\mathcal{G}(z)]U,
\end{aligned} \tag{3.8}$$

and with $\mathcal{G}_\pm(E) := \lim_{\epsilon\to 0^+} \mathcal{G}(E \pm \mathrm{i}\epsilon)$ and $\mathcal{T}_\pm(E) := \lim_{\epsilon\to 0^+} \mathcal{T}(E \pm \mathrm{i}\epsilon)$, we obtain the amplitude for the transition of state φ_{initial} into the state φ_{final}:

$$\begin{aligned}
\langle\varphi_{\text{final}}|\mathcal{T}_+(E)|\varphi_{\text{initial}}\rangle &= \langle\varphi_{\text{final}}|[1 + U\mathcal{G}_+(E)]U|\varphi_{\text{initial}}\rangle \\
&= \langle[1 + (\mathcal{G}_+(E))^\dagger U]\varphi_{\text{final}}|U|\varphi_{\text{initial}}\rangle \\
&= \langle[1 + \mathcal{G}_-(E)U]\varphi_{\text{final}}|U|\varphi_{\text{initial}}\rangle
\end{aligned} \tag{3.9}$$

(The operator of the pair interaction U is hermitian.). Eq. (3.9) contains the Møller-operator $\Omega := 1 + \mathcal{G}_-(E)U = 1 + \mathcal{G}_{0,-}(E)\mathcal{T}_-(E)$, which can be used to define

$$\psi_{\text{final}} := [1 + \mathcal{G}_-(E)U]\varphi_{\text{final}} = \Omega\varphi_{\text{final}}. \tag{3.10}$$

ψ_{final} is an eigenstate of $\mathcal{H}$ with energy E, if, as assumed here, φ_{final} is an eigenstate of $\mathcal{H}_0$ with the same energy E. This follows by applying $(E - \mathcal{H})$ to ψ_{final}

$$\begin{aligned}
(E - \mathcal{H})\psi_{\text{final}} &= (E - \mathcal{H})(1 + \mathcal{G}_-(E)U)\varphi_{\text{final}} \\
&= (E - \mathcal{H} + U)\varphi_{\text{final}} \\
&= (E - \mathcal{H}_0)\varphi_{\text{final}} \\
&= 0.
\end{aligned} \tag{3.11}$$

The exact transition amplitude can thus be written as the U-matrix element of an uncorrelated initial state φ_{initial} (eigenstate of $\mathcal{H}_0$) and a correlated final state ψ_{final} (eigenstate of $\mathcal{H}$)

$$\langle\psi_{\text{final}}|U|\varphi_{\text{initial}}\rangle. \tag{3.12}$$

The corresponding result in first order perturbation theory is $\langle\varphi_{\text{final}}|U|\varphi_{\text{initial}}\rangle$, where φ_{final} is the uncorrelated final state.

To obtain the reaction cross section which is relevant for $(e, 2e)$, one has to take the absolute square of the transition amplitude in Eq. (3.12), take into account the energy conservation (cf.

Eq. (2.1)), and allow for the fact that there maybe several valence electron states φ_2 contained in φ_{initial}. Further, a factor $\gamma \propto \sqrt{E_3 E_4}/\sqrt{E_1}$ is needed to make contact with the experimentally observable current densities. The $(e, 2e)$ transition cross section is thus

$$I^1_{3,4} = \gamma \sum_{\varphi_2} |\langle \psi_{\text{final}}|U|\varphi_{\text{initial}}\rangle|^2 \delta(E_2 - \underbrace{(E_3 + E_4 - E_1)}_{=:E}). \tag{3.13}$$

The effect of a finite lifetime of the valence electron state can approximately be described by adding a spatially uniform energy-dependent imaginary self-energy part V_{im} to the real one-particle potential. As a consequence, the delta-function in Eq. (3.13) is modified to a Lorentzian $\tilde{\delta}$ with the full width at half maximum $\Delta = 2\,V_{\text{im}}$. As a result, the valence electron energy E_2 is complex (corresponding to a finite lifetime), and the valence states are now quasiparticle states (for details see, e.g., Ref. [4]).

It is useful to rewrite Eq. (3.13), using $\tilde{\delta}$ instead of δ, in the form (cf. Eq. (3.3))

$$I^1_{3,4} = \gamma \sum_{\varphi_2} \langle \psi_{\text{final}}|U|\varphi_{\text{initial}}\rangle\langle\varphi_{\text{initial}}|U|\psi_{\text{final}}\rangle\, \tilde{\delta}(E_2 - E) \tag{3.14}$$

$$= \frac{1}{2}\gamma \sum_{\varphi_2} \langle \psi_{\text{final}}|U|\varphi_1 \otimes \varphi_2 - \varphi_2 \otimes \varphi_1\rangle\langle\varphi_1 \otimes \varphi_2 - \varphi_2 \otimes \varphi_1|U|\psi_{\text{final}}\rangle\, \tilde{\delta}(E_2 - E). \tag{3.15}$$

Using the antisymmetry of the final state ($\psi_{\text{final}}(\mathbf{r}_2, \mathbf{r}_1) = -\psi_{\text{final}}(\mathbf{r}_1, \mathbf{r}_2)$) and the symmetry of the pair interaction ($U(\mathbf{r}_2, \mathbf{r}_1) = U(\mathbf{r}_1, \mathbf{r}_2)$), we obtain

$$I^1_{3,4} = 2\gamma \sum_{\varphi_2} \langle \psi_{\text{final}}|U|\varphi_1 \otimes \varphi_2\rangle\langle\varphi_1 \otimes \varphi_2|U|\psi_{\text{final}}\rangle\, \tilde{\delta}(E_2 - E) \tag{3.16}$$

$$= 2\gamma \sum_{\varphi_2} \langle \psi_{\text{final}}|U\Big[|\varphi_1\rangle\langle\varphi_1| \otimes |\varphi_2\rangle\langle\varphi_2|\Big]U|\psi_{\text{final}}\rangle\, \tilde{\delta}(E_2 - E) \tag{3.17}$$

$$= 2\gamma \langle \psi_{\text{final}}|U\Big[|\varphi_1\rangle\langle\varphi_1| \otimes \sum_{\varphi_2} |\varphi_2\rangle\langle\varphi_2|\, \tilde{\delta}(E_2 - E)\Big]U|\psi_{\text{final}}\rangle. \tag{3.18}$$

The sum over the valence states $|\varphi_2\rangle$ can be expressed as the imaginary part of the retarded valence electron Green function

$$\sum_{\varphi_2} |\varphi_2\rangle\langle\varphi_2|\, \tilde{\delta}(E_2 - E) = -\frac{1}{\pi}\,\text{Im}\, G_2(E), \tag{3.19}$$

where, as described above, φ_2 are quasiparticle states and $\tilde{\delta}$ is a Lorentzian. The scattering cross section can then be written as

$$I^1_{3,4} = 2\gamma \langle \psi_{\text{final}}|U\Big[|\varphi_1\rangle\langle\varphi_1| \otimes \left(-\frac{1}{\pi}\right)\text{Im}\, G_2(E_3 + E_4 - E_1)\Big]U|\psi_{\text{final}}\rangle. \tag{3.20}$$

Writing the correlated final state $|\psi_{\text{final}}\rangle$ as $|3, 4\rangle$ and the primary electron state $|\varphi_1\rangle$ as $|1\rangle$, this can also be written as

$$I^1_{3,4} = 2\gamma \langle 3, 4|U|1\rangle \left(-\frac{1}{\pi}\right)\text{Im}\, G_2(E_3 + E_4 - E_1)\, \langle 1|U|3, 4\rangle. \tag{3.21}$$

Hence, in order to obtain the intensity $I^1_{3,4}$ we have to calculate the state $|1\rangle$ of the incoming electron, the valence electron Green-function $G_2(E)$, and the two-particle state $|3, 4\rangle$ of the outgoing electrons.

3.2 Solutions of the Dirac equation with magnetic field

In systems like magnetic iron, spin-orbit coupling (SOC) effects are, overall, small compared to the influence of magnetism and hence may for many purposes be neglected. On the other hand for materials like the rare earth magnets with relatively large atomic number Z or heavy metals alloyed with Fe, Co, Ni (e.g., Fe_3Pt or Co adsorbed on W), SOC effects cannot be neglected any more and hence the effective one-particle functions $\varphi(\mathbf{r}, t)$ should be determined as solutions of the associated Dirac equation

$$\mathrm{i}\frac{\partial}{\partial t}\varphi(\mathbf{r}, t) = H(\mathbf{r})\varphi(\mathbf{r}, t). \tag{3.22}$$

The effective one-particle Dirac Hamilton operator for a semi-infinite solid is (cf. [27, 28])

$$H(\mathbf{r}) = c\,\boldsymbol{\alpha}\cdot\mathbf{p} + c^2\beta + V(\mathbf{r})\ , \quad \mathbf{r}\in\mathbb{R}^3\ , \tag{3.23}$$

where $V(\mathbf{r})$ is a potential matrix of the form (1_2 is the 2×2 unit matrix)

$$V(\mathbf{r}) = \begin{pmatrix} v_+(\mathbf{r}) & 0 \\ 0 & v_-(\mathbf{r}) \end{pmatrix}, \quad v_\pm(\mathbf{r}) = v(\mathbf{r})1_2 \pm \boldsymbol{\sigma}\cdot\mathbf{B}(\mathbf{r})\ , \quad \mathbf{r}\in\mathbb{R}^3\,, \tag{3.24}$$

where (with the Pauli spin matrices $\sigma_1, \sigma_2, \sigma_3$)

$$\boldsymbol{\sigma} = (\sigma_1, \sigma_2, \sigma_3)^t\,, \quad \boldsymbol{\alpha} = (\alpha_1, \alpha_2, \alpha_3)^t\,, \quad \alpha_k = \begin{pmatrix} 0 & \sigma_k \\ \sigma_k & 0 \end{pmatrix}, \quad \text{and} \quad \beta = \begin{pmatrix} 1_2 & 0 \\ 0 & -1_2 \end{pmatrix}. \tag{3.25}$$

By Eq. (3.24) the internal magnetic field $\mathbf{B}(\mathbf{r})$ is defined.

$V(\mathbf{r})$ is in general complex. Its imaginary part describes the effect of loss processes in the many-body system.

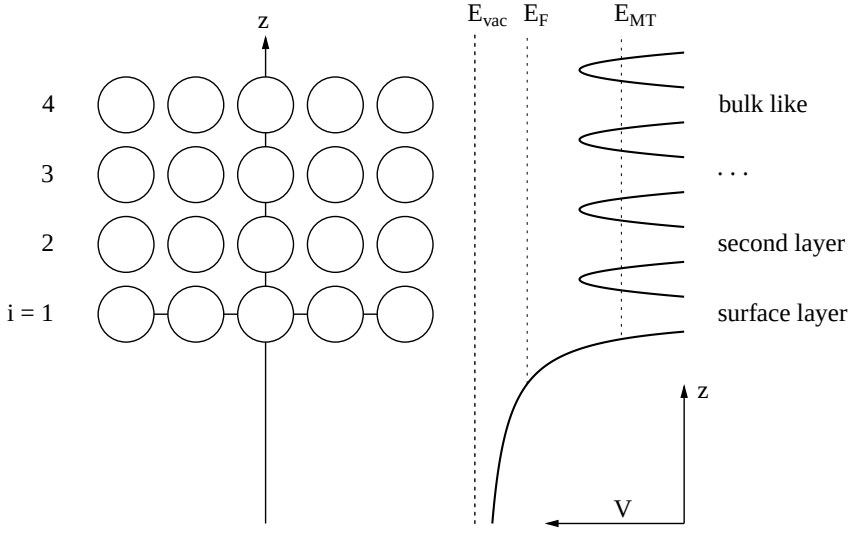

Fig. 3.2: Schematic sketch of surface geometry and potential $V(\mathbf{r})$. E_{MT} is the muffin-tin zero, E_F is the Fermi-energy, and E_{vac} is the vacuum threshold.

The potential V has two-dimensional lattice periodicity (parallel to the surface), i.e., $V(\mathbf{r} + \mathbf{R}^{\|}) = V(\mathbf{r})$ for all $\mathbf{R}^{\|}$ from a two dimensional Bravais lattice. The surface is parallel to the (x, y) plane and the z axis is pointing into the crystal.

The components of the 4×4 potential matrix V can be written as the sum over non-overlapping potentials belonging to the i-th layer (forming the matrix V_i where $V_i(\mathbf{r}) = V(\mathbf{r})$ in the i-th layer and $V_i(\mathbf{r}) = 0$ elsewhere) and a surface barrier potential (forming the matrix V_{surf}):

$$\begin{aligned} V(\mathbf{r}) = \begin{pmatrix} v_+(\mathbf{r}) & 0 \\ 0 & v_-(\mathbf{r}) \end{pmatrix} &= V_{\mathrm{surf}}(\mathbf{r}) + \sum_{i=1}^{\infty} V_i(\mathbf{r}) \\ &= V_{\mathrm{surf}}(\mathbf{r}) + \sum_{i=1}^{\infty} \sum_{\mathbf{R}^{\|}} V_{i,a}(\mathbf{r} - (\mathbf{c}_i + \mathbf{R}^{\|})) \ . \end{aligned} \tag{3.26}$$

In the second equation, the potential V_i of the i-th layer is written as a superposition of (non-overlapping) single-site potentials $V_{i,a}(\mathbf{r})$ of the i-th layer (coordinates with respect to the center of the muffin-tin sphere). $\mathbf{c}_i$ denotes a translation from the origin to a representative atomic site in the i-th layer ($i = 1, 2, \dots$). For the purpose of calculating $(e, 2e)$ intensities it is convenient to approximate $V(\mathbf{r})$ by the so called muffin-tin approximation, where the single-site potentials $V_{i,a}(\mathbf{r})$ outside the muffin-tin spheres (defined by radii $r_{i,\mathrm{MT}}$) are averaged to a constant value. Inside the muffin-tin spheres the potentials are spherically averaged. The surface potential barrier V_{surf} is approximated by a suitable z-dependent expression with image-potential asymptotics.

As a basis for evaluating $(e, 2e)$ matrix elements it is necessary to calculate single-particle states and the valence electron Green function (cf. Section 3.1). The construction of the Green function (cf. [29]) uses not only eigensolutions of the Dirac equation (in this context called right-hand solutions Z^R) but also solutions of the adjoint equation (called left-hand solutions Z^L). This is due to the fact that H (containing a complex-valued potential $V(\mathbf{r})$) is non-hermitian. Therefore, it is necessary to find pairs of solutions Z^R and Z^L

$$(E - H)Z^R = 0 \quad \text{and} \quad (E^* - H^\dagger)Z^L = 0, \quad \mathbf{r} \in \mathbb{R}^3, \tag{3.27}$$

where

$$H^\dagger = c\,\boldsymbol{\alpha} \cdot \mathbf{p} + c^2\beta + V^\dagger \quad \text{and} \quad V^\dagger(\mathbf{r}) = \begin{pmatrix} (v_+(\mathbf{r}))^\dagger & 0 \\ 0 & (v_-(\mathbf{r}))^\dagger \end{pmatrix}. \tag{3.28}$$

The form of the potential $V(\mathbf{r})$ (cf. Eq. (3.24)), with contributions $v_\pm(\mathbf{r}) = v(\mathbf{r})1_2 \pm \boldsymbol{\sigma} \cdot \mathbf{B}(\mathbf{r})$, allows us to write the adjoint operator $H^\dagger$ as

$$H^\dagger(\mathbf{B}) = TH(-\mathbf{B})T^{-1} = T^{-1}H(-\mathbf{B})T, \tag{3.29}$$

where the operator T (time reversal operator) is defined as

$$T = -\mathrm{i} \begin{pmatrix} \sigma_y & 0 \\ 0 & \sigma_y \end{pmatrix} K, \quad T^{-1} = -T. \tag{3.30}$$

The operator K denotes complex conjugation. Due to Eq. (3.29) it is possible to obtain left-hand solutions from right-hand solutions. From $[E - H(-\mathbf{B})]\tilde{Z}^R = 0$ we find

$$\begin{aligned}[E^* - H^\dagger(\mathbf{B})]T\tilde{Z}^R &= [TET^{-1} - TH(-\mathbf{B})T^{-1}]T\tilde{Z}^R \\ &= T[E - H(-\mathbf{B})]\tilde{Z}^R = 0,\end{aligned} \tag{3.31}$$

so $Z^L = Z^L(\mathbf{B}) = T\tilde{Z}^R(-\mathbf{B})$ is a left-hand solution in the presence of the magnetic field $\mathbf{B}$ if $\tilde{Z}^R$ is a solution for the field $-\mathbf{B}$.

We use the layer-KKR method (cf., e.g., [27,30,31], and references therein) to calculate one-particle states and to construct the valence electron Green function. In this method, firstly the scattering properties of individual scattering centers are calculated and described by site-specific scattering matrices $t^{(i)}$. Since we assume (cf. Eq. (3.26)) that each (individual) layer consists of identical scattering sites, this amounts to calculating the matrices $t^{(i)}$ for the potentials $V_{i,a}$. In a second step the scattering properties of each layer are calculated and characterized by a layer-specific scattering matrix $M^{(i)}$. To calculate the matrices $M^{(i)}$ one only needs the (representative) $t^{(i)}$ of that layer and the atomic site locations, i.e., the two-dimensional Bravais lattice. The matrices $M^{(i)}$ contain effects of multiple scattering within the layer. Similarly the scattering properties of the surface barrier V_{surf} are described by a scattering matrix $M^{(0)}$. Combining the scattering properties of the layers results in the scattering properties of the semi-infinite crystal.

In the following Section 3.2.1 formal solutions of the single-site Dirac equation, from which the matrices $t^{(i)}$ can be obtained, are presented. In Section 3.2.2 expressions of the matrices $M^{(i)}$ in terms of the matrices $t^{(i)}$ are given.

3.2.1 Solutions for a single atomic site[1]

We first describe how to solve the Dirac equation for a single atomic site with potential $V_{i,a}$ located at the origin (see Eq. (3.26)) to obtain (for each layer index i) a system of regular and irregular solutions as well as the single-site matrices $t^{(i)}$. The single-site Hamiltonian is

$$H_{i,a}(\mathbf{r}) = c\,\boldsymbol{\alpha}\cdot\mathbf{p} + c^2\beta + V_{i,a}(\mathbf{r}), \quad V_{i,a}(\mathbf{r}) = \begin{pmatrix} v_+^{(i)}(\mathbf{r}) & 0 \\ 0 & v_-^{(i)}(\mathbf{r}) \end{pmatrix}, \quad \mathbf{r}\in\mathbb{R}^3, \tag{3.32}$$

with $V_{i,a}(\mathbf{r}) = 0$ for $r \geq r_{\mathrm{MT},i}$. To find right-hand and left-hand bispinor eigenfunctions of $H_{i,a}$ and $(H_{i,a})^\dagger$, respectively (cf. Eq. (3.27)), we expand the bispinors $Z^{i,R}$ and $Z^{i,L}$ in terms of products of radial wave functions and spin-angular functions

$$Z^{i,R}(\mathbf{r}) = \sum_{\kappa\mu}\begin{pmatrix} \psi^{i,R}_{\kappa\mu}(r)\chi^\mu_\kappa(\hat{\mathbf{r}}) \\ \mathrm{i}\phi^{i,R}_{\kappa\mu}(r)\chi^\mu_{-\kappa}(\hat{\mathbf{r}}) \end{pmatrix} \quad \text{and} \quad Z^{i,L}(\mathbf{r}) = \sum_{\kappa\mu}\begin{pmatrix} \left(\psi^{i,L}_{\kappa\mu}(r)\right)^* \chi^\mu_\kappa(\hat{\mathbf{r}}) \\ \mathrm{i}\left(\phi^{i,L}_{\kappa\mu}(r)\right)^* \chi^\mu_{-\kappa}(\hat{\mathbf{r}}) \end{pmatrix}, \tag{3.33}$$

where the spin-angular functions χ^μ_κ are defined as

$$\chi^\mu_\kappa(\hat{\mathbf{r}}) = \sum_{\tau=\pm\frac{1}{2}} C(l,\frac{1}{2},j;\mu-\tau,\tau)Y_l^{\mu-\tau}(\hat{\mathbf{r}})\chi^\tau. \tag{3.34}$$

[1] A large part of this section has been adapted from earlier publications [24, 29].

$C(l, \frac{1}{2}, j; \mu - \tau, \tau)$ are Clebsch-Gordon coefficients, $Y_l^m(\hat{\mathbf{r}})$ denote the spherical harmonics, and χ^τ are the two-component Pauli spinors:

$$\chi^{\frac{1}{2}} = \begin{pmatrix} 1 \\ 0 \end{pmatrix} \quad \text{and} \quad \chi^{-\frac{1}{2}} = \begin{pmatrix} 0 \\ 1 \end{pmatrix}. \tag{3.35}$$

κ is a (compound) quantum number which determines orbital and total angular momentum l and j:

$$\kappa = \begin{cases} l & \text{for } j = l - \frac{1}{2} \\ -l-1 & \text{for } j = l + \frac{1}{2} \end{cases} \quad \text{or} \quad l = \begin{cases} \kappa & \text{if } \kappa > 0 \\ -\kappa - 1 = |\kappa| - 1 & \text{if } \kappa < 0 \end{cases}, \quad j = \kappa - \frac{1}{2} S_\kappa. \tag{3.36}$$

Substituting the expansion of $Z^{i,R}$ (Eq. (3.33)) into the Dirac equation (Eq. (3.32)) yields a system of coupled differential equations for the radial functions $\psi^{i,R}_{\kappa\mu}(r)$ and $\phi^{i,R}_{\kappa\mu}(r)$:

$$\begin{pmatrix} E - c^2 & -\mathrm{i}c\left(\frac{d}{dr} + \frac{-\kappa+1}{r}\right) \\ -\mathrm{i}c\left(\frac{d}{dr} + \frac{\kappa+1}{r}\right) & E + c^2 \end{pmatrix} \begin{pmatrix} \psi^{i,R}_{\kappa\mu}(r) \\ \mathrm{i}\phi^{i,R}_{\kappa\mu}(r) \end{pmatrix} = \sum_{\kappa'\mu'} \begin{pmatrix} v^{(i),+}_{\kappa\mu\kappa'\mu'}(r)\psi^{i,R}_{\kappa'\mu'}(r) \\ v^{(i),-}_{\kappa\mu\kappa'\mu'}(r)\mathrm{i}\phi^{i,R}_{\kappa'\mu'}(r) \end{pmatrix}, \tag{3.37}$$

where the potential coefficient functions $v^{(i),\pm}_{\kappa\mu\kappa'\mu'}(r)$ are obtained by integrating over $\hat{\mathbf{r}} = (\vartheta, \varphi)$ (for arbitrary but fixed r):

$$v^{(i),+}_{\kappa\mu\kappa'\mu'}(r) = \langle \chi^\mu_\kappa | v^{(i)}_+(\mathbf{r}) | \chi^{\mu'}_{\kappa'} \rangle \quad \text{and} \quad v^{(i),-}_{\kappa\mu\kappa'\mu'}(r) = \langle \chi^\mu_{-\kappa} | v^{(i)}_-(\mathbf{r}) | \chi^{\mu'}_{-\kappa'} \rangle. \tag{3.38}$$

Analogously, we get for $Z^{i,L}$:

$$\begin{pmatrix} E - c^2 & -\mathrm{i}c\left(\frac{d}{dr} + \frac{-\kappa+1}{r}\right) \\ -\mathrm{i}c\left(\frac{d}{dr} + \frac{\kappa+1}{r}\right) & E + c^2 \end{pmatrix} \begin{pmatrix} \psi^{i,L}_{\kappa\mu}(r) \\ \mathrm{i}\phi^{i,L}_{\kappa\mu}(r) \end{pmatrix} = \sum_{\kappa'\mu'} \begin{pmatrix} v^{(i),+}_{\kappa'\mu'\kappa\mu}(r)\psi^{i,L}_{\kappa'\mu'}(r) \\ v^{(i),-}_{\kappa'\mu'\kappa\mu}(r)\mathrm{i}\phi^{i,L}_{\kappa'\mu'}(r) \end{pmatrix}. \tag{3.39}$$

If, in a first step, we consider the case $V(\mathbf{r}) = V_0 = \text{const}$, the equations for the radial functions (Eqs. (3.37) and (3.39)) decouple with respect to $\kappa\mu$, and the eigenvalue equations have the following particular right-hand and left-hand solutions:

$$j^R_{\kappa\mu}(\mathbf{r}) = \begin{pmatrix} j_l(kr)\chi^\mu_\kappa(\hat{\mathbf{r}}) \\ \mathrm{i}ckS_\kappa/(E + c^2) j_{\bar{l}}(kr)\chi^\mu_{-\kappa}(\hat{\mathbf{r}}) \end{pmatrix}, \tag{3.40a}$$

$$h^R_{\kappa\mu}(\mathbf{r}) = \begin{pmatrix} h^{(1)}_l(kr)\chi^\mu_\kappa(\hat{\mathbf{r}}) \\ \mathrm{i}ckS_\kappa/(E + c^2) h^{(1)}_{\bar{l}}(kr)\chi^\mu_{-\kappa}(\hat{\mathbf{r}}) \end{pmatrix}, \tag{3.40b}$$

$$j^L_{\kappa\mu}(\mathbf{r}) = \begin{pmatrix} \{j_l(kr)\}^* \chi^\mu_\kappa(\hat{\mathbf{r}}) \\ \mathrm{i}\left\{ckS_\kappa/(E + c^2) j_{\bar{l}}(kr)\right\}^* \chi^\mu_{-\kappa}(\hat{\mathbf{r}}) \end{pmatrix}, \tag{3.41a}$$

$$h^L_{\kappa\mu}(\mathbf{r}) = \begin{pmatrix} \left\{h^{(1)}_l(kr)\right\}^* \chi^\mu_\kappa(\hat{\mathbf{r}}) \\ \mathrm{i}\left\{ckS_\kappa/(E + c^2) h^{(1)}_{\bar{l}}(kr)\right\}^* \chi^\mu_{-\kappa}(\hat{\mathbf{r}}) \end{pmatrix}, \tag{3.41b}$$

with $k = \sqrt{(E - V_0)^2 - c^4}/c$, $S_\kappa = \operatorname{sgn}\kappa$, and $\bar{l} = l - S_\kappa$. j_l are the spherical Bessel functions, and $h^{(1)}_l$ are the spherical Hankel functions of first kind. $j^R_{\kappa\mu}$ and $j^L_{\kappa\mu}$ are regular at the origin, and

$h^R_{\kappa\mu}$ and $h^L_{\kappa\mu}$ are irregular (diverging) at the origin. For a muffin-tin potential $V(\mathbf{r})$ — which is constant for $r \geq r_{\mathrm{MT},i}$ — the functions $j^R_{\kappa\mu}$, $j^L_{\kappa\mu}$, $h^R_{\kappa\mu}$, and $h^L_{\kappa\mu}$ (and arbitrary linear combinations thereof) are still solutions for $r \geq r_{\mathrm{MT},i}$. This can be used to generate solutions in the whole space with prescribed forms outside the muffin-tin sphere (cf. [29]):

$$J^{i,R}_{\kappa\mu}(\mathbf{r}) = \sum_{\kappa'\mu'} \begin{pmatrix} \psi^{i,R(1)}_{\kappa\mu\kappa'\mu'}(r)\chi^{\mu'}_{\kappa'}(\hat{\mathbf{r}}) \\ \mathrm{i}\phi^{i,R(1)}_{\kappa\mu\kappa'\mu'}(r)\chi^{\mu'}_{-\kappa'}(\hat{\mathbf{r}}) \end{pmatrix} \quad \xrightarrow[r\geq r_{\mathrm{MT},i}]{} \quad j^R_{\kappa\mu}(\mathbf{r}) + \sum_{\kappa'\mu'} t^{i,R}_{\kappa\mu\kappa'\mu'} h^R_{\kappa'\mu'}(\mathbf{r}) \tag{3.42a}$$

$$H^{i,R}_{\kappa\mu}(\mathbf{r}) = \sum_{\kappa'\mu'} \begin{pmatrix} \psi^{i,R(2)}_{\kappa\mu\kappa'\mu'}(r)\chi^{\mu'}_{\kappa'}(\hat{\mathbf{r}}) \\ \mathrm{i}\phi^{i,R(2)}_{\kappa\mu\kappa'\mu'}(r)\chi^{\mu'}_{-\kappa'}(\hat{\mathbf{r}}) \end{pmatrix} \quad \xrightarrow[r\geq r_{\mathrm{MT},i}]{} \quad h^R_{\kappa\mu}(\mathbf{r}) \tag{3.42b}$$

and

$$J^{i,L}_{\kappa\mu}(\mathbf{r}) = \sum_{\kappa'\mu'} \begin{pmatrix} \left(\psi^{i,L(1)}_{\kappa\mu\kappa'\mu'}(r)\right)^* \chi^{\mu'}_{\kappa'}(\hat{\mathbf{r}}) \\ \mathrm{i}\left(\phi^{i,L(1)}_{\kappa\mu\kappa'\mu'}(r)\right)^* \chi^{\mu'}_{-\kappa'}(\hat{\mathbf{r}}) \end{pmatrix} \quad \xrightarrow[r\geq r_{\mathrm{MT},i}]{} \quad j^L_{\kappa\mu}(\mathbf{r}) + \sum_{\kappa'\mu'} t^{i,L}_{\kappa\mu\kappa'\mu'} h^L_{\kappa'\mu'}(\mathbf{r}) \tag{3.43a}$$

$$H^{i,L}_{\kappa\mu}(\mathbf{r}) = \sum_{\kappa'\mu'} \begin{pmatrix} \left(\psi^{i,L(2)}_{\kappa\mu\kappa'\mu'}(r)\right)^* \chi^{\mu'}_{\kappa'}(\hat{\mathbf{r}}) \\ \mathrm{i}\left(\phi^{i,L(2)}_{\kappa\mu\kappa'\mu'}(r)\right)^* \chi^{\mu'}_{-\kappa'}(\hat{\mathbf{r}}) \end{pmatrix} \quad \xrightarrow[r\geq r_{\mathrm{MT},i}]{} \quad h^L_{\kappa\mu}(\mathbf{r}). \tag{3.43b}$$

$J^{i,R}_{\kappa\mu}$ (i.e., essentially the coefficients $t^{i,R}_{\kappa\mu\kappa'\mu'}$ of the matrix $t^{(i)}$ (cf. Eq. (3.42a))) is determined by requiring that $J^{i,R}_{\kappa\mu}$ is regular at the origin and that it is the linear combination of (exactly) one incoming Bessel type function $j^R_{\kappa\mu}$ and a sum of outgoing waves $h^R_{\kappa'\mu'}$. Thus, for each pair of quantum numbers $\kappa\mu$ associated with the function $j^R_{\kappa\mu}$, we obtain one regular solution $J^{i,R}_{\kappa\mu}$ of Eq. (3.37). Similarly, $H^{i,R}_{\kappa\mu}$ (for each index pair $\kappa\mu$) denotes a solution of Eq. (3.37) which is identical to $h^R_{\kappa\mu}$ outside the muffin-tin sphere. $H^{i,R}_{\kappa\mu}$ is uniquely determined by $h^R_{\kappa\mu}$ and so $H^{i,R}_{\kappa\mu}$ is also labeled by $\kappa\mu$. $H^{i,R}_{\kappa\mu}$ is in general irregular at the origin. The functions $J^{i,L}_{\kappa\mu}$ and $H^{i,L}_{\kappa\mu}$ are obtained analogously (cf. Eq. (3.43a)) and are regular and irregular solutions of Eq. (3.39).

From a general pair of a right-hand and left-hand solutions $Z^{i,R}$ and $Z^{i,L}$ of Eqs. (3.37) and (3.39), one can obtain a Wronskian relation which is useful to calculate the functions $J^{i,R}_{\kappa\mu}$, $H^{i,R}_{\kappa\mu}$, $J^{i,L}_{\kappa\mu}$, and $H^{i,L}_{\kappa\mu}$. Furthermore, this relation is used in the construction of the single-particle Green function. Expanding $Z^{i,R}$ and $Z^{i,L}$ as in Eq. (3.33), the following combination of radial functions is independent of the radius r and can therefore be calculated at the most convenient position (for another pair of solutions the constant value might of course be different):

$$\begin{aligned} W\left(Z^{i,L}, Z^{i,R}\right) &:= \sum_{\kappa\mu} \left\{ cr^2 \left(\psi^{i,L}_{\kappa\mu}(r)\phi^{i,R}_{\kappa\mu}(r) - \phi^{i,L}_{\kappa\mu}(r)\psi^{i,R}_{\kappa\mu}(r)\right)\right\} \\ &= \text{const.} \end{aligned} \tag{3.44}$$

In particular, we get for the functions $J^{i,R}_{\kappa\mu}$, $H^{i,R}_{\kappa\mu}$, $J^{i,L}_{\kappa\mu}$, and $H^{i,L}_{\kappa\mu}$ (cf. Eqs. (3.42) and (3.43)) using

their asymptotic behavior for large values of r:

$$W\left(J^{i,L}_{\kappa\mu}, H^{i,R}_{\kappa'\mu'}\right) = w\,\delta_{\kappa\kappa'}\delta_{\mu\mu'} \tag{3.45a}$$

$$W\left(H^{i,L}_{\kappa\mu}, J^{i,R}_{\kappa'\mu'}\right) = -w\,\delta_{\kappa\kappa'}\delta_{\mu\mu'} \tag{3.45b}$$

$$W\left(J^{i,L}_{\kappa\mu}, J^{i,R}_{\kappa'\mu'}\right) = W\left(H^{i,L}_{\kappa\mu}, H^{i,R}_{\kappa'\mu'}\right) = 0, \tag{3.45c}$$

with

$$w = -\frac{1}{\mathrm{i}k}\frac{c^2}{E+c^2}. \tag{3.46}$$

In the general case, $\mathbf{B} = \mathbf{B}(\mathbf{r})$, a direct solution of the coupled radial equations is very time consuming and cumbersome. Hence we confine ourselves to the special case $\mathbf{B} = B(r)\hat{\mathbf{e}}$, i.e., the absolute value of the magnetic field can depend on the radius r, but the magnetic field points always in the direction of an (arbitrarily selectable) unit vector $\hat{\mathbf{e}}$.

For the solution of the radial equations it is furthermore useful to select $\mathbf{B}$ parallel to the z direction. In this case the potential inside the muffin-tin sphere takes the form

$$V_{i,a}(\mathbf{r}) = \begin{pmatrix} v(r)1_2 + \sigma_z B(r) & 0 \\ 0 & v(r)1_2 - \sigma_z B(r) \end{pmatrix} \tag{3.47}$$

and the radial equations partly decouple. An arbitrary orientation of $\mathbf{B}$ can then be included by proper coordinate transformations of the solutions obtained for the case $\mathbf{B}\,||\,\mathbf{z}$ (cf. [30]). By incorporating the potential in Eq. (3.47) into Eq. (3.37), the system of equations for the radial wave functions reduces to (the argument r of the radial wave functions is not written):

$$c\frac{d}{dr}\psi^{i,R}_{\kappa\mu} = -c\frac{\kappa+1}{r}\psi^{i,R}_{\kappa\mu} + \left[E + c^2 - v(r)\right]\phi^{i,R}_{\kappa\mu} - \sum_{\kappa'\mu'} B(r)\langle\chi^{\mu}_{-\kappa}|\sigma_z|\chi^{\mu'}_{-\kappa'}\rangle\phi^{i,R}_{\kappa'\mu'}\,, \tag{3.48a}$$

$$c\frac{d}{dr}\phi^{i,R}_{\kappa\mu} = -c\frac{-\kappa+1}{r}\phi^{i,R}_{\kappa\mu} - \left[E - c^2 - v(r)\right]\psi^{i,R}_{\kappa\mu} + \sum_{\kappa'\mu'} B(r)\langle\chi^{\mu}_{\kappa}|\sigma_z|\chi^{\mu'}_{\kappa'}\rangle\psi^{i,R}_{\kappa'\mu'}\,. \tag{3.48b}$$

In the case of a vanishing magnetic field only radial functions with identical quantum numbers κ and μ are coupled and the solutions do not depend on μ (cf. [30]). To simplify these equations in the presence of a magnetic field, the following relations are very helpful (cf., e.g., [24, 30]):

$$\langle\chi^{\mu}_{\kappa}|\sigma_z|\chi^{\mu'}_{\kappa'}\rangle = \begin{cases} -\frac{\mu}{\kappa+1/2} & \text{if } \kappa' = \kappa \text{ and } \mu' = \mu, \\ -\left[1 - \left(\frac{\mu}{\kappa+1/2}\right)^2\right]^{1/2} & \text{if } \kappa' = -\kappa - 1 \text{ and } \mu' = \mu, \\ 0 & \text{otherwise.} \end{cases} \tag{3.49}$$

The system of equations (Eqs. (3.48a) and (3.48b)) then only couples radial functions ψ and ϕ with identical quantum number index μ and $\kappa' = \kappa$ or $\kappa' = -\kappa - 1$. Hence, we obtain radial

equations for the functions $\psi^{i,R}_{\kappa\mu}$ and $\phi^{i,R}_{\kappa\mu}$

$$\begin{aligned} c\frac{d}{dr}\psi^{i,R}_{\kappa\mu} = &-c\frac{\kappa+1}{r}\psi^{i,R}_{\kappa\mu} + \left[E + c^2 - v\right]\phi^{i,R}_{\kappa\mu} - B\langle\chi^{\mu}_{-\kappa}|\sigma_z|\chi^{\mu}_{-\kappa}\rangle\phi^{i,R}_{\kappa\mu} \\ &- B\langle\chi^{\mu}_{-\kappa}|\sigma_z|\chi^{\mu}_{\kappa-1}\rangle\phi^{i,R}_{-\kappa+1,\mu} \end{aligned} \tag{3.50a}$$

$$\begin{aligned} c\frac{d}{dr}\phi^{i,R}_{\kappa\mu} = &-c\frac{-\kappa+1}{r}\phi^{i,R}_{\kappa\mu} - \left[E - c^2 - v\right]\psi^{i,R}_{\kappa\mu} + B\langle\chi^{\mu}_{\kappa}|\sigma_z|\chi^{\mu}_{\kappa}\rangle\psi^{i,R}_{\kappa\mu} \\ &+ B\langle\chi^{\mu}_{\kappa}|\sigma_z|\chi^{\mu}_{-\kappa-1}\rangle\psi^{i,R}_{-\kappa-1,\mu}\,. \end{aligned} \tag{3.50b}$$

The coupling between $\psi^{i,R}_{\kappa\mu}$ and $\phi^{i,R}_{-\kappa+1,\mu}$ in Eq. (3.50a), i.e., between states with quantum numbers l and $l \pm 2$, has only very little influence on the resulting radial functions and can therefore be neglected (cf. [27, 30]). Hence, for each pair of indices (κ, μ) one obtains a set of four coupled radial equations which have to be solved simultaneously.

$$c\frac{d}{dr}\psi^{i,R}_{\kappa\mu} = -c\frac{\kappa+1}{r}\psi^{i,R}_{\kappa\mu} + \left[E + c^2 - v\right]\phi^{i,R}_{\kappa\mu} - B\langle\chi^{\mu}_{-\kappa}|\sigma_z|\chi^{\mu}_{-\kappa}\rangle\phi^{i,R}_{\kappa\mu} \tag{3.51a}$$

$$\begin{aligned} c\frac{d}{dr}\phi^{i,R}_{\kappa\mu} = &-c\frac{-\kappa+1}{r}\phi^{i,R}_{\kappa\mu} - \left[E - c^2 - v\right]\psi^{i,R}_{\kappa\mu} + B\langle\chi^{\mu}_{\kappa}|\sigma_z|\chi^{\mu}_{\kappa}\rangle\psi^{i,R}_{\kappa\mu} \\ &+ B\langle\chi^{\mu}_{\kappa}|\sigma_z|\chi^{\mu}_{-\kappa-1}\rangle\psi^{i,R}_{-\kappa-1,\mu} \end{aligned} \tag{3.51b}$$

$$c\frac{d}{dr}\psi^{i,R}_{-\kappa-1,\mu} = c\frac{\kappa}{r}\psi^{i,R}_{-\kappa-1,\mu} + \left[E + c^2 - v\right]\phi^{i,R}_{-\kappa-1,\mu} - B\langle\chi^{\mu}_{\kappa+1}|\sigma_z|\chi^{\mu}_{\kappa+1}\rangle\phi^{i,R}_{-\kappa-1,\mu} \tag{3.51c}$$

$$\begin{aligned} c\frac{d}{dr}\phi^{i,R}_{-\kappa-1,\mu} = &-c\frac{\kappa+2}{r}\phi^{i,R}_{-\kappa-1,\mu} - \left[E - c^2 - v\right]\psi^{i,R}_{-\kappa-1,\mu} + B\langle\chi^{\mu}_{-\kappa-1}|\sigma_z|\chi^{\mu}_{-\kappa-1}\rangle\psi^{i,R}_{-\kappa-1,\mu} \\ &+ B\langle\chi^{\mu}_{-\kappa-1}|\sigma_z|\chi^{\mu}_{\kappa}\rangle\psi^{i,R}_{\kappa\mu}\,. \end{aligned} \tag{3.51d}$$

Contrary to the nonmagnetic case, the radial wavefunctions depend on the magnetic quantum number μ. This dependence is particularly strong for d-type valence electron states in ferromagnetic iron. As an example, solutions $\psi_{\kappa\mu\kappa'\mu'}(r) = \psi^{1,R(1)}_{\kappa\mu\kappa'\mu'}(r)$ (cf. Eq. (3.42a)) of the radial Dirac equations (Eqs. (3.51a)–(3.51d)) for the topmost surface layer of Fe(001) at 0.8 eV below E_F are shown in Fig. 3.3. As can be seen, the real parts of the $\psi_{\kappa\mu\kappa\mu}$ show a strong systematic dependence on μ, where $\psi_{2,\mu,2,\mu}(r)$ closely resemble $\psi_{-3,-\mu,-3,-\mu}(r)$. The imaginary parts, on the other hand, show only a relatively weak dependence on μ. Moreover, one finds that

$$\psi_{\kappa\mu\kappa\mu}(-\mathbf{B}, r) = \psi_{\kappa,-\mu,\kappa,-\mu}(\mathbf{B}, r). \tag{3.52}$$

The lower panels in Fig. 3.3 show the associated radial functions $\psi_{\kappa,\mu,-\kappa-1,\mu}$ which exhibit a clearly less dramatic dependence. Their amplitudes, however, are comparable to those of the original $\psi_{\kappa\mu\kappa\mu}$. For the associated functions one finds the relations

$$\psi_{\kappa,\mu,-\kappa-1,\mu}(r) = \psi_{-\kappa-1,\mu,\kappa,\mu}(r) \tag{3.53}$$

and

$$\psi_{\kappa,\mu,-\kappa-1,\mu}(-\mathbf{B}, r) = -\psi_{\kappa,-\mu,-\kappa-1,-\mu}(\mathbf{B}, r). \tag{3.54}$$

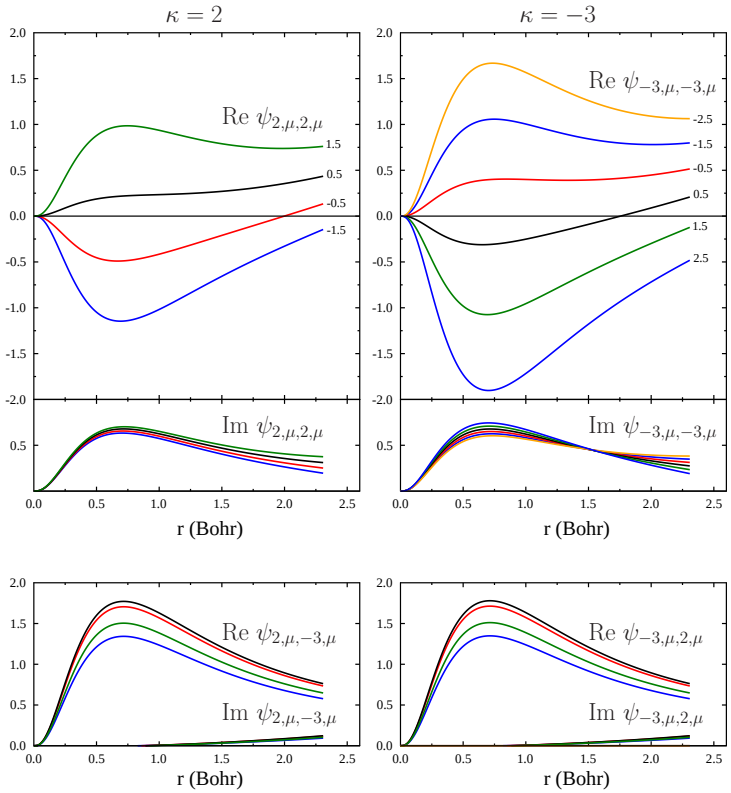

Fig. 3.3: Valence electron state $|2\rangle$: Regular radial wave functions $\psi_{\kappa\mu\kappa'\mu'}(r)$ for $l = 2$ in the topmost surface layer of Fe(001). $E = 0.8$ eV below E_F. Left-hand side: $\kappa = 2$; right-hand side: $\kappa = -3$.

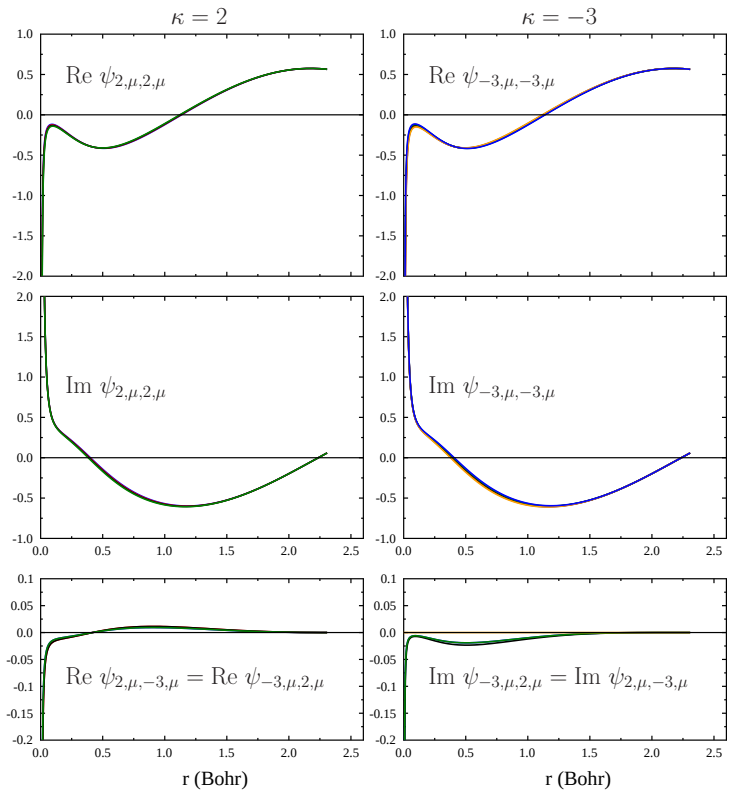

Fig. 3.4: Valence electron state $|2\rangle$: Irregular radial wave functions $\psi_{\kappa\mu\kappa'\mu'}(r)$ for $l = 2$ in the topmost surface layer of Fe(001). $E = E_F - 0.8$ eV. Left-hand side: $\kappa = 2$; right-hand side: $\kappa = -3$.

The corresponding irregular wavefunctions (Fig. 3.4), on the other hand, show almost no dependence on μ. In contrast to the case for the regular functions, the associated functions $\psi_{\kappa,\mu,-\kappa-1,\mu}$ are rather small and play only a minor role.

A similar behaviour can be seen for radial wavefunctions with higher kinetic energies (typical for the outgoing states $|3\rangle$ and $|4\rangle$): a relatively weak dependence on μ and very small associated functions $\psi_{\kappa,\mu,-\kappa-1,\mu}$. A typical example is shown in Fig. 3.5.

Hence we conclude that the presence of a magnetic field and spin-orbit coupling mainly affects the valence states of $l \geq 2$ character. *sp*-type states, as well as the states representing the outgoing electrons, are clearly less sensitive with respect to these influences.

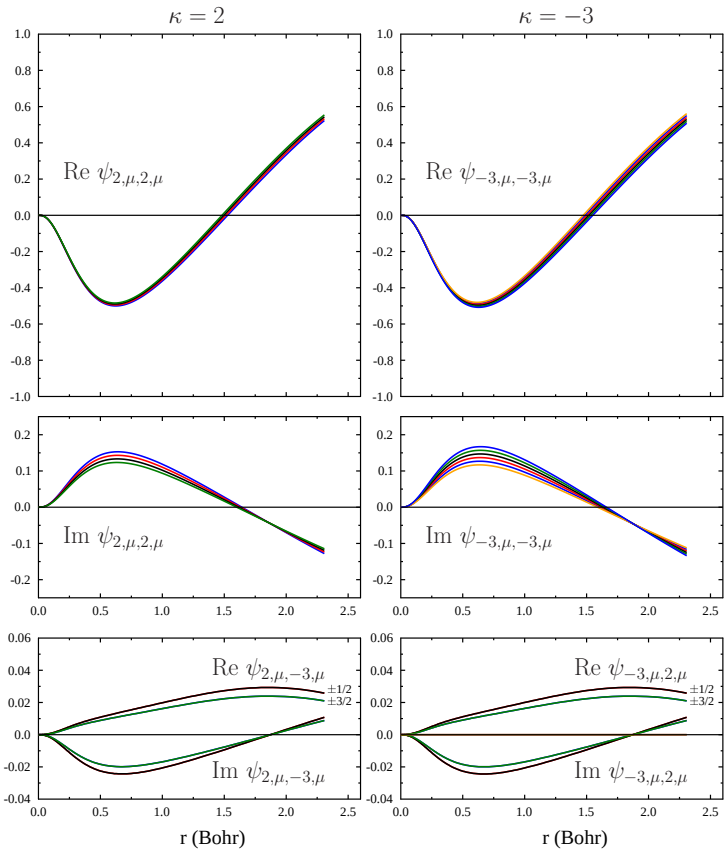

Fig. 3.5: Final one-electron states $|3\rangle$ or $|4\rangle$: Regular radial wave functions $\psi_{\kappa\mu\kappa'\mu'}(r)$ for $l = 2$ in the topmost surface layer of Fe(001). $E = 12$ eV. Left-hand side: $\kappa = 2$; right-hand side: $\kappa = -3$.

3.2.2 Multiple scattering in atomic layers

Scattering by a single monoatomic layer

We next consider the scattering by a single monoatomic layer, where (identical) atomic muffin-tin potentials are centered at the sites of a two-dimensional Bravais lattice which is supposed to lie in the (x, y) plane with the centers of the muffin-tin spheres at $z = 0$. In particular, a representative atom should be located at $\mathbf{r} = 0$. The potential inside the spheres is not necessarily radially symmetric, but it is supposed to go smoothly to the value in the interstitial region. The potential

matrix outside the muffin-tin spheres consists of spin-dependent constant elements:

$$V_0^\tau = V_{\rm re}^\tau + {\rm i}V_{\rm im}^\tau \quad \text{with} \quad \tau = \pm. \tag{3.55}$$

The real part $V_{\rm re}^\tau$ is already spin-dependent in the underlying *ab initio* calculations for the ground state, and the spin-dependence of the imaginary part $V_{\rm im}^\tau$ reflects the spin-dependence of the inelastic mean free path for LEED electrons (cf. [32–34]) and the spin-dependence of the valence hole lifetime (see, e.g., [35], and reference therein).

In previous work (cf. [27]) relativistic multiple scattering in ferromagnets was treated with the restriction that the quantities $V_{\rm re}^\tau$ and $V_{\rm im}^\tau$ are spin independent. Here we allow for spin-dependent constants $V_{\rm re}^\tau$ and $V_{\rm im}^\tau$.

To describe the scattering properties of the monoatomic layer, we first note that outside the atomic layer, i.e., in the region of a constant potential, the following linear combinations of plane waves are solutions of the Dirac equation (on the left-hand side of the layer: $z < 0$ and on the right-hand side: $z > 0$):

$$\psi(\mathbf{r}) = \begin{cases} \sum\limits_{\mathbf{g},\tau} u_{\mathbf{g},\tau}^{+} \begin{pmatrix} \chi^\tau \\ \frac{c\,\boldsymbol{\sigma}\cdot\mathbf{k}_{\mathbf{g}}^{+,\tau}}{E+c^2}\chi^\tau \end{pmatrix} e^{{\rm i}\mathbf{k}_{\mathbf{g}}^{+,\tau}\cdot\mathbf{r}} + \sum\limits_{\mathbf{g},\tau} v_{\mathbf{g},\tau}^{-} \begin{pmatrix} \chi^\tau \\ \frac{c\,\boldsymbol{\sigma}\cdot\mathbf{k}_{\mathbf{g}}^{-,\tau}}{E+c^2}\chi^\tau \end{pmatrix} e^{{\rm i}\mathbf{k}_{\mathbf{g}}^{-,\tau}\cdot\mathbf{r}} & \text{for } z < 0 \\ \sum\limits_{\mathbf{g},\tau} u_{\mathbf{g},\tau}^{-} \begin{pmatrix} \chi^\tau \\ \frac{c\,\boldsymbol{\sigma}\cdot\mathbf{k}_{\mathbf{g}}^{-,\tau}}{E+c^2}\chi^\tau \end{pmatrix} e^{{\rm i}\mathbf{k}_{\mathbf{g}}^{-,\tau}\cdot\mathbf{r}} + \sum\limits_{\mathbf{g},\tau} v_{\mathbf{g},\tau}^{+} \begin{pmatrix} \chi^\tau \\ \frac{c\,\boldsymbol{\sigma}\cdot\mathbf{k}_{\mathbf{g}}^{+,\tau}}{E+c^2}\chi^\tau \end{pmatrix} e^{{\rm i}\mathbf{k}_{\mathbf{g}}^{+,\tau}\cdot\mathbf{r}} & \text{for } z > 0 \end{cases}, \tag{3.56}$$

with $\mathbf{k}_{\mathbf{g}}^{\pm,\tau} = (\mathbf{k}^\parallel + \mathbf{g}^\parallel, \pm k_{\mathbf{g}}^{z,\tau})$, $k_{\mathbf{g}}^{z,\tau} = \sqrt{(k^\tau)^2 - |\mathbf{k}^\parallel + \mathbf{g}^\parallel|^2}$, and $k^\tau = \sqrt{(E - \tilde{v}_0^\tau)^2 - c^2}/c$. Because of the two-dimensional periodicity, the parallel momentum $\mathbf{k}^\parallel$ is conserved (modulo a reciprocal lattice vectors $\mathbf{g}^\parallel$).

$u_{\mathbf{g},\tau}^{\pm}$ denotes coefficients of plane waves moving towards the layer (incoming plane waves; +(-): movement in positive (negative) z direction) and $v_{\mathbf{g},\tau}^{\pm}$ are coefficients of plane waves moving away from the layer (outgoing plane waves). The coefficients $u_{\mathbf{g},\tau}^{\pm}$ and $v_{\mathbf{g},\tau}^{\pm}$ have to be chosen such that one obtains solutions of the Dirac equation which are continuously differentiable in the whole space. For example, by given coefficients $u_{\mathbf{g},\tau}^{\pm}$, the coefficients $v_{\mathbf{g},\tau}^{\pm}$ are determined by

$$v_{\mathbf{g},\tau}^{s} = \sum_{s'=\pm} \sum_{\mathbf{g}'} \sum_{\tau'=\pm} M_{\mathbf{g}\mathbf{g}'\tau\tau'}^{ss'}\, u_{\mathbf{g}',\tau'}^{s'}, \quad s = \pm, \tag{3.57}$$

where the scattering matrix M can be calculated by an intra-layer multiple scattering formalism. A description of this method can be found for the non-relativistic case in [31] and for the relativistic case in [27, 28, 30]. The following explicit expression for the relativistic case is an important contribution to the Green function:

$$\begin{aligned} M_{\mathbf{g}\mathbf{g}'\tau\tau'}^{ss'} = \delta_{\mathbf{g}\mathbf{g}'\tau\tau'}^{ss'} + \frac{8\pi^2}{k^\tau A_c k_{\mathbf{g}}^{z,\tau}} \sum_{\substack{\kappa\mu \\ \kappa'\mu' \\ \kappa''\mu''}} {\rm i}^{-l+l'} C(l, \frac{1}{2}, j; \mu-\tau, \tau) Y_l^{\mu-\tau}(\hat{\mathbf{k}}_{\mathbf{g}}^{s,\tau}) \\ \times C(l', \frac{1}{2}, j'; \mu'-\tau', \tau') [Y_{l'}^{\mu'-\tau'}(\hat{\mathbf{k}}_{\mathbf{g}'}^{s',\tau'})]^*\, t_{\kappa\mu,\kappa'\mu'}^R\, [1-X]_{\kappa''\mu'',\kappa'\mu'}^{-1}. \end{aligned} \tag{3.58}$$

The matrix M contains the single-site scattering matrix ($t^R_{\kappa\mu,\kappa'\mu'}$) (cf. Eq. (3.42a)) and the geometry of the two-dimensional Bravais lattice, which is contained in the matrix X:

$$X_{\kappa\mu\kappa'\mu'} = \sum_{j'} \sum_{\kappa''\mu''} \exp(\mathrm{i}\mathbf{k}^{\parallel} \cdot \mathbf{R}^{\parallel}_{j'})\, t^R_{\kappa''\mu'',\kappa'\mu'}\, G_{\kappa''\mu'',\kappa\mu}(-\mathbf{R}^{\parallel}_{j'}) \ . \tag{3.59}$$

The matrix G describes the expansion of the outgoing waves $h^R_{\kappa\mu}$ (cf. Eq. (3.40b)) from the j'-th atomic site in terms of incoming waves $j^R_{\kappa'\mu'}$ (cf. Eq. (3.40a)) at the (representative) site at the origin:

$$h^R_{\kappa\mu}(\mathbf{r} - \mathbf{R}_{j'}) = \sum_{\kappa'\mu'} G_{\kappa\mu,\kappa'\mu'}(-\mathbf{R}^{\parallel}_{j'})\, j^R_{\kappa'\mu'}(\mathbf{r}) \ . \tag{3.60}$$

Explicitly one has (see, e.g., [28])

$$\begin{aligned} G_{\kappa'\mu',\kappa\mu}(-\mathbf{R}^{\parallel}_j) = \sum_{\tau} \sum_{l''m''} & 4\pi\, \mathrm{i}^{l-l'-l''} (-1)^{m''+m'} h^{(1)}_{l''}(k^\tau |\mathbf{R}^{\parallel}_j|) Y^{-m''}_{l''}(-\hat{\mathbf{R}}^{\parallel}_j) \\ & \times \int Y^m_l(\hat{\mathbf{r}}) Y^{m''}_{l''}(\hat{\mathbf{r}}) Y^{-m'}_{l'}(\hat{\mathbf{r}})\, d\Omega\, C(l, \frac{1}{2}, j; \mu - \tau, \tau) C(l', \frac{1}{2}, j'; \mu' - \tau, \tau) \ . \end{aligned} \tag{3.61}$$

Scattering by the surface potential barrier

In addition one has to take into account the scattering by the surface potential barrier. For this purpose it is convenient to neglect the two-dimensional corrugation of the surface potential parallel to the surface. The resulting differential equation for the one-dimensional potential $V_{\mathrm{surf}}(z)$ can easily be solved (for details see, e.g., [24, 30], and references therein), and the scattering by $V_{\mathrm{surf}}(z)$ is then also described by a scattering matrix.

The functional form of the surface potential barrier $V_{\mathrm{surf}}(z)$ which is used in this work (for different approaches see, e.g., [24]) is as follows:

$$V_{\mathrm{surf}}(z) = \begin{cases} \frac{1}{4|z-z_1|} & \text{for } z < z_2 \quad \text{(image potential asymptotics)} \\ p_3(z) & \text{for } z_2 \le z < 0 \quad \text{(third order polynomial)} \\ V_{0r} & \text{for } z = 0 \quad \text{(matching condition to inner potential)} \end{cases} \ . \tag{3.62}$$

This means that for values of $z > z_2$ (on the vacuum side of the barrier), $V_{\mathrm{surf}}(z)$ has the form of an image potential with the image plane located at z_1. The potential in the region between z_2 and $z = 0$ (internuclear plane of the first layer) is approximated by a third order polynomial $p_3(z)$ which matches the image potential at z_2 and the inner potential at $z = 0$. This polynomial is uniquely determined by the values of z_1, z_2, V_{0r}, and the condition of continuous differentiability of $V_{\mathrm{surf}}(z)$ at the matching points z_2 and $z = 0$.

3.2.3 Valence electron Green function

In this section the construction of the $\mathbf{k}^{\parallel}$-resolved valence electron Green function $G_2(\mathbf{r}, \mathbf{r}'; E, \mathbf{k}^{\parallel})$ for a semi-infinite crystal is described (cf., e.g., [24,28,36], and references therein). $G_2(\mathbf{r}, \mathbf{r}'; E, \mathbf{k}^{\parallel})$ follows from $G_2(\mathbf{r}, \mathbf{r}'; E)$ (Eq. (3.63)) by a two-dimensional lattice Fourier transform. A Dyson equation for $G_2(\mathbf{r}, \mathbf{r}'; E)$, containing a so called empty layer Green function, is transformed to a Dyson equation for the $\mathbf{k}^{\parallel}$-resolved Green function $G_2(\mathbf{r}, \mathbf{r}'; E, \mathbf{k}^{\parallel})$.

$G_2(\mathbf{r}, \mathbf{r}'; E, \mathbf{k}^{\parallel})$ is used to evaluate $(e, 2e)$- and (p, ep)-matrix elements (see Section 3.1). Moreover, by integrating the imaginary part of $G_2(\mathbf{r}, \mathbf{r}; E, \mathbf{k}^{\parallel})$ over a layer, the corresponding $\mathbf{k}^{\parallel}$-resolved density of states is obtained, which is a useful tool to understand electronic properties of surface systems and particularly $(e, 2e)$ and (p, ep) spectra.

The valence electron Green function $G_2(\mathbf{r}, \mathbf{r}'; E)$ (for the complex energy E) is a solution of the following inhomogeneous partial differential equation ($\delta(\mathbf{r} - \mathbf{r}')$ denotes the (scalar valued) Dirac delta function and 1_4 is the 4×4 unit matrix.):

$$(E - H(\mathbf{r}))G_2(\mathbf{r}, \mathbf{r}'; E) = \delta(\mathbf{r} - \mathbf{r}')1_4, \qquad \mathbf{r}, \mathbf{r}' \in \mathbb{R}^3, \tag{3.63}$$

where the Hamiltonian $H = H_0 + V$, the potential $V(\mathbf{r})$, and the partitioning of V are as in Eqs. (3.23) and (3.26):

$$\begin{aligned} H(\mathbf{r}) &= H_0 + V_{\text{surf}}(\mathbf{r}) + \sum_{i=1}^{\infty} V_i(\mathbf{r}) \\ &= H_0 + V_{\text{surf}}(\mathbf{r}) + \sum_{i=1}^{\infty} \sum_{\mathbf{R}^{\parallel}} V_{i,a}(\mathbf{r} - (\mathbf{c}_i + \mathbf{R}^{\parallel})). \end{aligned} \tag{3.64}$$

$H_0 = c\,\boldsymbol{\alpha} \cdot \mathbf{p} + c^2\beta$ is the Hamiltonian of a free electron.

To calculate $G_2(\mathbf{r}, \mathbf{r}'; E)$ for $\mathbf{r}$ in the i-th and $\mathbf{r}'$ in the j-th layer, respectively, it is useful to introduce the following Green functions (cf. [24, 28, 36]): the empty space Green function $G_0(\mathbf{r}, \mathbf{r}'; E)$, the single-site (atomic) Green function $G_{j,a}(\mathbf{r}, \mathbf{r}'; E)$, and the empty-layer Green function $G^j_{\text{empty}}(\mathbf{r}, \mathbf{r}'; E)$. These Green functions are required to satisfy equations analogous to Eq. (3.63) for modified potentials ($\mathbf{r}, \mathbf{r}' \in \mathbb{R}^3$):

$$[E - H_0]\, G_0(\mathbf{r}, \mathbf{r}'; E) = \delta(\mathbf{r} - \mathbf{r}')1_4, \tag{3.65}$$

$$[E - (H_0 + V_{j,a}(\mathbf{r}))]\, G_{j,a}(\mathbf{r}, \mathbf{r}'; E) = \delta(\mathbf{r} - \mathbf{r}')1_4, \tag{3.66}$$

$$\left[E - (H_0 + V^j_{\text{empty}}(\mathbf{r}))\right] G^j_{\text{empty}}(\mathbf{r}, \mathbf{r}'; E) = \delta(\mathbf{r} - \mathbf{r}')1_4, \tag{3.67}$$

with

$$V^j_{\text{empty}}(\mathbf{r}) = V_{\text{surf}}(\mathbf{r}) + \sum_{\substack{i=1 \\ i \neq j}}^{\infty} V_i(\mathbf{r}). \tag{3.68}$$

$G^j_{\text{empty}}(\mathbf{r}, \mathbf{r}'; E)$ is therefore calculated for a system where formally the potential of the j-th layer $V_j(\mathbf{r})$ is removed from the system ($V_j(\mathbf{r}) = 0$).

Because of $H = H_0 + V^j_{\text{empty}} + V_j$, the valence electron Green function satisfies a Dyson equation containing G^j_{empty} and the perturbation V_j:

$$G_2(\mathbf{r}, \mathbf{r}'; E) = G^j_{\text{empty}}(\mathbf{r}, \mathbf{r}'; E) + \int_{\mathbb{R}^3} G^j_{\text{empty}}(\mathbf{r}, \mathbf{r}''; E) V_j(\mathbf{r}'') G_2(\mathbf{r}'', \mathbf{r}'; E)\, d\mathbf{r}''. \tag{3.69}$$

The $\mathbf{r}''$ integration has formally to be performed over the whole space. However, the potential V_j vanishes outside the j-th layer, and so the $\mathbf{r}''$ integration reduces effectively to the region of

the j-th layer. Then the expression $G_2(\mathbf{r}'', \mathbf{r}'; E)$ in the integral (Eq. (3.69)) has to be evaluated only for $\mathbf{r}''$, $\mathbf{r}'$ in the j-th layer. This is the reason for choosing the empty layer with respect to $\mathbf{r}'$.

Furthermore, the empty layer Green function fulfills a Dyson equation containing G_0 and the perturbation V^j_{empty}:

$$G^j_{\text{empty}}(\mathbf{r}, \mathbf{r}'; E) = G_0(\mathbf{r}, \mathbf{r}'; E) + \int_{\mathbb{R}^3} G_0(\mathbf{r}, \mathbf{r}''; E) V^j_{\text{empty}}(\mathbf{r}'') G^j_{\text{empty}}(\mathbf{r}'', \mathbf{r}'; E)\, d\mathbf{r}''. \tag{3.70}$$

The $\mathbf{k}^{\parallel}$-resolved valence electron Green function $G_2(\mathbf{r}, \mathbf{r}'; E, \mathbf{k}^{\parallel})$ is defined as the two-dimensional lattice Fourier transform of $G_2(\mathbf{r}, \mathbf{r}'; E)$:

$$G_2(\mathbf{r}, \mathbf{r}'; E, \mathbf{k}^{\parallel}) := \sum_{\mathbf{R}^{\parallel}} G_2(\mathbf{r} - \mathbf{R}^{\parallel}, \mathbf{r}'; E) e^{\mathrm{i}\mathbf{k}^{\parallel} \cdot \mathbf{R}^{\parallel}}, \tag{3.71}$$

where the sum has to be taken over all lattice vectors $\mathbf{R}^{\parallel}$ of the two-dimensional Bravais lattice. Analogously, one finds for $G_0(\mathbf{r}, \mathbf{r}'; E)$ and $G^j_{\text{empty}}(\mathbf{r}, \mathbf{r}'; E)$:

$$G_0(\mathbf{r}, \mathbf{r}'; E, \mathbf{k}^{\parallel}) := \sum_{\mathbf{R}^{\parallel}} G_0(\mathbf{r} - \mathbf{R}^{\parallel}, \mathbf{r}'; E) e^{\mathrm{i}\mathbf{k}^{\parallel} \cdot \mathbf{R}^{\parallel}}, \tag{3.72}$$

$$G^j_{\text{empty}}(\mathbf{r}, \mathbf{r}'; E, \mathbf{k}^{\parallel}) := \sum_{\mathbf{R}^{\parallel}} G^j_{\text{empty}}(\mathbf{r} - \mathbf{R}^{\parallel}, \mathbf{r}'; E) e^{\mathrm{i}\mathbf{k}^{\parallel} \cdot \mathbf{R}^{\parallel}}. \tag{3.73}$$

Due to the two-dimensional lattice periodicity, the functions $G_2(\mathbf{r}, \mathbf{r}'; E)$ and $G^j_{\text{empty}}(\mathbf{r}, \mathbf{r}'; E)$ have the property

$$G_2(\mathbf{r} + \mathbf{R}^{\parallel}, \mathbf{r}' + \mathbf{R}^{\parallel}; E) = G_2(\mathbf{r}, \mathbf{r}'; E), \quad G_{\text{empty}}(\mathbf{r} + \mathbf{R}^{\parallel}, \mathbf{r}' + \mathbf{R}^{\parallel}; E) = G_{\text{empty}}(\mathbf{r}, \mathbf{r}'; E) \tag{3.74}$$

for an arbitrary lattice vector $\mathbf{R}^{\parallel}$ of the two-dimensional Bravais lattice. Then, using Eq. (3.74) and the two-dimensional periodicity of $V(\mathbf{r})$ and $V^j_{\text{empty}}(\mathbf{r})$, it follows that the Dyson equations (Eqs. (3.69) and (3.70)) are also valid for the $\mathbf{k}^{\parallel}$-resolved Green functions:

$$G_2(\mathbf{r}, \mathbf{r}'; E, \mathbf{k}^{\parallel}) = G^j_{\text{empty}}(\mathbf{r}, \mathbf{r}'; E, \mathbf{k}^{\parallel}) + \int\limits_{V_{\text{cell},j}} G^j_{\text{empty}}(\mathbf{r}, \mathbf{r}''; E, \mathbf{k}^{\parallel}) V_j(\mathbf{r}'') G_2(\mathbf{r}'', \mathbf{r}'; E, \mathbf{k}^{\parallel})\, d\mathbf{r}'' \tag{3.75}$$

(where the $\mathbf{r}''$ integration is over a representative unit cell $V_{\text{cell},j}$ of the j-th layer),

$$G^j_{\text{empty}}(\mathbf{r}, \mathbf{r}'; E, \mathbf{k}^{\parallel}) = G_0(\mathbf{r}, \mathbf{r}'; E, \mathbf{k}^{\parallel}) + \int G_0(\mathbf{r}, \mathbf{r}''; E, \mathbf{k}^{\parallel}) V^j_{\text{empty}}(\mathbf{r}'') G^j_{\text{empty}}(\mathbf{r}'', \mathbf{r}'; E, \mathbf{k}^{\parallel})\, d\mathbf{r}''. \tag{3.76}$$

Furthermore, the Green functions $G_2(\mathbf{r}, \mathbf{r}'; E, \mathbf{k}^{\parallel})$, $G^j_{\text{empty}}(\mathbf{r}, \mathbf{r}'; E, \mathbf{k}^{\parallel})$, and $G_0(\mathbf{r}, \mathbf{r}'; E, \mathbf{k}^{\parallel})$ fulfill the Bloch condition

$$G_2(\mathbf{r} + \mathbf{R}^{\parallel}, \mathbf{r}'; E, \mathbf{k}^{\parallel}) = G_2(\mathbf{r}, \mathbf{r}'; E, \mathbf{k}^{\parallel}) e^{\mathrm{i}\mathbf{k}^{\parallel} \cdot \mathbf{R}^{\parallel}}, \quad \mathbf{r}, \mathbf{r}' \in \mathbb{R}^3 \tag{3.77}$$

(analogously for $G^j_{\text{empty}}(\mathbf{r},\mathbf{r}';E,\mathbf{k}^{\parallel})$ and $G_0(\mathbf{r},\mathbf{r}';E,\mathbf{k}^{\parallel})$), which follows from their definitions (Eqs. (3.71), (3.72), and (3.73)).

To obtain $G_2(\mathbf{r},\mathbf{r}';E,\mathbf{k}^{\parallel})$ we start from $G_0(\mathbf{r},\mathbf{r}';E)$ (cf. Eq. (3.65)) and expand the function $G_0(\mathbf{r},\mathbf{r}';E,\mathbf{k}^{\parallel})$ (cf. Eq. (3.72)) in a plane wave representation. Then, $G^j_{\text{empty}}(\mathbf{r},\mathbf{r}';E,\mathbf{k}^{\parallel})$ is obtained (in plane wave representation) and transformed to a local representation. Finally, the Dyson equation (cf. Eq. (3.75)) is used.

The empty space Green function G_0 can be obtained from the non-relativistic one

$$\begin{aligned} G_0(\mathbf{r},\mathbf{r}';E) &= \frac{1}{c^2}(E+H_0)\left(-\frac{1}{4\pi}\frac{\exp\left(\mathrm{i}k|\mathbf{r}-\mathbf{r}'|\right)}{|\mathbf{r}-\mathbf{r}'|}1_4\right) \\ &= \frac{1}{w}\sum_{\kappa,\mu}\begin{cases} j^R_{\kappa\mu}(\mathbf{r})\left(h^L_{\kappa\mu}(\mathbf{r}')\right)^{\dagger} & \text{for } r<r' \\ h^R_{\kappa\mu}(\mathbf{r})\left(j^L_{\kappa\mu}(\mathbf{r}')\right)^{\dagger} & \text{for } r>r' \end{cases}, \quad \mathbf{r},\mathbf{r}'\in\mathbb{R}^3, \end{aligned} \tag{3.78}$$

with $k=\sqrt{E^2-c^4}/4$, w is the Wronski determinant (see Eq. (3.46)), and $j^R_{\kappa\mu}$, $h^R_{\kappa\mu}$, $j^L_{\kappa\mu}$, and $h^L_{\kappa\mu}$ are the functions defined in Eqs. (3.40) and (3.41). By substituting Eq. (3.78) into Eq. (3.72), we get the $\mathbf{k}^{\parallel}$-resolved empty space Green function (cf. [24, 37] and references therein):

$$G_0(\mathbf{r},\mathbf{r}';E,\mathbf{k}^{\parallel}) = \frac{1}{\mathrm{i}A_c}\sum_{\mathbf{g}^{\parallel}}\frac{1}{k^z_{\mathbf{g}}}\begin{pmatrix} \frac{E+c^2}{c^2}1_2 & \frac{\boldsymbol{\sigma}\cdot\mathbf{k}^{\pm}_{\mathbf{g}}}{c} \\ \frac{\boldsymbol{\sigma}\cdot\mathbf{k}^{\pm}_{\mathbf{g}}}{c} & \frac{E-c^2}{c^2}1_2 \end{pmatrix} e^{\pm\mathrm{i}k^z_{\mathbf{g}}(z-z')}e^{\mathrm{i}\mathbf{k}^{\parallel}_{\mathbf{g}}\cdot(\mathbf{r}^{\parallel}-\mathbf{r}'^{\parallel})}, \tag{3.79}$$

with $\pm$ for $z-z'\gtrless 0$, $k=\sqrt{E^2-c^4}/4$, $k^z_{\mathbf{g}}=\sqrt{k^2-|\mathbf{k}^{\parallel}+\mathbf{g}^{\parallel}|^2}$, and $\mathbf{k}^{\pm}_{\mathbf{g}}=(\mathbf{k}^{\parallel}+\mathbf{g}^{\parallel},\pm k^z_{\mathbf{g}})$. A_c is the area of the unit cell of the two-dimensional real lattice. The summation is over the reciprocal lattice vectors $\mathbf{g}^{\parallel}$.

If $\mathbf{r}=\mathbf{c}_i+\mathbf{r}_i+\mathbf{R}^{\parallel}$ is in the i-th layer and $\mathbf{r}'=\mathbf{c}_j+\mathbf{r}_j+\mathbf{R}'^{\parallel}$ is in the j-th layer, where $\mathbf{c}_i$ and $\mathbf{c}_j$ are the position vectors to the representative atomic sites in the i-th layer and j-th layer, respectively (cf. Eq. (3.26)), and $\mathbf{R}^{\parallel}$ and $\mathbf{R}'^{\parallel}$ are surface-parallel lattice vectors such that $\mathbf{c}_i+\mathbf{r}_i:=\mathbf{r}-\mathbf{R}^{\parallel}$ and $\mathbf{c}_j+\mathbf{r}_j:=\mathbf{r}'-\mathbf{R}'^{\parallel}$ lie in the representative unit cells of the i-th and j-th layer, then we find for the $\mathbf{k}^{\parallel}$-resolved Green functions G_2 and G^j_{empty}

$$G_2(\mathbf{c}_i+\mathbf{r}_i+\mathbf{R}^{\parallel},\mathbf{c}_j+\mathbf{r}_j+\mathbf{R}'^{\parallel};E,\mathbf{k}^{\parallel}) = e^{\mathrm{i}\mathbf{k}^{\parallel}\cdot(\mathbf{R}^{\parallel}-\mathbf{R}'^{\parallel})}G_2(\mathbf{c}_i+\mathbf{r}_i,\mathbf{c}_j+\mathbf{r}'_j;E,\mathbf{k}^{\parallel}), \tag{3.80}$$

$$G^j_{\text{empty}}(\mathbf{c}_i+\mathbf{r}_i+\mathbf{R}^{\parallel},\mathbf{c}_j+\mathbf{r}_j+\mathbf{R}'^{\parallel};E,\mathbf{k}^{\parallel}) = e^{\mathrm{i}\mathbf{k}^{\parallel}\cdot(\mathbf{R}^{\parallel}-\mathbf{R}'^{\parallel})}G^j_{\text{empty}}(\mathbf{c}_i+\mathbf{r}_i,\mathbf{c}_j+\mathbf{r}'_j;E,\mathbf{k}^{\parallel}). \tag{3.81}$$

As a consequence, we can confine ourselves to the case where $\mathbf{r}=\mathbf{c}_i+\mathbf{r}_i$ and $\mathbf{r}'=\mathbf{c}_j+\mathbf{r}'_j$ lie in the representative unit cells of the i-th and j-th layer, respectively. Defining furthermore

$$G^{ij}_2(\mathbf{r}_i,\mathbf{r}'_j;E,\mathbf{k}^{\parallel}) := G_2(\mathbf{c}_i+\mathbf{r}_i,\mathbf{c}_j+\mathbf{r}'_j;E,\mathbf{k}^{\parallel}) \tag{3.82}$$

and

$$G^{ij}_{\text{empty}}(\mathbf{r}_i,\mathbf{r}'_j;E,\mathbf{k}^{\parallel}) := G^j_{\text{empty}}(\mathbf{c}_i+\mathbf{r}_i,\mathbf{c}_j+\mathbf{r}'_j;E,\mathbf{k}^{\parallel}), \tag{3.83}$$

we can rewrite Eq. (3.75) as

$$G^{ij}_2(\mathbf{r}_i,\mathbf{r}'_j;E,\mathbf{k}^{\parallel}) = G^{ij}_{\text{empty}}(\mathbf{r}_i,\mathbf{r}'_j;E,\mathbf{k}^{\parallel}) + \int\limits_{V_{\text{cell},j}} G^{ij}_{\text{empty}}(\mathbf{r}_i,\mathbf{r}''_j;E,\mathbf{k}^{\parallel})V_{j,a}(\mathbf{r}''_j)G^{jj}_2(\mathbf{r}''_j,\mathbf{r}'_j;E,\mathbf{k}^{\parallel})\,d\mathbf{r}''_j. \tag{3.84}$$

Because of

$$(E - H^j_{\text{empty}})G^{ij}_{\text{empty}}(\mathbf{r}_i, \mathbf{r}'_j; E, \mathbf{k}^{\|}) = \delta(\mathbf{r}_i - \mathbf{r}'_j)\delta_{ij} \tag{3.85}$$

and

$$(E - H)G^{ij}_2(\mathbf{r}_i, \mathbf{r}'_j; E, \mathbf{k}^{\|}) = \delta(\mathbf{r}_i - \mathbf{r}'_j)\delta_{ij}, \tag{3.86}$$

G^{ij}_{empty} and G^{ij}_2 are solutions of the inhomogeneous equation for $i = j$ and solutions of the homogeneous equation for $i \neq j$. Therefore, we may write

$$G^{ij}_{\text{empty}}(\mathbf{r}_i, \mathbf{r}'_j; E, \mathbf{k}^{\|}) = \begin{cases} G_0(\mathbf{r}_j, \mathbf{r}'_j; E) + \sum\limits_{\substack{\kappa\mu \\ \kappa'\mu'}} j^R_{\kappa\mu}(\mathbf{r}_j) D^{jj}_{\kappa\mu,\kappa'\mu'}(E, \mathbf{k}^{\|}) \left(j^L_{\kappa'\mu'}(\mathbf{r}'_j)\right)^\dagger & \text{for } i = j \\ \sum\limits_{\substack{\kappa\mu \\ \kappa'\mu'}} J^{i,R}_{\kappa\mu}(\mathbf{r}_i) D^{ij}_{\kappa\mu,\kappa'\mu'}(E, \mathbf{k}^{\|}) \left(j^L_{\kappa'\mu'}(\mathbf{r}'_j)\right)^\dagger & \text{for } i \neq j \end{cases} \tag{3.87}$$

$$G^{ij}_2(\mathbf{r}_i, \mathbf{r}'_j; E, \mathbf{k}^{\|}) = \begin{cases} G_{j,a}(\mathbf{r}_j, \mathbf{r}'_j; E) + \sum\limits_{\substack{\kappa\mu \\ \kappa'\mu'}} J^{j,R}_{\kappa\mu}(\mathbf{r}_j) U^{jj}_{\kappa\mu,\kappa'\mu'}(E, \mathbf{k}^{\|}) \left(J^{j,L}_{\kappa'\mu'}(\mathbf{r}'_j)\right)^\dagger & \text{for } i = j \\ \sum\limits_{\substack{\kappa\mu \\ \kappa'\mu'}} J^{i,R}_{\kappa\mu}(\mathbf{r}_i) U^{ij}_{\kappa\mu,\kappa'\mu'}(E, \mathbf{k}^{\|}) \left(J^{j,L}_{\kappa'\mu'}(\mathbf{r}'_j)\right)^\dagger & \text{for } i \neq j \end{cases}. \tag{3.88}$$

$D^{ij}_{\kappa\mu,\kappa'\mu'}$ and $U^{ij}_{\kappa\mu,\kappa'\mu'}$ are expansion coefficients. $G_{j,a}$ in Eq. (3.88) is the single-site (atomic) Green function for the potential $V_{j,a}$ and is constructed by the functions $J^{j,R}_{\kappa\mu}$, $H^{j,R}_{\kappa\mu}$, $J^{j,L}_{\kappa\mu}$, and $H^{j,L}_{\kappa\mu}$ (cf. Eqs. (3.42) and (3.43)):

$$G_{j,a}(\mathbf{r}_j, \mathbf{r}'_j; E) = \frac{1}{w} \sum_{\kappa,\mu} \begin{cases} J^{j,R}_{\kappa\mu}(\mathbf{r}_j) \left(H^{j,L}_{\kappa\mu}(\mathbf{r}'_j)\right)^\dagger & \text{for } r_j < r'_j \\ H^{j,R}_{\kappa\mu}(\mathbf{r}_j) \left(J^{j,L}_{\kappa\mu}(\mathbf{r}'_j)\right)^\dagger & \text{for } r_j > r'_j \end{cases}, \tag{3.89}$$

with $w = -\frac{1}{ik}\frac{c^2}{E+c^2}$ and $k = \frac{\sqrt{E^2-c^4}}{c}$.

As is shown in appendix A.1, inserting the expressions for G^{ij}_{empty} (Eq. (3.87)) and G^{ij}_2 (Eq. (3.88)) into the Dyson equation (Eq. (3.84)) yields

$$U^{ij}(E, \mathbf{k}^{\|}) = \begin{cases} \left(1 - \frac{\mathrm{i}}{2k} D^{jj}(E, \mathbf{k}^{\|}) t^{j,R}(E)\right)^{-1} D^{jj}(E, \mathbf{k}^{\|}) & \text{for } i = j \\ D^{ij}(E, \mathbf{k}^{\|}) \left(1 + \frac{\mathrm{i}}{2k} t^{j,R}(E) U^{jj}(E, \mathbf{k}^{\|})\right) & \text{for } i \neq j \end{cases}. \tag{3.90}$$

An important contribution to U^{ij} is the single-site scattering matrix $t^{j,R}$, which can be obtained by using the Dyson equation

$$J^{j,R}_{\kappa\mu}(\mathbf{r}_j) = j^R_{\kappa\mu}(\mathbf{r}_j) + \int_{V_{\text{cell},j}} G_0(\mathbf{r}_j, \mathbf{r}'_j; E) V_{j,a}(\mathbf{r}'_j) J^{j,R}_{\kappa\mu}(\mathbf{r}'_j)\, d\mathbf{r}'_j \tag{3.91}$$

for the case $|\mathbf{r}_j| \geq r_{\mathrm{MT},j}$ (with G_0 from Eq. (3.78) for $|\mathbf{r}_j| > |\mathbf{r}'_j|$):

$$J^{j,R}_{\kappa\mu}(\mathbf{r}_j) = j^R_{\kappa\mu}(\mathbf{r}_j) + \sum_{\kappa'\mu'} \left\{ \left(\frac{1}{w} \int_{V_{\mathrm{cell},j}} \left(j^L_{\kappa'\mu'}(\mathbf{r}'_j) \right)^\dagger V_{j,a}(\mathbf{r}'_j) J^{j,R}_{\kappa\mu}(\mathbf{r}'_j)\, d\mathbf{r}'_j \right) h^R_{\kappa'\mu'}(\mathbf{r}_j) \right\}. \tag{3.92}$$

Comparing this expression with the asymptotic form of $J^{j,R}_{\kappa\mu}$ in Eq. (3.42), we obtain

$$t^{j,R}_{\kappa'\mu'\kappa\mu} = \frac{1}{w} \int_{V_{\mathrm{cell},j}} \left(j^L_{\kappa'\mu'}(\mathbf{r}'_j) \right)^\dagger V_{j,a}(\mathbf{r}'_j) J^{j,R}_{\kappa\mu}(\mathbf{r}'_j)\, d\mathbf{r}'_j. \tag{3.93}$$

3.2.4 Primary one-electron state

Like in LEED theory the primary one-electron state can be written as

$$\varphi_1(E, \mathbf{B}, \mathbf{k}^{\parallel}, s) = G_+(E, \mathbf{B}) |E, \mathbf{k}^{\parallel}, s\rangle, \tag{3.94}$$

where $|E, \mathbf{k}^{\parallel}, s\rangle$ is a plane-wave state with well defined values of energy E, parallel momentum $\mathbf{k}^{\parallel}$, and spin s. G_+ is the retarded single-particle Green function

$$G_+(E, \mathbf{B}) = \frac{1}{E - H(\mathbf{B})}. \tag{3.95}$$

In order to calculate $(e, 2e)$-matrix elements, φ_1 is expanded in terms of $J^{i,R}_{\kappa\mu}(\mathbf{r}_i)$ inside the muffin-tin spheres of the respective layers (i is the layer index)

$$\varphi_1(\mathbf{r}_i) = \sum_{\kappa\mu} c^{(1)}_{\kappa\mu} J^{i,R}_{\kappa\mu}(\mathbf{r}_i) \tag{3.96}$$

$$= \sum_{\kappa\mu} c^{(1)}_{\kappa\mu} \sum_{\kappa'\mu'} \begin{pmatrix} \psi^{i,R(1)}_{\kappa\mu\kappa'\mu'}(r_i) \chi^{\mu'}_{\kappa'}(\hat{\mathbf{r}}_i) \\ \mathrm{i}\phi^{i,R(1)}_{\kappa\mu\kappa'\mu'}(r_i) \chi^{\mu'}_{-\kappa'}(\hat{\mathbf{r}}_i) \end{pmatrix}, \tag{3.97}$$

where χ^μ_κ are the spin-angular functions defined in Eq. (3.34) and $c^{(1)}_{\kappa\mu}$ are complex expansion coefficients. If $V(r)$ and $B(r)$ are radially symmetric (as in the muffin-tin approximation) and $\mathbf{B}$ is parallel to the z axis, we get

$$\varphi_1(\mathbf{r}_i) = \sum_{\kappa\mu} c^{(1)}_{\kappa\mu} \begin{pmatrix} \psi^{i,R(1)}_{\kappa\mu\kappa\mu}(r_i) \chi^\mu_\kappa(\hat{\mathbf{r}}_i) + \psi^{i,R(1)}_{\kappa\mu,-\kappa-1,\mu}(r_i) \chi^\mu_{-\kappa}(\hat{\mathbf{r}}_i) \\ \mathrm{i}\phi^{i,R(1)}_{\kappa\mu\kappa\mu}(r_i) \chi^\mu_{-\kappa}(\hat{\mathbf{r}}_i) + \mathrm{i}\phi^{i,R(1)}_{\kappa\mu,-\kappa-1,\mu}(r_i) \chi^\mu_{\kappa+1}(\hat{\mathbf{r}}_i) \end{pmatrix}. \tag{3.98}$$

3.2.5 Final one-electron states

Final single-particle states for $(e, 2e)$ from ferromagnets with spin-orbit coupling

Like the final state in photoemission theory (cf. [27] Eq. (79) p. 196), each of the two outgoing electron states $|f\rangle$ — with $f = \varphi_3, \varphi_4$ — can be expressed as

$$|f\rangle = G_-(E, \mathbf{B}) |E, \mathbf{k}^{\parallel}, s\rangle \tag{3.99}$$

where $|E, \mathbf{k}^{\parallel}, s\rangle$ is an outgoing plane-wave state with definite spin $s = \pm$ and $G_-(E, \mathbf{B})$ is the advanced single-particle Green function, which can be formally written as

$$G_-(E, \mathbf{B}) = \frac{1}{E - H^\dagger(\mathbf{B})}. \tag{3.100}$$

In what follows, it is shown that $|f\rangle$ is the time-reversed of a LEED state, which has to be calculated for the reversed magnetic field. Time reversal firstly reverses the sign of the scalar imaginary self-energy part $\mathrm{i}V_{\mathrm{im}}$ of the Hamiltonian $H(\mathbf{B})$. Secondly it changes $\boldsymbol{\sigma}$ into $-\boldsymbol{\sigma}$ and therefore reverses the sign of the $\boldsymbol{\sigma}\cdot\mathbf{B}$ part of $H(\mathbf{B})$. One therefore has the relation (cf. also [29])

$$H^\dagger(\mathbf{B}) = TH(-\mathbf{B})T^{-1}. \tag{3.101}$$

Hence the advanced Green function $G_-(E, \mathbf{B})$ (cf. Eq. (3.100)) is the time-reversed of the retarded Green function $G_+(E, -\mathbf{B})$:[2]

$$G_-(E, \mathbf{B}) = TG_+(E, -\mathbf{B})T^{-1} \quad \text{with} \quad G_+(E, -\mathbf{B}) = \frac{1}{E - H(-\mathbf{B})}. \tag{3.102}$$

Substitution into the final-state expression (Eq. (3.99)) yields

$$|f\rangle = TG_+(E, -\mathbf{B})T^{-1}|E, \mathbf{k}^{\parallel}, s\rangle \tag{3.103}$$

$$= TG_+(E, -\mathbf{B})|E, -\mathbf{k}^{\parallel}, -s\rangle. \tag{3.104}$$

The term $G_+(E, -\mathbf{B})|E, -\mathbf{k}^{\parallel}, -s\rangle$ is recognized as a LEED state in the reversed magnetic field, which originates from a plane-wave state with reversed surface-parallel momentum and reversed spin, and $|f\rangle$ is the time-reversed of this LEED state.

In the following it is shown, how $|f\rangle$ is calculated by applying the time-reversal operator to this LEED state.

Time-reversal without magnetic field

The state of an outgoing electron with prescribed spin s and parallel momentum $\mathbf{k}^{\parallel}$ can formally be described by a time-reversed LEED state with reversed $\mathbf{k}^{\parallel}$ and reversed s:

$$\Psi_{\mathrm{f}}(\mathbf{k}^{\parallel}, s) = T\Psi(-\mathbf{k}^{\parallel}, -s). \tag{3.105}$$

The first two components of the four spinor can be written as (cf. Eq. (3.98))

$$\tilde{\Psi}(\mathbf{r}, -\mathbf{k}^{\parallel}, -s) = \sum_{\kappa,\mu} C_{\kappa,\mu}(-\mathbf{k}^{\parallel}, -s) f_{\kappa,\mu}(r)\chi_\kappa^\mu(\hat{\mathbf{r}}). \tag{3.106}$$

Applying the time-reversal operator to $\tilde{\Psi}(\mathbf{r}, -\mathbf{k}^{\parallel}, -s)$, we find

$$T\tilde{\Psi}(\mathbf{r}, -\mathbf{k}^{\parallel}, -s) = \sum_{\kappa,\mu} C^*_{\kappa,\mu}(-\mathbf{k}^{\parallel}, -s) f^*_{\kappa,\mu}(r)\chi_\kappa^{-\mu-1}(\hat{\mathbf{r}}), \tag{3.107}$$

[2] Writing the Hamiltonian as $H = H_{\mathrm{herm}} + \mathrm{i}V_{\mathrm{im}}$ — with $V_{\mathrm{im}} < 0$ —, one sees from the above expressions that G_- (G_+) has poles in the upper (lower) complex half-plane. The Fourier transforms with respect to time are thence "advanced" ("retarded"), as it should be.

which corresponds to a transformation of the expansion coefficients $C_{\kappa,\mu}$:

$$T\tilde{\Psi}(\mathbf{r}, -\mathbf{k}^{\parallel}, -s) = \sum_{\kappa,\mu} D_{\kappa,\mu} f^*_{\kappa,\mu}(r)\chi^{\mu}_{\kappa}(\hat{\mathbf{r}}) \quad \text{with} \quad D_{\kappa,\mu} = C^*_{\kappa,-\mu-1}(-\mathbf{k}^{\parallel}, -s)(-1)^{\kappa-\mu+\ell}. \quad (3.108)$$

Time-reversal with magnetic field

The state of an outgoing particle with spin s and parallel momentum $\mathbf{k}^{\parallel}$ in the presence of a magnetic field $\mathbf{B}$ can be obtained by first calculating the LEED state for the reversed parallel momentum $-\mathbf{k}^{\parallel}$, reversed spin $-s$, and reversed magnetic field $-\mathbf{B}$ and then applying the time-reversal operator:

$$\Psi_{\mathrm{f}}(\mathbf{B}, \mathbf{k}^{\parallel}, s) = T\Psi(-\mathbf{B}, -\mathbf{k}^{\parallel}, -s). \quad (3.109)$$

In (κ, μ) representation, the first two components of the LEED state $\Psi(-\mathbf{B}, -\mathbf{k}^{\parallel}, -s)$ can be written in the form

$$\begin{aligned}\tilde{\Psi}(\mathbf{r}, -\mathbf{B}, -\mathbf{k}^{\parallel}, -s) &= \sum_{\kappa,\mu} C_{\kappa,\mu}(-\mathbf{B}, -\mathbf{k}^{\parallel}, -s)\left(f_{\kappa,\mu}(r, -\mathbf{B})\chi^{\mu}_{\kappa}(\hat{\mathbf{r}}) + \bar{f}_{-\kappa-1,\mu}(r, -\mathbf{B})\chi^{\mu}_{-\kappa-1}(\hat{\mathbf{r}})\right) \\ &= \sum_{\kappa,\mu}\Big[C_{\kappa,\mu}(-\mathbf{B}, -\mathbf{k}^{\parallel}, -s) f_{\kappa,\mu}(r, -\mathbf{B}) \\ &\qquad + C_{-\kappa-1,\mu}(-\mathbf{B}, -\mathbf{k}^{\parallel}, -s)\bar{f}_{\kappa,\mu}(r, -\mathbf{B})\Big]\chi^{\mu}_{\kappa}(\hat{\mathbf{r}}). \end{aligned} \quad (3.110)$$

Defining the contents of the square bracket as $F_{\kappa\mu}$, the LEED state reads

$$\tilde{\Psi}(\mathbf{r}, -\mathbf{B}, -\mathbf{k}^{\parallel}, -s) = \sum_{\kappa,\mu} F_{\kappa,\mu}(r, -\mathbf{B}, -\mathbf{k}^{\parallel}, -s)\chi^{\mu}_{\kappa}(\hat{\mathbf{r}}), \quad (3.111)$$

i.e., an expansion in terms of effective radial functions $F_{\kappa\mu}$. Time-reversal of the LEED state (Eq. (3.110)) yields

$$\begin{aligned}\tilde{\Psi}_{\mathrm{f}}(\mathbf{r}, \mathbf{B}, \mathbf{k}^{\parallel}, s) &= T\tilde{\Psi}(\mathbf{r}, -\mathbf{B}, -\mathbf{k}^{\parallel}, -s) \\ &= \sum_{\kappa,\mu}\left(C^*_{\kappa,\mu}(-\mathbf{B}, -\mathbf{k}^{\parallel}, -s) f^*_{\kappa,\mu}(r, -\mathbf{B}) + C^*_{-\kappa-1,\mu}(-\mathbf{B}, -\mathbf{k}^{\parallel}, -s)\bar{f}^*_{\kappa,\mu}(r, -\mathbf{B})\right)\chi^{\mu}_{-\kappa-1}(\hat{\mathbf{r}}) \\ &= \sum_{\kappa,\mu}(-1)^{\kappa-\mu+\ell}\Big[C^*_{\kappa,-\mu-1}(-\mathbf{B}, -\mathbf{k}^{\parallel}, -s) f^*_{\kappa,-\mu-1}(r, -\mathbf{B}) \\ &\qquad + C^*_{-\kappa-1,-\mu-1}(-\mathbf{B}, -\mathbf{k}^{\parallel}, -s)\bar{f}^*_{\kappa,-\mu-1}(r, -\mathbf{B}))\Big]\chi^{\mu}_{\kappa}(\hat{\mathbf{r}}). \end{aligned} \quad (3.112)$$

Defining furthermore $\tilde{F}_{\kappa,\mu}(r, \mathbf{B}, \mathbf{k}^{\parallel}, s) = (-1)^{\kappa-\mu+\ell}\left[C^*_{\kappa,-\mu-1} f^*_{\kappa,-\mu-1} + C^*_{-\kappa-1,-\mu-1}\bar{f}^*_{\kappa,-\mu-1}\right]$, the time-reversed LEED state takes the compact form

$$\tilde{\Psi}_{\mathrm{f}}(\mathbf{r}, \mathbf{B}, \mathbf{k}^{\parallel}, s) = \sum_{\kappa,\mu} \tilde{F}_{\kappa,\mu}(r, \mathbf{B}, \mathbf{k}^{\parallel}, s)\chi^{\mu}_{\kappa}(\hat{\mathbf{r}}). \quad (3.113)$$

3.2.6 Correlated two-electron final state

To calculate $(e,2e)$-matrix elements (cf. Eq. (3.12)) or $(e,2e)$ intensities (cf. Eqs. (3.13) and (3.20)), one needs a reasonable approximation of the correlated final state (cf. Eqs. (3.4) and (3.10))

$$\psi_{\text{final}} = \Omega\varphi_{\text{final}} \tag{3.114}$$

$$= \Omega\frac{1}{\sqrt{2}}(\varphi_3 \otimes \varphi_4 - \varphi_4 \otimes \varphi_3)\,. \tag{3.115}$$

Two write down an approximation for ψ_{final} it is useful to represent ψ_{final} in a basis $\{|\mathbf{r}_1, i_1\rangle \otimes |\mathbf{r}_2, i_2\rangle\}_{\mathbf{r}_1,\mathbf{r}_2\in\mathbb{R}^3, i_1,i_2=1,\ldots,4}$ of the two-particle state space. The corresponding basis vectors in the one-particle state space are defined as

$$|\mathbf{r}, i\rangle := \delta(\mathbf{r}' - \mathbf{r}) \begin{pmatrix} \delta_{i,1} \\ \delta_{i,2} \\ \delta_{i,3} \\ \delta_{i,4} \end{pmatrix}, \quad \text{e.g., } |\mathbf{r}, 2\rangle = \begin{pmatrix} 0 \\ \delta(\mathbf{r}' - \mathbf{r}) \\ 0 \\ 0 \end{pmatrix}. \tag{3.116}$$

In this two-particle basis the final state can be written as

$$\psi_{\text{final}}(\mathbf{r}_1, i_1, \mathbf{r}_2, i_2) = \langle(\mathbf{r}_1, i_1) \otimes (\mathbf{r}_2, i_2)|\psi_{\text{final}}\rangle\,. \tag{3.117}$$

As has been shown in Ref. [38], it is useful to write the correlated two-electron wavefunction as an antisymmetric product of the form

$$\psi_{\text{final}}(\mathbf{r}_1, i_1, \mathbf{r}_2, i_2) = \frac{1}{\sqrt{2}}\Big[\varphi_3(\mathbf{r}_1, i_1)\varphi_4(\mathbf{r}_2, i_2)f^c(\mathbf{r}_1, \mathbf{r}_2) - \varphi_4(\mathbf{r}_1, i_1)\varphi_3(\mathbf{r}_2, i_2)f^c(\mathbf{r}_2, \mathbf{r}_1)\Big], \tag{3.118}$$

with $\varphi_3(\mathbf{r}_1, i_1) := \langle\mathbf{r}_1, i_1|\varphi_3\rangle$ and $\varphi_4(\mathbf{r}_2, i_2) := \langle\mathbf{r}_2, i_2|\varphi_4\rangle$. φ_3 and φ_4 are one-particle solutions of the time-independent Dirac equation (cf. Eq. (3.22)) and the influence of the interaction potential is collected in the so called correlation factor $f^c(\mathbf{r}_1, \mathbf{r}_2)$ (cf. [38]). Writing the correlated final state ψ_{final} as $|3,4\rangle$, the states φ_3 and φ_4 as $|3\rangle$ and $|4\rangle$, respectively, and indicate the order of $\mathbf{r}_1$, $\mathbf{r}_2$ in the correlation factor by subscripts, Eq. (3.118) becomes

$$|3,4\rangle = \frac{1}{\sqrt{2}}\Big(|3\rangle|4\rangle f^c_{34} - |4\rangle|3\rangle f^c_{43}\Big). \tag{3.119}$$

It is at present not possible to calculate the exact form of the correlation factor f^c. A reasonable approach is possible by approximating the crystal background by a constant potential and using a feasible approximation of the interaction potential $U(\mathbf{r}_1, \mathbf{r}_2)$. In general, one has

$$U(\mathbf{k}, \omega) = \frac{U_0(\mathbf{k})}{\epsilon(\mathbf{k}, \omega)}\,, \tag{3.120}$$

where $U_0(\mathbf{k})$ is the bare Coulomb potential in $\mathbf{k}$ space and $\epsilon(\mathbf{k}, \omega)$ is the dielectric function. A reasonable choice of $\epsilon(\mathbf{k}, \omega)$ for the present work is provided by the Thomas-Fermi approximation. In this case we have, for $\omega = 0$,

$$\epsilon(\mathbf{k}, 0) = 1 + \frac{q^2_{\text{TF}}}{k^2}\,, \tag{3.121}$$

where q_{TF} is a parameter describing the strength of the screening inside the crystal. By Fourier transformation of Eq. (3.120), we obtain the two-particle interaction

$$U(\mathbf{r}_1, \mathbf{r}_2) = \frac{e^{-q_{\mathrm{TF}}|\mathbf{r}_1 - \mathbf{r}_2|}}{|\mathbf{r}_1 - \mathbf{r}_2|}\,. \tag{3.122}$$

In this case the one-particle states are plane waves and the correlation factors only depend on $\mathbf{r}_1 - \mathbf{r}_2$. Hence, we can use relative coordinates

$$\mathbf{R} = \frac{1}{2}(\mathbf{r}_1 + \mathbf{r}_2), \qquad \mathbf{r} = \mathbf{r}_1 - \mathbf{r}_2, \tag{3.123}$$

and

$$\mathbf{K} = \mathbf{k}_3 + \mathbf{k}_4, \qquad \boldsymbol{\kappa} = \frac{1}{2}(\mathbf{k}_3 - \mathbf{k}_4). \tag{3.124}$$

For the derivation of an approximate form of the correlation factor it is sufficient to use a two-component spinor formalism. In this case Eq. (3.118) takes the form

$$\tilde{\psi}_{\mathrm{final}}(\mathbf{R}, \mathbf{r}, s_3, s_4, \mathbf{K}, \boldsymbol{\kappa}) = \frac{1}{\sqrt{2}}\, e^{\mathrm{i}\mathbf{K}\cdot\mathbf{R}}\Big(e^{\mathrm{i}\boldsymbol{\kappa}\cdot\mathbf{r}}\chi_3^{s3}\chi_4^{s4} f^c(\mathbf{r}, \boldsymbol{\kappa}) - e^{-\mathrm{i}\boldsymbol{\kappa}\cdot\mathbf{r}}\chi_3^{s4}\chi_4^{s3} f^c(-\mathbf{r}, \boldsymbol{\kappa})\Big), \tag{3.125}$$

where $\chi_i^{s_j}$ is the Pauli spinor for state i with spin s_j. The correlation factor can then be determined by solving

$$\left(-\frac{1}{m}\Delta + U(r)\right)\varphi(\mathbf{r}; \boldsymbol{\kappa}) = \frac{k^2}{m}\varphi(\mathbf{r}; \boldsymbol{\kappa}) \tag{3.126}$$

for the relative-particle wavefunction $\varphi(\mathbf{r}; \boldsymbol{\kappa}) := e^{\mathrm{i}\boldsymbol{\kappa}\mathbf{r}} f^c(\mathbf{r}; \boldsymbol{\kappa})$ (cf. [38]). $U(r)$ is the interaction potential (e.g., a screened Coulomb potential inside the solid) in relative coordinates.

The resulting two-particle density ρ_2, which for a constant external potential $V_{\mathrm{ext}}(\mathbf{r}) = \mathrm{const}$ is identical to the pair correlation function $g(\mathbf{r}_1, \mathbf{r}_2, s_3, s_4, \boldsymbol{\kappa}) = g_{s_3,s_4}(\mathbf{r}, \boldsymbol{\kappa})$, is then independent of the total momentum $\mathbf{K}$ and the center of mass $\mathbf{R}$. For antiparallel spins we have in particular

$$g(\mathbf{r}, \boldsymbol{\kappa}) = \frac{1}{2}\Big(|f^c(\mathbf{r}, \boldsymbol{\kappa})|^2 + |f^c(-\mathbf{r}, \boldsymbol{\kappa})|^2\Big). \tag{3.127}$$

In the case of a screened Thomas-Fermi potential U, f^c can be calculated as shown in [38], where the range of U is determined by the inverse screening length q_{TF}. The case $q_{\mathrm{TF}} = 0$ describes a bare Coulomb potential.

In Fig. 3.6 we show density plots of $|f^c(\mathbf{r}, \boldsymbol{\kappa})|^2$ and $g_{\uparrow,\downarrow}$ obtained for selected values of q_{TF} with $\boldsymbol{\kappa}$ parallel to the z direction and $|\boldsymbol{\kappa}| = 1$ Bohr^{-1} (if one of the electrons is at rest, the kinetic energy of the second electron is 2 Hartree ≈ 54.4 eV). $|f^c(\mathbf{r}, \boldsymbol{\kappa})|^2$ effectively is the probability of finding electron 2 at $\mathbf{r}$ being scattered by electron 1 in the origin. For a bare Coulomb potential ($q_{\mathrm{TF}} = 0$) we find a paraboloid region of low probability for $z > 0$ and interference oscillations for $z < 0$. The results for small values of q_{TF} are very similar. For $q_{\mathrm{TF}} = 1$ Bohr^{-1} (relatively strong screening) the low probability region reduces to an ellipsoid form. The corresponding pair correlation functions which — in the chosen set up — seem not to differ much for different q_{TF}, exhibit a correlation hole at $\mathbf{r}_1 = \mathbf{r}_2$.

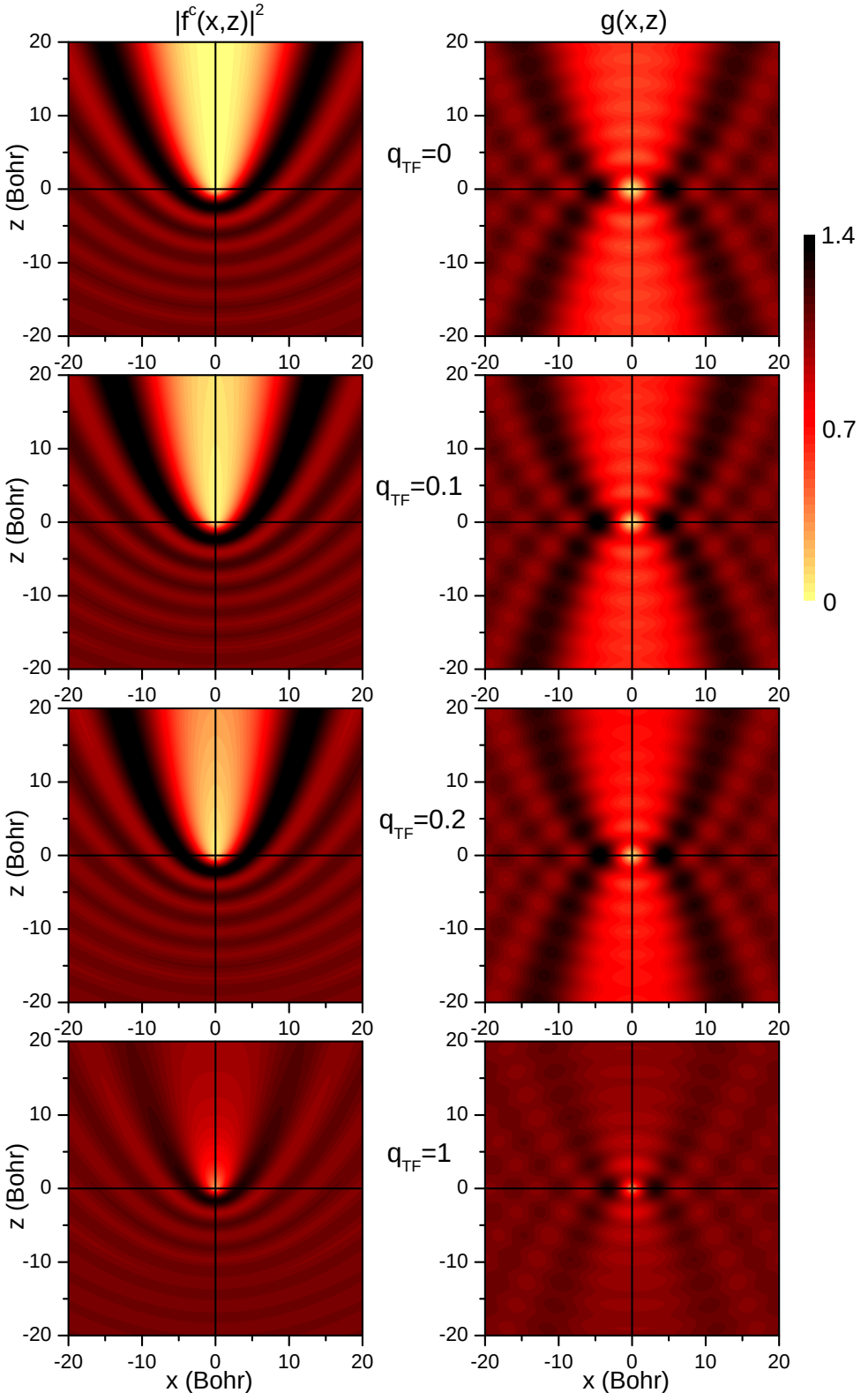

Fig. 3.6: Square of the correlation factor $|f^c(x,z)|^2$ (left-hand column) and pair correlation function $g(x,z)$ (Eq. (3.127)) for antiparallel spins (right-hand column) for plane waves with wave vector $\boldsymbol{\kappa} = (0,0,1)$ Bohr^{-1} calculated for selected values of the screening parameter q_{TF} (q_{TF} values in units of Bohr^{-1}).

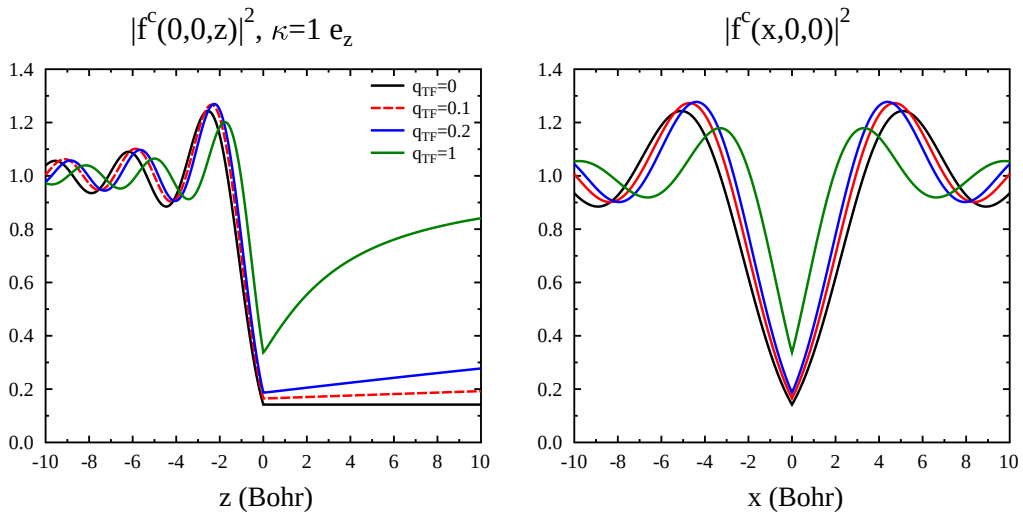

Fig. 3.7: $|f^c|^2$ along the z axis (left-hand panel) and along the x axis (right-hand panel) for selected values of q_{TF} and $|\boldsymbol{\kappa}| = 1$ Bohr^{-1}.

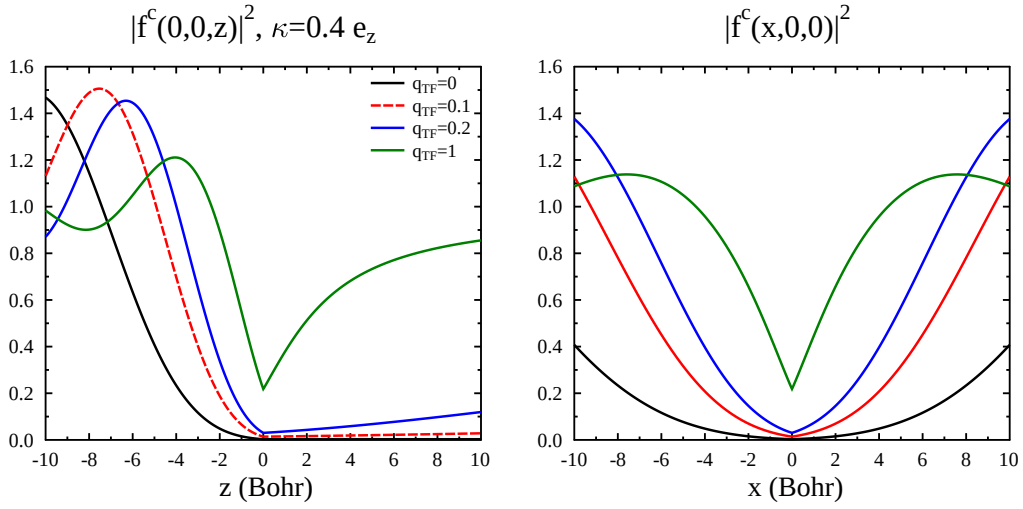

Fig. 3.8: Same as in Fig. 3.7 but with $\boldsymbol{\kappa} = 0.4\,\mathbf{e}_z$.

The differences become clearer in the linear plots of Fig. 3.7 and Fig. 3.8. For $z > 0$ the correlation factor $f^c(0, 0, z)$ is constant for $q_{\mathrm{TF}} = 0$, slightly increasing for weak screening, and forming a sharp cusp for strong screening ($q_{\mathrm{TF}} = 1$ Bohr^{-1}). For $\mathbf{r}$ normal to $\boldsymbol{\kappa}$, f^c is symmetric to the origin and forms a well pronounced correlation hole at $\mathbf{r} = 0$.

The value of κ is for a given total energy $E = \frac{1}{2}(k_3^2 + k_4^2)$ directly related to the angle between $\mathbf{k}_3$ and $\mathbf{k}_4$. If $|\mathbf{k}_3| = |\mathbf{k}_4|$ we have $\cos\vartheta = 1 - \frac{2\kappa^2}{E}$. Hence if $E = 2$ Hartree both electrons move in opposite directions for $\kappa = 1$ Bohr^{-1}.

For smaller values of κ the results for bare Coulomb potential and a weak screening potential (e.g. $q_{\mathrm{TF}} = 0.1$ Bohr^{-1}) become more and more different. For the given example $\kappa = 0.4$ Bohr^{-1} the energy difference is 0.32 Hartree (≈ 10 eV) and $\vartheta \approx 32.6°$. In this case the correlation hole due to bare Coulomb interaction is already considerably larger the that for $q_{\mathrm{TF}} = 0.1$ Bohr^{-1}. This discrepancy becomes larger for decreasing values of ϑ.

3.3 $(e, 2e)$ reaction cross sections and asymmetries

We now substitute into Eq. (3.20) the correlated final state according to Eqs. (3.114) and (3.115). This yields

$$I^1_{3,4} = 2\gamma\langle\Omega\varphi_{\text{final}}|U\Big[|\varphi_1\rangle\langle\varphi_1| \otimes \left(-\frac{1}{\pi}\right)\operatorname{Im} G_2(E_3+E_4-E_1)\Big]U|\Omega\varphi_{\text{final}}\rangle \tag{3.128}$$

$$= 2\gamma\langle\varphi_{\text{final}}|\Omega^\dagger U\Big[|\varphi_1\rangle\langle\varphi_1| \otimes \left(-\frac{1}{\pi}\right)\operatorname{Im} G_2(E_3+E_4-E_1)\Big]U\Omega|\varphi_{\text{final}}\rangle \tag{3.129}$$

$$= \gamma\langle\varphi_3\otimes\varphi_4-\varphi_4\otimes\varphi_3|\Omega^\dagger U\Big[|\varphi_1\rangle\langle\varphi_1| \otimes \left(-\frac{1}{\pi}\right)\operatorname{Im} G_2(E)\Big]U\Omega|\varphi_3\otimes\varphi_4-\varphi_4\otimes\varphi_3\rangle \tag{3.130}$$

$$\begin{aligned}
&= \gamma\langle\varphi_3\otimes\varphi_4|\Omega^\dagger U\Big[|\varphi_1\rangle\langle\varphi_1| \otimes \left(-\frac{1}{\pi}\right)\operatorname{Im} G_2(E)\Big]U\Omega|\varphi_3\otimes\varphi_4\rangle \\
&\quad - \gamma\langle\varphi_3\otimes\varphi_4|\Omega^\dagger U\Big[|\varphi_1\rangle\langle\varphi_1| \otimes \left(-\frac{1}{\pi}\right)\operatorname{Im} G_2(E)\Big]U\Omega|\varphi_4\otimes\varphi_3\rangle \\
&\quad - \gamma\langle\varphi_4\otimes\varphi_3|\Omega^\dagger U\Big[|\varphi_1\rangle\langle\varphi_1| \otimes \left(-\frac{1}{\pi}\right)\operatorname{Im} G_2(E)\Big]U\Omega|\varphi_3\otimes\varphi_4\rangle \\
&\quad + \gamma\langle\varphi_4\otimes\varphi_3|\Omega^\dagger U\Big[|\varphi_1\rangle\langle\varphi_1| \otimes \left(-\frac{1}{\pi}\right)\operatorname{Im} G_2(E)\Big]U\Omega|\varphi_4\otimes\varphi_3\rangle\,.
\end{aligned} \tag{3.131}$$

The intensity $I^1_{3,4}$ thus consists of four partial intensities. These are all different and have to be calculated separately. However, the structure of the four terms is identical and so the following discussion in restricted to the first term. Defining $K_{ij}(\mathbf{r}',\tilde{\mathbf{r}}') := \langle\mathbf{r}',i|\left(-\frac{1}{\pi}\right)\operatorname{Im} G_2(E)|\tilde{\mathbf{r}}',j\rangle$ and using $\psi_{\text{final}} = \Omega\varphi_{\text{final}} = \Omega\frac{1}{\sqrt{2}}(\varphi_3\otimes\varphi_4-\varphi_4\otimes\varphi_3)$ (Eqs. (3.114) and (3.115)) together with Eq. (3.118), we obtain in spatial representation

$$\begin{aligned}
&\gamma\langle\varphi_3\otimes\varphi_4|\Omega^\dagger U\Big[|\varphi_1\rangle\langle\varphi_1| \otimes \left(-\frac{1}{\pi}\right)\operatorname{Im} G_2(E)\Big]U\Omega|\varphi_3\otimes\varphi_4\rangle \\
&\quad = \gamma\int\limits_{\mathbb{R}^3} d\mathbf{r}\,d\mathbf{r}'d\tilde{\mathbf{r}}\,d\tilde{\mathbf{r}}'\,\varphi_3^\dagger(\mathbf{r})\varphi_1(\mathbf{r})f^{c*}(\mathbf{r},\mathbf{r}')U(\mathbf{r},\mathbf{r}')\varphi_4^\dagger(\mathbf{r}') \\
&\qquad \times K(\mathbf{r}',\tilde{\mathbf{r}}';E)\,\varphi_4(\tilde{\mathbf{r}}')f^c(\tilde{\mathbf{r}},\tilde{\mathbf{r}}')U(\tilde{\mathbf{r}},\tilde{\mathbf{r}}')\varphi_1^\dagger(\tilde{\mathbf{r}})\varphi_3(\tilde{\mathbf{r}})\,.
\end{aligned} \tag{3.132}$$

For the practical evaluation of the integral in Eq. (3.132) it is important to utilize the lattice periodicity parallel to the surface (with translation vectors $\mathbf{R}^{\parallel}$). For this it is also necessary to simplify the correlation factor. As already mentioned in Section 3.2.6, we replaced the exact $f^c(\mathbf{r},\mathbf{r}')$ in a first step by a correlation factor $f^c(\mathbf{r}-\mathbf{r}';\boldsymbol{\kappa})$ with $\boldsymbol{\kappa} = \frac{1}{2}(\mathbf{k}-\mathbf{k}')$) (cf. Eq. (3.124)) obtained for plane waves. In a second step, we approximate $f^c(\mathbf{r}-\mathbf{r}';\boldsymbol{\kappa})$ by its spherical average

$$\tilde{f}^c(|\mathbf{r}-\mathbf{r}'|;\boldsymbol{\kappa}) := \int f^c(\mathbf{r}-\mathbf{r}';\boldsymbol{\kappa})\,d\Omega\,, \tag{3.133}$$

which in an additional step can be approximately written in the form

$$\tilde{f}^c(|\mathbf{r}-\mathbf{r}'|;\boldsymbol{\kappa}) = 1 - be^{-\gamma|\mathbf{r}-\mathbf{r}'|}\,. \tag{3.134}$$

b and γ are real parameters that depend on $\boldsymbol{\kappa} = \frac{1}{2}(\mathbf{k} - \mathbf{k}')$ and q_{TF}. Then we obtain (cf. Eq. (3.122))

$$f^c(\mathbf{r}, \mathbf{r}')U(\mathbf{r}, \mathbf{r}') \approx (1 - be^{-\gamma|\mathbf{r}-\mathbf{r}'|})\frac{e^{-q_{\mathrm{TF}}|\mathbf{r}-\mathbf{r}'|}}{|\mathbf{r} - \mathbf{r}'|} \tag{3.135}$$

$$= \frac{e^{-q_{\mathrm{TF}}|\mathbf{r}-\mathbf{r}'|}}{|\mathbf{r} - \mathbf{r}'|} - b\frac{e^{-(q_{\mathrm{TF}}+\gamma)|\mathbf{r}-\mathbf{r}'|}}{|\mathbf{r} - \mathbf{r}'|} \tag{3.136}$$

To calculate the integral in Eq. (3.132), it is therefore sufficient to find an effective method to calculate integrals of the form

$$\tilde{I} = \int\limits_{\mathbb{R}^3} d\mathbf{r}\, d\mathbf{r}' d\tilde{\mathbf{r}}\, d\tilde{\mathbf{r}}'\, \varphi_3^\dagger(\mathbf{r})\varphi_1(\mathbf{r})\tilde{U}(\mathbf{r}, \mathbf{r}')\varphi_4^\dagger(\mathbf{r}') \times K(\mathbf{r}', \tilde{\mathbf{r}}'; E)\, \varphi_4(\tilde{\mathbf{r}}')\tilde{U}(\tilde{\mathbf{r}}, \tilde{\mathbf{r}}')\varphi_1^\dagger(\tilde{\mathbf{r}})\varphi_3(\tilde{\mathbf{r}})\,, \tag{3.137}$$

where $\tilde{U}(\mathbf{r}, \mathbf{r}') = \frac{e^{-\tilde{q}|\mathbf{r}-\mathbf{r}'|}}{|\mathbf{r}-\mathbf{r}'|}$ is a screened Coulomb potential with a general screening parameter $\tilde{q}$. Following reference [24], we write $\tilde{U}(\mathbf{r} + \mathbf{R}^\parallel, \mathbf{r}' + \mathbf{R}'^\parallel)$ as

$$\begin{aligned}\tilde{U}(\mathbf{r} + \mathbf{R}^\parallel, \mathbf{r}' + \mathbf{R}'^\parallel) &= \frac{e^{-\tilde{q}|\mathbf{r}'+\mathbf{R}'^\parallel-(\mathbf{r}+\mathbf{R}^\parallel)|}}{|\mathbf{r}' + \mathbf{R}'^\parallel - (\mathbf{r} + \mathbf{R}^\parallel)|} \\ &= \int d\mathbf{k}\, \frac{e^{\mathrm{i}\mathbf{k}\cdot(\mathbf{r}'+\mathbf{R}'^\parallel-(\mathbf{r}+\mathbf{R}^\parallel))}}{\tilde{q}^2 + k^2} \\ &= \int d\mathbf{k}^\parallel\, e^{\mathrm{i}\mathbf{k}^\parallel\cdot(\mathbf{R}'^\parallel-\mathbf{R}^\parallel)}\tilde{U}(\mathbf{r}, \mathbf{r}'; \mathbf{k}^\parallel)\end{aligned} \tag{3.138}$$

with

$$\tilde{U}(\mathbf{r}, \mathbf{r}'; \mathbf{k}^\parallel) := \int dk^\perp \frac{e^{\mathrm{i}\mathbf{k}\cdot(\mathbf{r}'-\mathbf{r})}}{\tilde{q}^2 + k^2}\,. \tag{3.139}$$

It is convenient to write the single particle states $\varphi_\nu(\mathbf{r})$ in the form $\varphi_\nu(\mathbf{c}_i + \mathbf{R}^\parallel + \mathbf{r})$, where $\mathbf{r}$ lies only in the unit cell, $\mathbf{c}_i$ specifies the position of a representative unit cell of the i-th layer and $\mathbf{R}^\parallel$ are the translation vectors parallel to the surface. We then obtain

$$\begin{aligned}\tilde{I} = &\sum_{\substack{i,i'\\j,j'}}\sum_{\substack{m,m'\\n,n'}}\int\limits_{\mathrm{EZ}} d\mathbf{r}\, d\mathbf{r}'\, d\tilde{\mathbf{r}}\, d\tilde{\mathbf{r}}' \\ &\times \varphi_3^\dagger(\mathbf{c}_i + \mathbf{R}_m^\parallel + \mathbf{r})\varphi_1(\mathbf{c}_i + \mathbf{R}_m^\parallel + \mathbf{r})U(\mathbf{c}_i + \mathbf{R}_m^\parallel + \mathbf{r}, \mathbf{c}_{i'} + \mathbf{R}_{m'}^\parallel + \mathbf{r}')\varphi_4^\dagger(\mathbf{c}_{i'} + \mathbf{R}_{m'}^\parallel + \mathbf{r}') \\ &\times K(\mathbf{c}_{i'} + \mathbf{R}_{m'}^\parallel + \mathbf{r}', \mathbf{c}_{j'} + \mathbf{R}_{n'}^\parallel + \tilde{\mathbf{r}}'; E) \\ &\times \varphi_4(\mathbf{c}_{j'} + \mathbf{R}_{n'}^\parallel + \tilde{\mathbf{r}}')U(\mathbf{c}_j + \mathbf{R}_n^\parallel + \tilde{\mathbf{r}}, \mathbf{c}_{j'} + \mathbf{R}_{j'}^\parallel + \tilde{\mathbf{r}}')\varphi_1^\dagger(\mathbf{c}_j + \mathbf{R}_n^\parallel + \tilde{\mathbf{r}})\varphi_3(\mathbf{c}_j + \mathbf{R}_n^\parallel + \tilde{\mathbf{r}}) \\ = &\int\limits_{\mathrm{EZ}} d\mathbf{r}\, d\mathbf{r}'\, d\tilde{\mathbf{r}}\, d\tilde{\mathbf{r}}' \int d\mathbf{k}^\parallel \sum_{\mathbf{k}_2^\parallel} \int d\tilde{\mathbf{k}}^\parallel \sum_{\substack{i,i'\\j,j'}}\sum_{\substack{m,m'\\n,n'}} \\ &\times e^{\mathrm{i}(-\mathbf{k}_3^\parallel\cdot\mathbf{R}_m^\parallel+\mathbf{k}_1^\parallel\cdot\mathbf{R}_m^\parallel+\mathbf{k}^\parallel\cdot\mathbf{R}_m^\parallel-\mathbf{k}^\parallel\cdot\mathbf{R}_{m'}^\parallel-\mathbf{k}_4^\parallel\cdot\mathbf{R}_{m'}^\parallel)}(\varphi_3^i(\mathbf{r}))^\dagger\varphi_1^i(\mathbf{r})U^{i,i'}(\mathbf{r}, \mathbf{r}'; \mathbf{k}^\parallel)(\varphi_4^{i'}(\mathbf{r}'))^\dagger \\ &\times e^{\mathrm{i}(\mathbf{k}_2^\parallel\cdot\mathbf{R}_{m'}^\parallel-\mathbf{k}_2^\parallel\cdot\mathbf{R}_{n'}^\parallel)}K^{i',j'}(\mathbf{r}', \tilde{\mathbf{r}}'; E, \mathbf{k}_2^\parallel) \\ &\times e^{\mathrm{i}(\mathbf{k}_4^\parallel\cdot\mathbf{R}_{n'}^\parallel+\tilde{\mathbf{k}}^\parallel\cdot\mathbf{R}_n^\parallel-\tilde{\mathbf{k}}^\parallel\cdot\mathbf{R}_{n'}^\parallel-\mathbf{k}_1^\parallel\cdot\mathbf{R}_n^\parallel+\mathbf{k}_3^\parallel\cdot\mathbf{R}_n^\parallel)}\varphi_4^{j'}(\tilde{\mathbf{r}}')U^{j,j'}(\tilde{\mathbf{r}}, \tilde{\mathbf{r}}'; \tilde{\mathbf{k}}^\parallel)(\varphi_1^j(\tilde{\mathbf{r}}))^\dagger\varphi_3^j(\tilde{\mathbf{r}})\,.\end{aligned} \tag{3.140}$$

By using

$$\begin{aligned}
&\sum_{m,m',n,n'} \Big\{ e^{\mathrm{i}(-\mathbf{k}_3^\parallel\cdot\mathbf{R}_m^\parallel+\mathbf{k}_1^\parallel\cdot\mathbf{R}_m^\parallel+\mathbf{k}^\parallel\cdot\mathbf{R}_m^\parallel-\mathbf{k}^\parallel\cdot\mathbf{R}_{m'}^\parallel-\mathbf{k}_4^\parallel\cdot\mathbf{R}_{m'}^\parallel)} \times e^{\mathrm{i}(\mathbf{k}_2^\parallel\cdot\mathbf{R}_{m'}^\parallel-\mathbf{k}_2^\parallel\cdot\mathbf{R}_{n'}^\parallel)} \\
&\qquad \times e^{\mathrm{i}(\mathbf{k}_4^\parallel\cdot\mathbf{R}_{n'}^\parallel+\tilde{\mathbf{k}}^\parallel\cdot\mathbf{R}_n^\parallel-\tilde{\mathbf{k}}^\parallel\cdot\mathbf{R}_{n'}^\parallel-\mathbf{k}_1^\parallel\cdot\mathbf{R}_n^\parallel+\mathbf{k}_3^\parallel\cdot\mathbf{R}_n^\parallel)} \Big\} \\
&= \left(\sum_m e^{\mathrm{i}(-\mathbf{k}_3^\parallel+\mathbf{k}_1^\parallel+\mathbf{k}^\parallel)\cdot\mathbf{R}_m^\parallel}\right)\left(\sum_{m'} e^{\mathrm{i}(-\mathbf{k}_4^\parallel-\mathbf{k}^\parallel+\mathbf{k}_2^\parallel)\cdot\mathbf{R}_{m'}^\parallel}\right) \\
&\quad \times \left(\sum_n e^{\mathrm{i}(-\mathbf{k}_1^\parallel+\mathbf{k}_3^\parallel+\tilde{\mathbf{k}}^\parallel)\cdot\mathbf{R}_n^\parallel}\right)\left(\sum_{n'} e^{\mathrm{i}(\mathbf{k}_4^\parallel-\mathbf{k}_2^\parallel+\tilde{\mathbf{k}}^\parallel)\cdot\mathbf{R}_{n'}^\parallel}\right) \\
&\propto \delta_{\mathbf{k}^\parallel,\mathbf{k}_3^\parallel-\mathbf{k}_1^\parallel}\,\delta_{\mathbf{k}^\parallel,\mathbf{k}_2^\parallel-\mathbf{k}_4^\parallel}\,\delta_{\tilde{\mathbf{k}}^\parallel,\mathbf{k}_1^\parallel-\mathbf{k}_3^\parallel}\,\delta_{\tilde{\mathbf{k}}^\parallel,\mathbf{k}_4^\parallel-\mathbf{k}_2^\parallel}, \qquad (3.141)
\end{aligned}$$

we finally obtain

$$\begin{aligned}
\tilde{I} \propto \int_{\mathrm{EZ}} d\mathbf{r}\, d\mathbf{r}'\, d\tilde{\mathbf{r}}\, d\tilde{\mathbf{r}}' \sum_{\substack{i,i'\\ j,j'}} & \\
&\times (\varphi_3^i(\mathbf{r}))^\dagger \varphi_1^i(\mathbf{r}) U^{i,i'}(\mathbf{r},\mathbf{r}';\mathbf{k}_3^\parallel-\mathbf{k}_1^\parallel)(\varphi_4^{i'}(\mathbf{r}'))^\dagger \\
&\times K^{i',j'}(\mathbf{r}',\tilde{\mathbf{r}}';E,\mathbf{k}_3^\parallel+\mathbf{k}_4^\parallel-\mathbf{k}_1^\parallel) \\
&\times \varphi_4^{j'}(\tilde{\mathbf{r}}') U^{j,j'}(\tilde{\mathbf{r}},\tilde{\mathbf{r}}';\mathbf{k}_1^\parallel-\mathbf{k}_3^\parallel)(\varphi_1^j(\tilde{\mathbf{r}}))^\dagger \varphi_3^j(\tilde{\mathbf{r}})\,. \qquad (3.142)
\end{aligned}$$

In the last equation, the coordinates $\mathbf{r}$, $\mathbf{r}'$, $\tilde{\mathbf{r}}$, and $\tilde{\mathbf{r}}'$ are restricted to the unit cells of the layers. As a consequence of Eq. (3.141), a transition is only possible when the parallel momentum (modulo a reciprocal lattice vector $\mathbf{g}^\parallel$) is conserved

$$\mathbf{k}_1^\parallel + \mathbf{k}_2^\parallel = \mathbf{k}_3^\parallel + \mathbf{k}_4^\parallel + \mathbf{g}^\parallel \quad \text{and} \quad \tilde{\mathbf{k}}^\parallel = -\mathbf{k}^\parallel. \qquad (3.143)$$

The above derivation, made for the first term in Eq. (3.131), is also applicable to the other three terms. In particular, the conservation law (Eq. (3.143)) is valid for all terms and therefore also for the total intensity $I_{3,4}^1$ (cf. Eq. (3.128)). In summary, the $(e, 2e)$ transition is restricted by energy and parallel momentum conservation:

$$E_1 + E_2 = E_3 + E_4 \quad \text{and} \quad \mathbf{k}_1^\parallel + \mathbf{k}_2^\parallel = \mathbf{k}_3^\parallel + \mathbf{k}_4^\parallel + \mathbf{g}^\parallel\,, \qquad (3.144)$$

where $\mathbf{g}^\parallel$ is a surface reciprocal lattice vector.

Because of these conservation laws, the intensity $I_{3,4}^1$ depends explicitly only on the state of the incoming electron (1) and the states of the outgoing electrons (3, 4). If these one-particle states are characterized by quantum numbers E_i, $\mathbf{k}_i^\parallel$, and σ_i, $(i = 1, 3, 4)$, where E_i denotes the energy, $\mathbf{k}_i^\parallel$ the parallel momentum, and σ_i the spin-orientation with respect to a given axis, the intensity can be written as

$$\begin{aligned}
I_{3,4}^1 &= I(E_1,\mathbf{k}_1^\parallel,\sigma_1,E_3,\mathbf{k}_3^\parallel,\sigma_3,E_4,\mathbf{k}_4^\parallel,\sigma_4) \qquad (3.145)\\
&=: I_{\sigma_3\sigma_4}^{\sigma_1\mu}(E_1,\mathbf{k}_1^\parallel,E_3,\mathbf{k}_3^\parallel,E_4,\mathbf{k}_4^\parallel). \qquad (3.146)
\end{aligned}$$

In the case of a ferromagnetic material, the majority spin orientation, with respect to an axis, is indicated by the additional label μ.

The above-derived expressions for $I^{\sigma_1\mu}_{\sigma_3\sigma_4}$, in which the valence electron enters via its Green function, are of advantage for numerical calculations and are used for these in the present work. For the purpose of gaining more physical insight and of interpreting results, a matrix element expression is more useful, in which the valence electron enters via its quasiparticle wave function. The equivalence of these two ways of treating the valence electron has been explained earlier (cf. Ref. [4] and Eqs. (3.13) to (3.21) of the present work). Starting from Eq. (3.13) and substituting the initial and final states in the forms derived in the previous sections, one readily obtains

$$I^{\sigma_1\mu}_{\sigma_3\sigma_4} = \frac{k_3 k_4}{k_1} \sum_{E_2, \mathbf{k}_2^{\parallel}, \sigma_2, n_2} |f^{\sigma_1\sigma_2 n_2\mu}_{\sigma_3\sigma_4} - g^{\sigma_1\sigma_2 n_2\mu}_{\sigma_3\sigma_4}|^2 \, \delta(E_1 + E_2 - E_3 + E_4) \, \delta(\mathbf{k}_1^{\parallel} + \mathbf{k}_2^{\parallel} - \mathbf{k}_3^{\parallel} - \mathbf{k}_4^{\parallel} - \mathbf{g}^{\parallel}), \tag{3.147}$$

which contains so called direct matrix elements

$$f^{\sigma_1\sigma_2 n_2\mu}_{\sigma_3\sigma_4} = \langle \varphi_3 \otimes \varphi_4 | f^{c*} U | \varphi_1 \otimes \varphi_2^{n_2} \rangle \qquad (= \langle 3 | \langle 4 | f^{c*} U | 1 \rangle | 2 \rangle) \tag{3.148}$$

and exchange matrix elements

$$g^{\sigma_1\sigma_2 n_2\mu}_{\sigma_3\sigma_4} = \langle \varphi_4 \otimes \varphi_3 | f^{c} U | \varphi_1 \otimes \varphi_2^{n_2} \rangle \qquad (= \langle 4 | \langle 3 | f^{c} U | 1 \rangle | 2 \rangle) \,. \tag{3.149}$$

$k_i = \sqrt{2E_i}$ (for $i = 1, 3, 4$) and $\mathbf{g}^{\parallel}$ is a surface-parallel reciprocal lattice vector. The index n_2 accounts for the fact that for a fixed set (E_2, $\mathbf{k}_2^{\parallel}$, and σ_2) it is possible that there are several linearly independent initial states, which we denote by $\varphi_2^{n_2}$.

For each majority spin orientation ($\mu = \pm$), there are thus eight spin-dependent $(e, 2e)$ intensities $I^{\sigma_1\mu}_{\sigma_3\sigma_4}$. Generally, they are all nonzero and different from each other. In particular, there are, as a consequence of SOC, "spin-flip" intensities like $I^{+,\mu}_{-,-}$, i.e., the primary electron has spin up and both ejected electrons have spin down.

Since the resolution of the outgoing electron spins σ_3 and σ_4 is — to our knowledge — not yet feasible experimentally, the currently observable $(e, 2e)$ intensities involve sums over the outgoing electron spins:

$$I^{\sigma_1\mu} := \sum_{\sigma_3, \sigma_4} I^{\sigma_1\mu}_{\sigma_3\sigma_4} \,. \tag{3.150}$$

In formal analogy to what was found to be useful in SPLEED (cf. Ref. [27], and references therein), these four intensities can be transformed into an intensity sum

$$I = \sum_{\sigma_1\mu} I^{\sigma_1\mu} \tag{3.151a}$$

and three asymmetries,

$$A_{\mathrm{so}} = \left[(I^{++} + I^{+-}) - (I^{-+} + I^{--}) \right] / I, \tag{3.151b}$$

$$A_{\mathrm{ex}} = \left[(I^{++} + I^{--}) - (I^{+-} + I^{-+}) \right] / I, \tag{3.151c}$$

$$A_{u} = \left[(I^{++} + I^{-+}) - (I^{+-} + I^{--}) \right] / I. \tag{3.151d}$$

In the limit of vanishing SOC the intensities $I^{\sigma_1\mu}$ depend only on the alignment of the primary spin relative to the magnetic field $\mathbf{B}$, i.e., $I^{\sigma_1\mu} = I^{-\sigma_1,-\mu}$. From Eqs. (3.151b) and (3.151d) it is then evident that A_{so} and A_u are zero. If the magnetic field $\mathbf{B}$ goes to zero (i.e., no ferromagnetism), $I^{\sigma_1\mu} = I^{\sigma_1,-\mu}$ and consequently $A_{\mathrm{ex}} = 0$ and $A_u = 0$. SOC is necessary and sufficient for nonvanishing A_{so}, as is ferromagnetism ("magnetic exchange") for A_{ex}, hence the subscripts "so" and "ex". Quantitatively, A_{so} is however influenced by magnetism and so is A_{ex} by SOC.

A_u requires for its existence both SOC and magnetism. Since the sum of two oppositely polarized primary beams ($\sigma_1 = \pm$) corresponds to an unpolarized beam, the sum of the first (last) two intensities in Eq. (3.151d) is the intensity due to an unpolarized primary beam for majority spin orientation $\mu = +$ ($\mu = -$). This means that the asymmetry A_u can be obtained using an unpolarized primary electron beam (hence the subscript "u") and reversing the magnetic field. It thus represents a form of magnetic dichroism and may be termed "dichroic asymmetry".

Chapter 4

Theory of positron-induced electron-positron emission $[(p, ep)]$

In the $(e, 2e)$ process the primary particle and both outgoing particles are electrons. Choosing a positron as primary particle, a possible reaction channel is the simultaneous emission of a correlated electron-positron pair. This process, for which we use the abbreviation (p, ep), has been verified for crystal surfaces (LiF) for the first time by van Riessen et al. [21]. Overall, the theoretical formalism to describe (p, ep) transition rates is similar to that for the $(e, 2e)$ case. There are, however, three basic differences:

1. For a positron inside a solid, the Coulomb interaction with the atomic nuclei is repulsive, and the interaction with the electrons is attractive, which is just the opposite as for an electron inside the solid. Consequently, the effective single-particle potential for a positron is completely different from the one for an electron.

2. The outgoing electron-positron pair is correlated by an attractive interaction.

3. The positron can be distinguished from all crystal electrons. Hence, the effective positron potential does not contain an exchange term, and the correlated two-particle wavefunctions are not antisymmetric with respect to particle interchange.

In this chapter we investigate the properties of the correlated electron-positron two-particle state and give an expression for the reaction cross section of the positron-induced emission of an electron-positron pair.

4.1 Correlated electron-positron state

The correlation between the outgoing electron and positron in the (p, ep) process can in principle be treated as for two interacting electrons (cf. Chapter 3). However, contrary to the electron-electron case the Coulomb interaction is now attractive and there is no exchange interaction. The resulting electron-positron two-particle wavefunction can be expressed as

$$\Psi(\mathbf{r}_1, \mathbf{r}_2) = \psi_1(\mathbf{r}_1)\psi_2(\mathbf{r}_2) f^c_{(e,e^+)}(\mathbf{r}_1, \mathbf{r}_2)\,, \tag{4.1}$$

where ψ_1 and ψ_2 are single-particle wavefunctions and $f^c_{(e,e^+)}(\mathbf{r}_1, \mathbf{r}_2)$ is an electron-positron correlation factor. As in the electron-electron case (cf. Section 3.2.6), the one-particle states $\psi_i(\mathbf{r}_i)$ are determined for the real crystal potential and the correlation factor for a constant external potential. In this case, f^c depends only on the relative coordinate $\mathbf{r} = \mathbf{r}_1 - \mathbf{r}_2$ and the relative momentum $\mathbf{k} = \mathbf{k}_1 - \mathbf{k}_2$ and can be determined by solving the differential equation

$$\left(-\frac{1}{m}\Delta + U(r)\right)\varphi(\mathbf{r}; \mathbf{k}) = \frac{k^2}{4m}\varphi(\mathbf{r}; \mathbf{k}) \tag{4.2}$$

for the relative-particle wavefunction $\varphi(\mathbf{r};\mathbf{k}) := e^{\mathrm{i}\frac{1}{2}\mathbf{kr}} f^c_{(e,e^+)}(\mathbf{r};\mathbf{k})$. $U(r)$ is now an attractive central potential. Here, also relative coordinates are used as in Eqs. (3.123) and (3.124).

Within the approximation of a constant background potential, where the one-particle states are plane waves, there is a close relation between the correlation factor f^c and the pair correlation function $\rho^c(\mathbf{r}_1, \mathbf{r}_2)$. For an electron-positron pair, $\rho^c_{(e,e^+)}(\mathbf{r}_1, \mathbf{r}_2)$ is simply given by

$$\rho^c_{(e,e^+)}(\mathbf{r}_1, \mathbf{r}_2) = \rho^c_{(e,e^+)}(\mathbf{r}_1 - \mathbf{r}_2; \mathbf{k}_1 - \mathbf{k}_2) = |f^c_{(e,e^+)}(\mathbf{r}_1 - \mathbf{r}_2; \mathbf{k}_1 - \mathbf{k}_2)|^2, \tag{4.3}$$

while for an electron-electron pair with antiparallel spins (cf. Eq. (3.127)) we have

$$\rho^c_{(e,e)}(\mathbf{r}_1 - \mathbf{r}_2; \mathbf{k}_1 - \mathbf{k}_2) = \frac{1}{2}\left(|f^c_{(e,e)}(\mathbf{r}_1 - \mathbf{r}_2; \mathbf{k}_1 - \mathbf{k}_2)|^2 + |f^c_{(e,e)}(\mathbf{r}_2 - \mathbf{r}_1; \mathbf{k}_1 - \mathbf{k}_2)|^2\right). \tag{4.4}$$

In Fig. 4.1 the pair correlation function $\rho^c_{(e,e^+)}$ for a free electron-positron pair is compared to the corresponding pair correlation function $\rho^c_{(e,e)}$ for an electron-electron pair with antiparallel spins. As interaction potential we have chosen a bare Coulomb potential and, for comparison, a screened Coulomb potential of Thomas-Fermi form. The relative $\mathbf{k}$ vector is oriented along the z axis. $|\mathbf{k}_1 - \mathbf{k}_2|$ is chosen to be 2 Bohr^{-1}.

While an electron-electron pair forms a correlation hole around $r = 0$ (Fig. 4.1, left-hand panels), we observe the opposite behavior for an electron-positron pair (right-hand panels). The correlation factor $f^c_{(e,e^+)}$, and hence the pair correlation function, is clearly increased around $r = 0$. For the bare Coulomb potential the maximum of $f^c_{(e,e^+)}$ extends to $z = \infty$, whereas one obtains a sharp peak at $r = 0$, a so called correlation hill, in the case of a screened potential.

The spatial dependence of $|f^c|^2$ can be semi-quantitatively understood by noting that $|f^c| = |\varphi|$ (cf. Eq. (4.2)) and by approximating the relative-particle wave function φ by a function $\tilde{\varphi}$ composed of an incident wave and a scattered wave:

$$\tilde{\varphi}(\mathbf{r}) = e^{\mathrm{i}\kappa z} + F(\Theta)e^{\mathrm{i}\kappa r}/r \tag{4.5}$$

where $\kappa = k/2$, F is a scattering amplitude and Θ the scattering angle (defined with respect to the positive z axis). Obviously, $\tilde{\varphi}$ is rotationally symmetric about the z axis. For $x = 0$ and $y = 0$, the z dependence is easily evaluated further. In the negative z direction we have $\tilde{\varphi}(0, 0, z) = \exp(-\mathrm{i}\kappa|z|) + F(\pi)\exp(\mathrm{i}\kappa|z|)/|z|$. $|\tilde{\varphi}|$ thence oscillates with decreasing amplitude and with a wavelength $\pi/\kappa = 2\pi/k$. In the positive z direction $\tilde{\varphi}(0, 0, z) = \exp(-\mathrm{i}\kappa z)(1+F(0)/z)$ and thence $|\tilde{\varphi}| = |1 + F(0)/z|$, i.e., going monotonically towards unity. The latter behavior is seen in Fig. 4.1 for the screened potential, for which the approximation equation (Eq. (4.5)) is more appropriate than for the bare Coulomb potential. In summary, we thus have for $z < 0$ an oscillatory behavior for both the electron-electron and the electron-positron pair, whereas in the half-space $z > 0$ there is a correlation hole in the electron-electron case and a correlation hill in the electron-positron case.

The complete spatial dependence of the pair correlation function $|f^c(\mathbf{r};\mathbf{k})|^2$ is implicit in the (x, z) plane contour plot in Fig. 4.1(b), since $|f^c(\mathbf{r};\mathbf{k})|^2$ is rotationally symmetric about the z axis for the present choice of $\mathbf{k} = (0, 0, k)$. As can be seen from Fig. 4.2, the maximal height of the electron-positron correlation hill is larger than the maximal depth of the electron-electron correlation hole. This is possible due to the fact that the probability density for finding two

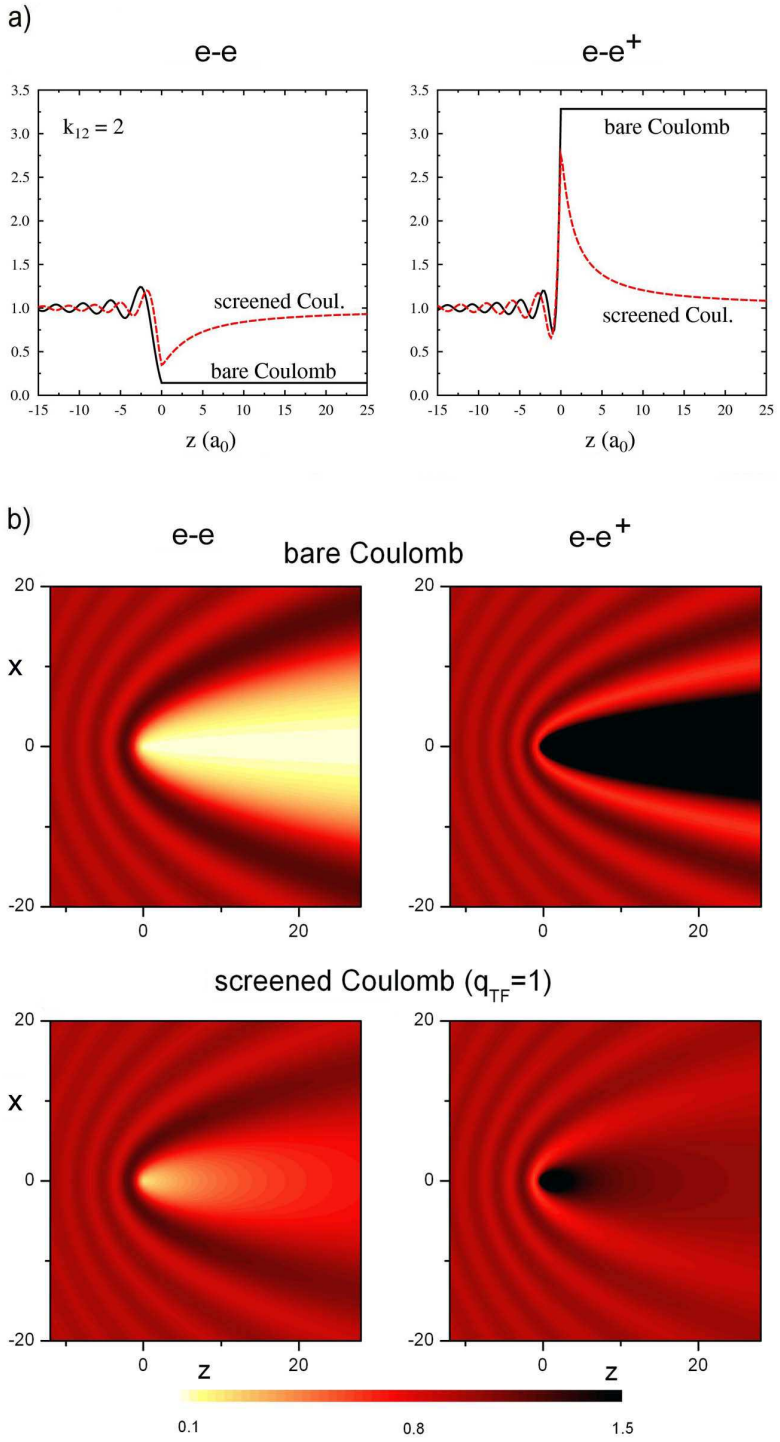

Fig. 4.1: Pair correlation function $\rho^c(\mathbf{r}_1 = 0, \mathbf{r}_2 = \mathbf{r}) = |f^c(\mathbf{r}; \mathbf{k})|^2$ (cf. Eqs. (4.4) and (4.3)) of a pair of free electrons (described by plane waves) of fixed antiparallel spins (left-hand panels) and of a free electron-positron pair (right-hand panels) with relative momentum $\mathbf{k} = \mathbf{k}_1 - \mathbf{k}_2$ along the z axis. (a) $|f^c(x = 0, y = 0, z; k = 2)|^2$ for bare Coulomb interaction (solid (black) line) and for a Thomas-Fermi-screened Coulomb interaction $\pm \exp(-q_{\mathrm{TF}} r)/r$ with $q_{\mathrm{TF}} = 1$ (in atomic units) (dashed (red) line). (b) Contour plots of $|f^c(x, y = 0, z; k = 2)|^2$ for bare (top panels) and for Thomas-Fermi-screened (bottom panels) Coulomb interaction.

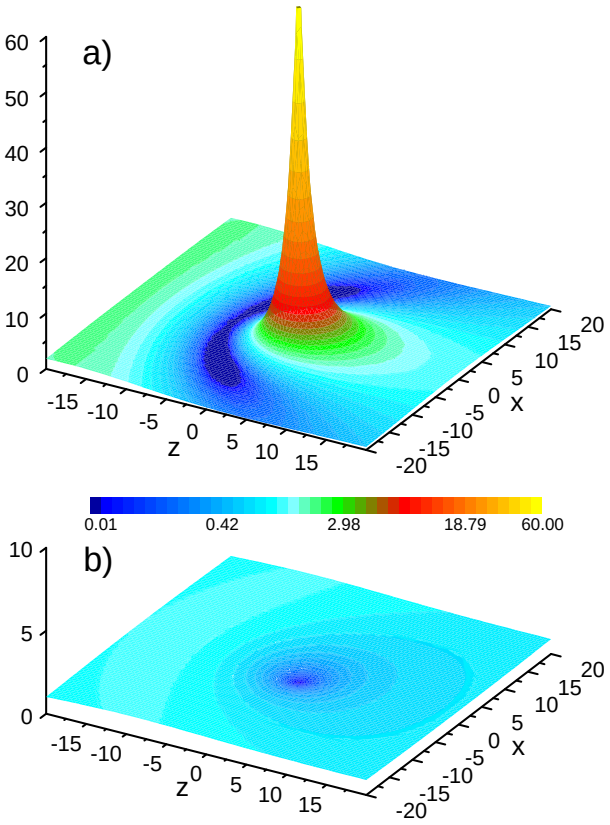

Fig. 4.2: Pair correlation function $|f^c(x, y = 0, z; k = 0.2)|^2$ (cf. Eq. (4.3)) for a Thomas-Fermi-screened Coulomb interaction with $q_{\mathrm{TF}} = 0.56$ Bohr^{-1}: (a) between a plane-wave positron and a plane-wave electron, (b) between two plane-wave electrons of fixed antiparallel spins.

electrons at $r = 0$ cannot be less than zero, whereas for the probability density for an electron and a positron there is no obvious upper limit. The maximum of the pair correlation function ρ^c increases significantly with smaller values of $k = |\mathbf{k}_1 - \mathbf{k}_2|$. Another situation where ρ^c becomes very large is when q_{TF} and k are chosen such that the electron-positron pair is about to form a positronium atom. Such an extreme case is shown in Fig. 4.2(a), where $\rho^c(r = 0)$ is larger than 60. Compared to the corresponding correlation hole for an electron pair with antiparallel spins, as shown in Fig. 4.2(b), the variation of the probability density is dramatically larger.

4.2 $(\boldsymbol{p}, \boldsymbol{ep})$ reaction cross section

Using a formalism which is formally equivalent to the one for $(e, 2e)$, the reaction cross section for the correlated emission of a positron with energy E_3, surface-parallel momentum $\mathbf{k}_3^{\parallel}$ and spin σ_3 and an electron with energy E_4 surface-parallel momentum $\mathbf{k}_4^{\parallel}$ and spin σ_4 induced by a positron with energy E_1, surface-parallel momentum $\mathbf{k}_1^{\parallel}$ and spin σ_1 can be written as (cf. Section 3.1)

$$I^{\sigma_1}_{\sigma_3,\sigma_4} = \frac{k_3 k_4}{k_1} \sum_{\sigma_2} \langle 3, 4|U|1\rangle \left(-\frac{1}{\pi}\right) \mathrm{Im}\, G_2^r(E_2, \mathbf{k}_2^{\parallel}, \sigma_2) \langle 1|U|3, 4\rangle. \tag{4.6}$$

In Eq. (4.6) the state $|1\rangle$ is a low-energy-positron-diffraction (LEPD) state with quantum numbers set asymptotically by the positron gun. G_2^r is, as in the $(e, 2e)$ case, the spin- and $\mathbf{k}^{\parallel}$-resolved

valence electron Green function with $E_2 = E_3 + E_4 - E_1$ and $\mathbf{k}_2^{\parallel} = \mathbf{k}_3^{\parallel} + \mathbf{k}_4^{\parallel} - \mathbf{k}_1^{\parallel} + \mathbf{g}^{\parallel}$ such that energy and surface-parallel momentum modulo a surface reciprocal lattice vector $\mathbf{g}^{\parallel}$ are conserved. U denotes the attractive screened Coulomb interaction between positron and electron. $|3, 4\rangle$ is the U-correlated positron-electron final state (see Eq. (4.1)) with boundary conditions such that a positron with energy E_3 and surface-parallel momentum $\mathbf{k}_3^{\parallel}$ arrives at one detector and an electron with E_4 and $\mathbf{k}_4^{\parallel}$ at the other detector.

Chapter 5

$(e, 2e)$ and (p, ep) from Cu(111)

In this chapter we present $(e, 2e)$ and (p, ep) calculations for a nonmagnetic material. We have chosen Cu(111) as a target, whose electronic properties are well investigated by a number of surface sensitive spectroscopic methods like LEED and photoemission. In particular, it offers a well-defined surface state – the Shockley surface state – which lies at the Γ point at 0.4 eV below the Fermi level. This surface state provides a single well-defined valence electron state of s-type character if energies and $\mathbf{k}^{\parallel}$ vectors of the primary and outgoing particles are chosen properly. Supplementing former $(e, 2e)$ and $(\gamma, 2e)$ investigations [38] and encouraged by experimental work of van Riessen *et al.* [21], who studied the pair correlation of positron-induced electron-positron emission, we want to present a comparison of theoretical $(e, 2e)$ and (p, ep) results from Cu(111). In particular, the different influence of the pair correlation in $(e, 2e)$ and (p, ep) is investigated. Apart from the different sign of the interaction (repulsive for the electron-electron case and attractive in (p, ep)), the positron and electron are distinguishable particles and therefore (p, ep) is not subject to the exchange interaction.

5.1 Single-particle properties of positrons and electrons in Cu(111)

In the following, we specify, for the case of the Cu(111) surface, the single-particle potentials required for calculating the four quasiparticle states, which enter, together with the Coulomb correlation factor f^c (cf. Eq. (4.1)), in the pair emission cross section (Eq. (4.6)).

As a common basis, we first performed a self-consistent calculation of the electronic structure of the ground state of Cu(111) within density functional theory by means of the full-potential linearized augmented plane-wave (FLAPW) program package FLEUR [39], using a nineteen-layer film geometry and a local density approximation (LDA) [40] for the exchange-correlation potential. We thus obtained the charge density $\rho(\mathbf{r})$ and the effective one-particle potential $V^-_{\mathrm{tot}}(\mathbf{r})$, which contains the Hartree Coulomb potential $V^-_{\mathrm{coul}}(\mathbf{r})$ and the exchange and correlation contributions $V_x(\mathbf{r})$ and $V_{\mathrm{corr}}(\mathbf{r})$. Our calculated electron work function for Cu(111) is 5.20 eV, i.e., close to the experimental value 4.94 ± 0.3 eV [41]. The occupied bulk bands are in very good agreement with those from other self-consistent ground state calculations using the same LDA (cf. [42] and references therein). Casting the shape-unrestricted ground state potential $V^-_{\mathrm{tot}}(\mathbf{r})$ into the muffin tin form and employing it in a layer-Kohn-Korringa-Rostoker (KKR) calculation yields practically the same bands.

For the interaction of the positron with the semi-infinite crystal, we first constructed a shape-unrestricted ground state potential V^+_{tot} as the sum of a Coulomb potential, which is the sign-reversed Coulomb potential $V^-_{\mathrm{coul}}(\mathbf{r})$ from the electron ground state calculation, and an attractive positron-electron correlation potential $V^+_{\mathrm{corr}}(\mathbf{r})$. Since the positron is distinct from all electrons

in the solid, there is no exchange potential V_x^+. The construction of these potentials is similar as described in [43, 44], but based on the charge density $\rho(\mathbf{r})$ from our self-consistent FLAPW film calculation. In particular, $V_{\text{corr}}^+(\rho(\mathbf{r}))$ inside the solid was obtained by using correlation energies of a positron in an electron gas of density ρ following from a many-body calculation [45] in a convenient parameterized form [46]. These correlation energies agree well with more recent many-body calculations [47]. To incorporate the positron correlation potential $V_{\text{corr}}^+(\mathbf{r})$ into the FLAPW/FLEUR package the FLEUR code was slightly extended.

In the vacuum region (in the half-space $z < 0$), where LDA ground state potentials fail to have the asymptotic image potential form, we used a local surface barrier model $V(z)$ (cf. Section 3.2.2 and [48]), which has as adjustable parameters an image plane position z_1 and a matching plane position $z_2 < z_1$ as described in Section 3.2.2 (cf. Eq. (3.62)). For $z < z_2$, $V(z)$ has (in atomic units) the image form $1/(4(z - z_1))$. For $z_2 < z < 0$, $V(z)$ is a third-order polynomial such that it matches, up to the first derivative, the image potential at z_2 and the real inner potential V_{0r} at $z = 0$. The value of V_{0r} affects not only the height but also the shape of the barrier. It is however not an adjustable parameter but rather determined by our ground state inner potential. The choice of z_1 and z_2 is guided by the near-surface form of the planar average of the ground state surface potential.

The thus obtained electron and positron potentials are compared in Fig. 5.1. $V_{\text{tot}}^+(\mathbf{r})$ and $V_{\text{tot}}^-(\mathbf{r})$ are shown as three-dimensional surface plots (3D) in Figs. 5.1(a) and 5.1(c). They clearly reveal the repulsive character of the positron potential and the attractive character of the electron potential. The line plots in Figs. 5.1(b) and 5.1(d) show the contributions V_{coul}, V_{corr}, and V_x (which vanishes for the positron) to the potential. Inside the solid, the interstitial average of $V_{\text{tot}}^+(\mathbf{r})$, which corresponds to the inner potential in a muffin tin approximation, is at 5.26 eV below the vacuum level, which is much less than its counterpart for an electron (12.91 eV). It is interesting to note that the positron correlation potential part $V_{\text{corr}}^+(\rho(\mathbf{r}))$ is substantially stronger than the correlation potential for an electron. In particular, its interstitial average of -8.63 eV (cf. Fig. 5.1(b)) is about six times larger than its electron counterpart (-1.4 eV). This is in line with our above finding (Section 4.1) that the pair correlation function $|f^c|^2$ for small r is much stronger for an electron-positron pair than for an electron-electron pair (cf. Figs. 4.1 and 4.2).

In the vacuum region, the actual positron potential $V_{\text{tot}}^+(\mathbf{r})$ forms a "correlation well" above the topmost atomic layer before joining the potential inside the solid. It hosts a Rydberg-like series of bound positron surface states, the lowest one of which has been observed at -2.8 eV (below the vacuum zero) for Cu(111) [49]. The theoretical energy of the lowest e^+ surface state $E_{\text{Ryd, min}}$ depends on the parameters z_1 and z_2 used to form the surface barrier. We have chosen this parameters such that $E_{\text{Ryd, min}}$ becomes identical to the experimental value.

The ground-state bulk band structure of copper as obtained by the FLAPW method is shown in Fig. 5.2 and agrees well with those found in the literature (see, e.g., [42] and references therein). Typically, the free electron-like *sp*-bands, which begin at -9 eV relative to the Fermi level are superimposed by flat *d* bands reaching from -5 eV to -1.5 eV. Because of their flatness the *d*-type states cause a very high density of states (DOS), which is shown in the right-hand panel

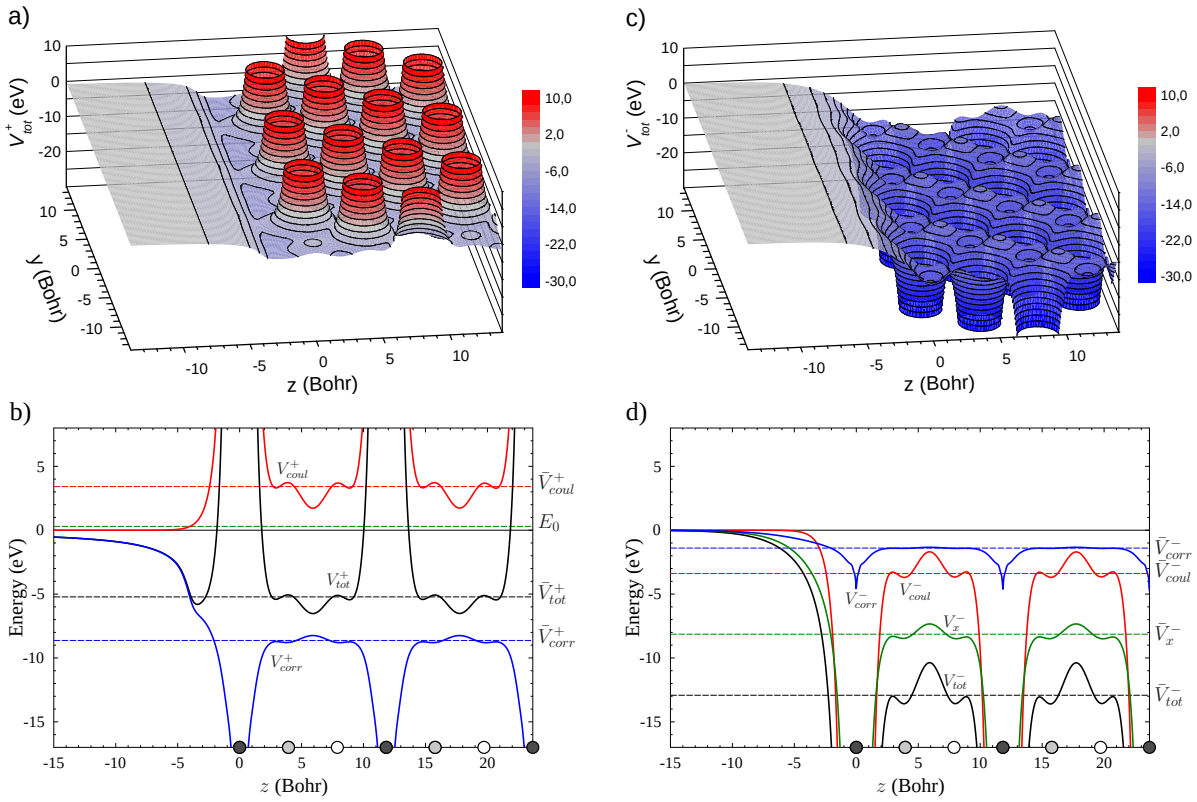

Fig. 5.1: Effective positron potential in Cu(111) (left-hand side) compared to the ground-state electron potential (right-hand side). (a) and (c): 3D plots of the total potentials $V^+_{\rm tot}(x=0,y,z)$ and $V^-_{\rm tot}(x=0,y,z)$, respectively. (b) and (d): Line plots of $V^\pm_{\rm tot}(x=0,y=0,z)$ (black solid line) and their constituent parts: $V^\pm_{\rm coul}$ (red dashed line) $V^\pm_{\rm corr}$ (blue dotted line) and $V^-_{\rm x}$ (green solid line). The corresponding horizontal lines mark the respective interstitial average potentials. The z axis is normal to the surface and the topmost internuclear plane is located at $z=0$; x is along the $[1,-1,0]$ direction and y along $[-1,-1,2]$. The green-dashed horizontal line in (b) indicates the energy E_0 of the lowest positron bulk state (0.3 eV above the vacuum level).

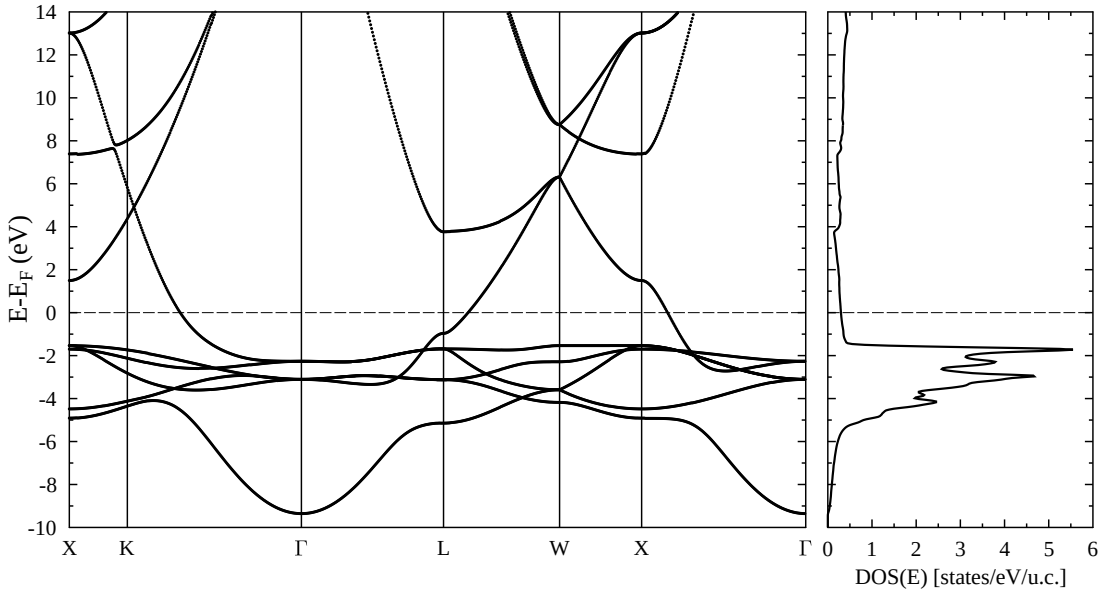

Fig. 5.2: FLAPW bulk band structure and corresponding density of states (integrated over the entire Brillouin zone) of Cu.

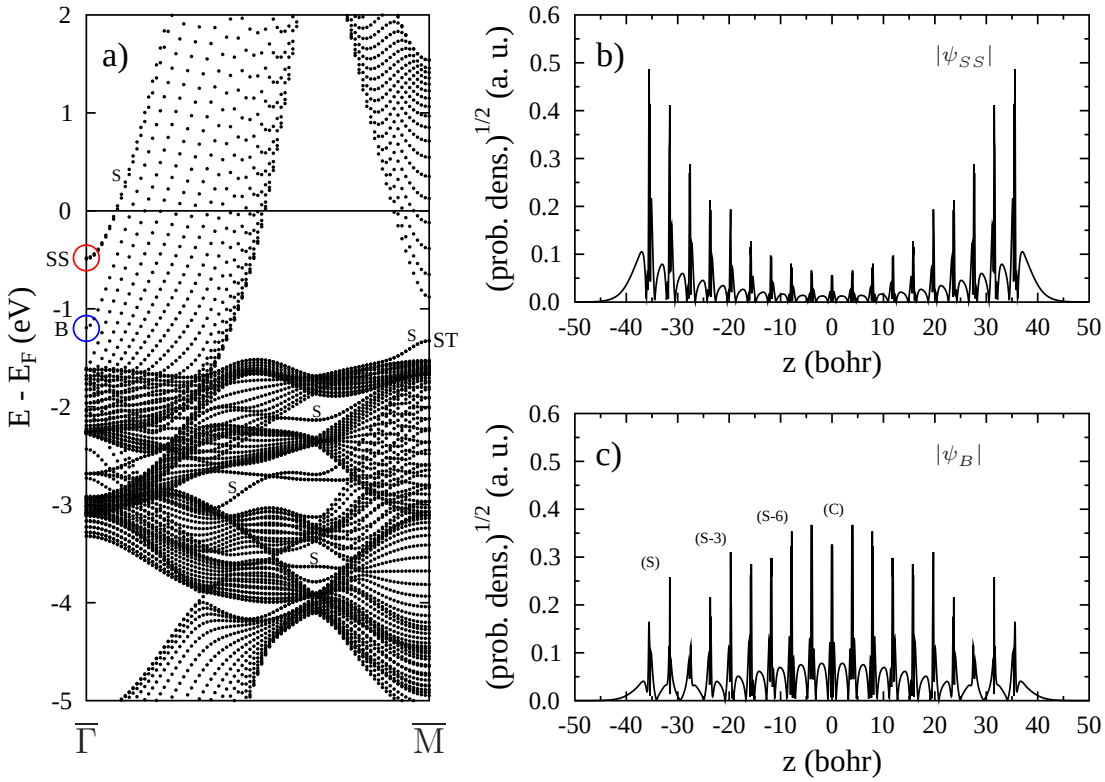

Fig. 5.3: a) FLAPW energy bands for Cu(111) 19-layer slab. b) $|\psi|$ for the Shockley surface state at $\overline{\Gamma}$ indicated by (SS). c) $|\psi|$ for uppermost bulk band state at $\overline{\Gamma}$ indicated by (B).

of Fig. 5.2. Near the Fermi level the DOS is relatively low, which is related to a relatively weak screening and hence partly responsible for the typical electric and thermal behavior of copper.

Energy bands of a Cu(111) 19-layer slab as a function of $\mathbf{k}^{\|}$ along the $\bar{\Gamma}$–$\bar{\mathrm{M}}$ direction are shown in Fig. 5.3(a). Besides a large number of bulk bands one also obtains some bands of surface states (some of which are indicated by S). SS indicates the well known Shockley surface state, the bottom of which lies at -0.4 eV relative to E_F. The density distributions of the Shockley surface state at $k = 0$ across the 19-layer slab is shown in Fig. 5.3(b) and compared to a respective distribution of a typical bulk-like state (indicated by B in Fig. 5.3(a)) as shown in Fig. 5.3(c). Whereas the density of the surface state is largest at the outermost layers and decreases significantly for the central layers, the situation is almost opposite to the bulk-like state. The still visible oscillation of the peak heights is a consequence of the limited number of slabs used in the film calculation.

The bulk energy bands for a positron in copper are shown in Fig. 5.4. Overall they resemble nearly free electron bands. This can also be seen from the density of states shown in the right-hand panel, which oscillates around the free-electron like parabola (indicated by the dashed curve). Contrary to the electron bands in Fig. 5.2, all bulk states are lying above vacuum level. The lowest positron bulk state is at the Γ point at 0.3 eV above the vacuum threshold, implying a positron work function of -0.3 eV close to the experimental value of -0.4 eV [49].

For the calculations of $(e, 2e)$ or (p, ep) intensities we need quasiparticle wave functions instead of ground state wave functions. The quasiparticle wave functions are solutions in effective potentials, which are obtained by modifying the ground-state potential by so called self-

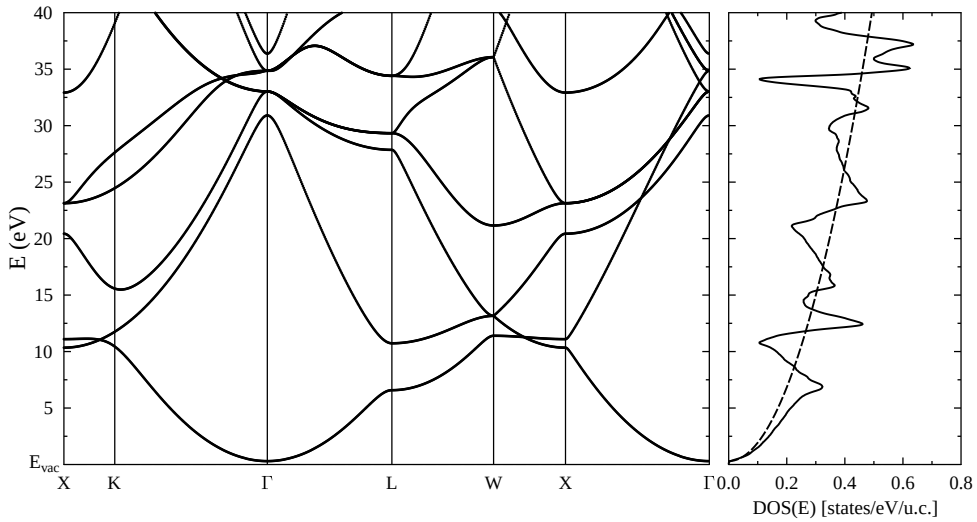

Fig. 5.4: FLAPW bulk band structure for a positron in Cu. The energy is relative to the vacuum level.

energy corrections. Lifetime effects and absorption are incorporated by an imaginary part of the potential ($V_{\rm im}$). Moreover, the energy levels of the quasiparticle states can considerably be shifted relative to the ground state levels. Both effects vanish for energies near the Fermi level and become more important with increasing distance from E_F. For the electron potential we use $V_{\rm im} = -0.05 - (E - E_F)^2/((E - E_F)^2 + 0.49)$ eV for the occupied states and $V_{\rm im} = -0.08\,(E - E_F)$ eV for the LEED-like states. The imaginary part of the effective positron potential has been estimated to be about twice as strong as for an electron [50]. With the latter as described above, we therefore used for the positrons the energy-dependent expression $-0.16\,(E - E_F)$ eV. Since the damping of the incident and the emitted positron state is thus stronger than in the electron case, one can expect (p, ep) to be generally more surface-sensitive than $(e, 2e)$.

Comparing the ground state band structure of copper to their counterparts determined experimentally by photoemission [42], the calculated sp-like bands agree fairly well, but the d-bands are about 0.5 eV too high in energy. A real effective potential for the occupied one-electron states in (p, ep) and $(e, 2e)$ was therefore constructed by adding contributions of a non-local density approximation to our self-consistent potential in a way that the experimental photoemission peaks are well reproduced (see Fig. 2(b) in [42]). Figure 5.5 shows the layer-resolved density of states (LDOS) $N_m(E, k_x, k_y)$, where m is the layer index, as a function of $(E, \mathbf{k}^{\parallel})$ in different representations by using this potential. In order to reveal more details only a very small imaginary part (-0.05 eV) was used. The bulk LDOS shown in Figs. 5.5(a) and 5.5(b) corresponds to the projection of the bulk band structure onto the surface. In particular, in Fig. 5.5(a) the features at $\mathbf{k}^{\parallel} = 0$ reflect very closely the bulk band structure along Γ−L, with the *sp* gap near the Fermi energy and the onset of the *d* bands at about -2 eV. In the first-layer LDOS (Figs. 5.5(c) and 5.5(d)) we would like to emphasize three features: around the center of the first surface Brillouin zone (SBZ) ($\bar{\Gamma}$) the Shockley surface state residing in the *sp* gap near E_F and the Tamm-like surface resonances in the *d*-band region (cf. [42] and references therein), and near $\overline{\rm M}$ the Tamm surface state, which was also previously observed by photoemission [51].

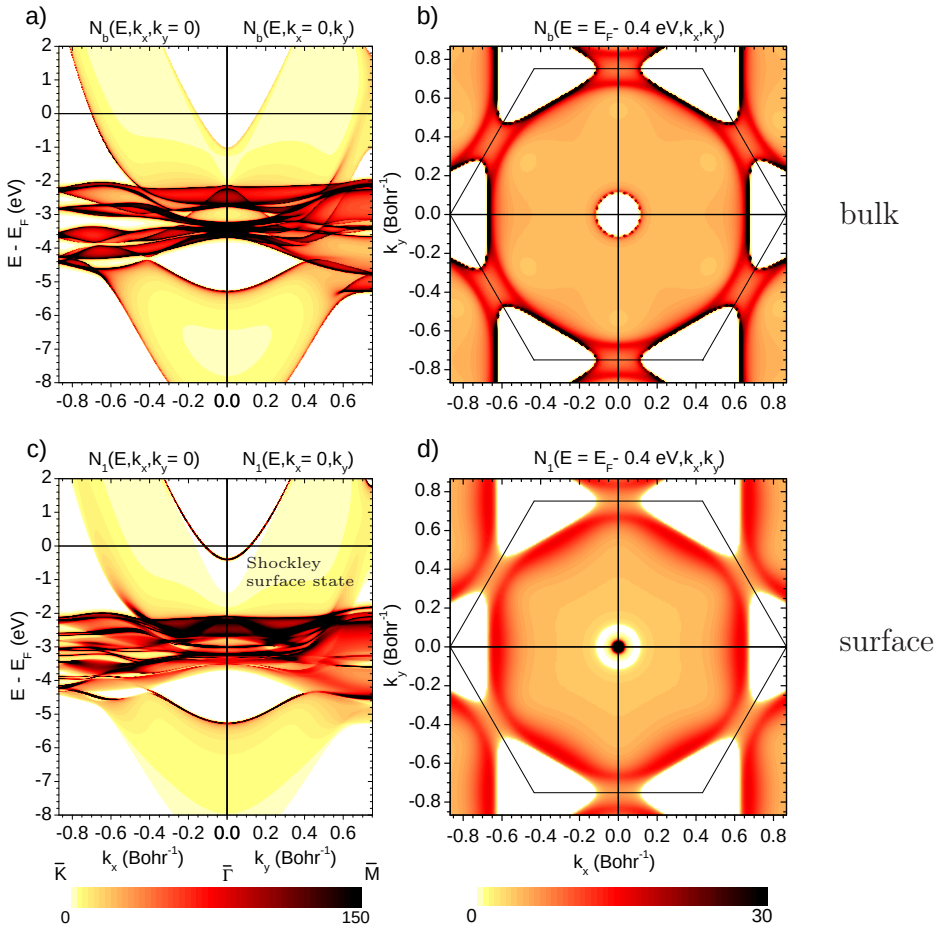

Fig. 5.5: $\mathbf{k}^{\parallel}$- and layer-resolved density of initially occupied quasi-electron states $N_m(E, k_x, k_y)$ on Cu(111). To reveal more details, the imaginary potential part has been chosen as a very small constant (0.005 eV). (a) For bulk layer: $N_b(E, k_x, k_y = 0)$ for $\mathbf{k}^{\parallel}$ along the $\overline{\Gamma}$–$\overline{\mathrm{K}}$ direction in the surface Brillouin zone (SBZ) and $N_b(E, k_x = 0, k_y)$ for $\mathbf{k}^{\parallel}$ along $\overline{\Gamma}$–$\overline{\mathrm{M}}$. (b) For bulk layer: $N_b(E, k_x, k_y)$ for fixed $E = E_F - 0.4$ eV. The hexagon indicates the SBZ. (c) As (a) but N_1 for topmost (surface) layer. (d) As (b) but N_1 for topmost (surface) layer.

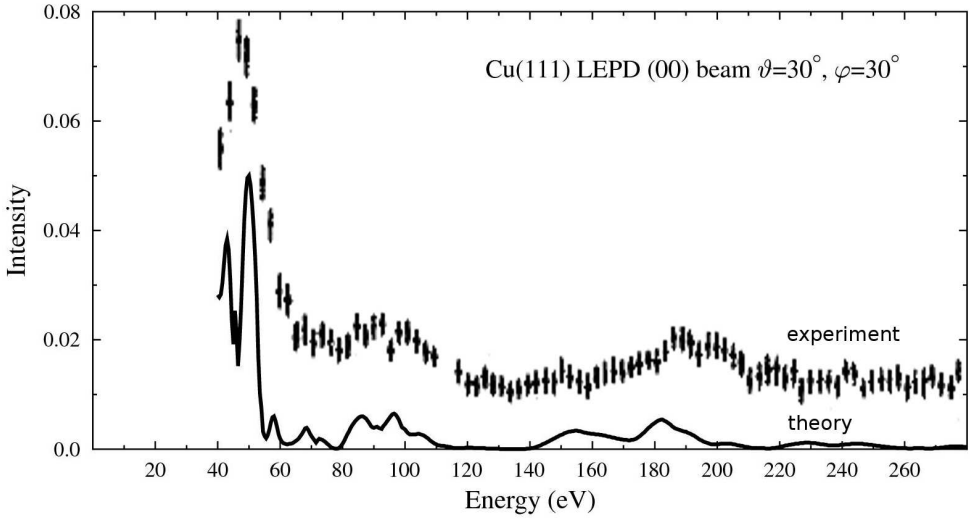

Fig. 5.6: Comparison of an experimental LEPD intensity of the (00) beam (cf. [52], Fig. 6) with its theoretical counterpart for $\vartheta = 30°$ and $\varphi = 30°$.

In Fig. 5.6 we show, as an example, a comparison between an observed LEPD spectrum (cf. reference [52]) and a calculated one, both obtained for $\vartheta = 30°$ and $\varphi = 30°$. Overall, there is a relatively good agreement between both curves. In particular, the peak width is well represented by the chosen imaginary part of the potential. Up to 120 eV the peak positions agree also very well. For larger energies a substantial shift in energy is visible. Because in our (p, ep) calculations the maximum primary energy is 30 eV, it is not necessary to modify our potential by a real self-energy shift.

In our (p, ep) calculations the energies of the outgoing particles lie between 6 eV and 19 eV. Because the $\mathbf{k}^{\parallel}$ dependence of the associated LEED/LEPD intensities will have an important effect on the $(e, 2e)$ and (p, ep) intensities, we have investigated the $\mathbf{k}^{\parallel}$ dependence of LEPD for some selected energies, which is presented in Fig. 5.7. The resulting intensities are of circular form, where the center refers to normal incidence ($\vartheta = 0°$) and the border to parallel incidence ($\vartheta = 90°$). The (00) beam (shown on the left-hand side) shows a sixfold symmetry as for each individual Cu(111) layer. Interestingly, the intensities of the non-specular beams (shown on the right-hand side) exhibit a pronounced threefold symmetry caused by the overall threefold symmetry of the Cu(111) surface. Striking structures in form of circular segments are due to surface resonances of the LEPD states (and similar for LEED states). These regions in the (k_x, k_y) plane correspond to threshold energies, where additional non-specular beams can emerge.

In a first approach these LEED/LEPD intensities multiplied by the density of states at the energy of the involved valence state will give a good guess for the $(e, 2e)$ and (p, ep) intensities.

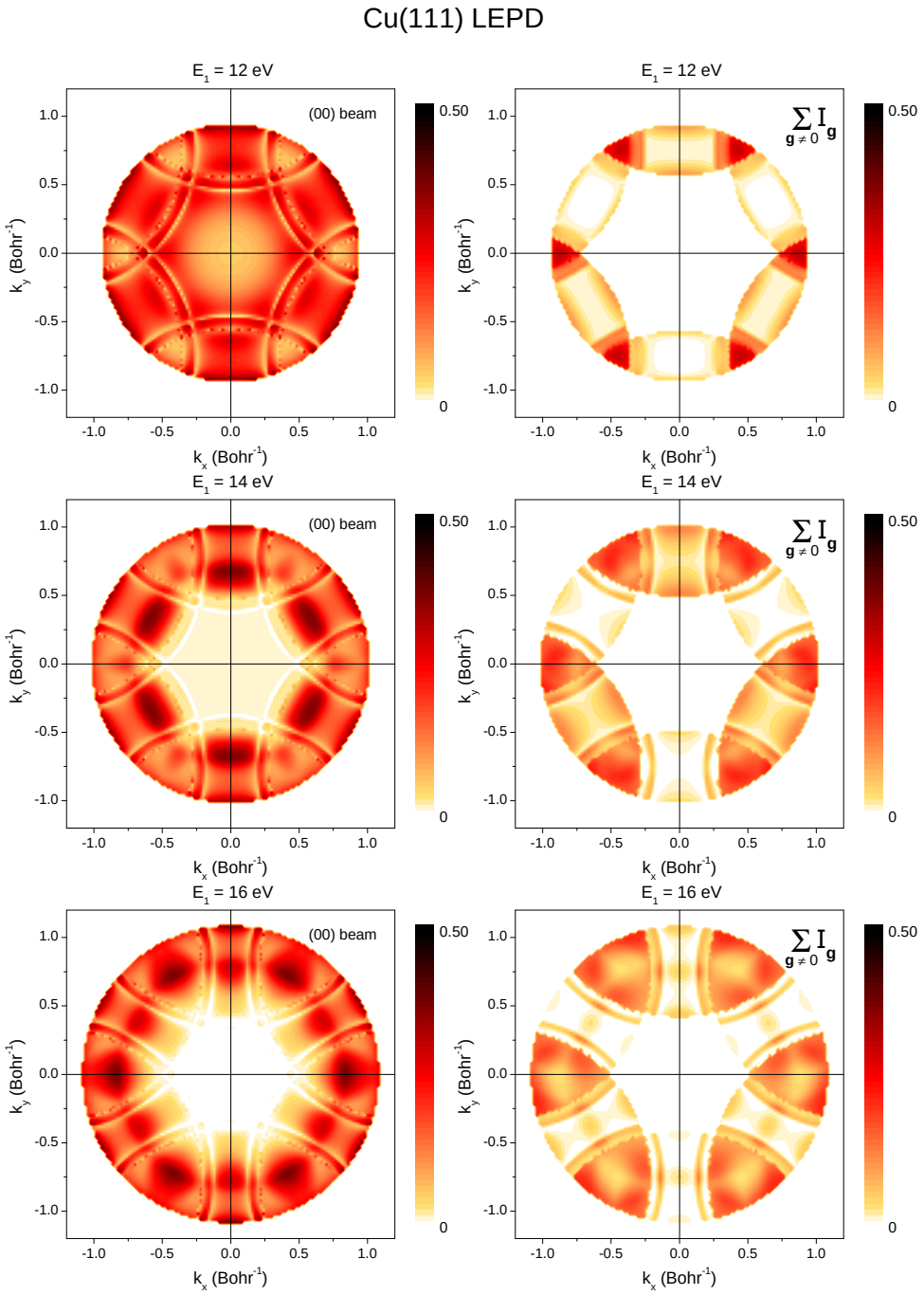

Fig. 5.7: (k_x, k_y)-dependent LEPD intensities for a Cu(111) surface for different primary energies: Left-hand side: Intensity of the (00) beam. Right-hand side: Sum of the intensities of the non-specular beams.

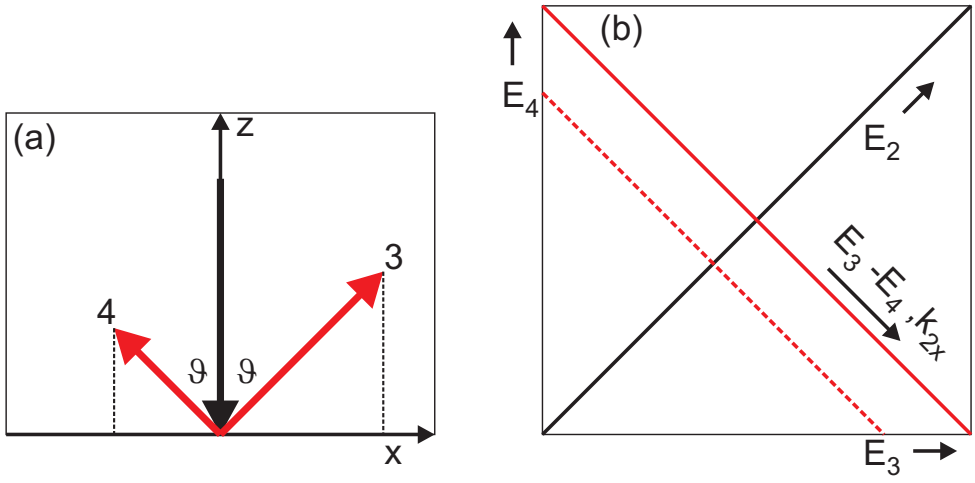

Fig. 5.8: (a) Coplanar symmetric setup for the discussed $(e, 2e)$ and (p, ep) processes: $\vartheta_1 = 0°$, $\vartheta_3 = \vartheta_4$, $\varphi_4 = \varphi_3 + 180°$. (b) Schematic diagram used to present the density of states N and the $(e, 2e)$ intensities I obtained with the setup in (a): For fixed energy E_1, N and I can be expressed as functions of E_3 and E_4. The black line corresponds to $E_3 = E_4$ and the red lines correspond to $E_3 + E_4 = \text{const}$ and $E_2 = \text{const}$.

5.2 $(e, 2e)$ and (p, ep) intensities

In order to assess to what extent pair emission spectroscopy may reflect the valence electron LDOS, we now consider a symmetric coplanar setup with normal incidence of the primary particle (i.e., $\mathbf{k}_1^{\parallel} = 0$) and fixed polar angles $\vartheta_3 = \vartheta_4$ of the two emitted particles. For a given reaction plane and primary energy E_1, the (p, ep) and the $(e, 2e)$ cross sections are then functions $I(E_3, E_4)$ of the energies of the two outgoing particles and can be represented by a contour plot in the (E_3, E_4) plane. Each pair (E_3, E_4) determines $(E_2, \mathbf{k}_2^{\parallel})$ of the valence electron because of $E_2 = E_3 + E_4 - E_1$ and $\mathbf{k}_2^{\parallel} = \mathbf{k}_3^{\parallel} + \mathbf{k}_4^{\parallel} - \mathbf{k}_1^{\parallel}$, where $\mathbf{k}_2^{\parallel}$ is not restricted to the first SBZ. Thus $\mathbf{k}_2^{\parallel}$ lies in the reaction plane, with the component

$$k_2^{\parallel} = \left(\sqrt{2E_3} - \sqrt{2E_4}\right) \sin\vartheta_3 \,. \tag{5.1}$$

The $\mathbf{k}_2^{\parallel}$-resolved density of states $N_m(E_2, \mathbf{k}_2^{\parallel})$ for the mth atomic layer parallel to the surface can therefore also be represented by a contour plot in the (E_3, E_4) plane. In this plot, the diagonal $E_3 = E_4$, on which $k_2^{\parallel} = 0$, can be viewed as the E_2 axis, and the other diagonal, which marks the Fermi energy, is associated with $k_2^{\parallel}$ (with a nonlinear scale according to Eq. (5.1)). In Fig. 5.9(a) the surface LDOS N_1 for Cu(111) is represented in this way for primary energy 30 eV and emission in the (x, z) plane at polar angles $\vartheta_3 = \vartheta_4 = 30°$. N_1 in Fig. 5.9(a) is seen to correspond to a small section (around Γ) of the surface LDOS along $\overline{\Gamma}$–$\overline{\mathrm{M}}$ shown in Fig. 5.5(c). In particular, it exhibits, near E_F, the Shockley surface state.

Prior to presenting calculated pair emission cross sections from Cu(111), we would like to address the relevance of spin-orbit coupling (SOC). SOC in valence electron states as well as in LEED and LEPD states generally causes the (p, ep) and the $(e, 2e)$ cross section to depend on the spin of the primary particle. Sizable asymmetries of this nature have previously been theoretically predicted [26] and experimentally verified [53] for $(e, 2e)$ from the large-Z material

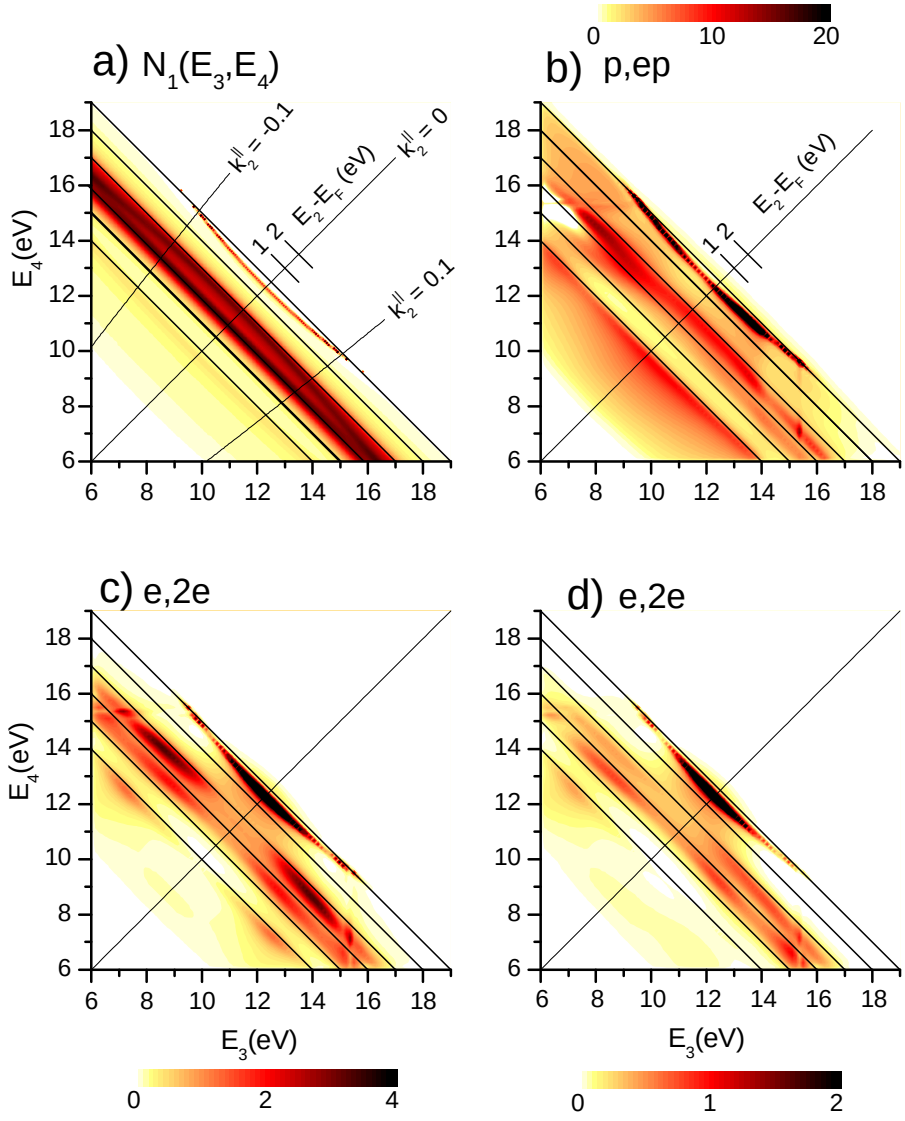

Fig. 5.9: Pair emission spectra $I(E_3, E_4)$ from Cu(111) for coplanar symmetric setup with normal incidence of primary positron or electron of energy $E_1 = 30$ eV and emitted particles with energies E_3 and E_4 and polar angle $\vartheta_3 = \vartheta_4 = 30°$. The reaction plane is the (x, z) plane (with x along the $[1, -1, 0]$ direction and z normal to the surface). The (y, z) plane is a mirror plane of the semi-infinite crystal. (a) First-layer valence electron density of states $N_1(E_3, E_4) = N_1(E_2, k_x; k_y = 0)$. The diagonal axis represents the valence electron energy E_2 with respect to the Fermi energy. The axis normal to it is associated with $k_x = k_2^{\parallel}$ (cf. Eq. (5.1)) as indicated by the iso-$k_2^{\parallel}$ lines (in atomic units). (b) $I(E_3, E_4)$ for (p, ep). (c) $I(E_3, E_4)$ for spin-unresolved $(e, 2e)$. (d) $I(E_3, E_4)$ for $(e, 2e)$ with fixed antiparallel spins of the emitted electrons.

W(001) (see also Chapter 7). In the presently studied case of Cu(111), they are, however, quite small (of the order of a few per cent) for $(e, 2e)$ because of the fairly low Z of Cu. For (p, ep) we found them to be even smaller, by at least an order of magnitude. To explain this, we recall that SOC effects are much smaller in LEPD than in LEED [54]. Consequently, in (p, ep) only two of the single-particle states (the outgoing electron state and the valence electron state) are significantly affected by SOC, whereas in $(e, 2e)$ this applies to all four states. We therefore do not elaborate on SOC effects for pair emission from copper surfaces and present only intensities averaged over the spin of the primary particle, which corresponds to an experiment with an unpolarized source.

The calculated (p, ep) energy distribution $I(E_3, E_4)$ for $E_1 = 30$ eV, which is associated with the surface LDOS in Fig. 5.9(a), is shown in Fig. 5.9(b), with E_3 and E_4 denoting the energies of the emitted positron and electron, respectively. For comparison, we show in Fig. 5.9(d) its counterpart for spin-resolved $(e, 2e)$, where E_3 and E_4 refer to the emitted spin-up and spin-down electron, respectively. While a substantial valence electron LDOS is obviously a prerequisite for strong intensity features, both the Shockley surface state and the *d*-like states manifest themselves in the pair emission distributions in a very inhomogeneous way due to differences in the final state wave functions in the integrals in the intensity expression Eq. (4.6).

In the (p, ep) energy distribution (Fig. 5.9(b)), the asymmetry with respect to the diagonal, i.e., to an interchange of positron and electron energies, is immediately plausible since the final state "fast positron, slow electron" (below the diagonal in Fig. 5.9(b)) is very different from the state "slow positron, fast electron" (above the diagonal). This asymmetry is most pronounced for the nearly parabolic feature, which reflects the Shockley surface state. Its very high intensity for the emitted-positron energy between 12.5 and 14 eV can be traced back to surface resonances in the LEPD state, which are associated with the emergence threshold for two non-specular LEPD beams. This kind of asymmetry has recently been observed by Brandt *et al.* [55], who experimentally studied the positron-electron coincidence emission from various surfaces (Ag, Co, and NiO).

In the fixed antiparallel spins $(e, 2e)$ energy distribution (Fig. 5.9(d)), the Shockley surface state is seen to appear symmetrically to the "equal-energy-sharing" diagonal, i.e., invariant to an interchange of the values of the energies E_3 and E_4. This is readily understood: the *sp*-like Shockley state is symmetric and the interchange does not alter the spatial part of the final two-electron state. In contrast, some of the valence *d* states (in the range 2–4 eV below E_F, cf. Fig. 5.5) are antisymmetric, which entails an asymmetry of $I(E_3, E_4)$ in this energy range.

The spin-unresolved $(e, 2e)$ energy distribution (Fig. 5.9(c)) is, as a consequence of exchange, the sum of a direct antiparallel spin part I_d, which is actually the intensity shown in Fig. 5.9(d), an exchange antiparallel spin part I_e, which is the mirror image of I_d with respect to the diagonal, and a parallel spin part I_par, which is mirror-symmetric (cf. [38, 56]). $I(E_3, E_4)$ in Fig. 5.9(c) is therefore symmetric and, I_par being comparatively small, close to the sum of $I(E_3, E_4)$ in Fig. 5.9(d) and its mirror image.

In the above energy distributions at constant emission angles the valence state and the final two-particle state are varied. For the study of correlation effects between the two emitted

particles, angular distributions obtained in a "constant initial state" setup like the one shown in Fig. 5.10(a) is more suitable. The primary particle has constant energy E_1 and surface-parallel momentum $\mathbf{k}_1^{\parallel}$, i.e., fixed polar and azimuthal angles of incidence (ϑ_1, φ_1). For the emitted particles we choose constant $E_3 = E_4$ and variable $\mathbf{k}_3^{\parallel} = -\mathbf{k}_4^{\parallel}$. According to energy and parallel-momentum conservation the valence state has thus a constant energy E_2 and $\mathbf{k}_2^{\parallel} = -\mathbf{k}_1^{\parallel}$. The pair emission intensity then depends only on $\mathbf{k}_3^{\parallel}$ or, equivalently, on (ϑ_3, φ_3).

In Fig. 5.10 we focus on the special case of normal incidence of the primary particle and consequently $\mathbf{k}_2^{\parallel} = 0$. Choosing further $E_1 = 30$ eV and $E_3 = E_4 = 12.3$ eV, the active valence electron is in the Shockley surface state at the center of the SBZ with energy $E_2 = E_F - 0.4$ eV.

In Fig. 5.10(b) we show the (p, ep) angular distribution $I(\mathbf{k}_3^{\parallel})$ calculated for this case. As one would qualitatively expect, the intensity is largest in the center, i.e., for small polar emission angles ϑ. The mirror symmetry with respect to the (y, z) plane and the threefold rotation symmetry about the surface normal correspond to the C_{3v} symmetry of the semi-infinite Cu(111) crystal. The $(e, 2e)$ angular distribution for the case of fixed antiparallel spins (Fig. 5.10(d)) also exhibits these symmetries, but only very small intensities for small emission angles. It is tempting to interpret this central depletion zone as a Coulomb correlation hole (cf. Figs. 5 and 6 in [38]). For the present energies, however, an angular distribution calculated without Coulomb correlation already exhibits, due to matrix element effects, a depletion zone almost as pronounced as the one shown in Fig. 5.10(d).

If the spins of the two electrons are not resolved, the distribution (shown in Fig. 5.10(c)) becomes sixfold by adding to the direct antiparallel spin part I_{d} an exchange antiparallel spin part I_{e}, which is rotated azimuthally by 180° with respect I_{d}. Further, it contains a parallel spin part I_{par}, which is inherently sixfold due to exchange.

While the occurrence of a central accumulation zone in (p, ep) as opposed to a central depletion zone in $(e, 2e)$ appears plausible, it is striking at first glance that also further out the (p, ep) intensity is much larger than its fixed spins' $(e, 2e)$ counterpart, e.g., for $(k_x, k_y)/k$ around $(0.65, 0.4)$ by a factor of about 5. (Note the different scales on the color bars.) To what extent this is due to the difference between the positron and electron single-particle states on the one hand and due to the Coulomb correlation in the emitted pair state on the other will be explored in the following.

In Fig. 5.11 we compare (p, ep) angular intensity distributions calculated, for normal incidence of a positron with energy 29 eV and 30 eV on Cu(111), without Coulomb correlation in the emitted pair state (by taking the correlation factor f^c (cf. Eq. (4.1)) as 1) (left-hand panels) with their counterparts calculated with Coulomb correlation (by using the numerically calculated f^c) (right-hand panels). Please note that in the plots the intensity of the "without" panels has been scaled up by a factor of two with respect to the "with" panels. The most important effect of the Coulomb correlation is, as one would expect, a strong enhancement for small emission angles. An enhancement, of about a factor two, is however also found for large emission angles. To understand this, we first note that in the intensity formula equation (Eq. (4.6)) the correlation factor $f^c(\mathbf{r}; \mathbf{k})$ (cf. Eq. (4.1)) can be taken out of the final two-particle state $|3, 4\rangle$ and incorporated into the Coulomb interaction $U(\mathbf{r})$. This amounts to an intensity formula with a correlation-

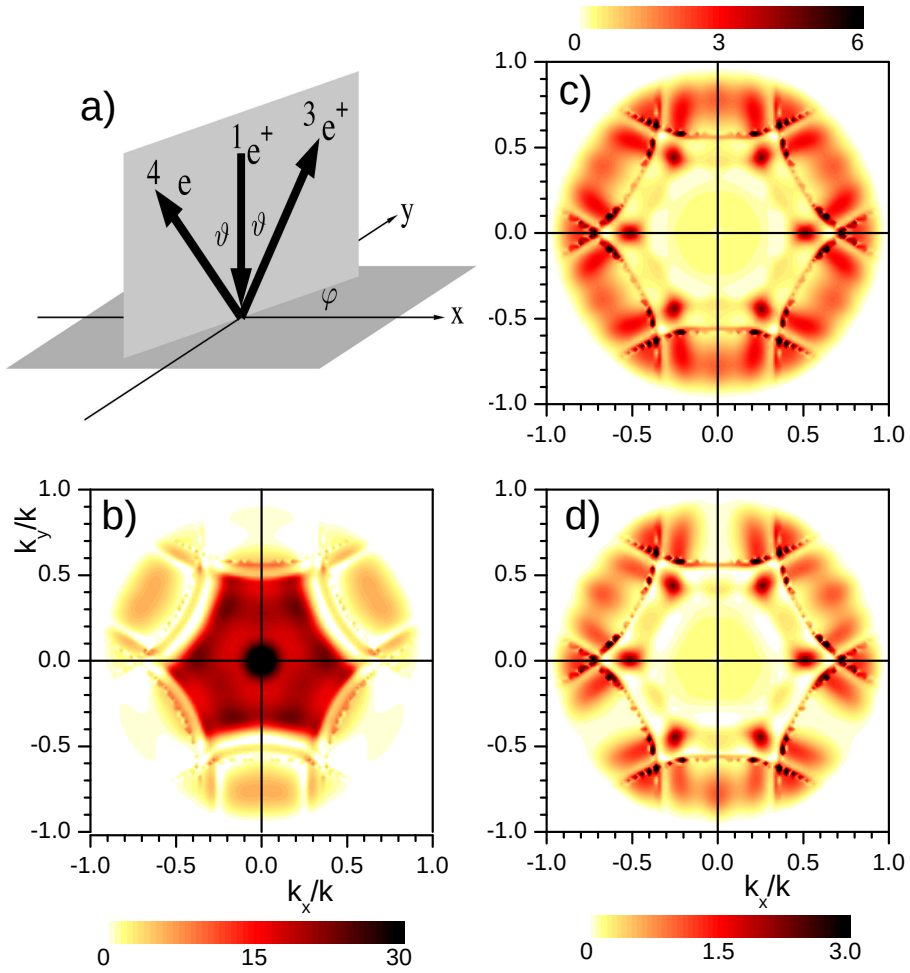

Fig. 5.10: Angular distribution of the pair emission intensity from Cu(111) upon normal incidence of an unpolarized positron or electron beam with energy $E_1 = 30$ eV. The setup is coplanar symmetric with fixed equal energies $E_3 = E_4 = 12.3$ eV and surface-parallel momenta $(k_3^x, k_3^y) = (-k_4^x, -k_4^y)$ of the emitted particles. The relevant valence state is thus the bottom of the Shockley surface state with energy $E_2 = E_F - 0.4$ eV and $\mathbf{k}_2^{\parallel} = 0$. (a) Sketch of the present (p, ep) setup. The angles ϑ and φ determine the above surface-parallel momentum components of the emitted positron as $k_3^x = k_3 \sin\vartheta \cos\varphi$ and $k_3^y = k_3 \sin\vartheta \sin\varphi$, where $k_3 = \sqrt{2E_3} = 0.95$ Bohr^{-1}. The $(e, 2e)$ setup is analogous. (b) Intensity $I(k_x/k, k_y/k)$ for (p, ep), where $(k_x, k_y) := (k_3^x, k_3^y)$ and $k := k_3$. (c) Intensity $I(k_x/k, k_y/k)$ for $(e, 2e)$ not spin-resolved. (d) Intensity $I(k_x/k, k_y/k)$ for $(e, 2e)$ with fixed antiparallel spins of the emitted electrons.

modified Coulomb potential

$$U^c(\mathbf{r};\mathbf{k}) = f^c(\mathbf{r};\mathbf{k})U(|\mathbf{r}|) \tag{5.2}$$

and an uncorrelated final two-particle state. Since for the positron-electron pair $|f^c|$ is much larger than unity for small k and r (cf. Figs. 4.1 and 4.2), a strong enhancement of the pair emission intensity at small angles is obvious. A closer inspection of $|f^c|$ as a function of the momentum difference k reveals that it is still fairly large for the maximal momentum difference in the case of Fig. 5.11, which is reached at grazing exit and amounts to $2\sqrt{2E_3} = 1.9$ Bohr^{-1}.

Returning to the above-raised question, why the "further-out" (p, ep) intensity around the position $(k_x, k_y)/k = (0.65, 0.4)$ is about five times larger than the corresponding $(e, 2e)$ intensity (cf. Figs. 5.10(b) and 5.10(d)), the lower panels of Fig. 5.11 show that the electron-positron correlation is responsible for a factor of about two. On the other hand, the $(e, 2e)$ intensity in Fig. 5.10(d), which was calculated including electron-electron correlation, is weaker by a factor of about two than its counterpart without correlation. Consequently, the Coulomb correlation is the main cause of this difference between (p, ep) and $(e, 2e)$.

The striking differences between the (p, ep) angular distributions for primary energy 29 eV (upper panels of Fig. 5.11) and primary energy 30 eV (lower panels of Fig. 5.11) are due to numerical differences in the respective integrals in Eq. (4.6). While correlation always enhances the central region more strongly than the outer one, such "matrix elements effects" may, as in the case of $E_1 = 29$ eV, dominate, with the consequence that there is eventually a central depletion zone instead of a naively expected "correlation hill".

The (p, ep) and $(e, 2e)$ angular distributions in Figs. 5.10 and 5.11 have a pronounced feature in common: the circular narrow structures, which intersect the k_x/k axis around 0.65, and those related to them by threefold rotation symmetry. These structures are manifestations of surface resonances in the LEED and LEPD states of the emitted particles, which are associated with the emergence thresholds of non-specular beams.

In the above "constant initial state" angular intensity distributions, the relevant valence electron is at the bottom of the Shockley surface state at the center of the surface Brillouin zone (SBZ). In the following we consider analogous (p, ep) angular distributions, which are associated with valence electron states further out in the SBZ. Since parallel-momentum conservation implies $\mathbf{k}_2^{\parallel} = -\mathbf{k}_1^{\parallel} + \mathbf{g}^{\parallel}$, a specific valence electron state can be selected by off-normal incidence of the primary particle with an appropriate $\mathbf{k}_1^{\parallel}$.

Two typical examples of the resulting (p, ep) angular distributions are shown in Fig. 5.12, for a 30 eV positron incident with azimuthal angle $\varphi_1 = 90°$, i.e., in the (y, z) mirror plane, and polar angle ϑ_1. Thus $\mathbf{k}_1^{\parallel} = (0, k_1^y) = (0, -\sqrt{2E_1}\sin\vartheta_1)$ and $\mathbf{k}_2^{\parallel} = (0, k_2^y) = (0, -k_1^y + g^y)$, where we choose the reciprocal lattice vector component g^y such that $\mathbf{k}_2^{\parallel}$ is in the first SBZ. The emitted particle energies are chosen, like in the previous examples, as $E_3 = E_4 = 12.3$ eV, which implies $E_2 = E_F - 0.4$ eV.

In the first example, a valence state with $k_2^y = 0.67$, i.e., associated with a high *sp*-like bulk density (cf. Fig. 5.5), is selected by choosing the angle of incidence $\vartheta_1 = 26.5°$. The resulting (p, ep) angular distribution (Fig. 5.12(a)), which is necessarily mirror-symmetric with respect to the (y, z) plane, exhibits, like in the above normal incidence case, a central accumulation

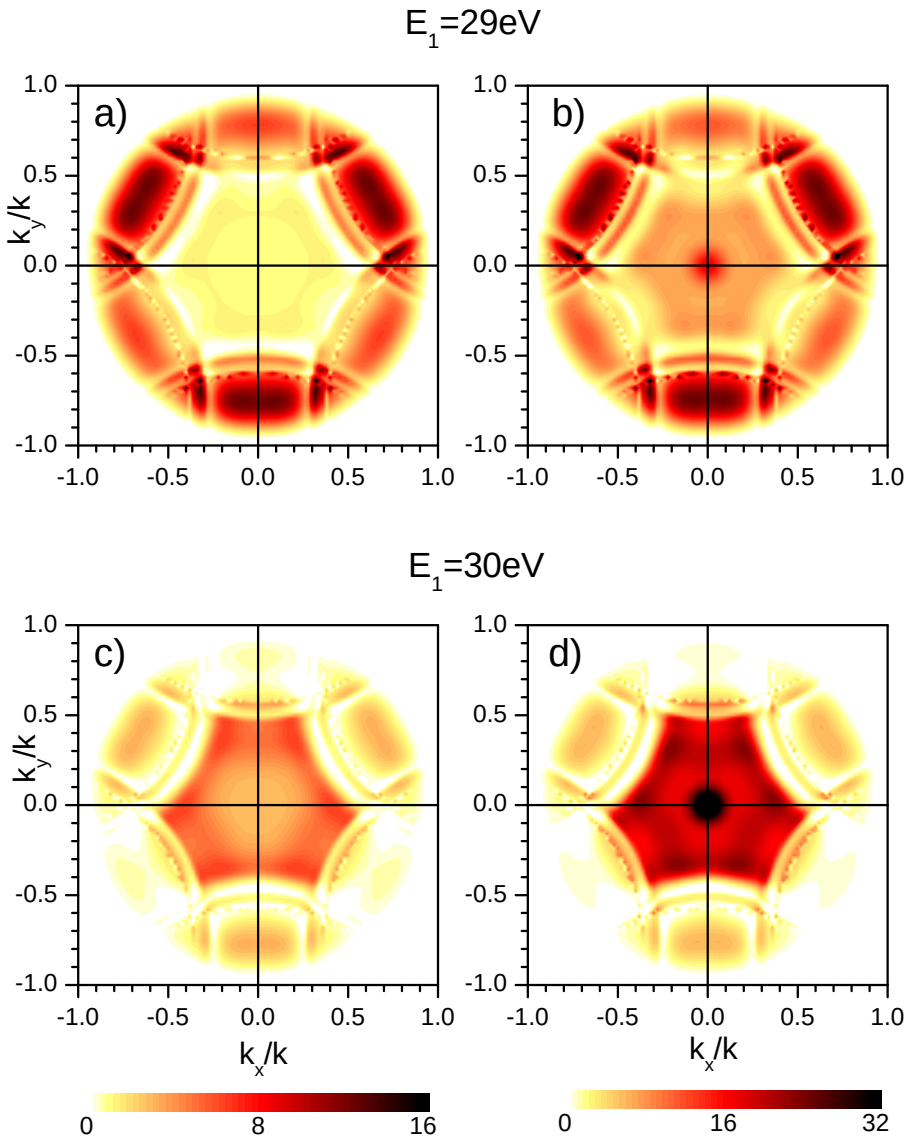

Fig. 5.11: Correlation effect in the angular distribution of (p, ep) from Cu(111) upon normal incidence of a positron. The setup is the same as described in the caption to Fig. 5.10, with $E_1 = 29$ eV and $E_3 = E_4 = 11.8$ eV (panels (a) and (b)), and $E_1 = 30$ eV and $E_3 = E_4 = 12.3$ eV (panels (c) and (d)), such that in both cases the electron is excited from the bottom of the Shockley surface state. The Coulomb correlation in the emitted electron-positron pair state has been neglected (by taking the correlation factor f^c (cf. Eq. (4.1)) as 1) in the left-hand panels (a) and (c), whereas it has been included (by using the numerically calculated f^c) in the right-hand panels (b) and (d). Note that the intensity scale in panels (b) and (d) is twice the one in panels (a) and (c).

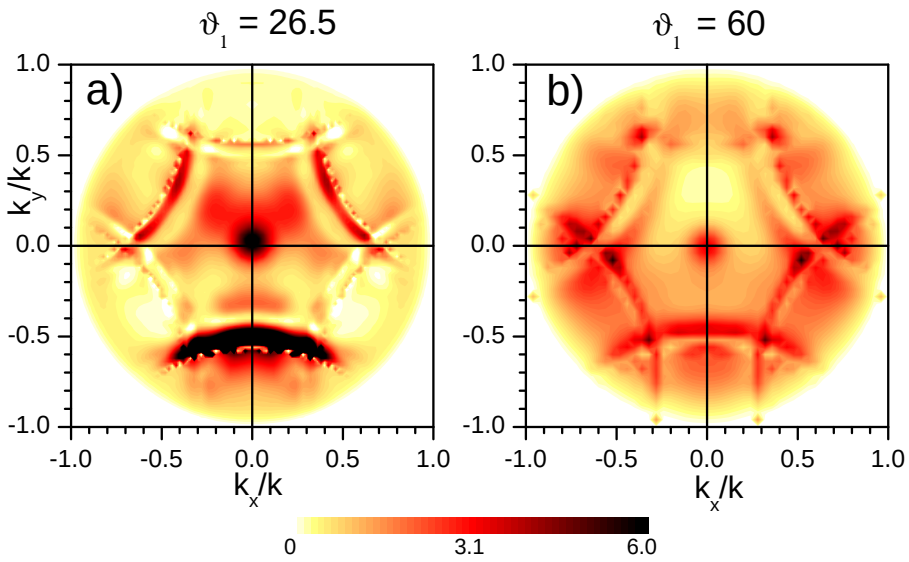

Fig. 5.12: Angular distribution of (p, ep) from Cu(111) for off-normal incidence of a positron with $E_1 = 30$ eV. The emission setup is the same as described in the caption to Fig. 5.10. The positron is incident in the (y, z) plane at polar angle $\vartheta_1 = 26.5°$ (panel (a)) and $\vartheta_1 = 60°$ (panel (b)). According to energy and momentum conservation, the valence electron thus has energy $E_2 = E_F - 0.4$ eV in both cases, and surface-parallel momentum $(k_2^x = 0, k_2^y)$ with $k_2^y = 0.67$ Bohr^{-1} for $\vartheta_1 = 26.5°$ and $k_2^y = 0.21$ Bohr^{-1} for $\vartheta_1 = 60°$.

zone due to the Coulomb correlation in the emitted electron-positron pair. Also, further out the circular structures due to LEPD and LEED surface resonances are present, but with a much stronger weight on the feature around $k_y/k = -0.6$, i.e., with $k_3^y = k_y = -0.57$, which is near to $k_1^y = -0.67$ of the primary positron.

For the larger angle of incidence $\vartheta_1 = 60°$, we have $k_1^y = -1.29$, which upon addition of the reciprocal lattice vector component $g^y = 1.50$ yields for the valence electron $k_2^y = 0.21$. We recall from above that $E_2 = E_F - 0.4$ eV. From Fig. 5.5 this valence state is seen to be in a region of very low *sp*-like density of states. The corresponding (p, ep) angular distribution is shown in Fig. 5.12(b). We notice again the circular structures and a central Coulomb correlation hill, which is however weaker than the one in Fig. 5.12(a).

Our finding that the central correlation hill and the circular structures are fairly similar for different initial states and identical final states is due to the fact that they are basically final state features arising from the electron-positron Coulomb correlation and LEPD/LEED surface resonances, respectively.

Chapter 6

$(e, 2e)$ from ferromagnetic Fe(001)

In this chapter we will investigate $(e, 2e)$ from a Fe(001) surface, which represents a typical magnetic material. In general this would mean that we have to deal with spin polarization (by magnetic effects) and spin-orbit coupling (SOC) simultaneously, which, if treated on equal footing, would considerably complicate the treatment of the underlying electronic structure and the calculation of $(e, 2e)$ intensities.

In a first step, we will show in Section 6.1 that SOC leads to relatively small effects on $(e, 2e)$ spectra for Fe(001) surfaces. As in the case of nonmagnetic copper (cf. Chapter 5), we therefore neglect SOC for the present purpose. This has the advantage that we can keep the relatively simple single group description of the valence-state symmetry which among others allows for a clear symmetry classification of the density of states and $(e, 2e)$ intensities and to specify simple selection rules for the $(e, 2e)$ intensities. The treatment of SOC and magnetic exchange effects on equal footing, applied to Co adsorbed on W(110), will be discussed in Chapter 7.

6.1 Influence of spin-orbit coupling

In Fig. 6.1 we compare layer-resolved densities of states (LDOS) and energy bands for Fe(001) obtained by a relativistic calculation including spin-orbit coupling (SOC) to respective results where SOC is neglected.

The presence of SOC leads to a reduction of the symmetry of the Hamilton operator and hence to typical band splittings, which in the case of Fe are of the order of 0.1 eV (to be seen at -1.8 eV and $+0.4$ eV). At these energies, SOC causes small dents in the DOS. Apart from these, the density of states is practically not modified by spin-orbit coupling.

In addition to the influence of the LDOS of the valence state, $(e, 2e)$ spectra are formed by the momenta, energies, and the spin orientation of the primary electron $(E_1, \mathbf{k}_1, \sigma_1)$ and momenta and energies of the outgoing particles $(E_3, E_4, \mathbf{k}_3, \mathbf{k}_4)$. In theory, the $(e, 2e)$ intensities are also spin resolved with respect to the states $|3\rangle$ and $|4\rangle$. However, since present $(e, 2e)$ experiments only deliver spin averaged intensities, we here also discuss the intensities averaged over the spins σ_3 and σ_4 of the outgoing electrons. From the numerous possible combinations of $(E_1, \mathbf{k}_1, \sigma_1; E_3, E_4, \mathbf{k}_3, \mathbf{k}_4)$, we have chosen two typical setups, giving (1) angle dependent equal-energy $(e, 2e)$ spectra (Fig. 6.2) and (2) energy sharing spectra $I^{\sigma_1,\mu}(E_3 - E_4)$ for fixed angles and constant sum energy $E_3 + E_4$ (Fig. 6.3).

The angle-dependent spectra shown in Fig. 6.2 were calculated for a primary energy $E_1 = 28$ eV and two typical values of the energy E_2 of the valence state, $-0,8$ eV and -1.8 eV below the Fermi energy, respectively. As can be seen, the intensities $I^{\sigma_1,\mu} = I^{+,+}$ and $I^{\sigma_1,\mu} = I^{-,+}$ in Fig. 6.2 are in both cases practically not affected by spin-orbit coupling.

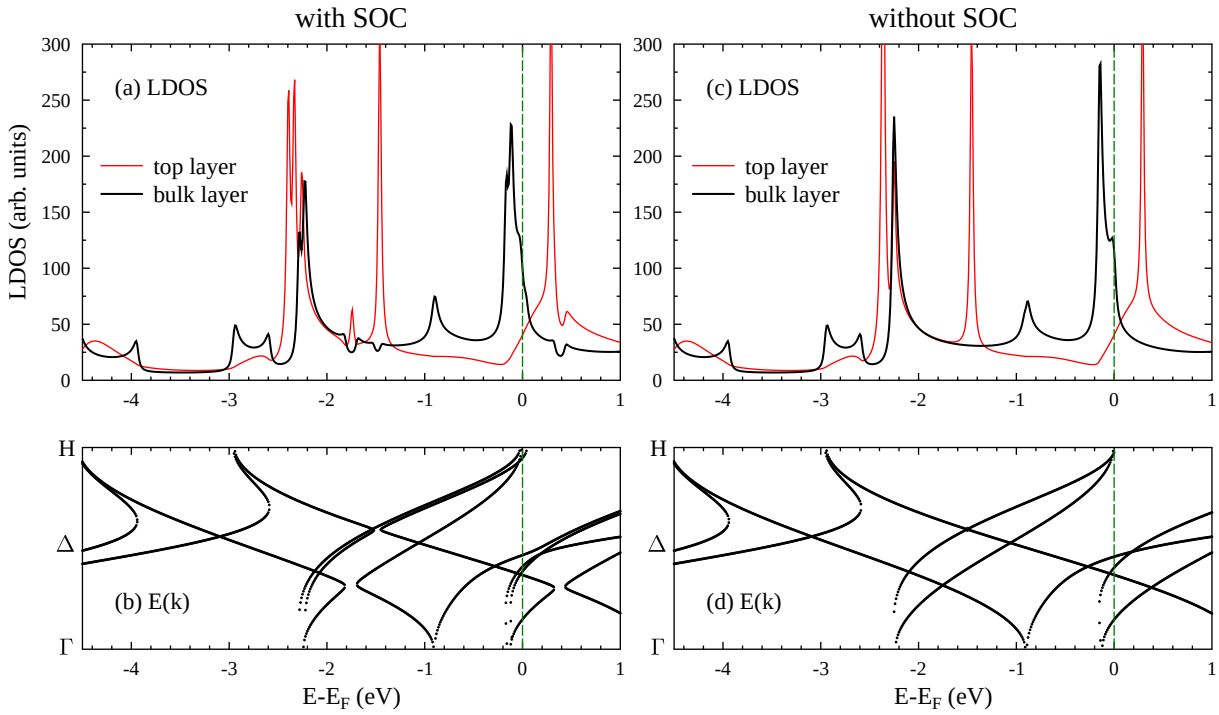

Fig. 6.1: Spin-summed layer-resolved densities of states (LDOS) and energy bands for Fe(001) for $k^{\parallel} = 0$ (center of the surface Brillouin zone): (a) relativistic LDOS (i.e., with spin-orbit coupling (SOC)) for the topmost surface layer and the bulk layer, (b) associated relativistic energy bands ($E(k)$), (c) LDOS calculated without SOC, (d) associated bands.

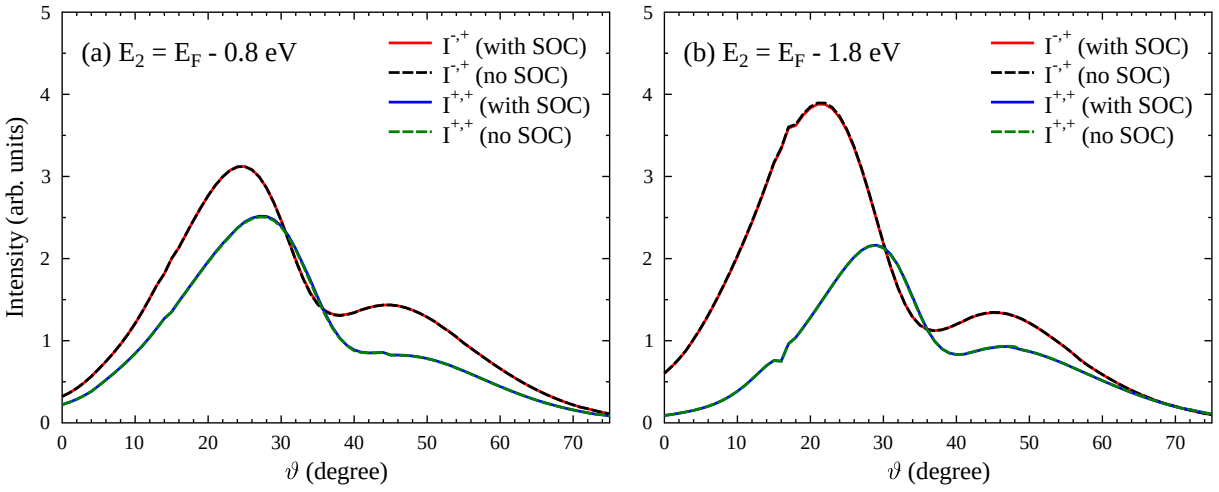

Fig. 6.2: Equal-energy $(e, 2e)$ intensities $I^{\sigma_1,\mu}$ for primary energy $E_1 = 28$ eV as functions of the polar angles of the outgoing electrons $\vartheta = \vartheta_3 = \vartheta_4$. Solid lines: spin-dependent intensities with SOC; dashed lines: without SOC. (a) $E_3 = E_4 = 11.265$ eV, $E_2 = E_F - 0.8$ eV. (b) $E_3 = E_4 = 10.765$ eV, $E_2 = E_F - 1.8$ eV.

In the case of the energy-sharing diagram, shown in Fig. 6.3, the resulting intensities are again not much influenced by SOC. There are, however, some qualitative changes. Without SOC the intensities are symmetric with respect to a change of the sign of $E_3 - E_4$, i.e., $I(E_4 - E_3) = I(E_3 - E_4)$ (which is equivalent to a change $\mathbf{k}_2^{\parallel} \to -\mathbf{k}_2^{\parallel}$). This symmetry is slightly broken by SOC leading to finite — but still very small — asymmetries A_u and A_{so}. The exchange asymmetry A_{ex} remains dominant and is practically not influenced by SOC. Overall, one can conclude that for the purpose of our present study of $(e, 2e)$ from the Fe(001) surface, in particular the comparison with recent experiments [9, 10], SOC plays a minor role and can justifiably be neglected in the present chapter.

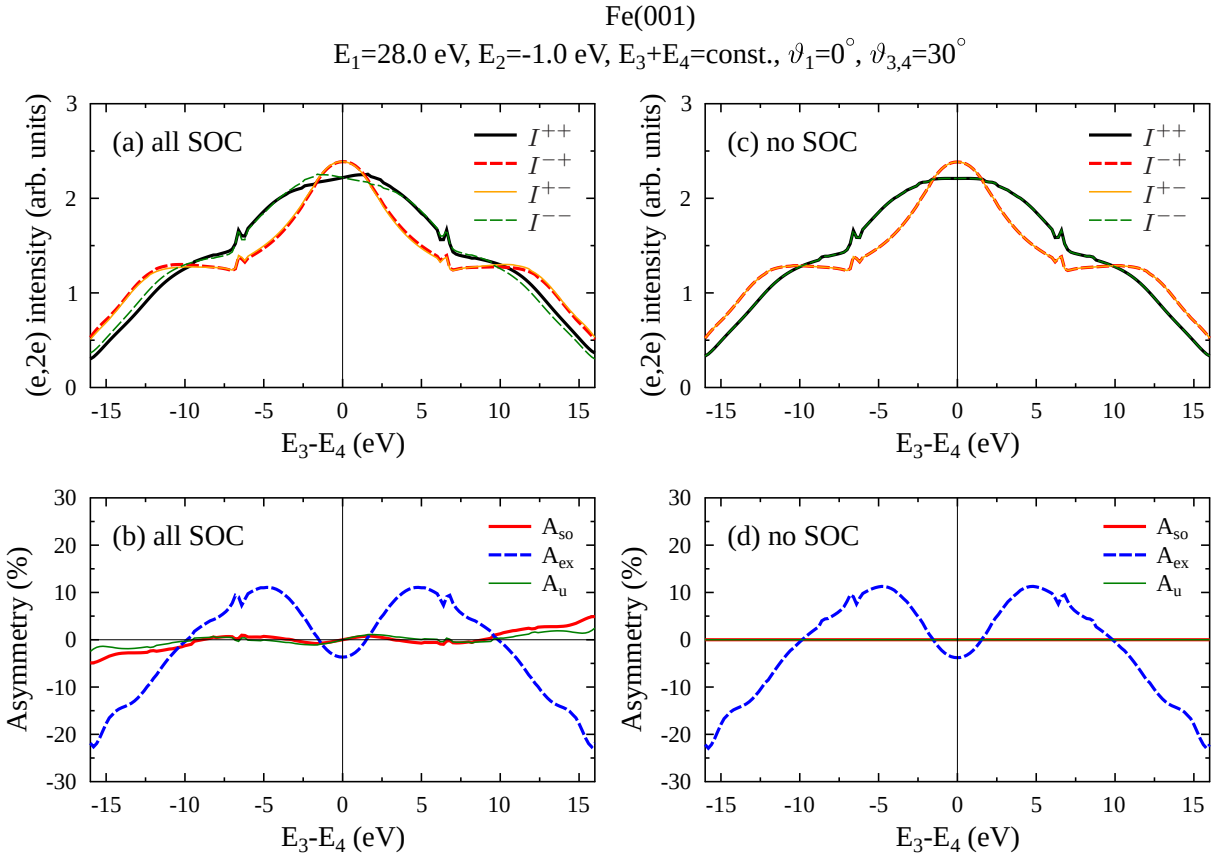

Fig. 6.3: Energy sharing curves $I^{\sigma_1\mu}(E_3 - E_4)$ for $E_3 + E_4 = 22.33$ eV and $\vartheta_3 = \vartheta_4 = 30°$ for normal incidence of the primary electron. The reaction plane is the (x, z) plane and the majority spin orientation μ is along the y axis. a) and b): Fully relativistic calculations. c) and d): SOC switched off.

6.2 General considerations and model specifications

While experimental $(e, 2e)$ spectra — for a given primary spin orientation — in general are a sum over contributions involving both spin-up and spin-down valence electrons (with energy and surface-parallel momentum determined by the respective conservation law), theory can obtain these contributions separately. This allows more detailed insight into exchange and Coulomb correlation effects. Calculating in addition the valence electronic structure, we can elucidate the

relationship between spin-dependent $(e, 2e)$ spectra and the spin-, momentum-, and symmetry-resolved valence electron density of states. The latter is furthermore useful for identifying energy and parallel-momentum conditions, for which valence electrons of one spin type and two spatial symmetry types predominate. As will be explained below, this makes it possible to separate exchange and Coulomb correlation effects directly in the experimental spectra.

For the calculation of the electronic structure of the ground state we also employed the *ab initio* full-potential linear augmented-plane-wave (FLAPW) method [39]. Using a local-density approximation for the exchange-correlation energy [40], we applied this method to a ferromagnetic Fe(001) film consisting of 21 monoatomic layers, with the first interlayer spacing reduced by 5% relative to the bulk Fe interlayer spacing and the second interlayer spacing expanded by 5%, as had been determined by a low-energy electron diffraction (LEED) analysis [57]. We thereby obtained the spin-, layer-, and symmetry-resolved density of states (referred to in the following as LDOS), which is the key quantity for interpreting $(e, 2e)$ spectra. Further, we calculated the spin-resolved charge density, which is needed for the construction of the quasiparticle potential input for our $(e, 2e)$ calculations.

For the calculation of $(e, 2e)$ reaction cross sections we used the formalism presented in Chapter 3. Due to the antisymmetrization there are two types of matrix elements: direct and exchange ones. Since we neglect spin-orbit coupling (cf. Section 6.1), the direct matrix elements reduce to the form

$$f^{\sigma\tau} = \langle 3^\sigma 4^\tau | U | 1^\sigma \rangle | 2^\tau \rangle \,, \tag{6.1}$$

where $|1^\sigma\rangle$ and $|2^\tau\rangle$ are the (spin-dependent) spatial parts of the primary and the valence electron states with spin orientations $\sigma = \pm$ and $\tau = \pm$ relative to the majority spin axis of the target. U denotes the screened Coulomb interaction. The two detected electrons are described by an antisymmetric two-electron state (cf. Section 3.2.6, Eqs. (3.118) and (3.119)), the direct spatial part of which is

$$|3^\sigma 4^\tau\rangle = |3^\sigma\rangle |4^\tau\rangle f^c(\mathbf{k}, \mathbf{r}) \,, \tag{6.2}$$

where $|3^\sigma\rangle$ and $|4^\tau\rangle$ are the spatial parts of time-reversed LEED states. These are coupled by the Coulomb correlation factor $f^c(\mathbf{k}, \mathbf{r})$, which is a function of the relative momentum $\mathbf{k}$ and the relative coordinate $\mathbf{r}$ obtained as the numerical solution of a relative-particle Schrödinger equation involving U (cf. Section 3.2.6 and [38]).

Because of the antisymmetry of the two-electron states we have, in addition to the direct matrix elements $f^{\sigma\tau}$ (cf. Eq. (6.1)), exchange matrix elements $g^{\sigma\tau}$, which are analogous to $f^{\sigma\tau}$, with 3^σ and 4^τ interchanged.

For the cases of spin σ of the primary electron parallel and antiparallel to the spin τ of the valence electron, i.e., $\tau = \sigma$ and $\tau = -\sigma = \bar{\sigma}$, we then have the fully spin-resolved $(e, 2e)$ reaction cross sections,

$$I^{\sigma\sigma} \propto |f^{\sigma\sigma} - g^{\sigma\sigma}|^2 \delta \quad \text{and} \quad I^{\sigma\bar{\sigma}} \propto (|f^{\sigma\bar{\sigma}}|^2 + |g^{\sigma\bar{\sigma}}|^2)\delta, \tag{6.3}$$

where δ symbolizes the conservation of energy and surface-parallel momentum. Summation over the valence electron spins yields the experimentally observable intensities

$$I^+ = I^{++} + I^{+-} \quad \text{for primary electron spin up,} \tag{6.4a}$$

$$I^- = I^{-+} + I^{--} \quad \text{for primary electron spin down.} \tag{6.4b}$$

For the application of the above $(e, 2e)$ formalism to Fe(001) we constructed from our ground-state spin densities spin-dependent effective quasiparticle potentials. These contain in particular spin-dependent imaginary self-energy parts V_{im}^{σ}, with $\sigma = +$ for spin up and $\sigma = -$ for spin down electrons. For the valence electrons, we took

$$V_{\text{im}}^{\sigma}(E) = a^{\sigma} \frac{|E - E_F|}{|E - E_F| + 10.0} - 0.025 \text{ (eV)}, \tag{6.5}$$

where E is the electron energy in eV and the constant coefficient a^{σ} is $a^+ = -4.05$ for spin up and $a^- = -1.35$ for spin down. In the energy range between the Fermi energy and about 4 eV below, which is relevant in our $(e, 2e)$ context, this simple form approximates reasonably well the numerical results obtained by a many-body (local-density approximation (LDA)–dynamical mean-field theory (DMFT)) calculation [35]. As an important feature, we note that the lifetime of majority spin holes is much shorter than that of minority spin holes.

For the primary electron and the two detected electrons, which are represented by LEED states, we assumed the imaginary self-energy part

$$V_{\text{im}}^{\sigma}(E) = a^{\sigma}(E + b^{\sigma})^{c^{\sigma}}, \tag{6.6}$$

where E is the kinetic energy in eV, V_{im}^{σ} is in eV, and the constant coefficients are $a^+ = -0.22$, $b^+ = 2.67$, $c^+ = 0.69$, $a^- = -0.33$, $b^- = 4.67$, $c^- = 0.62$. By virtue of the relation

$$\lambda^{\sigma} = \sqrt{2(\tilde{E} + \tilde{V}_r)}/(2\tilde{V}_{\text{im}}^{\sigma}), \tag{6.7}$$

where $\tilde{V}_r$ is the real part of the inner potential in Hartree atomic units and $\tilde{E}$ and $\tilde{V}_{\text{im}}^{\sigma}$ are the respective quantities in Hartree. This choice is in quantitative accordance with experimental data for the spin-dependent mean-free path λ^{σ}, which shows that spin-down electrons are more strongly damped than spin-up electrons [32–34]. In terms of the bulk interlayer spacing of Fe(001) (2.71 Bohr), some typical values of λ^{σ} are the following. For primary electrons with kinetic energy 25 eV, λ^+ and λ^- are 3.88 and 3.12, respectively. For the outgoing electron energy 10 eV, we have 5.18 and 3.77.

Using the above V_{im}^{σ} (Eq. (6.6)) in a spin-dependent LEED calculation from Fe(001), we obtained the best agreement with experimental data [58]. In our present $(e, 2e)$ calculations, this V_{im}^{σ} yields significantly better agreement with our experimental data than a spin-independent V_{im}.

As described in Section 3.2.6 (cf. Eq. (3.122)), the electron-electron interaction U is approximated by the Thomas-Fermi form $U \propto \exp(-q_{\text{TF}} r)/r$, where the strength of the Coulomb correlation is determined by the Thomas-Fermi wave number q_{TF}. In the present study of magnetic iron surfaces, q_{TF} was treated as a parameter, which we determined by comparing calculated

$(e, 2e)$ energy and momentum distributions with their experimental counterparts (see Section 6.5 below). The Coulomb repulsion in the vacuum region is not included explicitly, but mimicked by a weakening of the effective screening in the topmost atomic layers. Since the emission of low-energy electron pairs originates mainly from the first two layers, as will be demonstrated below, the thus obtained effective Thomas-Fermi wave number $q_{\mathrm{TF}} = 0.1$ Bohr^{-1} (see Section 6.5 below) accounts for the Coulomb interaction in the topmost layers and in the near-surface vacuum. Consequently it is much smaller than the bulk value $q_{\mathrm{TF}} = 0.9$ Bohr^{-1}.

The correlation hole in our $(e, 2e)$ momentum distributions is due to the Coulomb interaction after the collision. Its spatial origin is the following. In reality, it is made in a few near-surface atomic layers of the solid and in the near-surface vacuum region. In our formalism, with the above-discussed Thomas-Fermi screening, it originates in a few near-surface atomic layers, in which we adopt a weakening of the screening of the Coulomb interaction in order to mimic the repulsion in the near-surface vacuum region.

6.3 Electronic ground state

As the most pertinent result of our *ab initio* FLAPW calculation of the electronic structure of Fe(001) we show in Fig. 6.4 the spin-, $\mathbf{k}^{\parallel}$-, and layer-resolved valence electron density of states (LDOS) $N_m^{\tau}(E, k_x)$ (with k_x along the $\overline{\Gamma}(\Delta)\overline{H}$ direction in the surface Brillouin zone), with $\tau = \pm$ indicating majority/minority spin and $m = 1, 2,$ bulk referring to the topmost, second, and bulk layers parallel to the surface. Since the contour plots are rather self-explanatory, it may suffice to point out a few salient features. Just around the Fermi energy, there is a clear dominance of minority spin over majority spin as can be seen by $\mathbf{k}^{\parallel}$-integrated LDOS N_m^{τ} shown in Fig. 6.5. In particular, we note that at E_F minority spin exceeds majority spin in the surface layer (ratio $N_1^- : N_1^+ = 9.40$), whereas in the bulk it is the other way around ($N_1^- : N_1^+ = 0.24$). This agrees well with the results of earlier calculations [59]. Also in line with earlier work [59,60] is an enhancement of the magnetic moment at the surface by 30% with respect to the bulk magnetic moment. In accordance with these results, we find two strong minority surface state/resonance bands, as can be seen in panel (f) of Fig. 6.4 in comparison with panel (b). These results are in accordance with earlier *ab initio* calculations [59, 61].

Further below E_F, Fig. 6.4 reveals that there is mainly majority spin with pronounced second-layer and bulk LDOS features for small k_x between about -0.5 and -1.0 eV. As is seen in panel (e), in comparison to panel (a), there is a small majority-spin surface resonance band at $E = -1.8$ eV for small k_x and a very strong majority surface resonance band dispersing downward from $E = -2.2$ eV over the entire surface Brillouin zone.

In Fig. 6.6 we show the $\mathbf{k}^{\parallel}$-dependence of the LDOS for a fixed energy $E = E_F$. For the majority states the intensity of the LDOS decreases from the bulk layer to the surface layers in contrast to the minority states, where the LDOS is clearly strongest in the top surface layer. At the slightly lower energy $E = E_F - 0.8$ eV one obtains clearly different results, as shown in Fig. 6.7: there is relatively low LDOS in the first layer for both magnetization directions, and the majority spin LDOS dominates in the deeper lying layers.

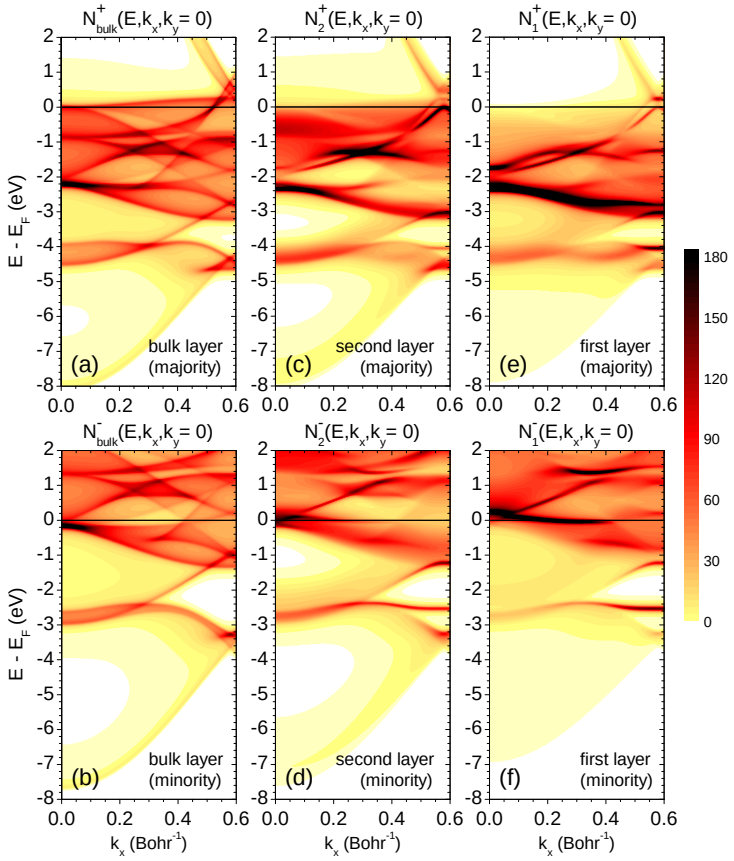

Fig. 6.4: $\mathbf{k}^{\|}$- and layer-resolved valence electron density of states (LDOS) $N_m^{\tau}(E, k_x)$ (with k_x along the $\overline{\Gamma}(\Delta)\overline{H}$ direction in the surface Brillouin zone). To reveal more details, the imaginary potential part has been chosen as a very small constant (-0.05 eV). (a), (b) Bulk layer majority and minority spin LDOS, respectively; (c), (d) second layer majority and minority spin LDOS, respectively; (e), (f) first layer majority and minority spin LDOS, respectively.

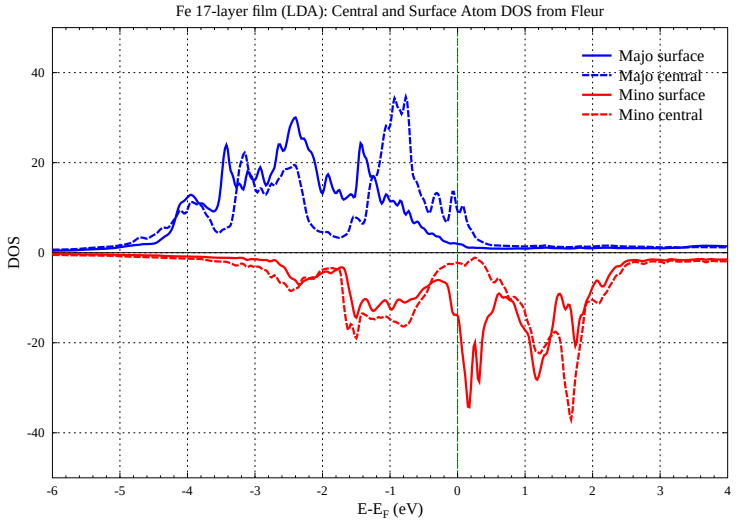

Fig. 6.5: $\mathbf{k}^{\|}$-integrated layer-resolved density of majority spin states (blue curves) and minority spin states (red curves) in the surface layer (full lines) and in the central layer (dotted lines) of a Fe(001) film (17 layers; surface layers relaxed; FLAPW-program FLEUR using LDA-VWN). Energies relative to the Fermi level (green dotted line).

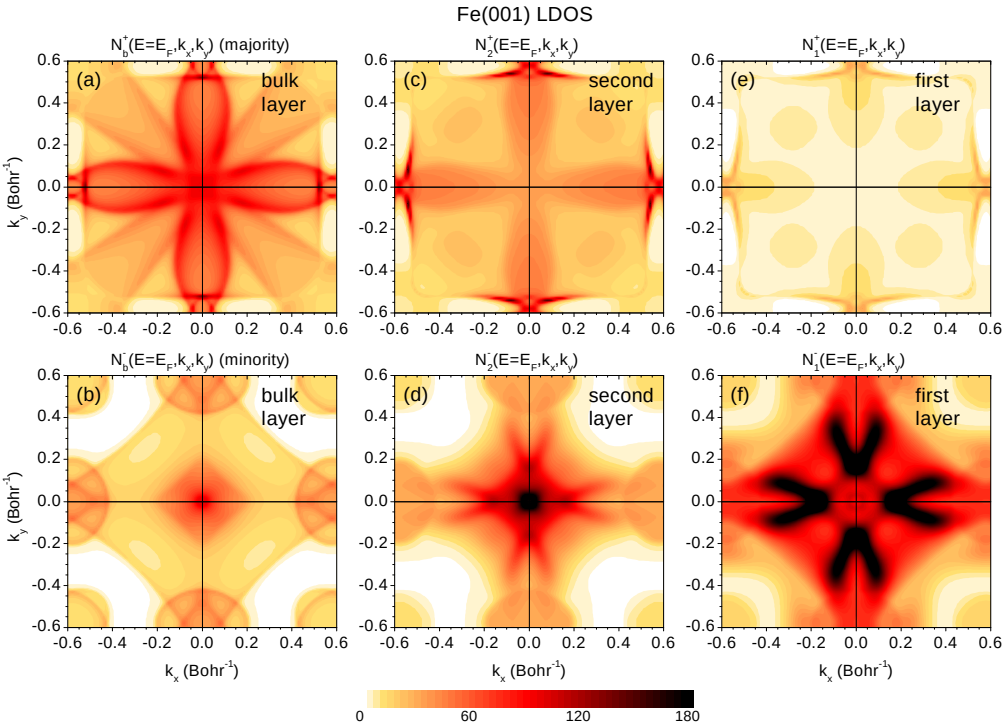

Fig. 6.6: $\mathbf{k}^{\|}$- and layer-resolved valence electron density of states (LDOS) $N_m^{\tau}(E, k_x, k_y)$ (with (k_x, k_y) in the surface Brillouin zone) for fixed energy $E = E_F$. To reveal more details, the imaginary potential part has been chosen as a very small constant (-0.05 eV). (a) and (b) bulk layer majority and minority spin LDOS, respectively; (c) and (d) second layer majority and minority spin LDOS, respectively; (e) and (f) first layer majority and minority spin LDOS, respectively.

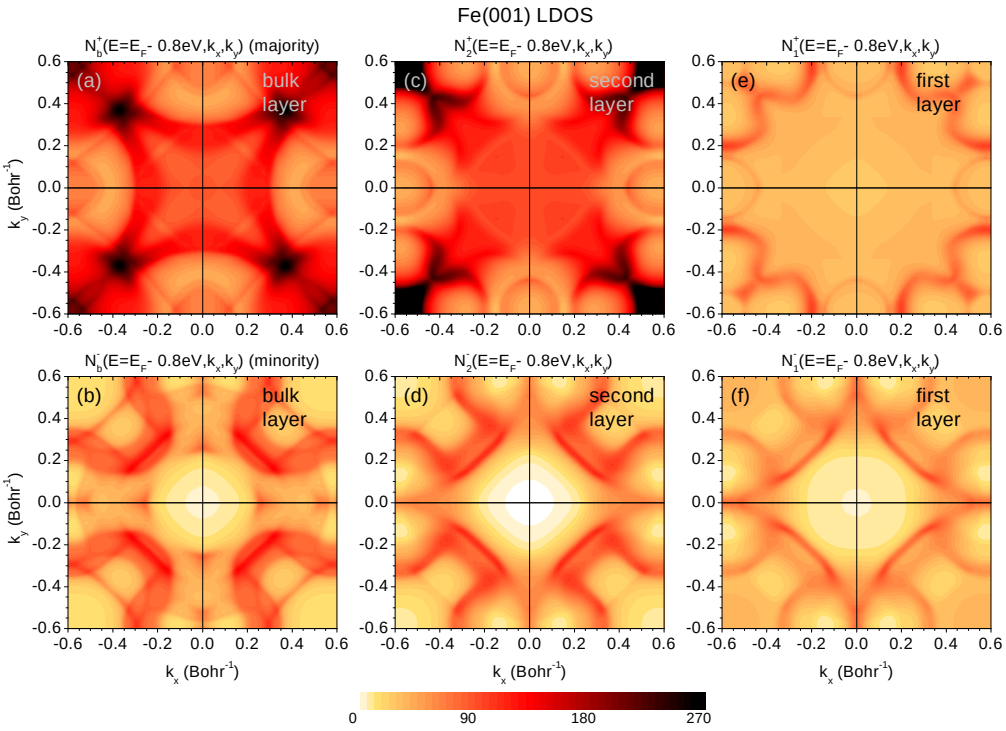

Fig. 6.7: As Fig. 6.6 except that the fixed energy is chosen as $E = E_F - 0.8$ eV.

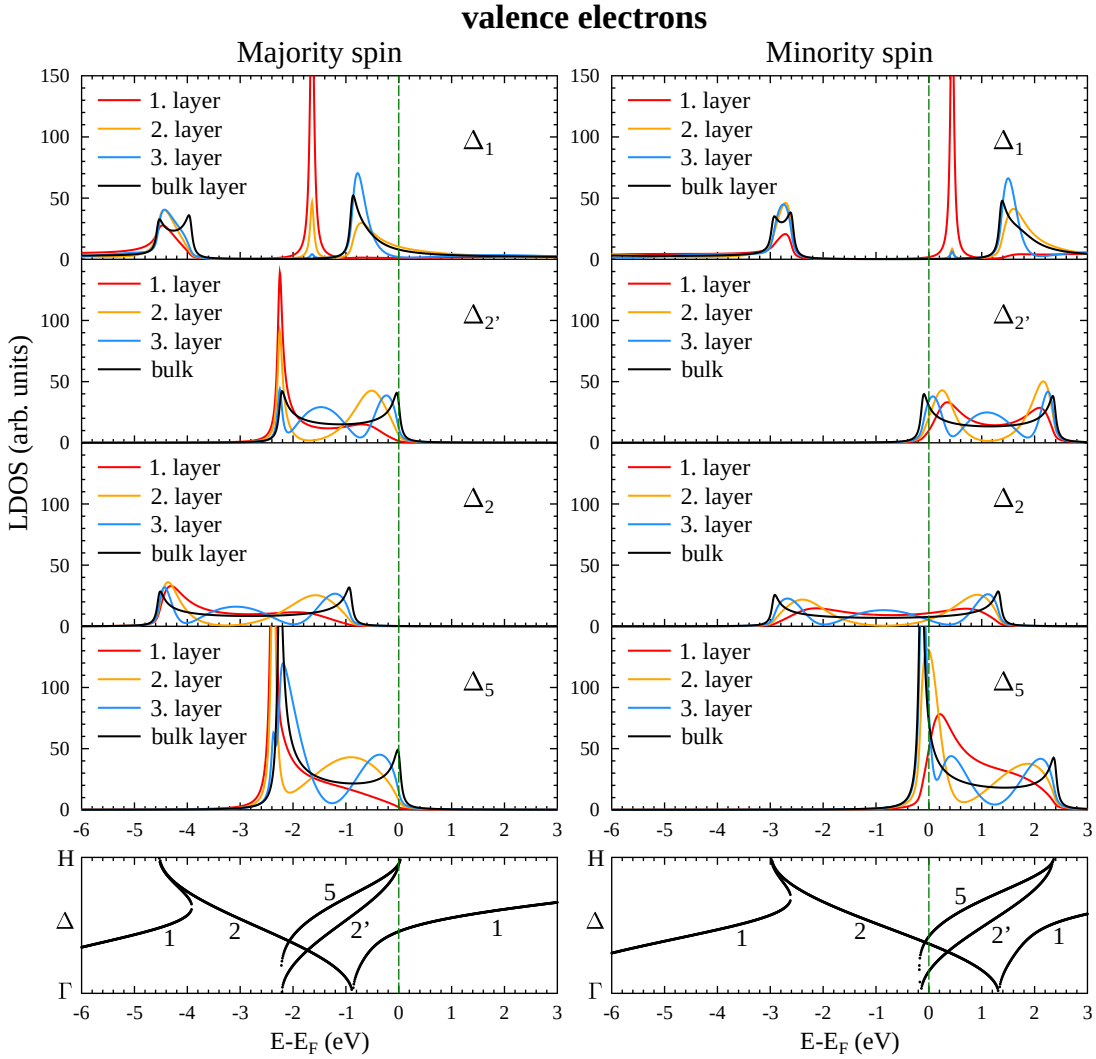

Fig. 6.8: Valence electron states of Fe(001) for $\mathbf{k}^{\parallel} = 0$. Bottom panels: majority and minority spin bulk band structure along $\Gamma(\Delta)H$ with the symbols 1, 2, 2′, and 5 indicating the spatial symmetry types $\Delta_1, \Delta_{2'}, \Delta_2, \Delta_5$ of the individual bands. Upper panels: spin- and layer-resolved densities of states (LDOS) of first (red lines), second (yellow lines), third (blue lines), and bulk (black lines) Fe layers for the individual Δ symmetry types as indicated in the panels. For clearer graphical presentation, a small constant imaginary part ($V_{\rm im} = -0.05$ eV) has been added to the (real) ground-state potential in the LDOS calculation.

In view of analyzing $(e, 2e)$ spectra with the aid of selection rules (cf. Refs. [62] and [56]) we show in Figs. 6.8 and 6.9 the LDOS of Fe(001) at the $\overline{\Gamma}$ point ($k_x = 0$) resolved not only with respect to spin and layers, but also with respect to the spatial symmetry types $\Delta_1, \Delta_{2'}, \Delta_2, \Delta_5$. In order to display individual LDOS features and their relation to the bulk band structure more clearly, we show in Fig. 6.8 results that have been computed with a very small constant imaginary potential part ($V_{\rm im} = -0.05$ eV) instead of the much larger energy-dependent $V_{\rm im}^{\sigma}$ (cf. Eq. (6.5)). For both majority and minority spin, the bulk layer LDOS curves are seen to correspond in the usual way to the respective bulk band structure along $\Gamma(\Delta)$H. A prominent highly localized minority spin surface state of Δ_1 symmetry is seen at 0.234 eV above E_F, in

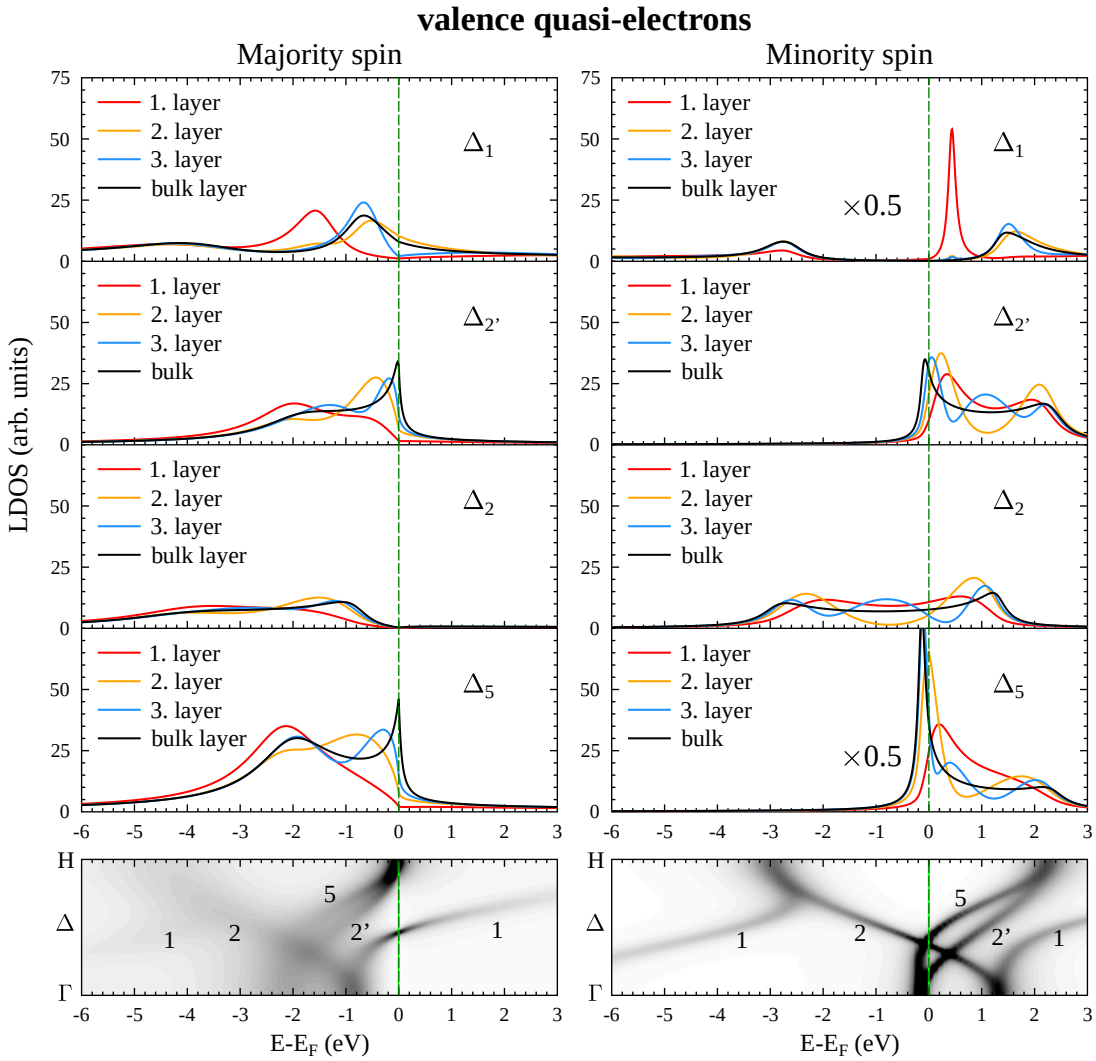

Fig. 6.9: Valence quasi-electrons of Fe(001) for $\mathbf{k}^{\parallel} = 0$, which are excited in the $(e, 2e)$ process. The individual panels are analogous to those in Fig. 6.8, but both bulk bands and LDOS have been calculated using the spin- and energy-dependent imaginary part $V_{\mathrm{im}}^{\sigma}(E)$ of Eq. (6.5).

line with the results of earlier calculations and of scanning tunneling experiments (cf. Refs. [61] and [63], and references therein). Turning to the states below E_F, which are relevant for $(e, 2e)$, we would like to emphasize the following. In a very close vicinity of E_F, minority spin states of Δ_5 symmetry strongly dominate. At energies below about -0.4 eV majority spin states of all symmetry types have sizable weight, whereas minority spin states appear only for Δ_2 with small weight over a wider range and for Δ_1 as a narrow peak around -2.8 eV. As can be seen in Fig. 6.9, these characteristics persist in the quasiparticle LDOS calculated with the realistic larger V_{im}^{σ} according to Eq. (6.5).

6.4 Theoretical $(e, 2e)$ spectra for Fe(001)

We now address the relationship between quasiparticle LDOS and observable $(e, 2e)$ spectra. First, we would like to explore how the LDOS $N_m^{\tau}(E, k_x)$ manifests itself in $(e, 2e)$ energy distri-

butions $I(E_3, E_4)$, where E_3 and E_4 are the energies of the two outgoing electrons. To this end, it is convenient to plot the LDOS as a function of E_3 and E_4 (cf. Figs. 5.8 and 5.9 in Section 5.2).

Since the LDOS near the surface differs from layer to layer, an adequate quantity for comparing with $(e, 2e)$ energy distributions $I^{\sigma\tau}$ is a weighted sum $N^{\sigma\tau}$ over the near-surface layer densities of states N_m^τ, with weight factors $w_m^{\sigma\tau}$ determined by the spin-dependent mean free path $\lambda^\pm$ (cf. Eq. (6.7)) of the primary and the outgoing electrons:

$$N^{\sigma\tau} = \sum_m w_m^{\sigma\tau} N_m^\tau \tag{6.8}$$

$$\text{with} \quad w_m^{\sigma\tau} := \exp\left[-d_m\left(\frac{1}{\lambda_1^\sigma} + \frac{1}{\lambda_2^\sigma} + \frac{1}{\lambda_2^\tau}\right)\right];$$

σ indicates the spin of the primary electron and of one of the outgoing ones, τ is the spin of the other outgoing electron; m counts the layers parallel to the surface, d_m is the distance between the nominal surface plane and the internuclear plane of the mth layer; λ_1^σ is the mean free path of the primary electron, and λ_2^σ and λ_2^τ are the mean free paths of the two outgoing electrons.

In Fig. 6.10 we demonstrate the relation between the LDOS sum $N^{\sigma\tau}$ (cf. Eq. (6.8)) and $(e, 2e)$ energy distributions $I^{\sigma\tau}(E_3, E_4)$ for the case of a normally incident primary electron with energy 25 eV and coplanar emission of the two electrons at equal polar angles 30°. The reaction plane is chosen as the (x, z) plane, which is a mirror plane of the semi-infinite crystal. Consequently, only valence electron states of even symmetry with respect to this plane are allowed to contribute to the $(e, 2e)$ intensity, as has been derived in [62]. We therefore have to restrict the LDOS sum $N^{\sigma\tau}$ to even states.

With the primary energy fixed (25 eV), the spin-dependent layer weight coefficients $w_m^{\sigma\tau}$ in Eq. (6.8) still depend on the energies of the emitted electrons. This dependence turned out, however, to be rather weak for the emitted electron energies under consideration. It therefore suffices to discuss the weight coefficients obtained for the case that both energies are equal to 10 eV. For both primary and valence electron spin up, we have $w_1^{++} = 0.74$, $w_2^{++} = 0.40$, and $w_3^{++} = 0.20$ for the first, second, and third layer, respectively. For both spins down, the corresponding values are $w_1^{--} = 0.67$, $w_2^{--} = 0.30$, and $w_3^{--} = 0.12$. In the two opposite-spin cases we have $w_m^{+-} > w_m^{-+}$ with values in between those of w_m^{++} and w_m^{--}. Comparing the coefficients with each other we first note a pronounced spin dependence, which increases from the first to the third layer. Second, the coefficients for a given spin configuration decrease rapidly from layer to layer, implying that $(e, 2e)$ is strongly surface sensitive.

Looking now in detail at the relation between LDOS sums (cf. Eq. (6.8)) and $(e, 2e)$ energy distributions, we first address the case of valence electron spin up. Comparing, for primary spin up, the LDOS sum N^{++} in Fig. 6.10(a) with the parallel-spin intensity I^{++} in Fig. 6.10(c), one first notices that for nearly equal energies of the two emitted electrons, corresponding to valence electron momentum $k^{||}$ between -0.1 and 0.1, and valence energy between about 0.5 and 2 eV below E_F, N^{++} is sizable and I^{++} is very strong. For very different energies of the emitted electrons, corresponding to $|k^{||}| > 0.2$, N^{++} is of similar magnitude as in the central region, but I^{++} is much weaker. Valence electron LDOS is thus seen to be a prerequisite for

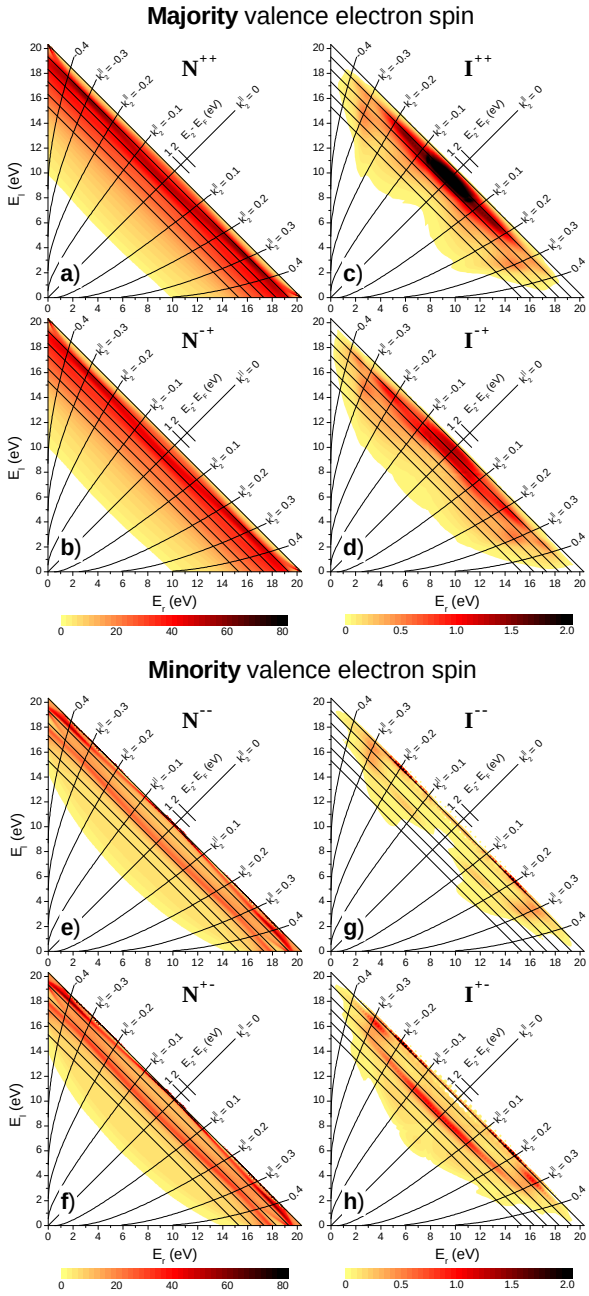

Fig. 6.10: Valence electron density of states and $(e, 2e)$ energy distributions from Fe(001) for normally incident primary electron with energy 25 eV and outgoing electrons in the (x, z) plane with equal polar angles $\vartheta_3 = \vartheta_4 = 30°$ and azimuthal angles $\varphi_3 = 0°$ and $\varphi_4 = 180°$. Upper half ((a)–(d)), for spin-up (majority) valence electrons: (a) Weighted sum N^{++} (cf. Eq. (6.8)) of the spin-up densities of even states $N_m^+(E, k_x)$ of the topmost three monoatomic layers parallel to the surface, which were calculated with the spin- and energy-dependent quasiparticle imaginary self-energy part $V_{\mathrm{im}}^{\sigma}(E)$ as in Eq. (6.5). In each panel, the diagonal axis represents the valence electron energy E with respect to the Fermi energy. The axis normal to it is associated with the parallel momentum $k_x =: k_2^{\parallel}$ of the valence electron as indicated by the iso-$k_2^{\parallel}$ lines (in Bohr^{-1}). (b) Weighted sum N^{-+} (cf. Eq. (6.8)). (c) Fully spin-resolved $(e, 2e)$ energy distribution $I^{++}(E_3, E_4)$ (cf. Eq. (6.3)) for primary electron spin up. (d) $I^{-+}(E_3, E_4)$ for primary electron spin down. Lower half ((e)–(h)), for spin-down (minority) valence electrons: (e),(f) Weighted LDOS sums N^{--} and N^{+-}. (g),(h) $(e, 2e)$ energy distributions $I^{--}(E_3, E_4)$ and $I^{+-}(E_3, E_4)$ for primary electron spin down and up, respectively.

$(e, 2e)$, but the actual size of the intensity depends on the four electron states entering in the $(e, 2e)$ matrix elements (cf. Eq. (6.1)). While the primary electron state is constant, the valence electron state and the outgoing electron states vary from point to point in the $(e, 2e)$ energy distribution. For primary spin down, comparison of Figs. 6.10(b) and 6.10(d) shows that the antiparallel-spin intensity I^{-+} is weak for $|k^{||}| > 0.2$. In the central region ($|k^{||}| < 0.1$), I^{-+} is appreciable, but significantly smaller than the parallel-spin intensity I^{++}. For valence electron spin down, analogous results are shown in Figs. 6.10(e)–6.10(h). In particular, we note that for $|k^{||}| < 0.1$ the antiparallel-spin intensity I^{+-} rather closely reflects the LDOS, whereas I^{--} is extremely small below $E_{\text{valence}} = -2$ eV despite a large LDOS in this region.

These features are, for $|k^{||}| = 0$, seen more quantitatively in Figs. 6.11(a)–6.11(d) in line scans across the diagonals of the individual panels of Fig. 6.10. Panels (a) and (c), which relate to majority-spin valence electrons, show that — despite very similar underlying weighted LDOS — I^{++} has a single large peak centered around -1.2 eV, whereas I^{-+} exhibits two maxima, which are much smaller. As a sufficient reason for a substantial difference between the two curves we point out that, by virtue of $(e, 2e)$ selection rules for 4-mm symmetry surfaces and the present reaction plane (cf. upper half of Table I in Ref. [56]), I^{++} involves exclusively majority-spin valence electrons of spatial symmetry Δ_5, whereas I^{-+} can contain contributions from Δ_1, Δ_2, and Δ_5 majority-spin valence electrons. The majority-spin LDOS curves (shown in Fig. 6.9) are in fact sizable for Δ_1 and Δ_5, and still appreciable for Δ_2.

Comparing the intensity curves in panel (c), which were calculated for polar emission angles $\vartheta_3 = \vartheta_4 = 30°$, with their analogs for 45° (panel (e)) we note substantial differences in size and shape. Since the underlying valence electron states are the same in the two cases, these differences must be due to the different outgoing electron states in the $(e, 2e)$ matrix elements. For minority valence electron spin, our findings are analogous and consistent with the symmetry-resolved minority LDOS curves (shown in Fig. 6.9), as can be seen in Figs. 6.11(b), 6.11(d), and 6.11(e).

From Fig. 6.11 it is obvious that the experimentally observable intensities I^{+} and I^{-} (i.e., $I^{\pm\tau}$ summed over the valence spin τ, cf. Eq. (6.4)) both arise almost exclusively from collisions with majority-spin valence electrons, except at energies very close to the Fermi energy and, for $\vartheta = 30°$, around -2.8 eV. This is in contrast to $(e, 2e)$ results from Fe(110) [62, 64], which show that — for equal energies of the two emitted electrons — I^{+} (I^{-}) is for most energies associated with minority (majority) valence electrons, i.e., there is mostly singlet scattering between the primary and the valence electron. The reason for this difference between Fe(001) and Fe(110) is that valence states, which are odd with respect to reflection at a plane perpendicular to the scattering plane and thence lead to triplet scattering, occur for Fe(110) only in a very small energy range well below E_F, whereas for Fe(001) they are present over a wide energy range (cf. the Δ_5 majority spin LDOS curves in Fig. 6.9).

Energy distributions — like the ones shown in Fig. 6.10 — necessarily involve valence electron states with a range of energies and of parallel momenta. In contrast, parallel-momentum distributions for opposite momenta of the two outgoing electrons ($\mathbf{k}_4 = -\mathbf{k}_3$) are associated with valence electrons of parallel momentum zero and fixed energy. Choosing — by virtue of

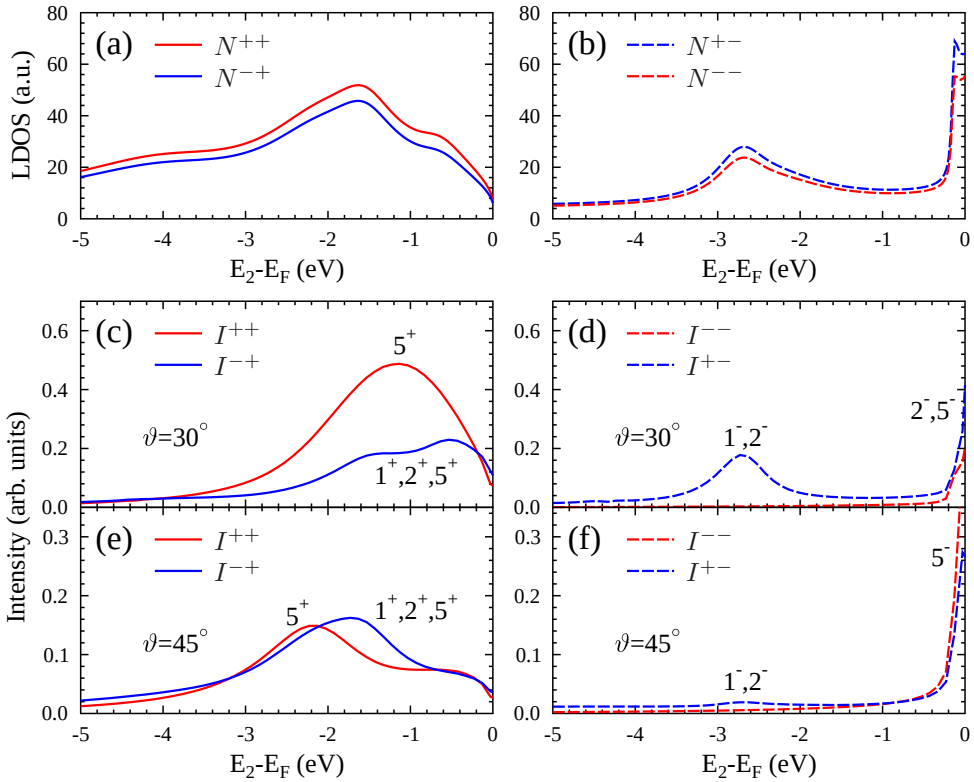

Fig. 6.11: For the same $(e, 2e)$ setup as in Fig. 6.10 we show the weighted valence electron LDOS and $(e, 2e)$ spectra for equal energies $E_3 = E_4$, which are line scans along the diagonals of the panels of Fig. 6.10. The parallel momentum of the valence electron is thus always zero. Its energy relative to the Fermi energy is $E - E_F = 25 - 2E_3 - \Phi$ (eV), and the $(e, 2e)$ spectra $I^{\sigma\tau}$ can therefore also be plotted as functions of $E - E_F$. (a) Weighted sums N^{++} (red line) and N^{-+} (blue line) (cf. Eq. (6.8)) for majority-spin valence electrons. (b) Weighted sums N^{+-} (blue line) and N^{--} (red line) for minority-spin valence electrons. (c) $(e, 2e)$ intensities I^{++} (red line) and I^{-+} (blue line) for polar angle $\vartheta = 30°$, associated with majority-spin valence electrons, i.e., line scans through Figs. 6.10(c) and 6.10(d). (d) $(e, 2e)$ intensities I^{+-} (red line) and I^{--} (blue line) for polar angle $\vartheta = 30°$, associated with minority-spin valence electrons, i.e., line scans through Figs. 6.10(g) and 6.10(h). (e),(f) As (c) and (d), respectively, but for polar angle $\vartheta = 45°$ instead of 30°. The labels 1^σ, 2^σ, and 5^σ next to the intensity curves indicate the symmetry types Δ_1, Δ_2, and Δ_5 and the spin ($\sigma = \pm$) of the valence electrons, from which contributions to the respective intensity are allowed by $(e, 2e)$ selection rules (cf. upper half of Table I in [56]). $\Delta_{2'}$ valence electrons cannot contribute at all, since their wave functions are antisymmetric with respect to the present $(e, 2e)$ reaction plane.

energy conservation in $(e, 2e)$ — this energy such that valence electrons of one spin orientation strongly dominate in the LDOS and that this domination persists in the $(e, 2e)$ spectra, one practically has an internal resolution of the valence electron spin over the entire parallel-momentum distribution.

We first select primary electron energy and outgoing electron energies such that the valence electron energy is E_F, where minority spin dominates (cf. Fig. 6.9). In Fig. 6.12 we show fully spin-resolved $(e, 2e)$ momentum distributions $I^{\sigma\tau}(k_x, k_y)$ (cf. Eq. (6.3)) from Fe(001) in the surface-parallel momentum plane $(k_x, k_y)/k$. As an obvious consequence of the dominance of minority valence electron spin, we note that I^{++} and I^{-+}, which involve majority valence spin, are overall much weaker than I^{--} and I^{+-}, which involve minority valence spin.

The most important conclusion is reached by comparing, for given valence electron spin, the momentum distributions for parallel spins with those for antiparallel spins. Going outward from the center to about $|\mathbf{k}^{\parallel}|/k = 0.5$, all distributions exhibit a region of small intensity. This depletion zone is seen to be much more pronounced for parallel spins than for antiparallel ones. Since outgoing electrons with parallel spins are subject to exchange and Coulomb interaction, whereas those with antiparallel spins are correlated only by the Coulomb interaction, the central depletion zones in I^{+-} and I^{-+} can be viewed as a Coulomb correlation hole and those in I^{++} and I^{--} as an exchange plus Coulomb correlation hole. Our momentum distributions thus imply that the latter hole is larger than the former.

Summation over the valence electron spin yields the experimentally accessible intensities I^{+} for primary spin up (Fig. 6.12(e)) and I^{-} for primary spin down (Fig. 6.12(f)). Due to the dominance of spin-down valence electrons at E_F, I^{+} pertains essentially to antiparallel spins and I^{-} to parallel spins.

In Fig. 6.13 we present fully spin-resolved $(e, 2e)$ momentum distributions $I^{\sigma\tau}(k_x, k_y)$ (cf. Eq. (6.3)) with primary and outgoing electron energies such that the valence electron energy is 0.8 eV below E_F, where majority spin strongly dominates. These results are in essence analogous to those in Fig. 6.12, with "spin up" and "spin down" interchanged. In particular, we find that the exchange plus Coulomb correlation hole exhibited by I^{++} (panel (a)) and in good approximation by I^{+} (panel (e)) is larger than the Coulomb correlation hole in I^{-+} (panel (d)) and I^{-} (panel (f)).

A more quantitative view of the fully spin-resolved momentum distributions associated with dominant majority spin valence electrons at -0.8 eV is provided in the bottom panels of Fig. 6.14 by line scans $I^{\sigma\tau}(k_x, k_y = 0)$ along the k_x axis through the corresponding angular distributions $I^{\sigma\tau}(k_x, k_y)$ shown in Fig. 6.13. The line scans in the bottom panels result from calculations for the complete Fe(001) half space, i.e., comprising all monoatomic layers parallel to the surface.

The very high surface sensitivity of $(e, 2e)$ from Fe(001), which follows from the mean-free-path-derived weight coefficients $w_m^{\sigma\tau}$ (cf. Eq. (6.8) and subsequent text), is demonstrated in a more quantitative and detailed way by the upper panels of Fig. 6.14. In these we show $(e, 2e)$ intensities, which arise from only the first N surface-parallel monoatomic layers of the semi-infinite crystal, with $N = 1, 2, 3$ in the first, second, and third row of panels, respectively.

For primary spin up (left-hand column of panels of Fig. 6.14) we first note that the dominant

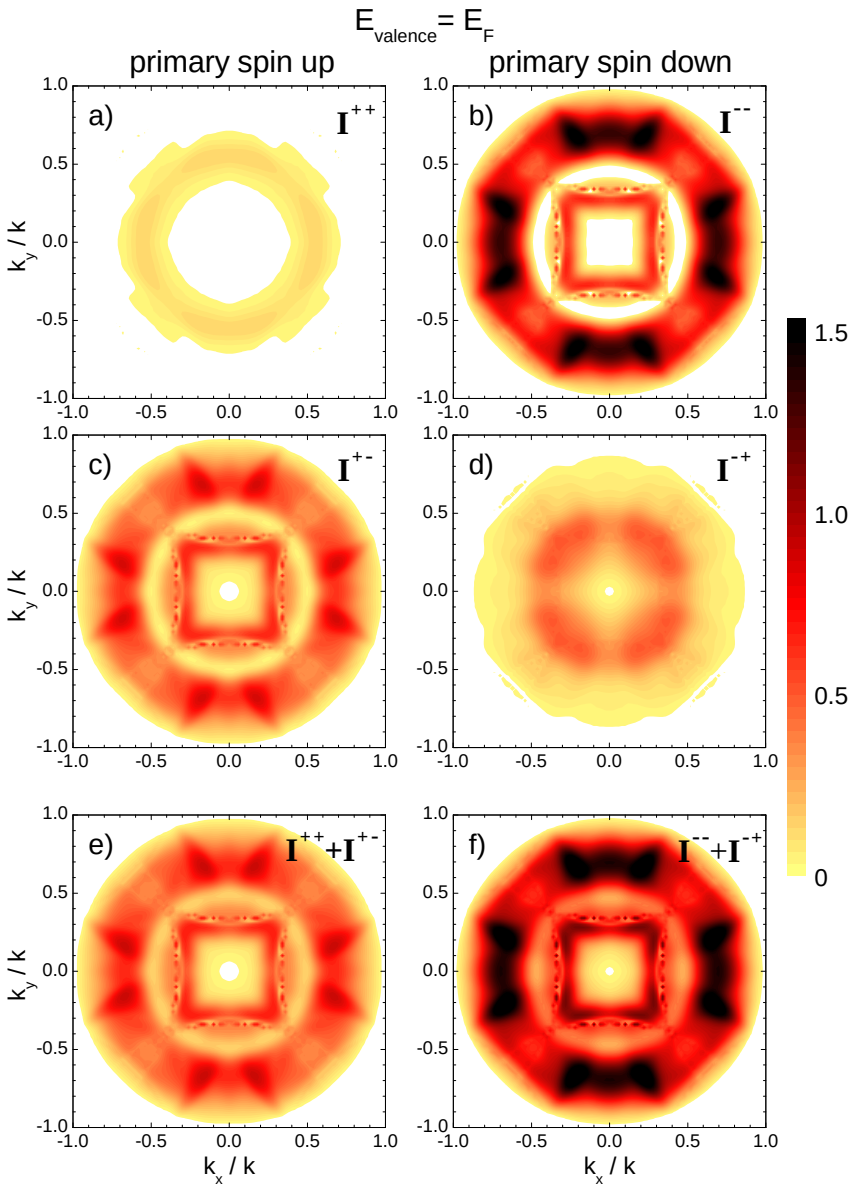

Fig. 6.12: Fully spin-resolved $(e, 2e)$ momentum distributions $I^{\sigma\tau}(k_x, k_y)$ (cf. Eq. (6.3)) from Fe(001) in the surface-parallel momentum plane $(k_x, k_y)/k$, with $\sigma = \pm$ and $\tau = \pm$ labeling the spin of the primary and of the valence electron, respectively. In an equal energy sharing coplanar symmetric setup, primary electrons with energy 25 eV are normally incident. The two electrons are emitted at polar angle ϑ and azimuthal angles φ and $\varphi + \pi$. They have equal energy $E = 10.165$ eV and surface-parallel momenta $(k_x, k_y) = \sqrt{2E}\sin\vartheta(\cos\varphi, \sin\varphi)$ and $(-k_x, -k_y)$. Taking into account the work function value 4.67 eV, the relevant valence electron thus has parallel momentum 0, energy 0 relative to the Fermi energy, and majority/minority spin $\tau = \pm$. In the calculations we employed the Thomas-Fermi wave number $q_{\rm TF} = 0.1$ Bohr^{-1} in the screened Coulomb interaction, which we determined by comparisons with the experimental data (see Figs. 6.15 and 6.16, and associated text), and the spin-dependent imaginary self-energy parts given by Eqs. (6.5) and (6.6). In (a) and (b) the spins are parallel, i.e., the two electrons are correlated by exchange and by Coulomb interaction. In the antiparallel spin case in panels (c) and (d), there is only Coulomb correlation between the two electrons. Panel (e) shows, for a spin-up primary electron, the sum over the contributions from spin-up and spin-down valence electrons, i.e., the sum over panels (a) and (c). Panel (f) is the analog for primary spin-down.

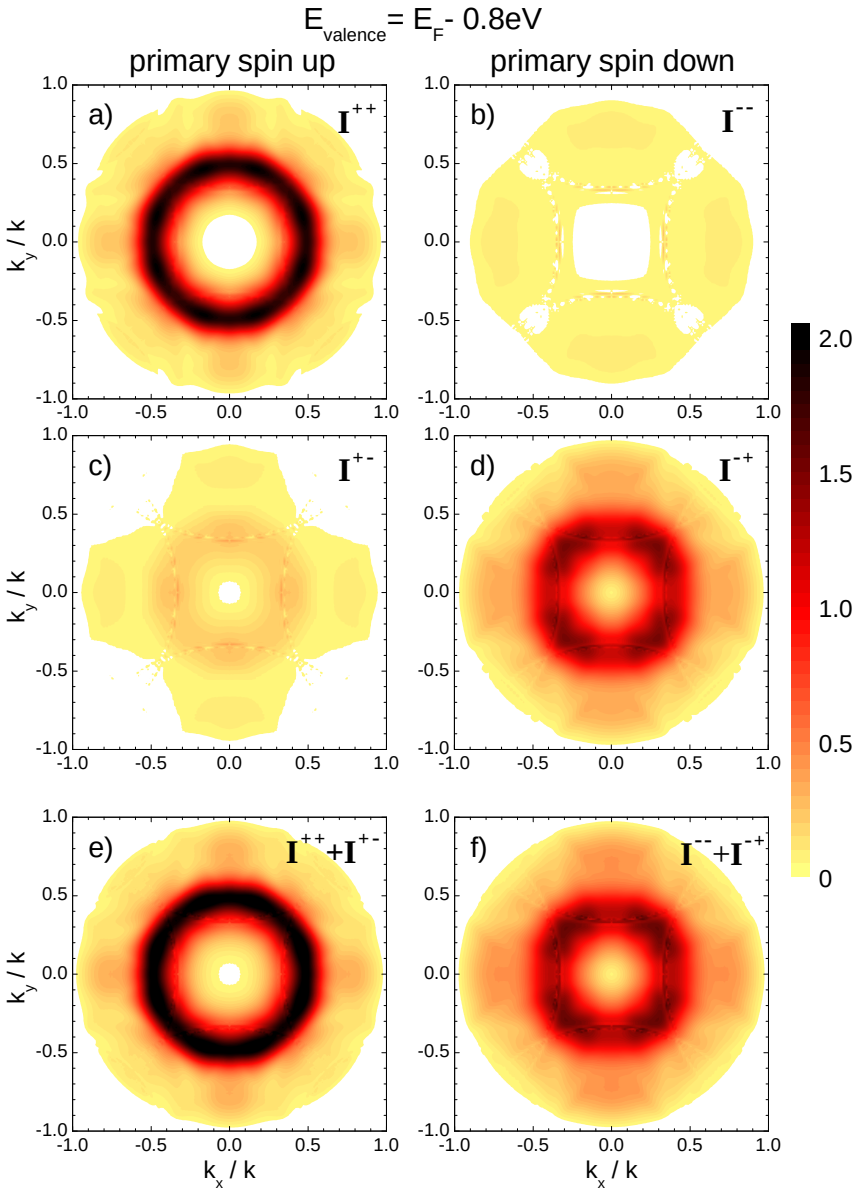

Fig. 6.13: As in Fig. 6.12 except that the energy of each of the two emitted electrons has been chosen as 9.765 eV, which implies that the energy of the relevant valence electron is -0.8 eV with respect to the Fermi level, where there is a strong dominance of majority spin.

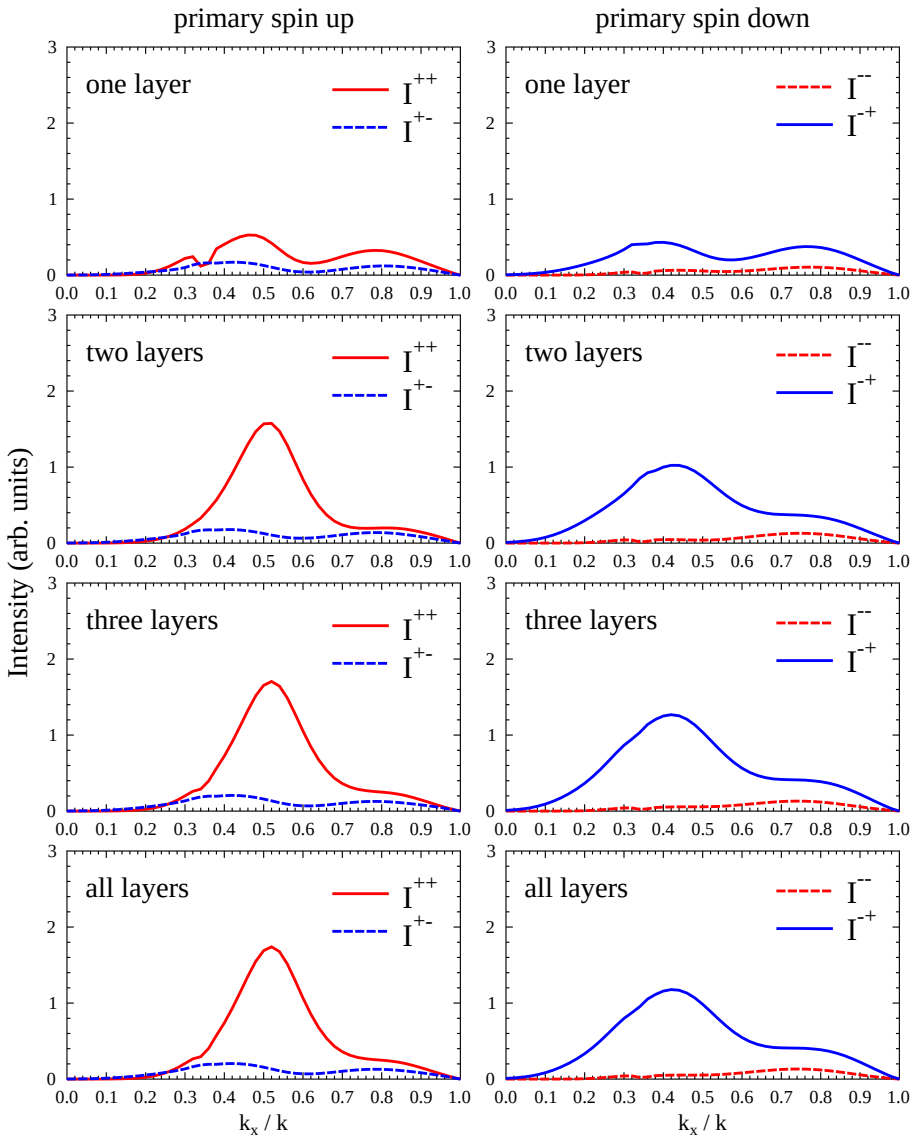

Fig. 6.14: Fully spin-resolved $(e, 2e)$ intensities $I^{\sigma\tau}(k_x, k_y = 0)$ (cf. Eq. (6.3)) from Fe(001) for valence electron energy -0.8 eV. The bottom panels are line scans along the k_x axis through the corresponding angular distributions $I^{\sigma\tau}(k_x, k_y)$ shown in Fig. 6.13. While they were obtained in calculations for the complete Fe(001) half space, i.e., for all monoatomic layers parallel to the surface, corresponding intensities, which arise from the first $N = 1, 2, 3$ layers, are shown in the upper panels (with N indicated in the respective panels).

I^{++} peak from two layers is more than twice the size of its counterpart from just the first layer. This appears plausible from the $(e, 2e)$ selection rules (cf. Table I in [56]), according to which parallel-spin intensities arise only from valence electron states of Δ_5 spatial symmetry, and from the observation (in Fig. 6.9) that at valence energy -0.8 eV the Δ_5 LDOS in the second layer is about twice as high as in the first layer. One may therefore wonder why the second maximum of the first layer I^{++}, which is associated with the very same valence electron state, gets reduced when two layers contribute. The puzzle of the different behavior of the two maxima is resolved by recognizing that the intensity from two layers is not a sum of the intensities from the individual layers but rather the absolute square of the sum of the amplitudes (matrix elements), which allows both constructive and destructive interference. Since the two-electron final state is quite different for the two maxima, so are the matrix elements. A high LDOS in a given layer is thus a necessary but by no means sufficient condition for a substantial intensity increase upon including this layer.

For primary spin down, the two maxima in the first layer I^{-+} are seen to change similarly when going to two layers. According to $(e, 2e)$ selection rules, (majority) valence electron states of spatial symmetry Δ_1, Δ_2, and Δ_5 are allowed to contribute. The LDOS in Fig. 6.9 shows that the former two types are, like the latter one, stronger in the second layer than in the first one. Therefore the behavior of the two I^{-+} maxima can be interpreted in the same way as above for I^{++}.

As can be seen in Fig. 6.14, the spectra from two layers are already very close to the complete ones, and those from three layers are practically the same.

6.5 Comparison of experiment and theory

In this section we present and discuss theoretical $(e, 2e)$ energy sharing and momentum distributions from Fe(001) and compare them with their experimental counterparts.[1] Energy distributions like the experimental spin-integrated one $I(E_3, E_4)$ in Fig. 7 of reference [10] and the theoretical spin-resolved ones $I^{\pm}(E_3, E_4)$ in Fig. 6.10 cover, for fixed emission angles, the whole range of the sum energy $E_{\mathrm{sum}} = E_3 + E_4$ and thereby of the valence electron energy, which is allowed by energy conservation. As was shown in Section II of reference [10] (see [10], Fig. 8 and associated text), more details are, however, revealed by so-called energy sharing curves, which are, for fixed E_{sum} and thence fixed E_{valence}, diagonal line scans across the corresponding energy distributions.

In Fig. 6.15 we show spin-dependent energy sharing curves $I^{\pm}(E_3 - E_4)$ from Fe(001) for a wide range of constant polar emission angles $\vartheta_3 = \vartheta_4 =: \vartheta$. The primary electron energy being 25 eV, we chose $E_{\mathrm{sum}} = 19.53$ eV. By virtue of energy conservation, the valence electron energy is then $E_F - 0.8$ eV, where there is a strong dominance of majority spin for small values of the surface-parallel momentum.

Experimental energy sharing curves are shown in the left-hand column of Fig. 6.15. For $\sin\vartheta = 0.2$, the spin contrast is essentially zero over the whole spectrum, and the probability

[1] The experiments were performed by F. O. Schumann, C. Winkler, and J. Kirschner at the MPI Halle and have been published in a joint paper [10].

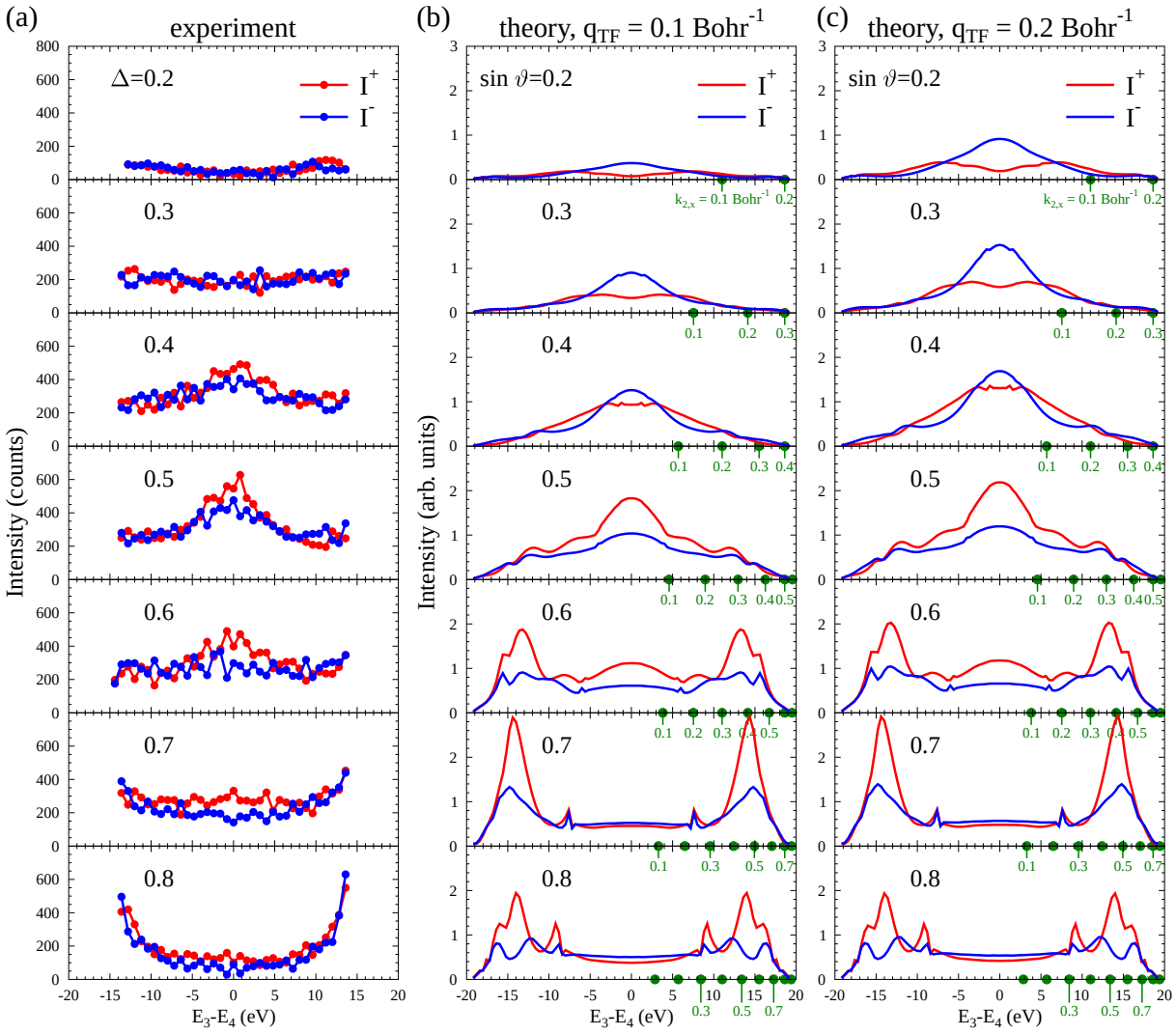

Fig. 6.15: $(e, 2e)$ energy sharing curves $I^{\pm}(E_3 - E_4)$ from Fe(001) for primary electrons with energy 25 eV and spin $\sigma = \pm$ and for constant sum energy $E_3 + E_4 = 19.53$ eV of the two outgoing electrons. By virtue of energy conservation, the valence electron energy thence is fixed as $E_F - 0.8$ eV. In all panels, the red (blue) curves represent I^+ (I^-) obtained for primary electron spin up (down). Left-hand column of panels: Experimental sharing curves from [10]. Central column of panels: Theoretical sharing curves for Coulomb screening parameter $q_{\mathrm{TF}} = 0.1$ Bohr^{-1}. All curves are for constant polar emission angles $\vartheta_3 = \vartheta_4 =: \vartheta$, with the value of $\sin\vartheta$ indicated in the individual panels. For equal energy sharing, i.e., $E_3 = E_4$, the valence electron has parallel momentum 0. For unequal energies $E_3 \neq E_4$, selected values of $E_3 - E_4$ are marked by fat green dots on the energy axis and the associated parallel momentum of the valence electron is indicated (in Bohr^{-1} units) by the green numbers next to each dot. The arbitrary intensity units are the same for all panels. Note that for $E_3 = E_4$ the intensity values are the same as those at the respective $k_x/k = \sin\vartheta$ in the momentum distribution line scans (when summed over the valence electron spins), which are shown in the bottom panel of Fig. 6.14. Right-hand column of panels: Theoretical sharing curves as in central column, but for screening parameter $q_{\mathrm{TF}} = 0.2$ Bohr^{-1}.

for both electrons to have the same energy is reduced compared to unequal energies. Going to $\sin\vartheta = 0.5$, we observe significant changes. First, there is a clear preference for equal energies. Second, the I^+ peak is higher than the I^- peak. Proceeding to larger values of $\sin\vartheta$, the sharing curves become very small and almost constant except for a rise close to the maximum energy difference, which we can detect.

In the central and in the right-hand column of Fig. 6.15 we show corresponding theoretical energy sharing curves $I^{\pm}(E_3 - E_4)$. In the calculations we included the Coulomb correlation between the two outgoing electrons — via the correlation factor $f^c(\mathbf{k}, \mathbf{r})$ (cf. Eq. (6.2)) — and used the spin-dependent imaginary self-energy parts (see Eqs. (6.5) and (6.6)). As for the screened Coulomb interaction in the Thomas-Fermi approximation, we regard the Thomas-Fermi wave number q_{TF}, which characterizes the screening strength, as a parameter to be determined by comparison with the experimental spectra. It suffices to show energy sharing curves for the values $q_{\mathrm{TF}} = 0.1$ Bohr^{-1} and 0.2 Bohr^{-1}, since significantly smaller and larger values can be excluded on the grounds of momentum distributions (see below Fig. 6.16 and its context).

In both theoretical sets we notice mostly the same features as above in the experimental set. For $\sin\vartheta = 0.5$, there is a pronounced spin-dependent maximum at equal energies, which turns into a minimum for larger angles. Going to smaller angles, I^+ has again a minimum, whereas for I^- there is some discrepancy between experiment and theory: the calculated I^- has a maximum at equal energies, which is, however, much smaller for $q_{\mathrm{TF}} = 0.1$ Bohr^{-1} than for $q_{\mathrm{TF}} = 0.2$ Bohr^{-1}. Since I^- pertains to antiparallel spins of the outgoing electrons, the size of this maximum is inversely related to the size of the correlation hole. Comparison of the two theoretical sets with experiment favours $q_{\mathrm{TF}} = 0.1$ Bohr^{-1}. For $q_{\mathrm{TF}} > 0.2$ Bohr^{-1} (stronger screening), the I^- peak at equal energies for $\sin\vartheta = 0.2$ increases further. Significantly smaller q_{TF} values can be ruled out by comparing calculated momentum distributions with their experimental counterparts, as will be demonstrated later on.

But first we would like to draw attention to two further features of the theoretical sharing curves at larger angles. All curves in the $\sin\vartheta = 0.6$ panels exhibit a fine structure around $|E_3 - E_4| = 6$ eV, which increases and moves toward larger $|E_3 - E_4|$ with increasing $\sin\vartheta$. This feature originates from a surface resonance in the lower-energy outgoing LEED state, which is associated with an emergence threshold of nonspecular beams.

The big peaks at large energy differences, which dominate the theoretical spectra for $\sin\vartheta \geq 0.6$, are seen (from the green k_x values in the plots) to involve valence electrons with $k_x > 0.3$. As is evident from the LDOS plots N_m^τ in Fig. 6.4, at the chosen energy -0.8 eV minority spin has similar weight as majority spin for these larger k_x. Consequently, I^+ (I^-) is no longer approximately equal to I^{++} (I^{-+}), as is the case for small k_x, but contains a sizable contribution I^{+-} (I^{--}).

In Fig. 6.16 we show spin-dependent momentum distribution line scans $I^{\pm}(k_x, k_y = 0)$ for $\varphi = 0$, i.e., emission in the (x, z) plane. We recall from above that the associated valence electron parallel momentum is zero. By virtue of energy conservation, the valence electron energy was chosen as -0.8 eV (± 0.2 eV experimentally), where majority spin strongly dominates over minority spin. As one would therefore expect and as has been explicitly shown in Fig. 6.14, I^+ (I^-) consists mainly of I^{++} (I^{-+}), i.e., is associated with parallel (antiparallel) spins of the two detected electrons.

The experimental spectra (in Fig. 6.16(a)) exhibit the following main features. There is a central depletion zone, i.e., reduced intensity for small momenta, which is due to exchange and Coulomb correlation. Going toward larger momentum values (corresponding to larger polar emission angles) all curves reach maxima, with the I^+ peaks being further out and exceeding the I^- peaks.

In Figs. 6.16(b)–6.16(e) we show corresponding theoretical momentum distributions. In all these calculations we included the Coulomb correlation between the two outgoing electrons via the correlation factor $f^c(\mathbf{k}, \mathbf{r})$ (cf. Eq. (6.2)). The sensitivity of the calculated momentum distributions to the assumed value of the Thomas-Fermi parameter q_{TF} is demonstrated by comparing with each other Figs. 6.16(b)–6.16(e), which were obtained for q_{TF} as indicated in the panels. The most striking effect is seen to occur in I^-, which pertains to antiparallel spins of the two outgoing electrons, at very small momentum values. For $q_{\mathrm{TF}} = 0.01$ Bohr^{-1} (Fig. 6.16(e)), there is a very extended depletion zone (correlation hole), which decreases with increasing q_{TF} (stronger screening). For $q_{\mathrm{TF}} = 0.5$ Bohr^{-1} (Fig. 6.16(b)) it is already almost absent. For larger q_{TF}, the central intensity gets even larger and one has a central accumulation zone (correlation hill) instead of a correlation hole. This correlation trend also affects I^+ (parallel spins), where it is, however, overshadowed by exchange, which causes a central depletion zone also for larger q_{TF}.

Comparing with the experimental momentum distributions in Fig. 6.16(a), we note the following. For the large q_{TF} values (strong screening), the correlation hole in I^-, which appears in the experimental spectra, is absent. For very small q_{TF} (like 0.01 Bohr^{-1} in panel (d)), the correlation hole in I^- as well as the exchange-correlation hole in I^+ are too extended. For $q_{\mathrm{TF}} = 0.1$ Bohr^{-1} and $q_{\mathrm{TF}} = 0.2$ Bohr^{-1}, the overall agreement with experiment is of equally good quality. Since the energy sharing curves in Fig. 6.15 have been found to discriminate between these two values in favor of $q_{\mathrm{TF}} = 0.1$ Bohr^{-1}, we consider the latter as the optimal one.

If the Coulomb correlation between the two detected electrons is neglected — by taking the Coulomb correlation factor $f^c \equiv 1$ instead of the function $f^c(\mathbf{k}, \mathbf{r})$ (cf. Eq. (6.2)) — the I^- curve, which pertains to antiparallel spins of the two outgoing electrons, is affected most strikingly (see Fig. 6.16(f)). Instead of the correlation hole in the curve in Fig. 6.16(d), there is a very pronounced maximum, which is in strong contradiction to our experimental data. From analogous calculations for different values of the screening parameter q_{TF} we find that this maximum even increases for larger q_{TF} and does not disappear for smaller ones.

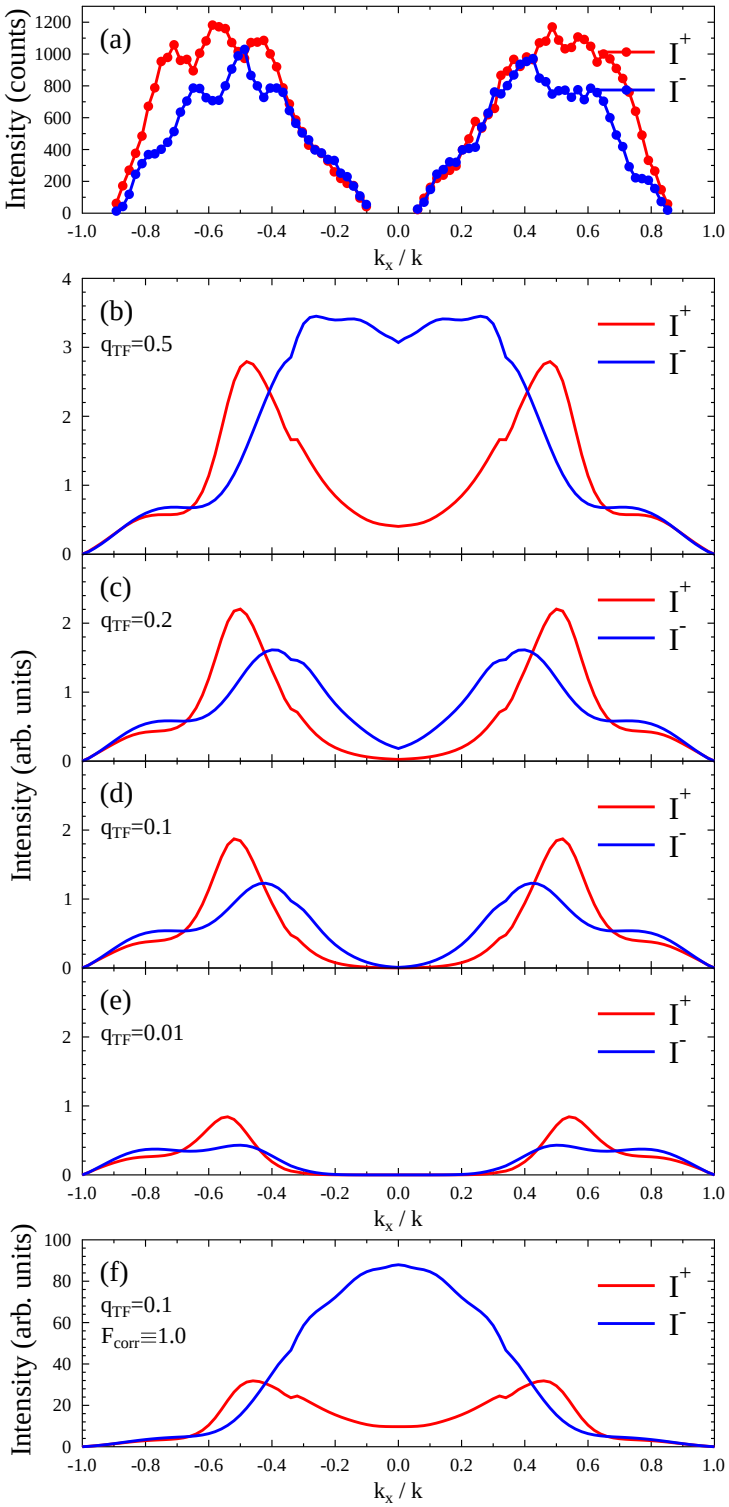

Fig. 6.16: Spin-dependent momentum distribution line scans $I^\sigma(k_x, k_y = 0)$ for $\varphi = 0$ for primary electron energy 25 eV, valence electron with energy $E_F - 0.8$ eV, and surface-parallel momentum 0. (a) Experiment; (b)–(e) theory (cf. Eq. (6.4)), with Coulomb correlation between the two outgoing electrons (via numerically calculated $f^c(\mathbf{k}, \mathbf{r})$ in Eq. (6.2)) for a range of Thomas-Fermi screening parameter q_{TF} values (in Bohr^{-1}) as indicated in the panels; (f) without Coulomb correlation (by setting $f^c(\mathbf{k}, \mathbf{r}) \equiv 1$) for screening parameter $q_{\mathrm{TF}} = 0.1$ Bohr^{-1}.

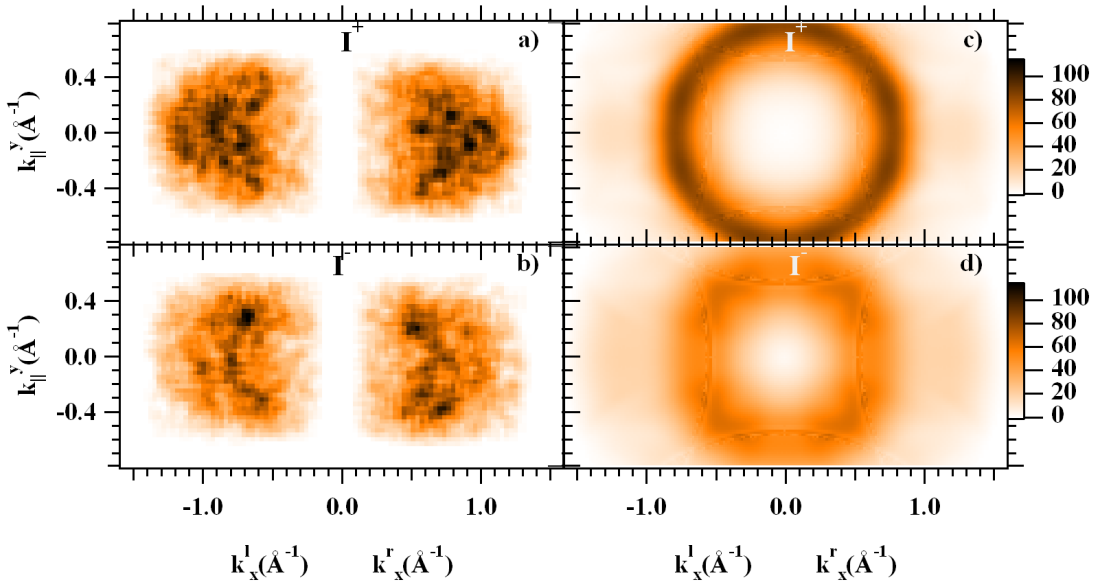

Fig. 6.17: Spin-dependent momentum distributions $I^+(k_x, k_y)$ and $I^-(k_x, k_y)$ for primary electron energy 25 eV and valence electron with energy $E_F - 0.8$ eV and surface-parallel momentum 0. (a),(b) Experiment; (c),(d): theory (cf. Eq. (6.4)), with screening parameter $q_{\mathrm{TF}} = 0.1$ Bohr^{-1} and Coulomb correlation (via $f^c(\mathbf{k}, \mathbf{r})$ in Eq. (6.2)).

To highlight the most important result of the present chapter, we complement the line scans shown in Fig. 6.16 by juxtaposing in Fig. 6.17 experimental spin-dependent momentum distributions $I^\sigma(k_x, k_y)$ and their theoretical counterparts (replotted from the bottom panels of Fig. 6.13 within the $\mathbf{k}^{\parallel}$ window, which is accessible experimentally). Exchange and Coulomb correlation produce a central depletion zone in the parallel-spin distribution I^+, which is more extended than its counterpart in the antiparallel-spin distribution I^-, which is due to Coulomb correlation only.

Because of the comparison with the experiment, the theoretical results discussed up to here were calculated for a primary energy of $E_1 = 25$ eV. Fig. 6.18 shows the influence of the primary energy on the $(e, 2e)$ momentum distributions in the range from $E_1 = 23$ eV to 31 eV. The valence electron energy is again chosen to be $E_2 = E_F - 0.8$ eV, where majority spin states strongly dominate over minority spin states. The left-hand column of Fig. 6.18 shows the results for primary spin up (I^+), i.e., primary spin parallel to majority spin; the central column shows the results for primary spin down (I^-) and the right-hand column the intensity difference $I^+ - I^-$. As expected, the spectra gradually change with the primary energy (caused by changes in the states of the primary and outgoing electrons). For example, I^+ has a ring of high intensity (for relative momenta between about 0.3 and 0.5) for 23–27 eV, which is reduced in the case of 29 eV and still visible for 31 eV. Similarly, I^- shows a ring of high intensity, which is most pronounced for 27 eV, but with a smaller radius than the one for I^+. Since, for the chosen valence energy E_2, the two outgoing electrons have parallel spins for a primary spin-up electron and antiparallel spins for a primary spin-down electron, these results confirm the observation that the depletion zone in the momentum distributions for parallel spins is larger than the one for antiparallel spins.

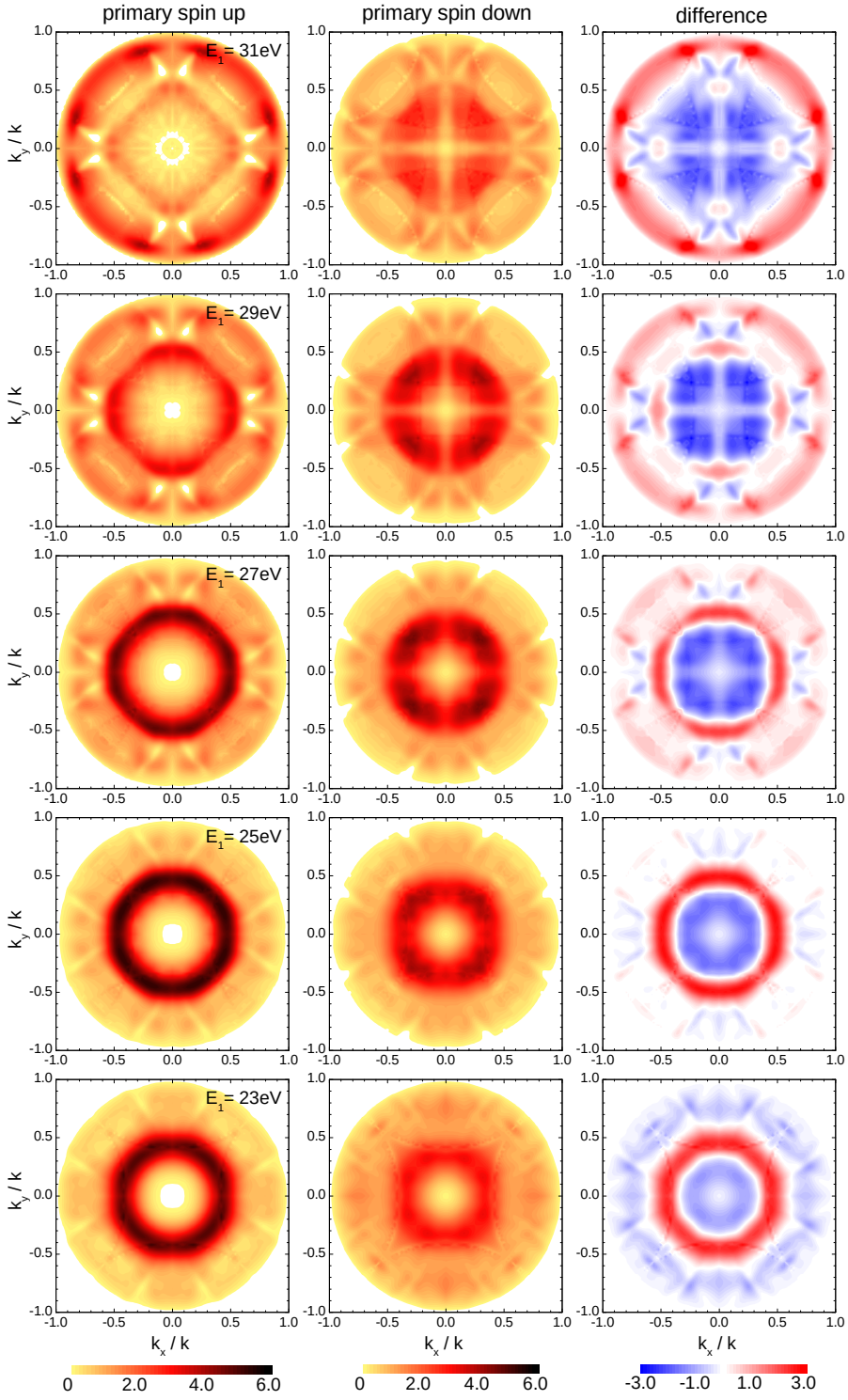

Fig. 6.18: $(e, 2e)$ momentum distributions from Fe(001) in the surface-parallel momentum plane $(k_x, k_y)/k$ as a function of the primary energy as indicated. The valence electron energy is $E_2 = E_F - 0.8$ eV. The two electrons are emitted at equal polar angles $\vartheta_3 = \vartheta_4$ and azimuthal angles φ and $\varphi + \pi$. Left-hand column of panels: momentum distribution for primary spin up (I^+), central column of panels: momentum distribution for primary spin down (I^-) and right-hand column of panels: $I^+ - I^-$.

Chapter 7

$(e, 2e)$ from W(110) and ferromagnetic Co on W(110)

We now investigate a system of Co layers on W(110), which represents a typical case where ferromagnetic exchange and spin-orbit coupling (SOC) are both of considerable importance. As for the case of Fe(001) (see Chapter 6), the intrinsic spin-orbit coupling in the Co layers is rather small. Nonetheless, one can expect a relatively large SOC effect on the electronic structure of the Co layers due to the interaction with the deeper lying W layers. On the other hand, there will be substantial ferromagnetic splittings in the topmost W layers induced by the magnetic Co adlayers. Moreover, we have chosen this system because $(e, 2e)$ from clean W(110) and Co adsorbed on W(110) has been experimentally investigated by Samarin *et al.* [48, 65–68].

7.1 Geometry

A sketch of the bcc(110) lattice in real space as well as in reciprocal space is shown in Fig. 7.1. The epitaxial growth of Co films on W(110) is rather complicated (cf. [69–71]). Initial growth is pseudomorphic. But before a pseudomorphic adlayer is complete, areas with hexagonally close packing are formed. Further Co deposition (at room temperature) leads to a structural change from pseudomorphic to hexagonally close-packed (hcp) and to a layer-by-layer growth of subsequent hcp monolayers. For $n > 2$ monolayers one thus obtains a strained hcp Co n-monolayer film, which is incommensurate with the W(110) substrate or has only a very large surface-parallel unit cell in common with it. Such a structure is not tractable in the electronic-structure computer code (FLAPW/FLEUR [39]), which we use, nor in our $(e, 2e)$ code. Moreover, the above complicated growth would obscure the basic evolution of spin-orbit coupling and ferromagnetic exchange effects in $(e, 2e)$ with an increasing number of adlayers, which we want to explore in the present study.

We therefore adopt the simpler geometrical model of a pseudomorphic layer-by-layer growth of Co on W(110). This Co film is commensurate with the W substrate, i.e., the lateral positions of the Co atoms are fixed. The interlayer distances $d_{\text{Co-Co}}$ and $d_{\text{Co-W}}$ are chosen as follows. First, we determine them such that the maximal muffin tin spheres do not overlap (with lattice constant $a_{\text{Co,bulk}} = 4.724$ Bohr and muffin tin radius $r_{\text{mt}} = 2.362$ Bohr for Co and lattice constant $a_{\text{W,bulk}} = 5.981$ Bohr and radius $r_{\text{mt}} = 2.590$ Bohr for W). This yields $d_{\text{Co-Co}} = 3.657$ Bohr, $d_{\text{Co-W}} = 3.947$ Bohr, and $d_{\text{W-W}} = 4.229$ Bohr. While for the clean W(110) surface the topmost interlayer spacing is contracted by 3 % relative to the bulk interlayer spacing (cf. [72–74]), the adsorption of Co is likely to lift this contraction. For the W(110) substrate beneath the Co films we therefore assume the topmost interlayer spacing to be the same as in the bulk.

For 1 ML to 3 ML Co films on W(110) with this geometrical structure, we have calculated the ground state electronic structure and in a second step constructed a quasiparticle potential

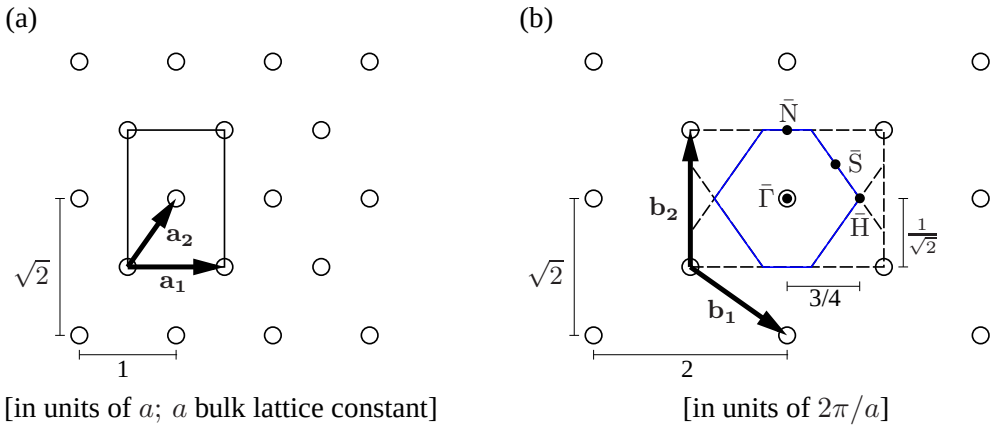

Fig. 7.1: Real (a) and reciprocal (b) surface lattice of a bcc(110) surface. The basis vectors are chosen to be $\mathbf{a}_1 = a\mathbf{e}_x$ and $\mathbf{a}_2 = a/2\mathbf{e}_x + a/\sqrt{2}\mathbf{e}_y$ where a is the bulk lattice constant. $\mathbf{b}_1$ and $\mathbf{b}_2$ are the respective reciprocal lattice vectors. $\overline{\Gamma}$ denotes the center of the two dimensional Brillouin zone, and $\overline{\mathrm{N}}$, $\overline{\mathrm{S}}$, and $\overline{\mathrm{H}}$ represent high symmetry points at the boundary of the surface Brillouin zone.

(for details see Section 7.3) as input for LEED calculations.

A comparison of the resulting LEED spectra for the (00) beam with corresponding experimental spectra is shown in Fig. 7.2. In the case of 1 ML Co on W(110), the theoretical results obtained with the above value for $\mathrm{d_{W\text{-}Co}}$ agree very well with the respective experiments. In view of the mentioned problems regarding the formation of 2 or 3 Co layers on W(110), the respective theoretical LEED curves agree surprisingly well with the experiments. This agreement can be improved a bit by using a slightly larger value of $\mathrm{d_{Co\text{-}Co}}$. The overall best fit is obtained by $\mathrm{d_{Co\text{-}Co}} = 0.891\ \mathrm{d_{W\text{-}W}} = 3.768$ Bohr, a value which is hence used in all following calculations.

7.2 Symmetry properties for cubic(110) surfaces

We focus here on the widely used coplanar geometry with primary electrons incident along the surface normal. The reaction plane is the (x, z) plane (with x along the [001] direction in the surface plane and z along the surface normal [110]). The primary electron spin polarization $\mathbf{P}_1$ and the magnetization are chosen normal to the reaction plane, i.e., along the y axis [1,-1,0].

We first recall that the point group $2mm$ for a nonmagnetic cubic(110) surface has four symmetry operations: the identity, a twofold rotation about the surface normal, the reflection m_y at the (x, z) plane, and the reflection m_x at the (y, z) plane. The single group has the four one-dimensional irreducible representations Σ^i, $i = 1, \ldots, 4$, and the double group (in the presence of SOC) has the single two-dimensional irreducible representation Σ_5. If the surface is ferromagnetic with magnetization along y, the symmetry is reduced to the point group m, with the two symmetry operations identity and m_y. Its double group has two one-dimensional irreducible representations, γ_+ and γ_-, which are degenerate by time reversal (cf., e.g., [78] and references therein).

Since the entire initial setup, including the primary polarization vector $\mathbf{P}_1$ (along y), is invariant under the mirror operation m_y, the polarization vectors $\mathbf{P}_3$ and $\mathbf{P}_4$ of the two emitted electrons can have only components along $\pm y$. Consequently, they can be completely character-

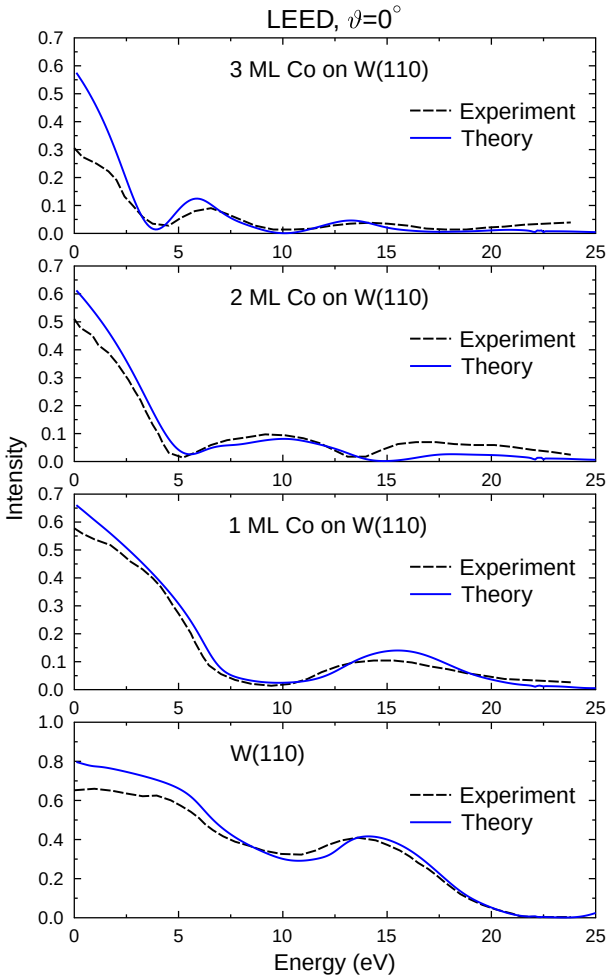

Fig. 7.2: Comparison of experimental and theoretical spin-averaged LEED spectra of the specular beam for normal incidence. The theoretical spectra are calculated for surface layer distances $d_{W\text{-}Co} = 0.933\ d_{W\text{-}W}$ and $d_{Co\text{-}Co} = 0.891\ d_{W\text{-}W}$. The experimental data are taken from [75] (with a correction of the kinetic energy by $\Delta E = -1$ eV [76, 77]).

ized by the spin labels $\sigma_3 = \pm$ and $\sigma_4 = \pm$.

We now turn to the symmetry properties of the spin-dependent $(e, 2e)$ intensities (cf. Eqs. (3.147) and (3.150)) and the asymmetries associated with them (cf. Eqs. (3.151b)–(3.151d)), which in our setup are all, as explained in Chapter 3 (cf. Eq. (3.146)), functions of the primary electron energy E_1, the energies E_3 and E_4 of the outgoing electrons, and of their parallel-momentum components k_{3x} and k_{4x}.

First consider the fully spin-resolved intensities $I^{\sigma_1\mu}_{\sigma_3\sigma_4}(E_3, E_4)$ (cf. Eq. (3.147)). The mirror operation m_x, which is a symmetry operation of the system without ferromagnetism, reverses the primary electron spin and the magnetization. Since in the present setup the primary electron momentum is normal to the surface, it is not affected by m_x. As for the outgoing electrons, m_x interchanges the energies E_3 and E_4, and interchanges and reverses the parallel momentum components k_{3x} and k_{4x} as well as the spin labels σ_3 and σ_4. Therefore, for fixed primary energy

E_1, we have

$$I^{\sigma_1\mu}_{\sigma_3\sigma_4}(E_3, k_{3x}; E_4, k_{4x}) = I^{-\sigma_1,-\mu}_{-\sigma_4,-\sigma_3}(E_4, -k_{4x}; E_3, -k_{3x}). \tag{7.1}$$

For the spin-summed intensities

$$I^{\sigma_1\mu}(E_3, k_{3x}; E_4, k_{4x}) = \sum_{\sigma_3,\sigma_4} I^{\sigma_1,\mu}_{\sigma_3,\sigma_4}(E_3, k_{3x}; E_4, k_{4x}) \tag{7.2}$$

this implies

$$I^{\sigma_1\mu}(E_3, k_{3x}; E_4, k_{4x}) = I^{-\sigma_1,-\mu}(E_4, -k_{4x}; E_3, -k_{3x}). \tag{7.3}$$

From this relation one obtains the following properties of the asymmetries (cf. Eqs. (3.151b)–(3.151d)):

$$A_{\mathrm{ex}}(E_3, k_{3x}; E_4, k_{4x}) = A_{\mathrm{ex}}(E_4, -k_{4x}; E_3, -k_{3x}), \tag{7.4a}$$

$$A_{\mathrm{so}}(E_3, k_{3x}; E_4, k_{4x}) = -A_{\mathrm{so}}(E_4, -k_{4x}; E_3, -k_{3x}), \tag{7.4b}$$

$$A_u(E_3, k_{3x}; E_4, k_{4x}) = -A_u(E_4, -k_{4x}; E_3, -k_{3x}). \tag{7.4c}$$

If the polar angles ϑ_3 and ϑ_4 are fixed, the parallel-momentum components k_{3x} and k_{4x} are determined by the energies E_3 and E_4 according to $k_{3x} = \sqrt{2E_3}\sin\vartheta_3$ and $k_{4x} = \sqrt{2E_4}\sin\vartheta_4$. As a consequence, the intensities (Eqs. (7.2) and (7.3)) as well as the asymmetries (Eqs. (7.4a)–(7.4c)) are then functions only of E_3 and E_4. Since from energy and parallel-momentum conservation (cf. Eq. (3.144)) it follows that a pair (E_3, E_4) corresponds uniquely to a pair (E_2, k_{2x}), the $(e, 2e)$ quantities can alternatively be represented as functions of the energy E_2 and the parallel-momentum component k_{2x} of the relevant valence electron. Since the mirror operation at the (y, z) plane transforms k_{2x} into $-k_{2x}$, we obtain for the intensities the symmetry relations

$$I^{\sigma_1\mu}_{\sigma_3\sigma_4}(E_2, k_{2x}) = I^{-\sigma_1,-\mu}_{-\sigma_4,-\sigma_3}(E_2, -k_{2x}), \tag{7.5}$$

$$I^{\sigma_1\mu}(E_2, k_{2x}) = I^{-\sigma_1,-\mu}(E_2, -k_{2x}). \tag{7.6}$$

For the asymmetries (cf. Eqs. (3.151b)–(3.151d) and (7.4)), Eq. (7.6) entails

$$A_{\mathrm{ex}}(E_2, k_{2x}) = A_{\mathrm{ex}}(E_2, -k_{2x}), \tag{7.7a}$$

$$A_{\mathrm{so}}(E_2, k_{2x}) = -A_{\mathrm{so}}(E_2, -k_{2x}), \tag{7.7b}$$

$$A_u(E_2, k_{2x}) = -A_u(E_2, -k_{2x}). \tag{7.7c}$$

For the spin- and layer-resolved valence electron density of states (LDOS alias spectral density) $N^{\sigma_2\mu}_m(E_2, k_{2x})$, where m indicates the atomic layer parallel to the surface and $\sigma_2 = \pm$ the valence electron spin with respect to the $+y$ direction, symmetry imposes a relation analogous to Eq. (7.6):

$$N^{\sigma_2\mu}_m(E_2, k_{2x}) = N^{-\sigma_2,-\mu}_m(E_2, -k_{2x}). \tag{7.8}$$

An important special case is the equality of the two emission angles: $\vartheta_3 = \vartheta_4$. If in this case the two energies E_3 and E_4 are equal, $k_{3x} = -k_{4x}$ and consequently $k_{2x} = 0$ (i.e., center of the

surface Brillouin zone). The above $(e, 2e)$ quantities and the LDOS are then functions of only the valence energy E_2. $A_{\rm so}$ and A_u are identically zero, whereas $A_{\rm ex}$ in general has some finite value.

All the above relations remain of course valid for nonmagnetic materials, with the simplification that the magnetic index μ is absent and $A_{\rm ex} = A_u = 0$.

7.3 Ground state properties and quasiparticle potentials

As for Fe(001) (cf. Section 6.2), the electronic structure of W(110) and n layers of Co on W(110), $n = 1, 2, 3$, was calculated by using FLAPW/FLEUR [39]. For the geometric structure we assumed a pseudomorphic arrangement as described in Section 7.1. In the following we use the abbreviation Co_n/W for n cobalt monolayers on W(110).

From calculations using the FLEUR package [39], we obtain in particular the ground state electronic potential $V(\mathbf{r})$ and the work function ϕ. In Table 7.1 the obtained work functions and the mean interstitial potentials, which are used for the incorporation of the potential in the Korringa-Kohn-Rostoker (KKR) code, are shown. For clean W(110) we found $\phi = 5.073$ eV, which agrees reasonably well with the experimental value of 5.25 eV [41]. Co adlayers reduce the work functions a little bit and for 3 ML Co on W(110) we obtained 4.909 eV, which compares well with the experimental value of 5.0 eV for pure Co [41].

	number of layers	ϕ [eV]	V_0 [eV]
W	11	5.073	-16.101
Co_1/W	13	4.759	-15.022
Co_2/W	15	4.834	-14.631
Co_3/W	17	4.909	-14.432

Table 7.1: Calculated work functions ϕ and potential constants V_0 (mean interstitial potential) of the systems W(110), 1 ML Co on W(110), 2 ML Co on W(110), and 3 ML Co on W(110).

Moreover, we obtained the magnetization direction and the layer-resolved magnetic moments from ground state calculations. The magnetization direction is in the surface plane along the $[1\bar{1}0]$ axis. In Table 7.2 we have collected the magnetic moments per layer for the three investigated Co_n/W-systems. Interestingly, the magnetic moment in the Co layer directly contacting the topmost W layer is approximately the same for all three systems and smaller than for bulk hcp Co (1.62 μ_B). In Co_2/W and Co_3/W one finds a relative large enhancement (by about 23–25% relative to the bulk) of the magnetic moment for the respective topmost layer. It is remarkable that only the topmost W layer in Co_1/W attains a noticeable induced magnetic moment. All other W layers remain nearly unmagnetized.

As already discussed in the case of iron (cf. Section 6.2), we also need to adapt the ground state potential by a self-energy correction to get the effective quasiparticle potentials. The (complex valued) self-energy correction Σ is in general a spatial-, energy- and spin-dependent function, i.e., $\Sigma = \Sigma(\mathbf{r}, E, \sigma)$. In absence of an exact expression for Σ, we make the following

	Co_1/W m $[\mu_B]$	Co_2/W m $[\mu_B]$	Co_3/W m $[\mu_B]$
Co layer (+3)	-	-	1.988
Co layer (+2)	-	2.017	1.982
Co layer (+1)	1.606	1.578	1.528
W layer (-1)	0.023	-0.004	-0.003
W layer (-2)	-0.003	-0.006	-0.012
W layer (c)	-0.001	-0.002	0.002

Table 7.2: Magnetic moments (m) in the muffin-tin spheres of the (topmost) layers of the systems 1 ML Co on W(110), 2 ML Co on W(110), and 3 ML Co on W(110). The integer numbers in the first column indicate the position of the respective layer relative to the Co/W interface; c denotes the central layer.

assumptions for the imaginary part of Σ:

$$\text{Im}\,\Sigma = V_{\text{im}} = \begin{cases} a\frac{|E-E_F|^2}{|E-E_F|^2+b^2} + d & \text{for valence electron states,} \\ a|E-E_F|^c & \text{for LEED- and time-reversed LEED-states.} \end{cases} \tag{7.9}$$

The values of the coefficients (a, b, c, d) depend, apart from the chosen element, on the energy and the spin orientation. Moreover, they are supposed to be identical in all Co layers and identical in all W layers, respectively. Based on studies described in [79] and [80], we find for W: $a = -1.0$, $b = 8.0$, $d = -0.025$ (valence electron states); $a = -0.1$, $c = 0.83$ (LEED states), and for Co: $a = -2.9$, $b = 2.3$, $d = -0.1$ (valence electron states, majority spin); $a = -1.6$, $b = 3.5$, $d = -0.1$ (valence electron states, minority spin); $a = -0.099$, $c = 0.89$ (LEED states, majority spin), $a = -0.179$, $c = 0.89$ (LEED states, minority spin). The resulting imaginary parts of Σ are plotted in Fig. 7.3.

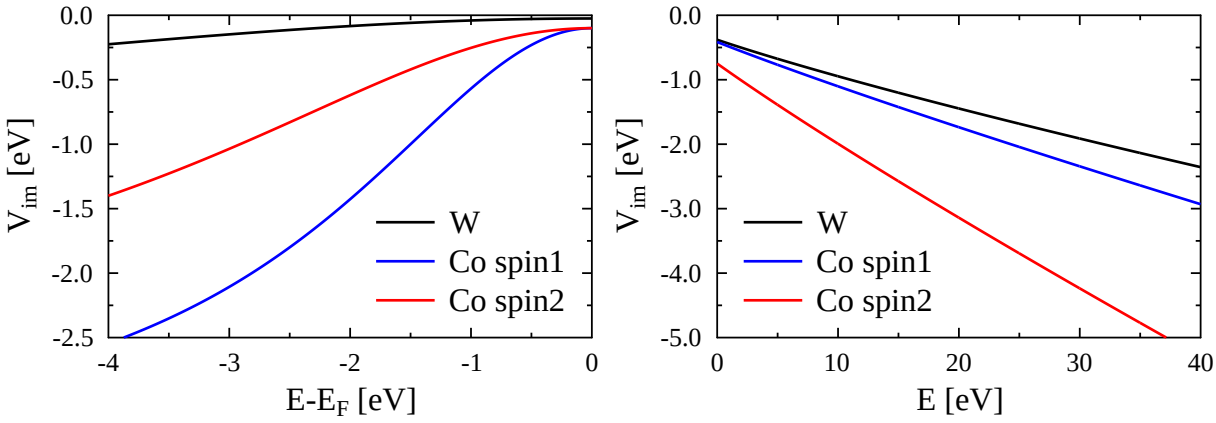

Fig. 7.3: Imaginary parts V_{im} of the quasiparticle potential in the W and Co layers. Blue lines: Co layers, majority spin states; red lines: Co layers, minority spin states; black lines: W layers. (a) V_{im} for valence electron states. (b) V_{im} for LEED states.

For Co, V_{im} is strongly spin-dependent. This spin-dependence is similar to the one for Fe

which has been discussed in detail in Section 6.2. Moreover, V_{im} (see Fig. 7.3) for the Co layers is much larger than V_{im} for the W layers, i.e., compared to W there is an increased absorption for electrons in Co layers.

7.4 Valence electron densities of states

7.4.1 Clean W(110)

Fig. 7.4 gives an overview of the layer-resolved density of states (LDOS) of a W(110) half space. Comparing panel (a) with (d) one recognizes strong surface state structures crossing the Fermi energy. These are, as can be deduced from (e) and (i), of odd symmetry and are hence not relevant for $(e, 2e)$ spectroscopy because of selection rules (Ref. [62]). The cross-like structure, which can be found 1 eV below E_F at $k = 0$, exhibits an interesting property: its ascending branch is mainly spin up (in y direction, i.e., $y+$) and its descending branch is mainly spin down ($y-$) as can be seen from the spin resolved spectra (e) and (i) of Fig. 7.4. This spin polarization is a consequence of spin-orbit coupling and the symmetry breaking of the three-dimensional crystal at the surface (Rashba effect, cf. Refs. [81–83] and references therein). This effect is still visible in the second layer (Fig. 7.4, panels (b), (f), and (j)) but decreases rapidly for deeper lying layers ((c), (g), (k)) and is absent in bulk layers.

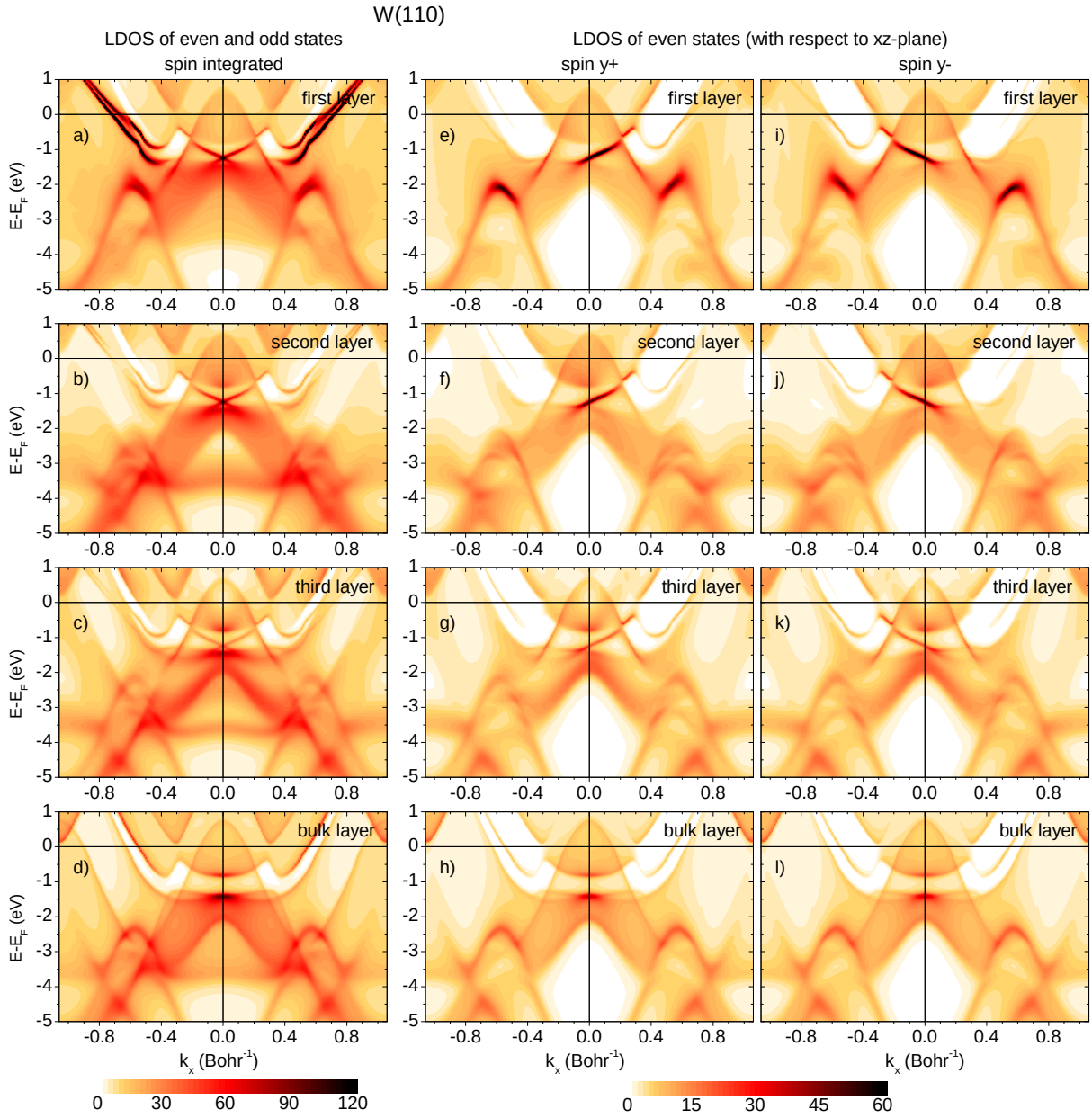

Fig. 7.4: Layer-resolved density of states (LDOS) of W(110) along the k_x direction. Panels (a)-(d) show the spin integrated LDOS of even and odd states of the first, second, third, and central (bulk) layer of an eleven layer film. Panels (e)-(h) show the even LDOS (which are symmetric with respect to the (x, z) plane) for spin-up electrons (spin-projection $+1/2$ in the $+y$ direction). Panels (i)-(l) show the even LDOS for spin-down electrons. The densities of states have been calculated using the energy-dependent $V_{\mathrm{im}}(E)$ (cf. Eq. (7.9) and Fig. 7.3)

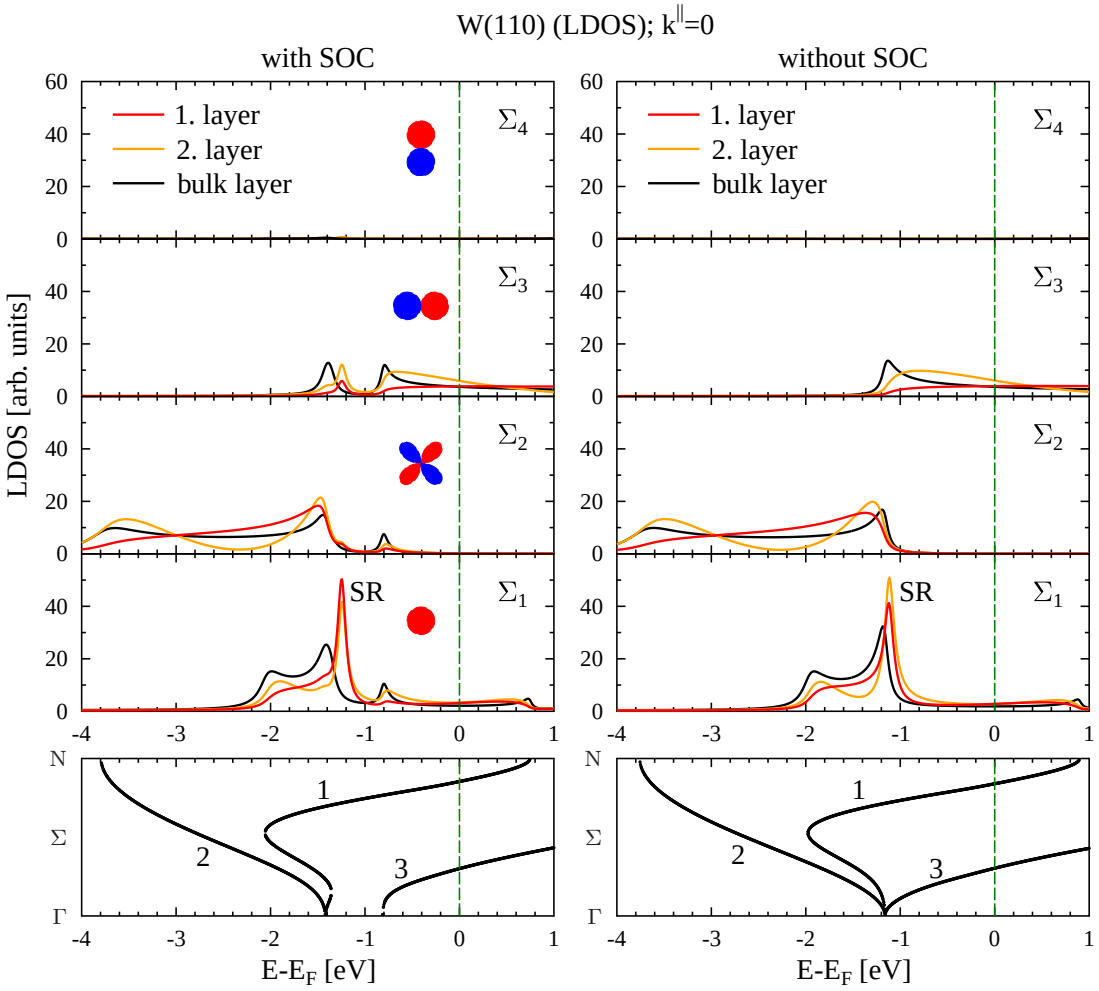

Fig. 7.5: Symmetry-resolved LDOS of W(110) for $k^{\parallel} = 0$. The densities of states have been calculated using the energy-dependent $V_{\mathrm{im}}(E)$. The red lines indicate the LDOS in the first layer, the orange lines the LDOS in the second layer, and the black lines the LDOS in the central (bulk) layer. The symbols in the left-hand panel symbolically sketch projections of the d parts ($l = 2$) for $z > 0$ of the respective states onto the surface parallel (x, y) plane. The bottom panel shows the corresponding bulk band structure of W along Γ−N. (a) Fully relativistic calculation; (b) Calculation with spin-orbit coupling (SOC) turned off.

The layer resolved DOS of W(110) for $k^{\parallel} = 0$ is shown in Fig. 7.5. The chosen symmetry resolution is due to the non-relativistic space group Σ, where Σ_1 refers to totally symmetric states. Σ_2 states are antisymmetric with respect to the (x, z) and (y, z) planes, Σ_3 states are symmetric with respect to the (x, z) plane and antisymmetric with respect to the (y, z) plane. Σ_4 states are antisymmetric with respect to the (x, z) plane und symmetric with respect to the (y, z) plane. If we choose the (x, z) plane as $(e, 2e)$ reaction plane, only states with Σ_1 or Σ_3 symmetry are important. In Table 1 of Ref. [62] the relevant selection rules for a bcc(110) surface are shown (see also the discussion in [84]).

Overall, the LDOS with and without spin-orbit coupling, shown in the left-hand and right-hand panels of Fig. 7.5, do not differ very much, apart from the region around −1 eV with the prominent spin-orbit gap at Γ. Within this gap we find the surface resonance (SR) which for

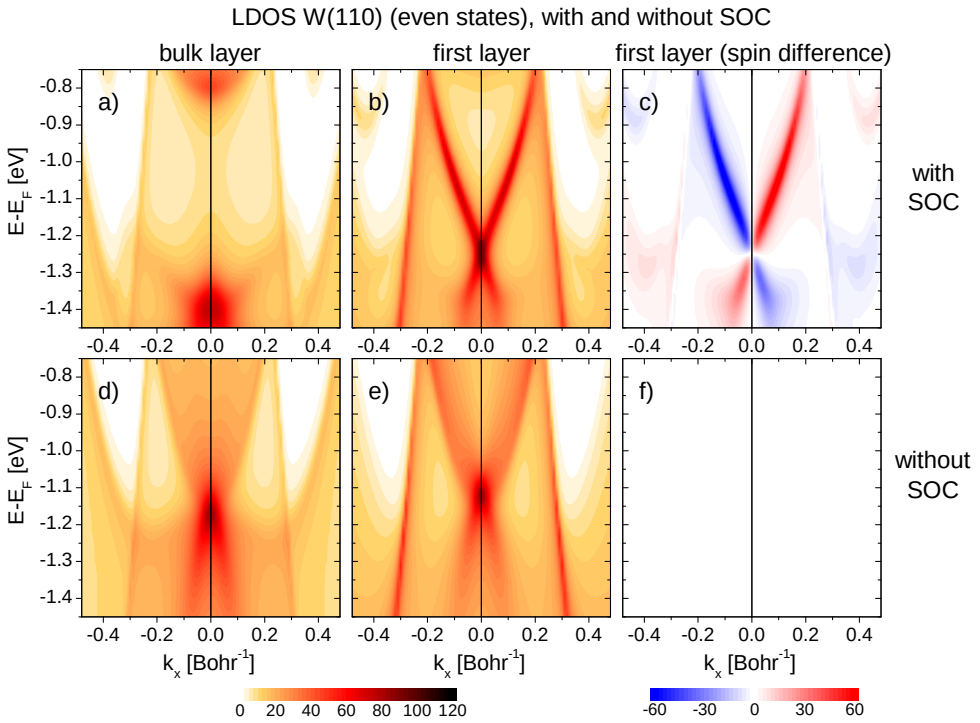

Fig. 7.6: Layer-resolved valence electron densities of states (LDOS) $N_m(E, k_x; k_y = 0)$ of W(110) (with k_x in the central part of the $\overline{\text{H}}$–$\overline{\Gamma}$–$\overline{\text{H}}$ line in the Surface Brillouin Zone, $\overline{\text{H}}$ being at $k_x = 0.79$ Bohr^{-1}) of even symmetry with respect to the (x, z) plane. The coordinates x and y are in the surface plane along [001] and [1 -1 0], respectively, and z is along the surface normal [110]. Spin-unresolved LDOS N_b for the bulk layer (a) and N_1 for the topmost atomic layer (b). Spin difference first layer (c). (d),(e),(f): Same as (a), (b), (c) but without spin-orbit coupling.

$k_x \neq 0$ shows the spin polarization discussed in Fig. 7.4. A prominent surface resonance exists already without SOC. This resonance is however of purely Σ_1 character for $k = 0$ and has no spin polarization for $k_x > 0$.

In Fig. 7.6 we show an enlarged part of the LDOS (cf. Fig. 7.4) of even xz mirror symmetry for $\mathbf{k}^{\parallel} = (k_x, k_y = 0)$ along the central part of the $\overline{\text{H}}$–$\overline{\Gamma}$–$\overline{\text{H}}$ line in the surface Brillouin zone (SBZ) around the cross-like structure. For $k_x = 0$ the bulk LDOS (Fig. 7.6(a)) exhibits, as a consequence of SOC, a gap between the peak features around -0.8 eV and -1.4 eV, respectively, which extends out to $k_x \neq 0$. In this gap, a surface state resides (see Fig. 7.6(b)), which at the center of the SBZ is at the energy -1.25 eV below E_F and disperses outward linearly up to about ± 0.11 Bohr^{-1} as a Dirac cone, in accordance with recent experimental photoemission results [85]. The even LDOS, which is shown in Fig. 7.6(a) because of its relevance for $(e, 2e)$, is in fact the vastly dominant part for the surface state, whereas its odd LDOS contribution is by an order of magnitude smaller. The mainly even (x, z) mirror symmetry of the Dirac cone surface state, which we thus found theoretically, was recently experimentally revealed by photoemission making use of selection rules for p- and s-polarized light [86].

The LDOS in Figs. 7.6(a) and 7.6(b) are not spin-resolved. Resolving it with respect to spin orientation along the y axis ([1 -1 0] in the surface plane) reveals that the Dirac-cone surface state consists of two parts with opposite spin polarization (Fig. 7.6(c)). (In the bulk layers the

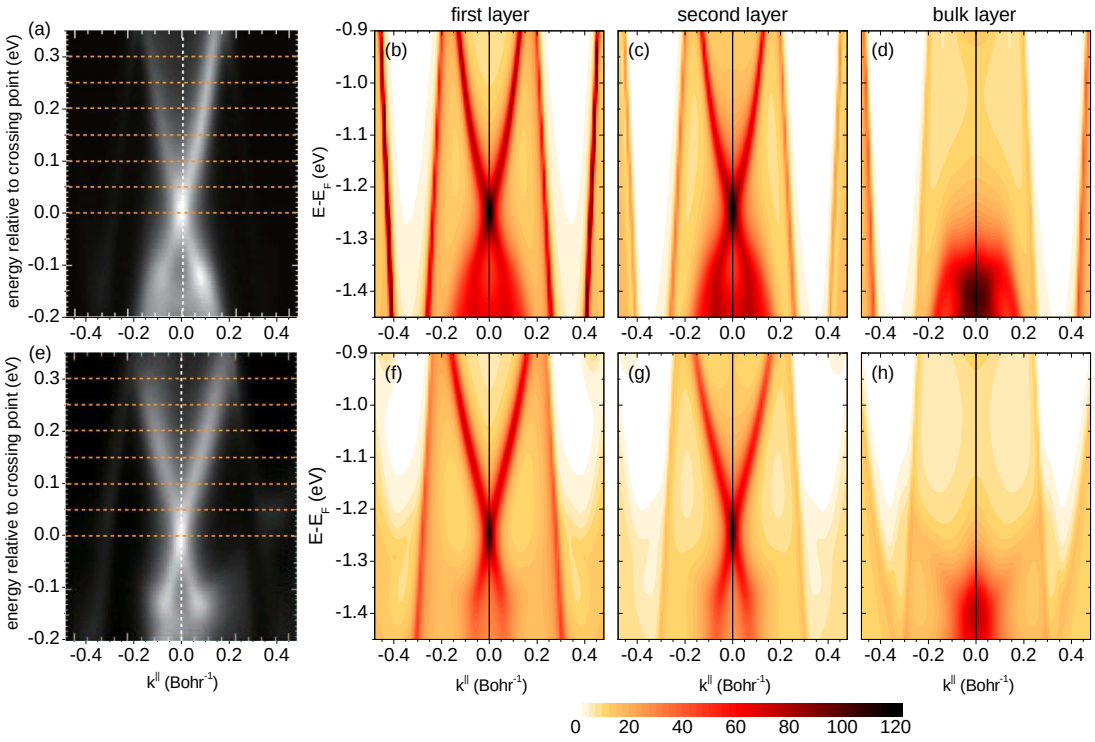

Fig. 7.7: Spin-integrated layer-resolved density of states (LDOS) of W(110) for $\mathbf{k}^{\parallel}$ along different directions in the surface Brillouin zone. (a) and (e): Experimental photoemission spectra (from [85]): along $\overline{\Gamma\mathrm{S}}$ (a) and along $\overline{\Gamma\mathrm{H}}$ (e). Theoretical LDOS along $\overline{\Gamma\mathrm{S}}$ (b)-(d) and along $\overline{\Gamma\mathrm{H}}$ (f)-(h). The theoretical plots are layer resolved as indicated in the respective panel. In the $\overline{\Gamma\mathrm{H}}$-direction only even states are plotted, whereas in the $\overline{\Gamma\mathrm{S}}$ even and odd states. Because of the symmetry resolution, the LDOS values at $\mathbf{k}^{\parallel} = 0$ are not identical for the different directions.

spin difference is zero.) As expected, the gap in the bulk layer vanishes when SOC is switched off (Fig. 7.6(d)). Surprisingly, even without spin-orbit coupling the cross-like surface state survives (Fig. 7.6(e)), which, however, exhibits no spin-polarization (Fig. 7.6(f)).

In Fig. 7.7 the LDOS around the Dirac cone is shown for different $\mathbf{k}^{\parallel}$ directions in the surface Brillouin zone (cf. Fig. 7.1). For $\mathbf{k}^{\parallel}$ along $\overline{\Gamma\mathrm{H}}$ (Figs. 7.7(b),(c)) and $\mathbf{k}^{\parallel}$ along $\overline{\Gamma\mathrm{S}}$ (Figs. 7.7(f),(g)), we find the same behavior: a well pronounced cross structure for the surface layers. In the bulk layer (Figs. 7.7(d),(h)), the LDOS in this region is relatively low and shows little structure. For comparison, the already mentioned corresponding photoemission experiments by Miyamoto *et al.* [85] are also shown in Fig. 7.7. For $\mathbf{k}^{\parallel}$ along $\overline{\Gamma\mathrm{H}}$ (Fig. 7.7(a)) and $\mathbf{k}^{\parallel}$ along $\overline{\Gamma\mathrm{S}}$ (Fig. 7.7(e)) the experimental results are in very good agreement with the calculated density of states.

The spin-polarization of the two branches of the cross-like structure in the surface layers will be discussed in more detail in Section 7.5 (in connection with $(e, 2e)$ calculations for W(110)).

7.4.2 Co on W(110)

The LDOS obtained for 1 ML Co on W(110) is shown in Fig. 7.8. In the top surface layer the LDOS is dominated by the exchange splitting due to the ferromagnetic nature of Co, which at $k_x = 0$, amounts to approximately 1.8 eV. The structures in the following W layers show still some magnetic anisotropy as in pure W(110), but are otherwise not very much influenced by the Co layer.

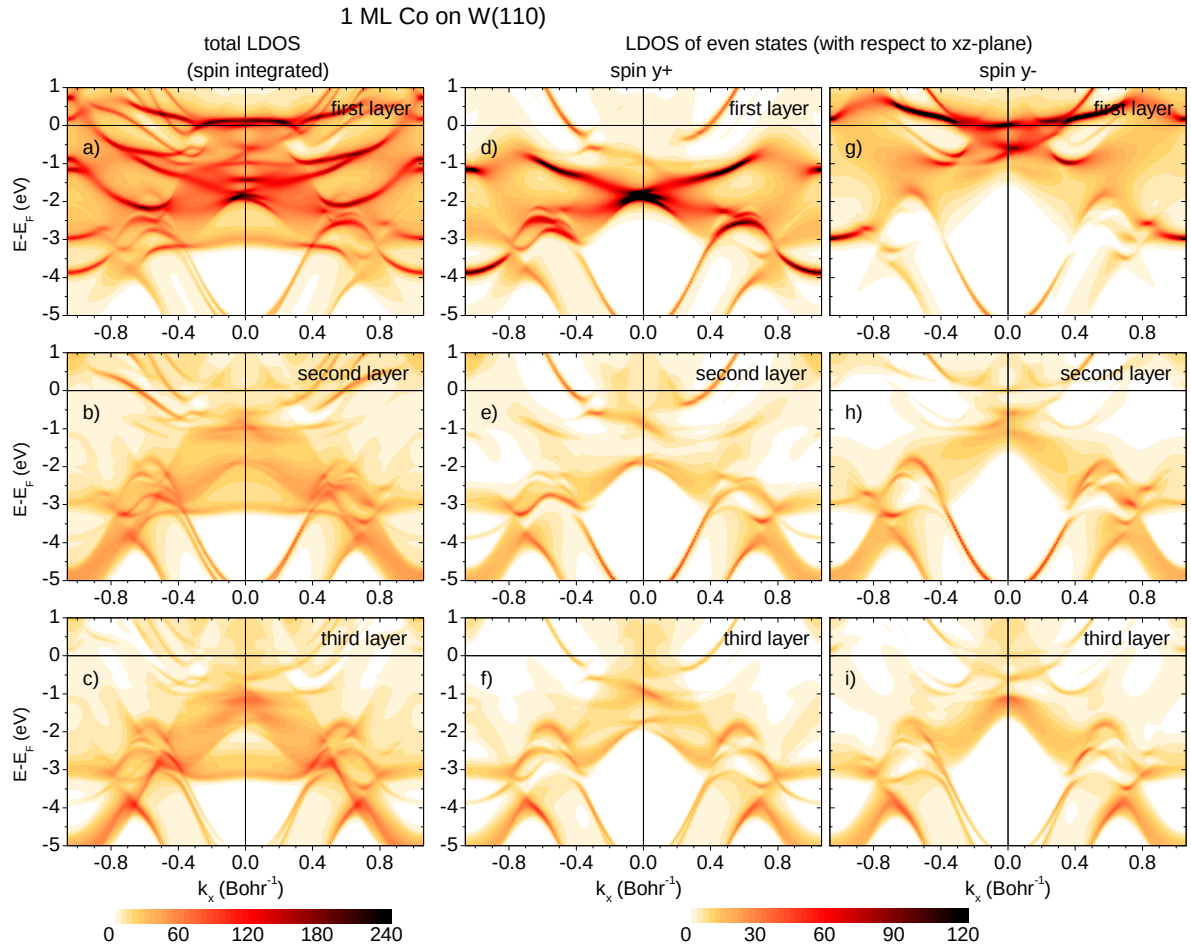

Fig. 7.8: Layer-resolved density of states (LDOS) of 1 ML Co on W(110) along the k_x direction. Panels (a)-(c) show the spin-summed LDOS of the first layer (Co), second (W), and third (W) layer of a 13 layer film. Panels (d)-(f) show the even LDOS for spin-up electrons (where even refers to states that are symmetric with respect to the (x, z) plane, and the spin is given relative to the y direction). Panels (g)-(i) show the even LDOS for spin-down electrons. To reveal more details, the densities of states have been calculated using a small constant imaginary part of the self-energy ($V_{\mathrm{im}} = -0.05$ eV).

The DOS for 2 ML Co on W(110) is shown in Fig. 7.9. The spin-split d band of the Co layers exhibit now a more detailed structure, especially for the majority case. The amount of the exchange splitting is for all Co layers of the same magnitude. In addition, the deeper lying parabolic band shows now, even in the W layers, a clear magnetic splitting which is about 0.7 eV.

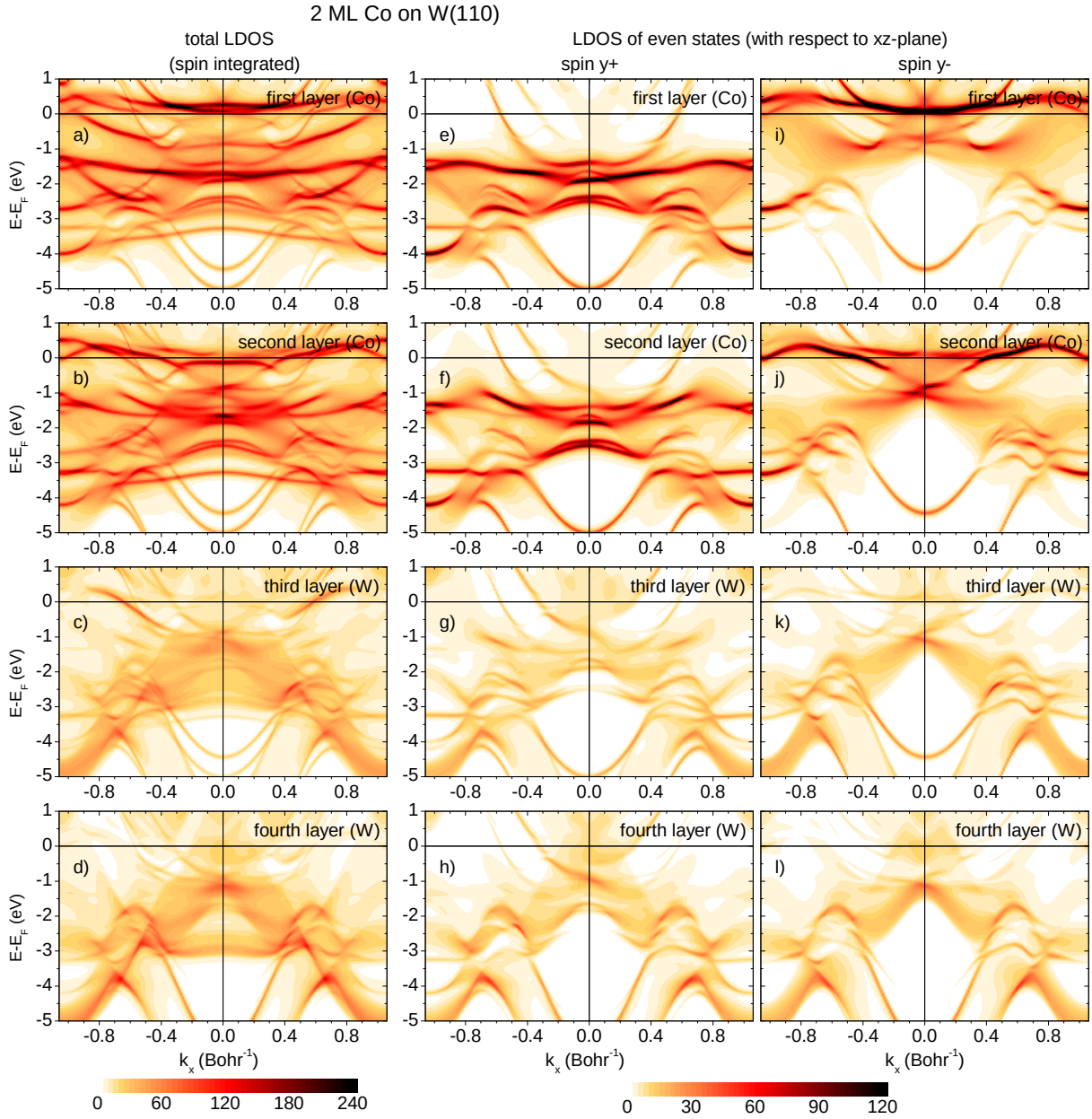

Fig. 7.9: Layer-resolved density of states (LDOS) of 2 ML Co on W(110) along the k_x direction. Panels (a)-(d) show the spin-summed LDOS of the first layer (Co), second (Co), third (W), and fourth (W) layer of a 15 layer film. Panels (e)-(h) show the even LDOS for spin-up electrons (cf. Fig. 7.8). Panels (i)-(l) show the even LDOS for spin-down electrons. The densities of states have been calculated using a small constant imaginary part of the self-energy ($V_{\mathrm{im}} = -0.05$ eV).

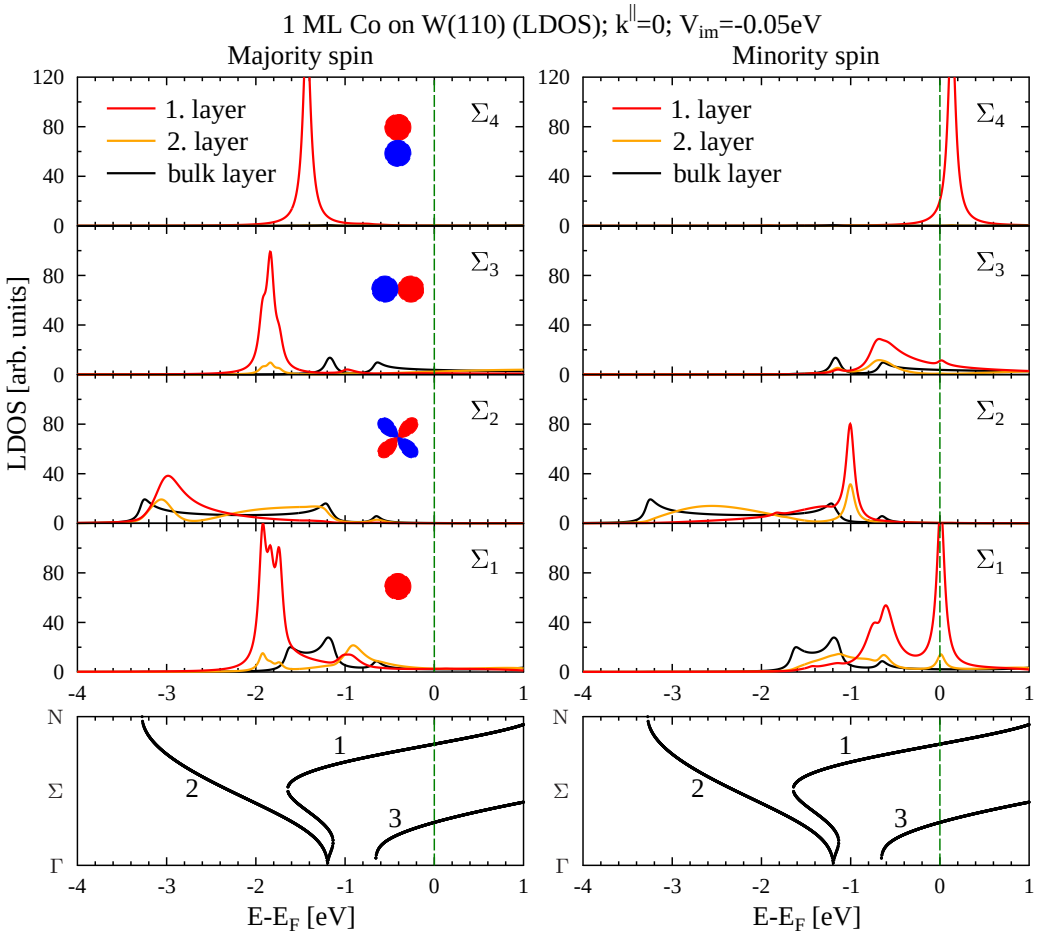

Fig. 7.10: Symmetry- and spin-resolved LDOS of 1 ML Co on W(110) for $\mathbf{k}^{\parallel} = 0$. Left-hand side: Majority spin, right-hand side: Minority spin LDOS. Red lines: first layer, orange lines: second layer and the black lines: central (bulk) layer. The symbols in the left-hand panel symbolically sketch the symmetry of the respective states (cf. Fig. 7.5). The bottom panel shows the corresponding bulk band structure of W(110) along $\Gamma-$N.

In Fig. 7.10 we show, for $\mathbf{k}^{\parallel} = 0$, the LDOS of 1 ML Co on W(110). The surface Bravais lattice is the same as the for the clean W(110) surface. Therefore, the symmetry resolution as in Fig. 7.5 is still appropriate. However, the electronic structure of the surface layers is significantly changed. The tungsten surface resonance is destroyed. For Σ_1 symmetry, but also for Σ_3 and Σ_4, the Co monolayer forms sharp DOS peaks which are spin-split by 1.6 to 1.8 eV.

As for clean W(110), the symmetry of the valence state involved in the $(e, 2e)$ process largely determines the resulting spectrum. Furthermore, the selection rules are the same as for the W(110) surface. The Σ_1 state is symmetric with respect to all relevant symmetry operations of a bcc(110) surface and hence plays an important role in $(e, 2e)$. In the present case of 1 ML on W(110) we have a large Σ_1 minority peak and a small Σ_3 minority at E_F, while the majority LDOS around E_F is relatively small.

If the valence state is antisymmetric with respect to the reaction plane, an $(e, 2e)$ transition is not possible. Hence in the case of normal incidence, an electron in a state with Σ_2 symmetry cannot be seen by $(e, 2e)$ spectroscopy if the reaction plane is parallel to the (x, z) plane nor if

it is parallel to the (y, z) plane. Electron states with Σ_3 symmetry can be measured by choosing the reaction plane parallel to the (x, z) plane. In order to measure states with Σ_4 symmetry the reaction plane has to be parallel to the (y, z) plane.

In Fig. 7.11 the LDOS for 2 ML Co on W(110) is shown. Compared to 1 ML Co the spin splitting appears to be increased, e.g., 2 eV (instead of 1.6 eV) for the Σ_4 states.

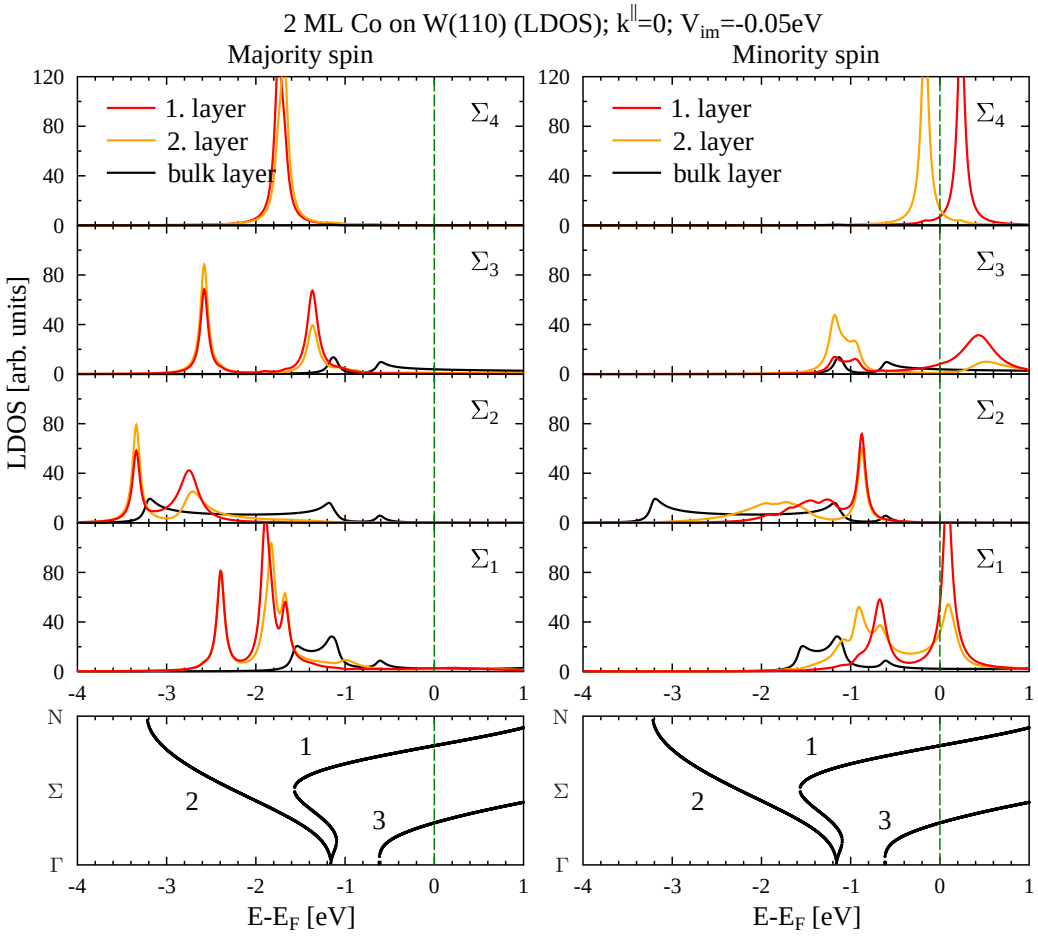

Fig. 7.11: As in Fig. 7.10 but for 2 ML Co on W(110).

7.5 $(e, 2e)$ response to a spin-polarized surface state on W(110)

Because of its striking properties, the spin-polarized surface state on W(110), which has been discussed in Section 7.4.1, offers a good opportunity for a detailed analysis by $(e, 2e)$ spectroscopy.

If the reaction plane (containing the momentum vectors of the incident electron and of the two outgoing ones) is a mirror plane of the semi-infinite surface system, then only valence electron states with even reflection symmetry are allowed to contribute to the $(e, 2e)$ reaction cross section. This is strictly valid in the absence of spin-orbit coupling (SOC). With SOC, the valence electron spinor generally contains both even and odd spatial parts, but its even spatial part is the most relevant one for $(e, 2e)$. The odd part may contribute because, due to SOC, the incident and outgoing electron spinors have also odd parts (inside the crystal). As demonstrated in Fig. 7.12,

which shows the k dependence of the LDOS at $E_F - 0.95$ eV, these are much smaller than their even parts. Hence, $(e, 2e)$ contributions involving odd valence electron parts are generally also much smaller. In the following, our coordinate system is such that z is along the (outward-directed) surface normal [110] and x and y are in the surface plane along [001] and [1 -1 0], respectively. Let the reaction plane be (x, z). Due to parallel momentum conservation (cf. Eq. (3.144)), the parallel momentum of the valence electron then only has an x component.

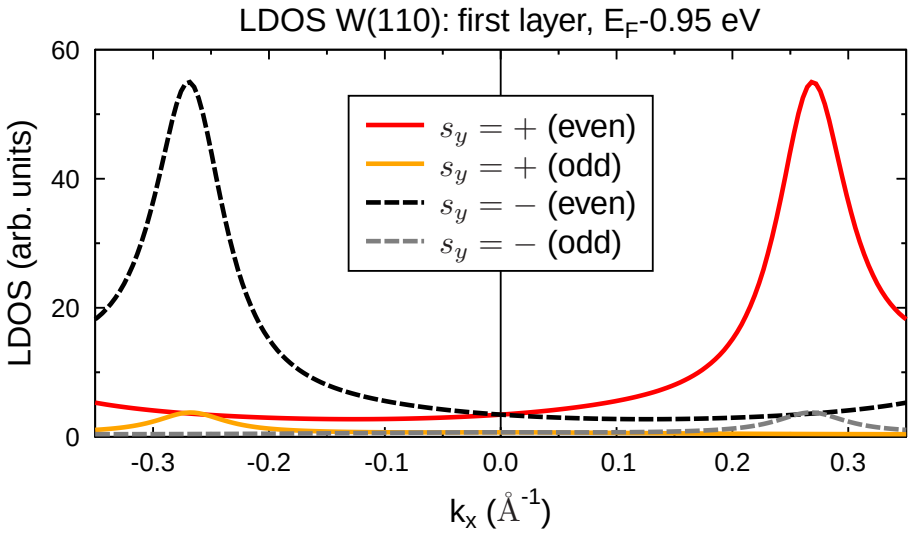

Fig. 7.12: Symmetry- and spin-resolved valence LDOS of the first layer (surface layer) of W(110) at energy $E_2 = E_F - 0.95$ eV as a function of the parallel momentum k_x (along $\overline{\Gamma\mathrm{H}}$ in the surface Brillouin zone). The red line represents the LDOS for states with even symmetry with respect to the (x, z) plane and spin in the $+y$ direction. The orange line represents the LDOS for states with odd symmetry with respect to the (x, z) plane and spin in the $+y$ direction. Analogously, the black and gray lines represent the LDOS for states with even/odd symmetry and spin in the $-y$ direction.

For a more quantitative and detailed view, we show in Figs. 7.13(a)–7.13(d) the spin- and layer-resolved even LDOS as line plots at the selected energy $E_F - 0.95$ eV. The weight of the oppositely spin-polarized surface states at $k_{2x} = \pm 0.27$ Å^{-1} $= \pm 0.143$ Bohr^{-1} is strongest in the topmost atomic layer and decreases monotonously for deeper layers.

We now want to explore the electron pair emission, which results from the collisions of these spin-polarized valence state electrons with spin-polarized electrons impinging on the surface. To this end, we first choose a coplanar $(e, 2e)$ setup, with normal incidence of the primary electron and the emitted electrons in the (x, z) plane at equal polar angles $\vartheta_3 = \vartheta_4$. For fixed primary energy E_1 and constant sum energy $E_3 + E_4$ of the outgoing electrons, energy conservation (cf. Eq. (3.144)) then dictates a fixed valence energy E_2. The reaction cross sections $I^{\sigma_1}_{\sigma_3,\sigma_4}$ (in nonmagnetic materials, the parameter μ in Eq. (3.147) can be omitted) then depend only on the energy difference $E_3 - E_4$, or, equivalently (as is easily derived from the conservation conditions given by Eq. (3.144)), on the valence electron parallel momentum component k_{2x}.

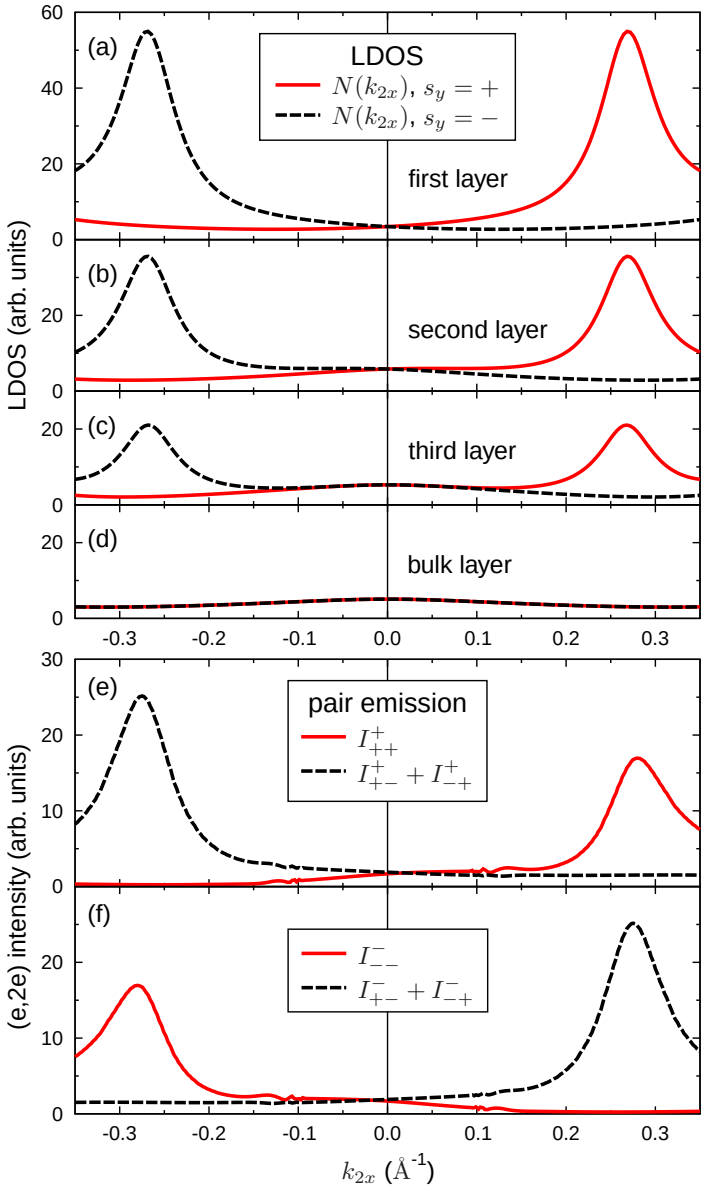

Fig. 7.13: Layer- and spin-resolved valence electron density of states (LDOS) of W(110) at energy $E_2 = E_F - 0.95$ eV as a function of k_{2x} along the $\overline{\Gamma\mathrm{H}}$ direction in the surface Brillouin zone for states of even symmetry with respect to the (x, z) plane (the reaction plane in our $(e, 2e)$ setup). Panels (a)–(c) show the LDOS of the three topmost layers and (d) shows the bulk layer LDOS. In panels (a)–(d), the black (dashed) lines represent the LDOS for states with spin in the $-y$ direction (in the surface plane), and the red (solid) lines represent the LDOS for spin in the $+y$ direction.
Panel (e) shows spin-dependent $(e, 2e)$ intensities $I^{\sigma_1}_{\sigma_3\sigma_4}$ (cf. Eq. (3.147)) associated with the above LDOS. The primary electron with energy 27 eV and spin $\sigma_1 = +$ in the y direction impinges normally on the surface. The two outgoing electrons with spins $\sigma_3 = \pm$ and $\sigma_4 = \pm$ propagate in the (x, z) plane with equal polar angles $\vartheta_3 = \vartheta_4 = 50°$ and azimuthal angles $\varphi_3 = 0°$ and $\varphi_4 = 180°$, respectively. The sum of the energies of the two outgoing electrons is constant such that — by virtue of energy conservation — the energy of the valence electron is the same as in the above LDOS panels. The intensities are plotted as functions of the valence electron parallel momentum component k_{2x}, which is uniquely determined by energy and parallel momentum conservation (cf. Eq. (3.144)). The black (dashed) curve relates to outgoing electrons with antiparallel spins, whereas the red (solid) curve is obtained for parallel spins. Panel (f) is analogous to (e), with all spins reversed.

By choosing the primary energy $E_1 = 27$ eV and the sum energy of the two emitted electrons $E_3 + E_4 = 20.98$ eV, we select the same valence energy $E_2 = E_F - 0.95$ eV $= -6.02$ eV (with the Fermi energy $E_F = -5.07$ eV relative to the vacuum level) as for the LDOS in Figs. 7.13(a)–7.13(d). In Figs. 7.13(e) and 7.13(f), we show for this energy the spin-dependent $(e, 2e)$ intensities $I^{\sigma_1}_{\sigma_3,\sigma_4}$ (cf. Eq. (3.147)) as functions of the valence electron parallel momentum component k_{2x}. Consider first the primary spin σ_1 in the $+y$ direction (Fig. 7.13(e)), i.e., parallel to the surface state electron spin around $k_{2x} = +0.27$ Å^{-1} $= +0.143$ Bohr^{-1} and antiparallel to the one around $k_{2x} = -0.27$ Å^{-1} $= -0.143$ Bohr^{-1}. Therefore, in the former case, the intensity I^+_{++} (with parallel spins of the two outgoing electrons) vastly dominates, whereas in the latter case, we have exclusively the intensity $I^+_{+-} + I^+_{-+}$ (with antiparallel spins of the outgoing electrons). If the primary spin is reversed (i.e., σ_1 in the $-y$ direction), then one obtains analogous results, with all spins reversed, as can be seen in Fig. 7.13(f). Due to spin-orbit coupling, it is possible that an incident spin-up (spin-down) electron produces two spin-down (spin-up) emitted electrons, i.e., that the intensities I^+_{--} and I^-_{++} are nonzero. They are, however, for the present geometry, vanishingly small and therefore not shown.

The manifestation of the $+y$ and $-y$ spin-polarized surface-state LDOS in pair emission spectra with parallel and antiparallel spins of the emitted electrons, which was found (in Fig. 7.13) for the valence state energy $E_2 = E_F - 0.95$ eV, persists over the entire energy range of the surface state, as is demonstrated in Fig. 7.14. Figures 7.14(a)–7.14(f) display the spin-resolved LDOS, which was shown in Fig. 7.6 by contour plots, for a representative selection of energies in the form of line plots. For primary spin polarization in the $+y$ direction, the corresponding pair emission spectra are shown in Figs. 7.14(g)–7.14(l). Comparing them with the adjacent LDOS panels, it is obvious that the dispersion of the $+y$ and the $-y$ polarized surface state is directly mapped by the pair emission intensities with parallel and antiparallel spins of the two emitted electrons, respectively. The fine structure in the spectra around $k_{2x} = \pm 0.1$ Å^{-1} $= \pm 0.53$ Bohr^{-1} can be traced back to a surface resonance in one of the inverse LEED states, which are correlated by the Coulomb interaction to form the outgoing two-electron state. Resonances of this type are well known to occur in two-electron and electron-positron emission [22] and also in photoemission [87], for which the final state is an inverse LEED state. In the present surface-state mapping, they can be avoided by choosing a different primary energy and/or different emission angles.

The option found above to obtain electron pairs either with parallel spins or with antiparallel ones allows a disentanglement of correlation effects due to exchange and to Coulomb interaction: for antiparallel spins, there is only the Coulomb correlation, whereas for parallel spins, there are both. In the following, we shall demonstrate this disentanglement for the exchange-correlation hole in the two-electron momentum distribution. To this end, we choose the energy and surface-parallel momentum conditions (cf. Eq. (3.144)) such that a valence state with polarization along $+y$ is picked out at energy $E_F - 0.95$ eV and surface-parallel momentum ($k_{2x} = +0.27$ Å^{-1} $= +0.143$ Bohr$^{-1}, k_{2y} = 0$). For the primary energy 27 eV, this is achieved, first, by choosing both outgoing electron energies as 10.49 eV and, second, by having the primary beam incident at polar angle $\vartheta_1 = 5.81°$ and azimuthal angle $\varphi_1 = 180°$, which implies $k_{1x} = -0.27$ Å^{-1} $= -0.143$ Bohr^{-1} (compensating the valence electron momentum), and observing the two equal-

energy outgoing electrons at equal polar but opposite azimuthal angles, i.e., with opposite parallel momenta $\mathbf{k}_4^{\parallel} = -\mathbf{k}_3^{\parallel}$.

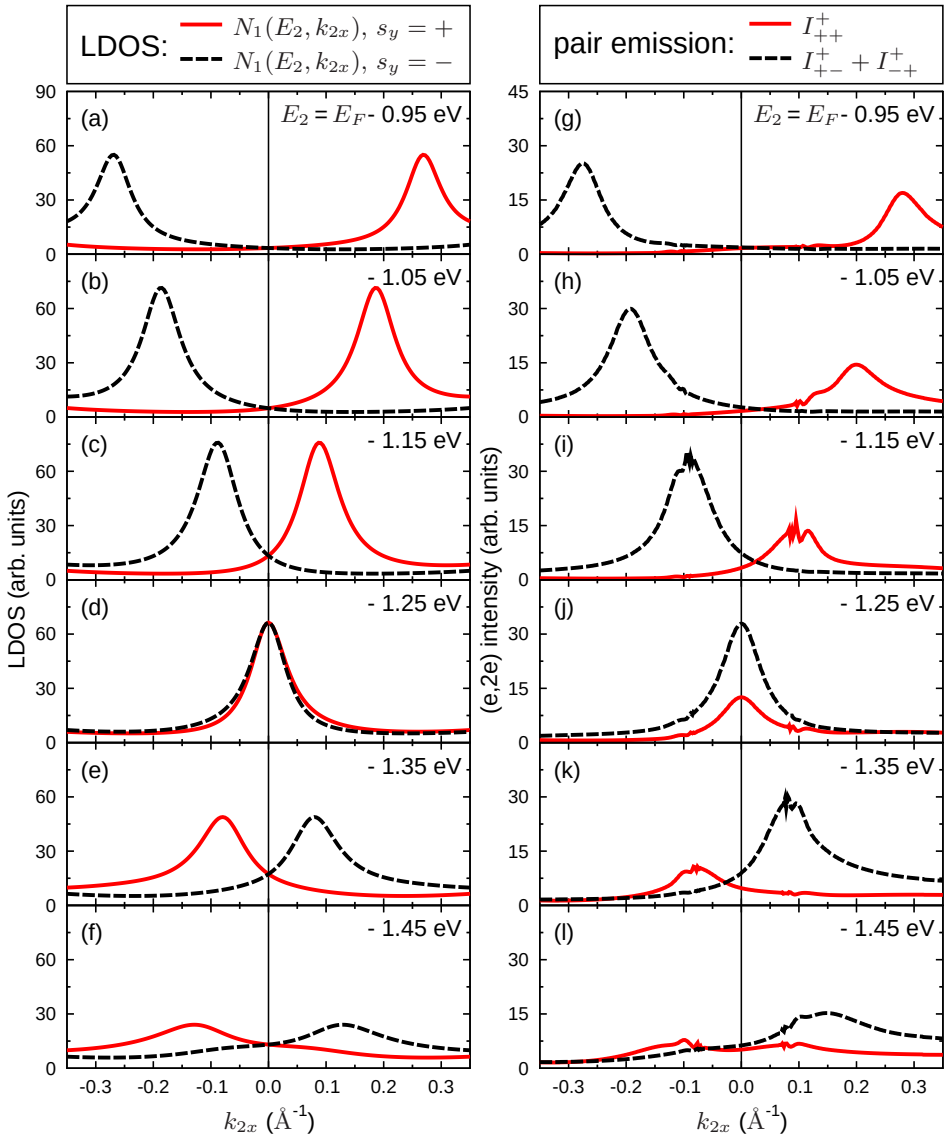

Fig. 7.14: Left-hand column: Spin-resolved valence electron density of states $N_1(E_2, k_{2x})$ of the topmost atomic layer of W(110) (with k_{2x} along the $\overline{\Gamma\mathrm{H}}$ direction in the surface Brillouin zone) for states of even symmetry with respect to the (x, z) plane (the reaction plane in our $(e, 2e)$ setup) for valence electron energy values E_2, as indicated in the individual panels. The black (dashed) lines represent the LDOS for states with spin in the $-y$ direction (in the surface plane), and the red (solid) lines represent the LDOS for spin in the $+y$ direction.
Right-hand column: Spin-dependent $(e, 2e)$ intensities (cf. Eq. (3.147)) from W(110) for primary electron energy 27 eV and spin in the $+y$ direction as functions of the valence electron parallel momentum k_{2x}, analogous to those shown in Fig. 7.13(e) and explained in its caption, except that the sum of the energies of the two outgoing electrons now assumes a series of constant values such that — by virtue of energy conservation — the energy of the valence electron (indicated in each panel) is the same as in the adjacent LDOS panel.

In Fig. 7.15, we show spin-resolved $(e, 2e)$ momentum distributions from W(110) in the surface-parallel momentum plane $(k_x, k_y)/k := (k_{3x}, k_{3y})/k = -(k_{4x}, k_{4y})/k$ of the outgoing electrons. We first address the fully spin-resolved distributions $I^{\sigma_1}_{\sigma_3\sigma_4}(k_x, k_y)$ (cf. Eq. (3.147)). For primary spin up ($\sigma_1 = +$), the intensity I^+_{++} with parallel spins up of the two emitted electrons (Fig. 7.15(a)) is seen to be overall much larger than I^+_{+-} and I^+_{-+} (Figs. 7.15(b) and 7.15(c)) with one of the emitted electrons having spin down. Since I^+_{++} originates mainly from a valence state with dominant spin up, whereas I^+_{+-} and I^+_{-+} require one of mainly spin down, this difference in magnitude is immediately plausible from the valence electron densities of states, which were shown in Fig. 7.13. For our chosen momentum component $k_{2x} = +0.27$ Å^{-1} $= +0.143$ Bohr^{-1}, the spin-up LDOS in the first few layers exhibits the very pronounced surface-state peak, whereas the spin-down LDOS, which reflects bulklike states, is by far smaller. In the case of primary spin down, this entails that I^-_{--} (Fig. 7.15(e)) is much weaker than I^-_{-+} and I^-_{+-} (Figs. 7.15(f) and 7.15(g)), which are associated with the surface state. The intensities I^+_{--} and I^-_{++}, which we already mentioned to exist due to SOC, are almost everywhere extremely small and therefore not shown in Fig. 7.15.

Next, we turn to the symmetry properties of the momentum distributions $I^{\sigma_1}_{\sigma_3\sigma_4}(k_x, k_y)$. Since the complete setup (crystal plus primary and emitted electrons) has mirror symmetry with respect to the (x, z) plane (normal to the surface), all of the momentum distributions are symmetric with respect to the k_x axis. The distributions with parallel spins of the two emitted electrons (Fig. 7.15(a) and 7.15(e)) are, furthermore, symmetric with respect to the k_y axis. This is due to the fact that changing (k_x, k_y) into $(-k_x, -k_y)$ leaves the physical situation unchanged. As regards the antiparallel-spin electrons, changing (k_x, k_y) into $(-k_x, -k_y)$ interchanges their spins. Consequently, the mirror operation at the k_y axis interchanges, for each primary spin $\sigma_1 = \pm$, the distributions $I^{\sigma_1}_{+-}$ and $I^{\sigma_1}_{-+}$, i.e., Figs. 7.15(b) and 7.15(c) for $\sigma_1 = +$ and Figs. 7.15(f) and 7.15(g) for $\sigma_1 = -$.

The most important conclusion is reached by comparing the momentum distributions for parallel spins of the outgoing electrons (Figs. 7.15(a) and 7.15(d)) with those for antiparallel spins (Figs. 7.15(b) and 7.15(c) and Figs. 7.15(f) and 7.15(g)). Going outward from the center, all distributions exhibit a region of small intensity. This depletion zone is seen to be much more pronounced for parallel spins than for antiparallel ones. Since outgoing electrons with parallel spins are subject to exchange and Coulomb interaction, whereas those with antiparallel spins are correlated only by the Coulomb interaction, the central depletion zones in the antiparallel-spin distributions $I^\pm_{+-}$ and $I^\pm_{-+}$ can be viewed as a Coulomb correlation hole and those in the parallel-spin ones I^+_{++} and I^-_{--} as an exchange plus Coulomb correlation hole. Our momentum distributions thus imply that the latter hole is much larger than the former. This finding is consistent with our $(e, 2e)$ results obtained for ferromagnetic iron (cf. Chapter 6).

With regard to an experimental realization, we note that — spin resolution of the outgoing electrons being presently not feasible — the observable quantities are, for primary spin $\sigma_1 = \pm$, the sums $I^\pm$ over the spins of the emitted electrons,

$$I^+ := I^+_{++} + I^+_{+-} + I^+_{-+} + I^+_{--}\,, \tag{7.10a}$$

$$I^- := I^-_{--} + I^-_{-+} + I^-_{+-} + I^-_{++}\,, \tag{7.10b}$$

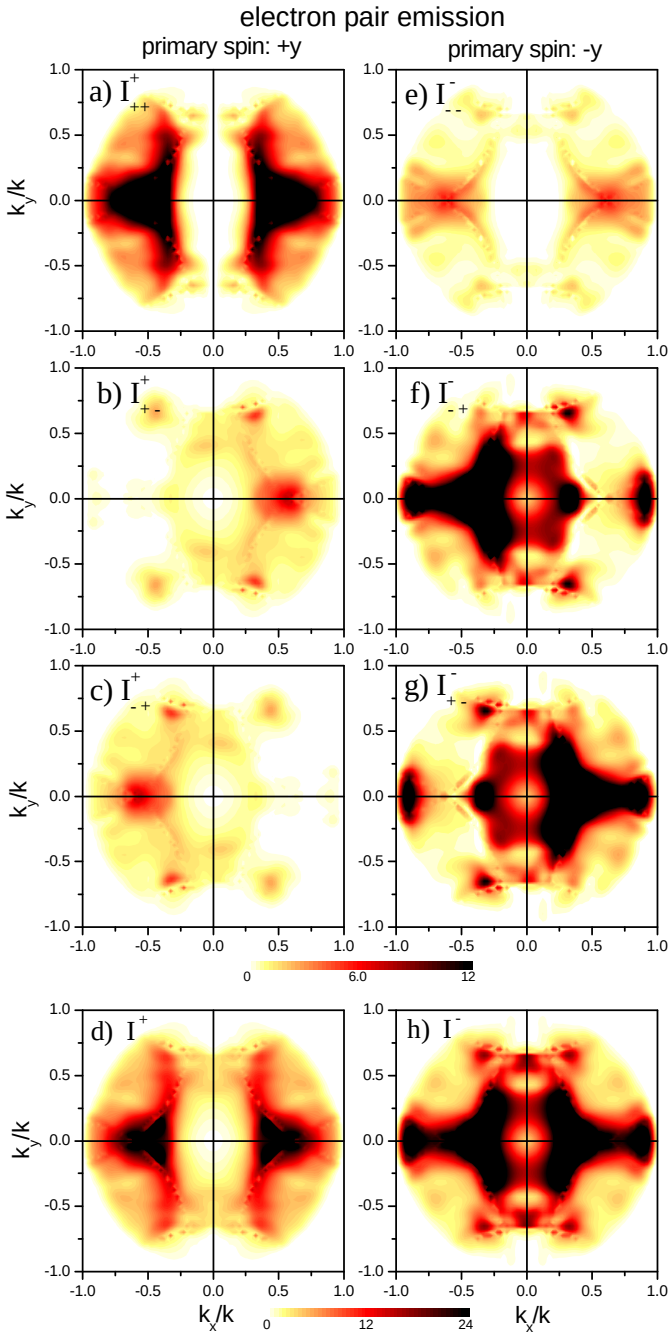

Fig. 7.15: Spin-resolved $(e, 2e)$ momentum distributions (cf. Eqs. (3.147) and (7.10)) from W(110) in the surface-parallel momentum plane $(k_x, k_y)/k$. Primary electrons with energy 27 eV are incident at polar angle $\vartheta_1 = 5.81°$ and azimuthal angle $\varphi_1 = 0°$, i.e., in the (x, z) plane with surface-parallel momentum component $k_{1x} = -0.27$ Å^{-1} $= -0.143$ Bohr^{-1}. The two electrons are emitted at polar angle ϑ, and azimuthal angles φ and $\varphi + \pi$, respectively. They have equal energies $E = 10.49$ eV and surface-parallel momenta $(k_x, k_y) = \sqrt{2E}\sin\vartheta(\cos\varphi, \sin\varphi)$ and $(-k_x, -k_y)$. The relevant valence electron thus has energy -0.95 eV relative to the Fermi energy and parallel momentum components $k_{2x} = 0.27$ Å^{-1} $= 0.143$ Bohr^{-1} and $k_{2y} = 0$. As can be seen from the LDOS in Fig. 7.14(a), it is a surface-state electron with spin polarization in the $+y$ direction. Panels (a)–(c) and (e)–(g) show the fully spin-resolved intensities $I^{\sigma_1}_{\sigma_3\sigma_4}(k_x, k_y)$ (cf. Eq. (3.147)) with spin quantization along the y axis and values $\pm$ of the primary electron spin σ_1 and the spins σ_3 and σ_4 of the emitted electrons, as indicated in the individual panels. The total intensities I^+ and I^- (cf. Eq. (7.10)) for primary spin up and down are presented in panels (d) and (h), respectively.

i.e., essentially the sums over Figs. 7.15(a)–7.15(c) and 7.15(e)–7.15(g), respectively. As is evident from Fig. 7.15, the I^+ distribution (Fig. 7.15(d)) still exhibits the main features of the resolved parallel-spin intensity I^+_{++} (Fig. 7.15(a)), and I^- (Fig. 7.15(h)) exhibits those of the sum of the antiparallel-spin intensities I^-_{-+} (Fig. 7.15(f)) and I^-_{+-} (Fig. 7.15(g)). A separation of Coulomb and exchange correlation appears therefore experimentally possible.

7.6 $(e, 2e)$ results for Co on W(110)

We now study pair emission spectra for one and two ferromagnetic monolayers of Co on W(110) (and for clean W(110)) in conjunction with the underlying spin- and layer-resolved valence electron densities of states (LDOS). With the quasiparticle potentials discussed in Section 7.3, we have calculated $(e, 2e)$ energy distributions

$$I^{\sigma_1 \mu}_{\sigma_3 \sigma_4}(E_1, \mathbf{k}_1^{\parallel}, E_3, \mathbf{k}_3^{\parallel}, E_4, \mathbf{k}_4^{\parallel}) \tag{7.11}$$

according to the formalism, which has been presented in Chapter 3, Eqs. (3.128) to (3.146). We recall that the sets $(E_i, \mathbf{k}_i^{\parallel}, \sigma_i)$ with $i = 1, 3, 4$ characterize the primary electron and the two outgoing electrons, respectively. In contrast to nonmagnetic W(110) the intensity now depends on the additional index μ which refers to the orientation of the majority spin for a ferromagnetic surface system.

Our calculations were done for the coplanar geometrical setup, which is shown in Fig. 7.16. This setup is the same as in the experiments by Samarin *et al.* (cf. Ref. [67]). In particular, the reaction plane is the (x, z) plane (with the z axis along the surface normal [110] and the x axis in the surface plane along [001]). The primary electron with fixed energy E_1 is incident normal ($\vartheta_1 = 0°$) to the surface. As a typical primary energy we have chosen $E_1 = 27$ eV. Furthermore, we have fixed polar angles $\vartheta_3 = \vartheta_4 = 50°$ and azimuthal angles $\varphi_3 = 0°$ and $\varphi_4 = 180°$ for the outgoing electrons. This setup implies $k_{2y} = 0$ for the valence electron. With these parameters fixed, the intensities $I^{\sigma_1 \mu}_{\sigma_3 \sigma_4}$ only depend on the energies E_3 and E_4: $I^{\sigma_1 \mu}_{\sigma_3 \sigma_4} = I^{\sigma_1 \mu}_{\sigma_3 \sigma_4}(E_3, E_4)$.

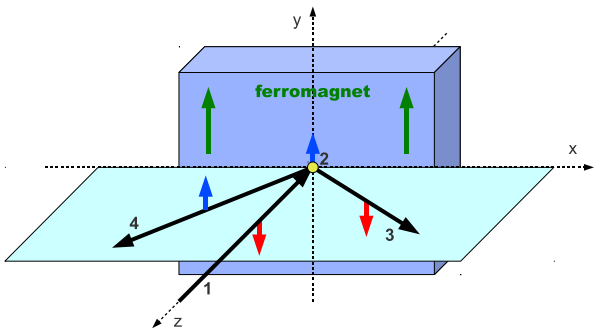

Fig. 7.16: Sketch of the $(e, 2e)$ setup. The numbers 1 to 4 indicate the four ingredient one-electron states $|i\rangle$ with energies E_i, surface-parallel momenta $\mathbf{k}_i^{\parallel}$, and spin labels $\sigma_i = \pm$ (for spin quantization axis y). After the collision of a primary electron (state $|1\rangle$) with a valence electron (state $|2\rangle$), two electrons (correlated states $|3\rangle$ and $|4\rangle$) are emitted and detected. The two long vertical arrows symbolize the majority spins of the ferromagnetic crystal aligned in the $+y$ direction. The blue and red arrows exhibit one possible combination of spins of the four involved one-particle states.

For this setup (cf. Section 7.2), by virtue of energy and parallel momentum conservation, there is a unique correspondence between (E_3, E_4), $(E_2, E_3 - E_4)$, and (E_2, k_{2x}), where E_2 is the energy and k_{2x} the nonvanishing parallel momentum component of the valence electron. In the following we choose the representation $I^{\sigma_1\mu}_{\sigma_3\sigma_4}(E_2, k_{2x})$. This representation has the advantage of directly revealing the relationship between $(e, 2e)$ spectra and the associated valence electron LDOS $N^{\sigma_2}_m(E_2, k_{2x})$.

The $(e, 2e)$ spectra $I^{\sigma_1\mu}_{\sigma_3\sigma_4}(E_2, k_{2x})$ comprise two special cases of particular interest: (a) $k_{2x} = 0$ (i.e., center of the surface Brillouin zone), which for equal emission angles $\vartheta_3 = \vartheta_4$ corresponds to equal outgoing energies $E_3 = E_4$ and (b) $E_2 = \text{const}$, which according to Eq. (3.144) — with E_1 fixed — corresponds to a constant sum energy $E_3 + E_4$.

In view of exploring the relation between the valence electron structure and the pair emission spectra, it is important to recall two $(e, 2e)$ selection rules (cf. Section 7.5 and Ref. [62]), which hold for our above-specified geometry: (1) Since our reaction plane (x, z) is a mirror plane of the semi-infinite surface system, only valence states with even mirror symmetry are allowed to contribute. (2) For the special case of equal-energy distributions, for which the valence electron parallel momentum is zero, only valence states with spatial parts of (single-group) symmetry types Σ_1 and Σ_3 are relevant: both types can contribute to antiparallel spin intensities, whereas parallel-spin intensities can only originate from Σ_3.

These selection rules are strictly valid in the absence spin-orbit coupling. However, as already discussed at the beginning of Section 7.5 in the case of clean W(110), these rules can also be well applied when SOC is present.

7.6.1 Valence electron momentum $\mathbf{k}_2^{\parallel} = 0$

We first present results for the case of valence electron momentum $\mathbf{k}_2^{\parallel} = 0$ (center of the surface Brillouin zone). In Fig. 7.17(A) we show for clean W(110) $(e, 2e)$ spectra $I^{\sigma_1}_{\sigma_3\sigma_4}(E_2)$ together with the underlying valence electron layer-resolved densities of states (LDOS) $N^{\sigma_2}_m(E_2)$ of the single group symmetry types Σ_1 and Σ_3. Since $\mathbf{k}_2^{\parallel} = 0$ it suffices to show the results for valence electron spin up (parallel to the y direction in the surface plane), because for spin down the LDOS results are the same, and so are the $(e, 2e)$ intensities with all spin labels reversed. In this case the symmetry relations (Eqs. (7.5) and (7.8)) simplify to

$$I^{\sigma_1\mu}_{\sigma_3\sigma_4}(E_2) = I^{-\sigma_1,-\mu}_{-\sigma_4,-\sigma_3}(E_2), \tag{7.12}$$

$$N^{\sigma_2\mu}_m(E_2) = N^{-\sigma_2,-\mu}_m(E_2). \tag{7.13}$$

In order to identify and analyze spin-orbit effects, we performed calculations including SOC (i.e., fully relativistic) and neglecting SOC (i.e., scalar relativistic).

Let us first consider the LDOS calculated without SOC (Fig. 7.17(A), panels (f) and (g)). The bulk LDOS reflects the bulk band structure along the surface normal, with a Σ_1 band below -1.15 eV and a Σ_3 band above. The first and second layer LDOS reveals a surface state of purely Σ_1 symmetry at -1.12 eV, which is split off from the Σ_1 bulk band edge at -1.15 eV. This surface state owes its existence to the 3% inward relaxation of the topmost layer.

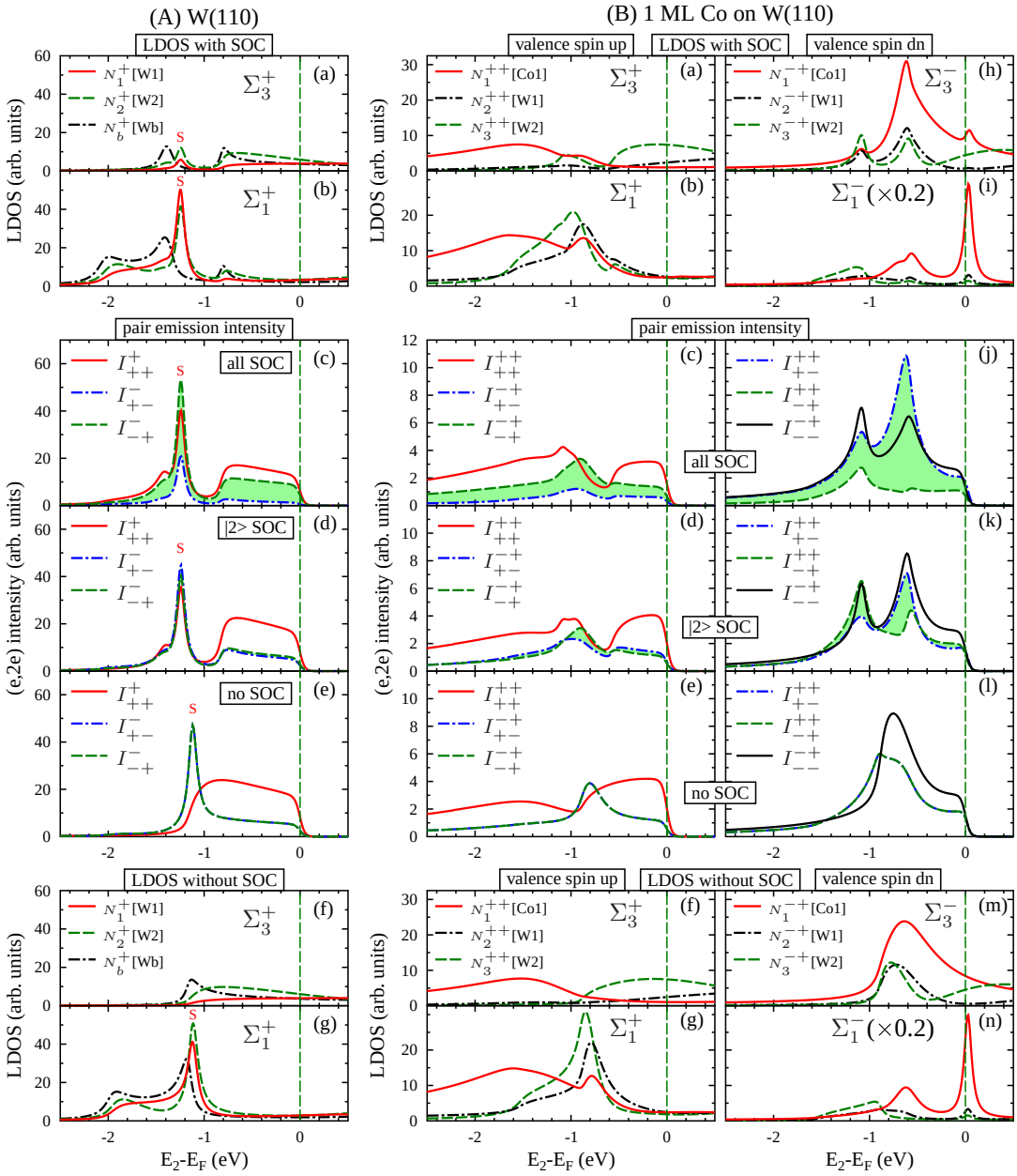

Fig. 7.17: Spin- and layer-resolved valence electron densities of states (LDOS) of spatial symmetry types Σ_1 and Σ_3 for $\mathbf{k}_2^{\parallel} = 0$ and spin-resolved $(e, 2e)$ intensities as functions of the valence electron energy E_2. Primary electrons with energy $E_1 = 27$ eV and spin $\sigma_1 = \pm$ are incident along the surface normal, and correlated electrons with $\sigma_3 = \pm$ and $\sigma_4 = \pm$ go out at polar angles $\vartheta_3 = \vartheta_4 = 50°$ and azimuthal angles $\varphi_3 = 0°$ and $\varphi_4 = 180°$. The symbols Σ_i^+ and Σ_i^- (with $i = 1, 3$) in the LDOS panels stand for valence electron symmetry type Σ_i and spin $\pm$. In the pair emission intensity panels, the labels "all SOC", "$|2\rangle$ SOC", and "no SOC" indicate that the spectra were calculated with SOC in all four one-electron states, only in the valence state $|2\rangle$, and in none of the states, respectively. For clean W(110) we show in column A the valence electron LDOS $N_m^{\sigma_2}(E_2)$ with spin $\sigma_2 = +$ and the $(e, 2e)$ intensities $I_{\sigma_3\sigma_4}^{\sigma_1}(E_2)$ associated with it. (For $\sigma_2 = -$ the LDOS results are the same, and so are the $(e, 2e)$ intensities with all spin labels reversed.) For the magnetic system 1 ML Co on W(110), $N_m^{\sigma_2\mu}(E_2)$ and $I_{\sigma_3\sigma_4}^{\sigma_1\mu}(E_2)$ are shown in column B (only for $\mu = +$, since the results for $\mu = -$ are related to them by Eqs. (7.13) and (7.12)). The left-hand (right-hand) panels pertain to valence electron spin $\sigma_2 = +$ $(-)$. In the LDOS panels Co1, W1, W2, and Wb refer to the Co adlayer, topmost, second, and bulk layer of W, respectively.

SOC induces a gap between bulk bands of Σ_5 symmetry (i.e., with both Σ_1 and Σ_3 spatial parts), as can be seen in Fig. 7.17(A), panels (a) and (b), from the bulk layer LDOS (labeled Wb). Inside this gap, the first- and second-layer LDOS exhibit the SOC-modified surface state S, which now has, in addition to the Σ_1 part, a substantial Σ_3 contribution. Without the inward relaxation of the surface layer, it would still exist, but be shifted by about 0.05 eV towards lower energy.

The corresponding spin-resolved $(e, 2e)$ spectra as functions of valence energy E_2 are presented in panels (c), (d), and (e) of Fig. 7.17(A). With SOC switched off in all four electron states (Fig. 7.17(A), panel (e)), the prominent Σ_1 surface state S strongly appears in the antiparallel-spin intensities I^-_{-+} and I^-_{+-}, but is completely absent in the parallel-spin spectrum I^+_{++}, which is in line with the above-quoted $(e, 2e)$ selection rules. If SOC is switched on only in the valence state (Fig. 7.17(A), panel (d)), S manifests itself — due its presence in the Σ_3 LDOS (Fig. 7.17(A), panel (a)) — also in I^+_{++}. With SOC in all states (Fig. 7.17(A), panel (c)), there is, in addition to the presence of S in I^+_{++}, a strong splitting between the antiparallel-spin intensities I^-_{-+} (direct process) and I^-_{+-} (exchange process). This splitting, marked by the green area, reflects mainly the SOC-induced left-right asymmetry in the two outgoing electron states.

Next we present in Fig. 7.17(B) analogous results for the ferromagnetic system 1 ML Co on W(110). The bottom panels show the valence electron LDOS at the center of the surface Brillouin zone, calculated without SOC. For spatial symmetry Σ_3 (Fig. 7.17(B), panels (f) and (m)), the Co layer has two broad LDOS peaks, one with spin up around -1.5 eV and one with spin down around -0.7 eV. Since above about -1 eV, Σ_3 orbitals of W are available for hybridization, a pronounced spin-down peak is also found in each of the two topmost W layers. For symmetry Σ_1, the Co spin-up LDOS (Fig. 7.17(B), panel (g)) is similar to the one for Σ_3, with an additional peak around -0.8 eV, which extends into the adjacent W layers. This peak as well as the peak at -0.6 eV in the Σ_1 spin-down LDOS are due to interference with backward diffraction from the W substrate. If the W substrate is replaced by a refracting but nonreflecting surface barrier, these two peaks are absent, whereas they appear in the case of a reflecting step barrier, with their energy depending sensitively on the distance of the step barrier from the internuclear plane of the Co layer.

Including SOC, pronounced qualitative changes are seen in the Σ_3 LDOS. For spin up (Fig. 7.17(B), panel (a)) it reflects the Σ_1 peak around -0.9 eV for Co and W layers. For spin down (Fig. 7.17(B), panel (h)) the Co and adjacent W Σ_3 LDOS mirror the Σ_1 peak around 0 eV (Fermi energy) and exhibit a sharp feature at -0.7 eV.

We now turn to the pair emission intensities $I^{\sigma_1\mu}_{\sigma_3\sigma_4}(E_2)$ for $k_{2x} = 0$. Since according to Eq. (7.12) the intensities for minority spin index $\mu = -$ are then the same as those for $\mu = +$ with all the electron spins reversed, it suffices to show only $I^{\sigma_1+}_{\sigma_3\sigma_4}$. Let us first consider the parallel-spin intensities I^{++}_{++}, which according to the selection rules originate only from valence state spatial parts with symmetry Σ_3. Without SOC in all states (Fig. 7.17(B), panel (e)), there are two broad peaks, which correspond to the Σ_3 LDOS without SOC (panel (f)). If SOC is switched on in the valence state (panel (d)), a third peak appears around -1 eV, which is due to the SOC-induced Σ_3 LDOS in Fig. 7.17(B), panel (a). Including SOC also in the LEED-type states leads

to comparatively small changes (panel (c)). In the parallel-spin intensities I_{--}^{-+}, there is also a prominent peak (around -1.1 eV in panels (j) and (k)), which owes its existence to SOC in the valence state. The intensities I_{+-}^{-+} and I_{-+}^{-+} with antiparallel spins of the two outgoing electrons are, for no SOC at all, equal and dominated by a peak around -0.8 eV (Fig. 7.17(B), panel (e)), which corresponds to the Σ_1 LDOS feature in panel (g). SOC causes these two intensities to differ substantially from each other, as is emphasized by the green area in Fig. 7.17(B), panels (c) and (d). The same holds for the antiparallel-spin intensities I_{+-}^{++} and I_{-+}^{++} (panels (j), (k), and (l)).

Comparing in Fig. 7.17 the heights of peaks of the $(e, 2e)$ spectra for Co/W(110) with those for clean W(110), it is seen that the former are by a factor between 5 and 10 smaller than the latter. We ascribe this to the fact that W — with its much larger atomic number — produces much stronger elastic scattering amplitudes than Co. Since there are three LEED-type states in the $(e, 2e)$ matrix elements, this effect is, loosely speaking, enhanced to the third power in $(e, 2e)$.

For 2 ML Co on W(110), $(e, 2e)$ intensities $I_{\sigma_3\sigma_4}^{\sigma_1+}(E_2)$ — calculated with SOC in all states — and the associated LDOS at the surface Brillouin zone center are shown in Fig. 7.18. For spin up, the LDOS in the Co layer adjacent to the substrate (labeled Co1 in Figs. 7.18(a) and 7.18(b)) closely resembles that of 1 ML Co on W(110). The LDOS of the topmost Co layer (labeled Co2) is similar except for the absence of the peak at -0.9 eV, which we ascribed above to interference with backscattering from the substrate. In line with selection rules, the parallel-spin $(e, 2e)$ intensities I_{++}^{++} and I_{--}^{-+} exhibit peaks at energies of maximal Σ_3 LDOS (below E_F). The relative difference between the direct and exchange antiparallel-spin intensities (marked in Fig. 7.18(c) and 7.18(f) by the green shading), which is a hallmark of SOC, is less than for 1 ML Co on W(110), but still sizable.

Comparing the heights of $(e, 2e)$ peaks in Fig. 7.18 with those for 1 ML Co on W(110) (Fig. 7.17(B)), they are seen to be smaller. This is plausible since, first, as mentioned above, W is a much stronger scatterer than Co, and second, most of the $(e, 2e)$ intensity comes from the topmost two layers, which now both consist of Co.

7.6.2 Constant valence electron energy

We now turn to the special case that the valence electron energy E_2 is kept constant and spectra are obtained as functions of the valence electron parallel-momentum component k_{2x}. As a representative value of E_2, we have chosen $E_F - 0.25$ eV. Regarding the LDOS, we recall the selection rule that only spatial parts of even symmetry with respect to the reaction plane (x, z) can contribute to the $(e, 2e)$ matrix elements.

First, we address results for clean W(110) shown in column A of Fig. 7.19. Without SOC, the spin-up LDOS $N_m^+(k_{2x})$ is equal to the spin-down LDOS $N_m^-(k_{2x})$ and mirror symmetric with respect to $k_{2x} = 0$ (see panel (e)). With SOC, this still holds for the bulk LDOS (see panel (a)). For the near-surface layers, however, $N_m^+(k_{2x})$ (shown in panel (a) for $m = 1$ and 2, i.e., the first and second layer) is strongly asymmetric. So is $N_m^-(k_{2x})$, which is its mirror image, i.e., $N_m^-(k_{2x}) = N_m^+(-k_{2x})$. By virtue of this relation it is obvious from panel (a) of Fig. 7.19(A) that

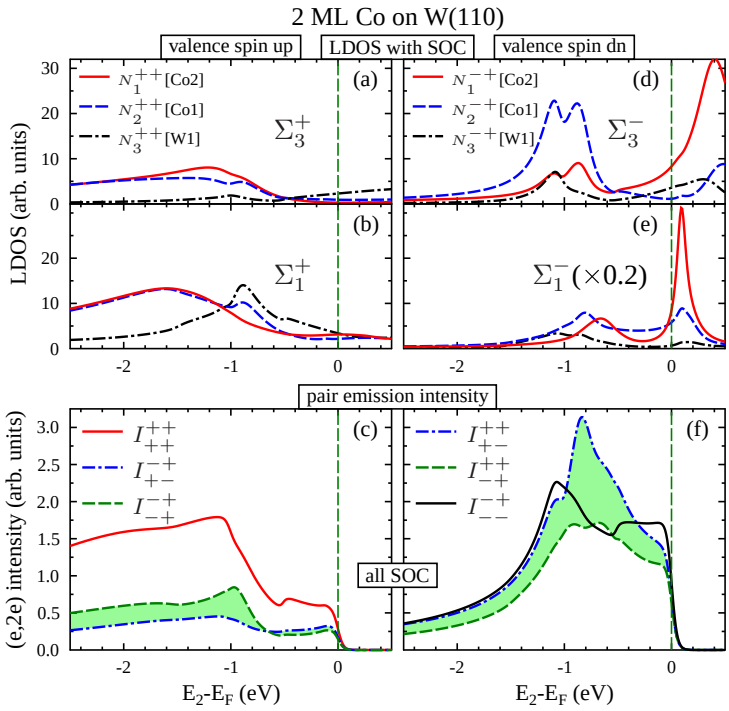

Fig. 7.18: LDOS and $(e, 2e)$ intensities for 2 ML Co on W(110). The layout and the notations used are analogous to those for 1 ML Co in Fig. 7.17, except that we now show only the results with SOC in all the four one-electron states. In the LDOS panels, the labels W1, Co1, and Co2 refer to the topmost W layer, the adjacent Co layer and the topmost Co layer, respectively.

there is a substantial spin difference $N_m^+(k_{2x}) - N_m^-(k_{2x})$.

The $(e, 2e)$ intensities I_{++}^+, I_{+-}^-, and I_{-+}^-, which originate from spin-up valence electrons, are shown in Fig. 7.19(A), panels (b), (c), and (d). Those from spin-down valence electrons are obtained from them by virtue of the relation (cf. Eq. (7.12)) $I_{-\sigma_3,-\sigma_4}^{-\sigma_1}(k_{2x}) = I_{\sigma_3,\sigma_4}^{\sigma_1}(-k_{2x})$. The spectra obtained without any SOC (panel (d)) are seen to be symmetric, in line with the symmetry of the corresponding LDOS. This symmetry is already broken by including SOC only in the valence state (panel (c)) and even more so if SOC is present in all states (panel (b)).

For the ferromagnetic system 1 ML Co on W(110), results for spin-up and spin-down valence electrons are of course different, and both are therefore shown, in column B of Fig. 7.19. Without SOC, the LDOS (panels (e) and (j)) is symmetric. For spin up, it is dominated by two peaks, at ± 0.33 Bohr^{-1}, which have the most weight in the Co layer and in the adjacent W layer. With SOC, the LDOS becomes asymmetric to a similar degree as in the case of clean W(110). This is most noteworthy for the Co layer, in which SOC is much weaker than in W.

Turning to the $(e, 2e)$ intensities $I_{\sigma_3\sigma_4}^{\sigma_1\mu}(k_{2x})$ for 1 ML Co on W(110), we recall that according to Eq. (7.12) the intensities for $\mu = -$ are obtainable from those for $\mu = +$. We therefore show only the latter (in Fig. 7.19(B)). In much the same way as for clean W(110), the symmetry of the no-SOC spectra is seen to be broken by including SOC in the valence state and furthermore in all states.

Since the resolution of the spins of the two emitted electrons is to date not feasible experimentally, it is of particular interest to consider the spin-summed intensities $I^{\sigma_1\mu}(k_{2x})$ (cf. Eq.

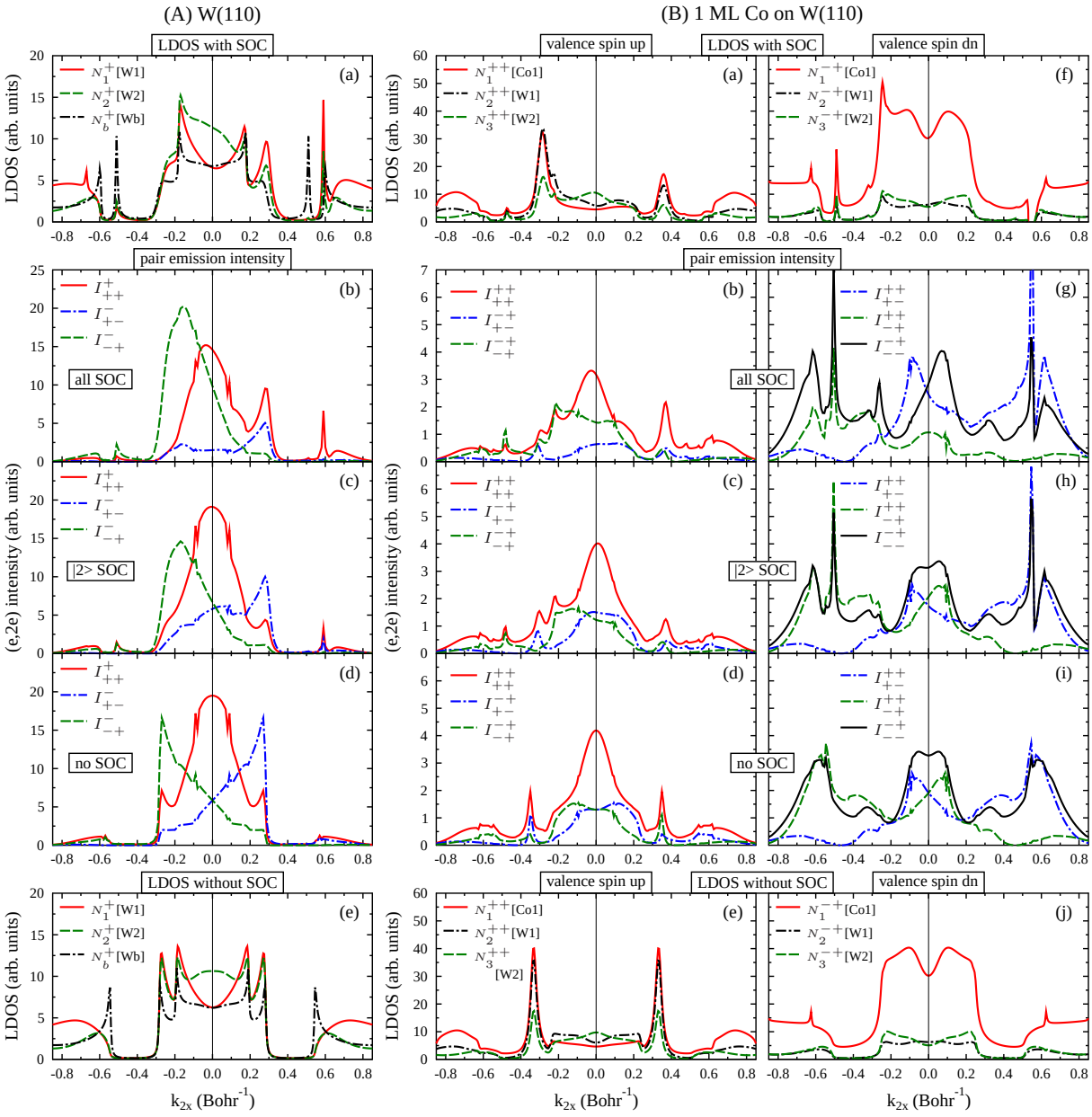

Fig. 7.19: Spin-resolved valence electron densities of even (with respect to the xz plane) states $N_m^{\sigma_2}(E_2, k_{2x}, k_{2y} = 0)$ for fixed energy $E_2 = E_F - 0.25$ eV as functions of the valence electron surface-parallel momentum component k_{2x} and corresponding $(e, 2e)$ intensities (cf. Eq. (7.11)) for normally incident primary electrons with energy 27 eV and spin $\sigma_1 = \pm$. For clean W(110) we show in column A the valence electron LDOS $N_m^{\sigma_2}(k_{2x})$ with spin $\sigma_2 = +$ and the $(e, 2e)$ intensities $I_{\sigma_3\sigma_4}^{\sigma_1}(k_{2x})$ associated with it. (For $\sigma_2 = -$, the LDOS is — according to Eq. (7.13) — the mirror image of the $\sigma_2 = +$ case and so are the $(e, 2e)$ intensities with all spin labels reversed.) For the magnetic system 1 ML Co on W(110), $N_m^{\sigma_2\mu}(k_{2x})$ and $I_{\sigma_3\sigma_4}^{\sigma_1\mu}(k_{2x})$ are shown in column B (only for $\mu = +$, since the results for $\mu = -$ are related to them by Eqs. (7.13) and (7.12)). The left-hand (right-hand) panels pertain to valence electron spin $\sigma_2 = +$ $(-)$. In the $(e, 2e)$ panels, the labels "all SOC", "$|2\rangle$ SOC", and "no SOC" indicate that the spectra were calculated with SOC in all four one-electron states, only in the valence state $|2\rangle$, and in none of the states, respectively. In the LDOS panels Co1, W1, W2, and Wb refer to the Co adlayer, topmost, second, and bulk layer of W, respectively.

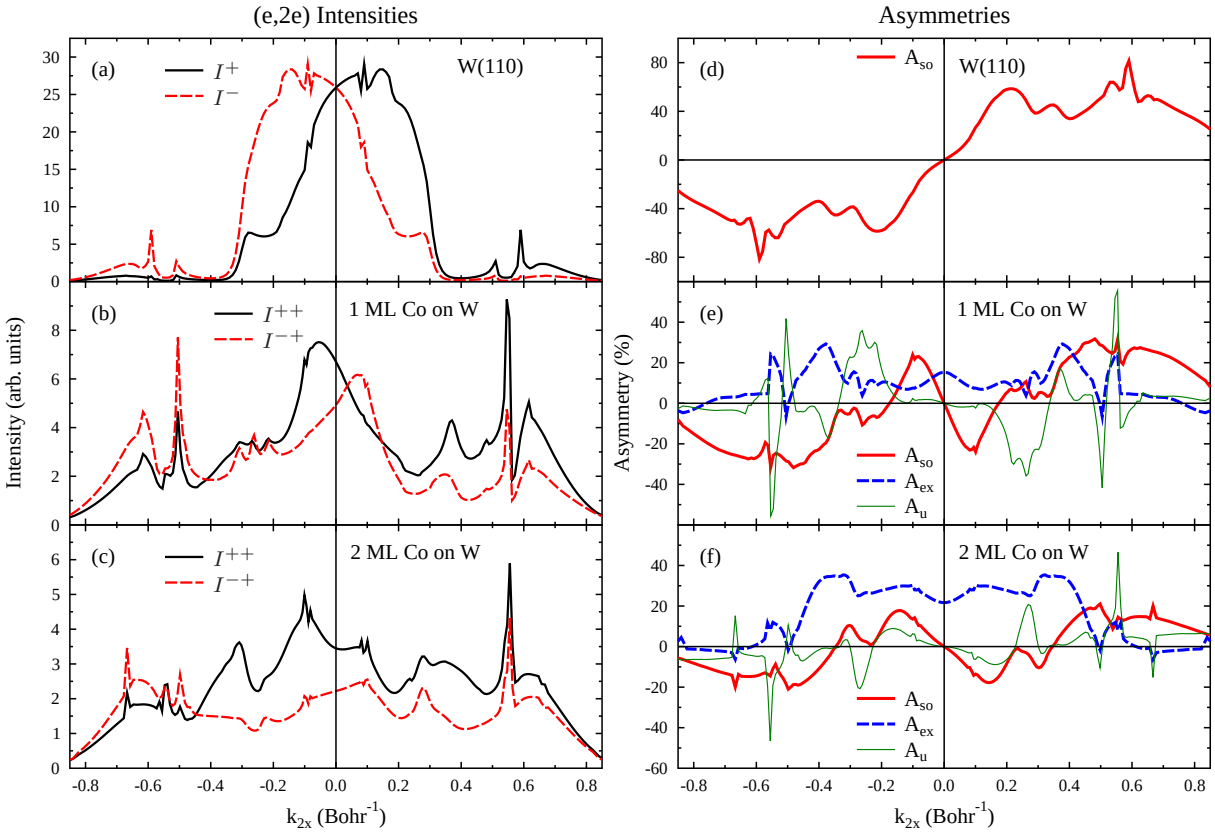

Fig. 7.20: Panels (a), (b), and (c) display the spin-summed $(e, 2e)$ intensities $I^{\sigma_1}(k_{2x})$ for clean W(110) and $I^{\sigma_1+}(k_{2x})$ for Co on W (cf. Eq. (3.150)) with primary spin $\sigma_1 = \pm$. The fixed primary and valence electron energies are 27 eV and $E_F - 0.25$ eV. The corresponding spin-orbit and exchange asymmetries $A_{\rm so}$ and $A_{\rm ex}$ as well as the dichroic asymmetry A_u (cf. Eqs. (3.151b), (3.151c), and (3.151d)) are shown in panels (d), (e), and (f).

(3.150)). Because of the relation $I^{\sigma_1-}(k_{2x}) = I^{-\sigma_1+}(-k_{2x})$ (cf. Eq. (7.12)) it suffices to show only $I^{\sigma_1+}(k_{2x})$ with $\sigma_1 = \pm$ (see Figs. 7.20(a)–7.20(c)). Without SOC, all the curves would be mirror symmetric, i.e., $I^{\sigma_1}(k_{2x}) = I^{\sigma_1}(-k_{2x})$. The absence of this mirror symmetry in the intensities in Fig. 7.20, which were calculated fully relativistically, is therefore a manifestation of SOC. While strongest for clean W(110), it is still fairly big for 1 ML Co on W(110) and clearly visible for 2 ML Co on W(110).

To separate, for the magnetic systems, the effects of exchange interaction and SOC, and to compare the latter with the SOC effect for clean W(110), we show (in panels (d)–(f) of Fig. 7.20) the exchange and spin-orbit asymmetries $A_{\rm ex}$ and $A_{\rm so}$ plus the magnetic dichroic asymmetry A_u, which are obtained from the intensities according to Eqs. (3.151b)–(3.151d). In accordance with the analytical results (cf. Eqs. (7.4a)–(7.4c)), $A_{\rm so}$ and A_u are indeed antisymmetric, whereas $A_{\rm ex}$ is symmetric. $A_{\rm so}$ is seen to be strongest for clean W (with peak heights up to about 70%, cf. Fig. 7.20d). For 1 ML Co, it still reaches about 30%, and for 2 ML Co on W(110) about 20%. We note that the latter values are much larger than typical values which we obtained for a semi-infinite Co crystal surface. In the range $|k_{2x}| < 0.4$ Bohr^{-1}, A_u has similar magnitude as $A_{\rm so}$, whereas for $|k_{2x}| > 0.4$ Bohr^{-1} it exhibits several very narrow peaks of almost 50%. These

originate from valence electron surface states as shown, for the case of 1 ML Co, in Fig. 7.19.

The asymmetries shown in Fig. 7.20 were calculated with SOC in all four one-electron states. In order to get more physical insight, we performed analogous calculations with SOC only in the valence state, SOC only in the primary and outgoing electron states, and with no SOC at all. The results for clean W(110) and for 1 ML Co on W(110) are presented in Fig. 7.21 (only for $k_{2x} \geq 0$ because of the mirror symmetry or antisymmmetry as seen in Fig. 7.20). For clean W(110), panels (a), (b), and (c) of Fig. 7.21 reveal that $A_{\rm so}$ is largely determined by SOC in the LEED-type states $|1\rangle$, $|3\rangle$, and $|4\rangle$, whereas SOC in the valence state $|2\rangle$ has an appreciable influence only for small k_{2x} below about 0.4 Bohr^{-1} and near 0.6 Bohr^{-1}. For 1 ML Co on W(110) panels (e), (f), and (g) support a similar conclusion for $A_{\rm so}$, with SOC in state $|2\rangle$ playing an even minor role. For $A_{\rm ex}$, comparison of panels (e) to (h) shows that the peaks around $k_{2x} = 0$ and $k_{2x} = 0.39$ Bohr^{-1} are hardly at all affected by SOC. In the regions around 0.25 and 0.55 Bohr^{-1}, SOC only in state $|2\rangle$, and only in states $|1\rangle$, $|3\rangle$, $|4\rangle$ has fairly little effect, whereas the joint action of SOC in all four states (see panel (e)) leads to appreciable changes.

With regard to the dichroic asymmetry A_u, the curve obtained with SOC in all states (Fig. 7.21(e)) is very similar to the one with SOC only in the valence state $|2\rangle$ (Fig. 7.21(f)). This appears plausible for the following reason. The left-right asymmetries, which are produced by SOC in each of the LEED-type states, are approximately averaged out, since A_u involves a sum over the primary electron spin (cf. Eq. (3.151d)) together with the sum over the spins of the two outgoing electrons (cf. Eq. (3.150)). Therefore, there remains mainly SOC in $|2\rangle$ to produce A_u.

The above properties of the asymmetries $A_{\rm so}$ and A_u, which were gleaned from Fig. 7.21 for the fixed valence electron energy $E_F - 0.25$ eV, are corroborated by the results of analogous calculations for other valence energies (Figs. 7.22(a)–7.22(h)) and for 2 ML Co on W(110) (Figs. 7.22(i)–7.22(p)). For $A_{\rm ex}$, the effect of SOC is mostly rather small.

The theoretical $(e, 2e)$ intensities and asymmetries as functions of the valence electron momentum component k_{2x} shown in Fig. 7.20 were obtained for fixed valence electron energy E_2 (as determined by energy conservation) and fixed emission angles $\vartheta_3 = \vartheta_4 = 50^\circ$ and $\varphi_3 = 0^\circ$ and $\varphi_4 = 180^\circ$. In view of making contact with the experimental asymmetries published by Samarin *et al.* [67], we have to note that the latter were obtained for valence electron energies E_2 within a 0.5 eV band just below the Fermi energy and for a range of emission angles, which correspond to the acceptance angles of the two position-sensitive detectors (cf. Ref. [67]). Furthermore, there may be some divergence of the primary electron beam around its nominal direction of incidence.

To take care of these experimental conditions, we adopted the following statistical approach. For a given primary beam energy E_1 and each fixed k_{2x}, a large number of sets $(E_2, \vartheta_3, \vartheta_4, \varphi_3, \varphi_4, \vartheta_1, \varphi_1)$ is randomly generated subject to the conditions that (1) the valence electron energy E_2 lies within the range chosen in the experiment, (2) the emission directions are within the acceptance angles of the detectors, and (3) the primary beam has a specified cone of divergence around the surface normal. According to conservation of energy and surface-parallel momentum (cf. Eq. (3.144)) each of these sets is equivalent to a set $(E_3, E_4, \mathbf{k}_3^{\parallel}, \mathbf{k}_4^{\parallel}, \mathbf{k}_1^{\parallel})$. For each of the latter sets, the $(e, 2e)$ intensities $I^{\sigma_1 \mu}(E_3, E_4, \mathbf{k}_3^{\parallel}, \mathbf{k}_4^{\parallel}, \mathbf{k}_1^{\parallel})$ are calculated, and then

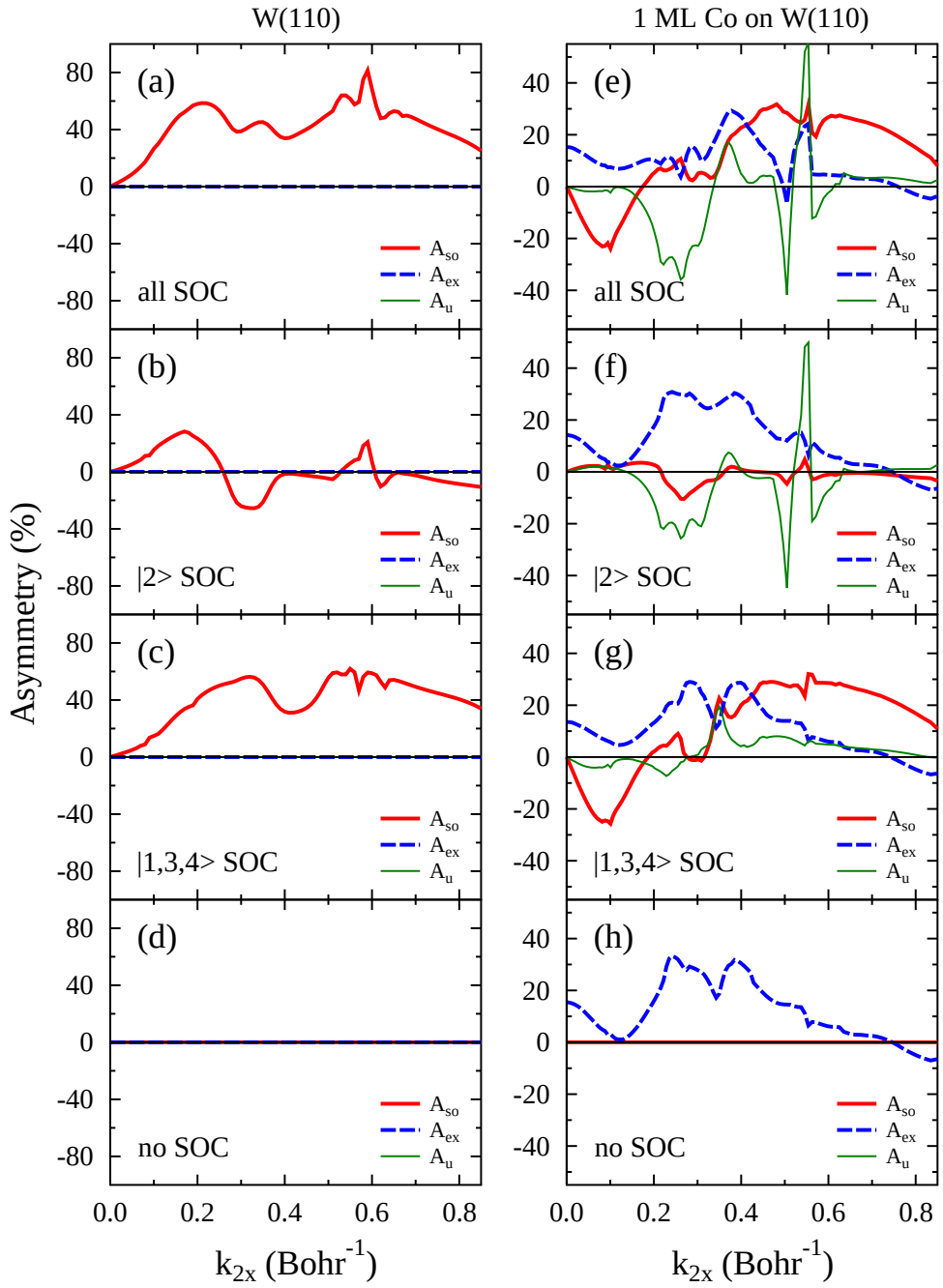

Fig. 7.21: For clean W(110) and for 1 ML Co on W(110), the three asymmetries A_{so}, A_{ex}, and A_u (cf. Eqs. (3.151b), (3.151c), and (3.151d)), which were shown in Figs. 7.20(d) and 7.20(e), are displayed with SOC selectively present only in some of the one-electron states. In the individual panels, the labels "all SOC", "$|2\rangle$ SOC", "$|1, 3, 4\rangle$ SOC", and "no SOC" indicate that the asymmetries were obtained with SOC in all four one-electron states, only in the valence state $|2\rangle$, only in the primary state $|1\rangle$ and in the outgoing electron states $|3, 4\rangle$, and in none of the states, respectively. Note that the curves are shown only in the momentum range from 0 to 0.85 Bohr^{-1}, since in the range from -0.85 to 0 Bohr^{-1} they are equivalent by symmetry (as shown explicitly in Fig. 7.20).

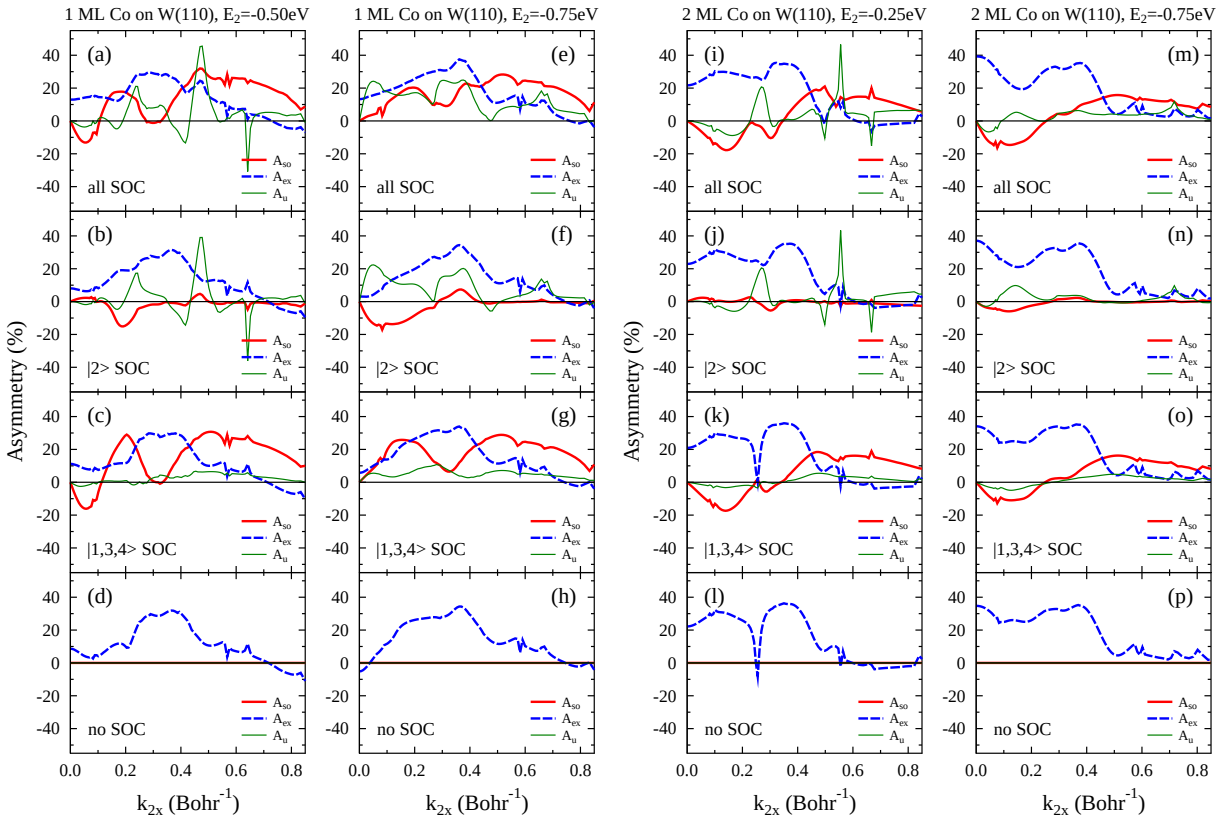

Fig. 7.22: Analogous to Fig. 7.21, asymmetries A_{so}, A_{ex}, and A_u for 1 ML Co on W(110) and 2 ML Co on W(110): (a)–(d) 1 ML Co on W(110), valence electron energy $E_2 = E_F - 0.5$ eV, (e)–(h) 1 ML Co on W(110), $E_2 = E_F - 0.75$ eV; (i)–(l) 2 ML Co on W(110), $E_2 = E_F - 0.25$ eV, (m)–(p) 2 ML Co on W(110), $E_2 = E_F - 0.75$ eV.

averaged over the sets to yield the k_{2x} intensity distributions $I^{\sigma_1\mu}(k_{2x})$. As appropriate for the experiment [67], we chose the opening angle of the acceptance cone for the detected electrons as 20°, the primary beam divergence as 2°, and the valence energy interval $[E_F - 0.5\ \mathrm{eV}, E_F]$. In addition, we performed calculations for the interval $[E_F - 1.0\ \mathrm{eV}, E_F - 0.5\ \mathrm{eV}]$.

For a valid comparison with experimental data, it is furthermore pertinent to address the following issue. While our theoretical $(e, 2e)$ intensities only involve electron pairs produced in a single collision process between the primary electron and a valence electron, experimental data may in addition comprise electron pairs, which originate from multiple collision processes. Since for the latter pairs the energy and momentum conservation (Eq. (3.144)) does not hold, the $(e, 2e)$ intensities can no longer be represented as functions of the valence electron energy E_2 and momentum component k_{2x} (cf. Eq. (7.12)) and be related to the valence electron densities of states. More generally, these pairs degrade the physical information content of $(e, 2e)$. It is therefore important to ensure that they are far outnumbered by the pairs from single collisions. For a given primary energy E_1, this can be achieved by choosing the total energy $E_{\mathrm{sum}} = E_3 + E_4$ of the detected pair within a suitable range. Since the maximal valence electron energy (with respect to the vacuum level) is $E_2^{\mathrm{max}} = -\Phi = E_F$, where Φ is the work function and E_F the Fermi energy, energy conservation (cf. Eq. (3.144)) implies that the maximal total energy is

$E_{\rm sum}^{\rm max} = E_1 + E_F$. Electron pairs with $E_{\rm sum}^{\rm max}$ can only originate from a single collision of the primary electron with an electron at the Fermi energy E_F, since additional collision events entail energy losses and the emitted pair has $E_{\rm sum} < E_{\rm sum}^{\rm max}$. Pairs with $E_{\rm sum} = E_{\rm sum}^{\rm max} - \Delta E$ can stem from a single collision with a valence electron with energy $E_F - \Delta E$ or from a multiple collision process with an energy loss between 0 and ΔE. It is therefore clear that the number of pairs from multiple collisions increases with increasing ΔE. An estimate of the ratio of these undesirable pairs to those from single collisions has been obtained experimentally by Samarin *et al.* [88] for the W(001) surface: for ΔE up to a few eV, i.e., for $E_{\rm sum}$ up to a few eV below $E_{\rm sum}^{\rm max}$, pairs generated by single collisions predominate. This finding was corroborated by a good overall agreement between experimental $(e, 2e)$ data and their theoretical counterparts [25].

With regard to the single collisions, we would like to recall an essential aspect. After the collision, the two electrons move mainly in the forward direction. One might therefore expect most of them to disappear into the crystal. Elastic reflection at atomic layers inside the crystal however can redirect the primary electron before the collision or the two electrons after the collision towards the surface and thus allow the two electrons to reach the detectors. The vital importance of elastic reflection for low energy $(e, 2e)$ from surfaces has been demonstrated by numerical calculations in Ref. [25] (see in particular Fig. 5), where also references to further evidence are given.

A final point to be taken into account is inherent in the experimental coincidence technique used by Samarin *et al.* [67]. In addition to the true pair emission events, which involve a collision, there is an additional contribution to the measured intensities, which arises from so-called "spurious coincidence events": two primary electrons leave the electron gun within the time interval; each of them is inelastically backscattered from the surface, and one is detected in one detector, the other in the other detector. Thus there are actually two single events instead of a genuine pair event. According to Ref. [89], this contribution amounts to about 10% of the peak intensities and is hardly spin dependent. To make more appropriate contact with the experimental data, we therefore augmented our calculated pair emission intensities by a spin-independent constant value taken as 10% of the main peak heights. From these augmented intensities, asymmetry distributions $A_{\rm so}(k_{2x})$ and $A_{\rm ex}(k_{2x})$ were then obtained according to Eqs. (3.151b) and (3.151c).

These results are presented in Fig. 7.23 together with the experimental data from Ref. [67]. For Co on W(110), it must be noted that the theoretical asymmetries are those for two pseudomorphic monolayers, whereas the experimental asymmetries were obtained for an incommensurate hcp-like Co film of nominally three monolayers. Given this difference, the agreement between theoretical and experimental exchange asymmetry $A_{\rm ex}$ in Fig. 7.23(c) is rather good in shape and the theoretical maxima are significantly higher than the experimental ones. In the momentum range from -0.4 to $+0.4$, the calculated and measured spin-orbit asymmetries $A_{\rm so}$ for both Co on W(110) and for clean W(110) agree similarly well, with the theoretical extrema for W(110) exceeding the experimental ones by a factor of about 1.5. Comparing $A_{\rm so}$ for clean W and Co on W, experiment and theory have two results in common. First, around -0.2 ($+0.2$) there is a minimum (maximum) for clean W and a maximum (minimum) for Co on W. Second, the magnitude of these extrema is much smaller for Co on W, but still appreciable, and much

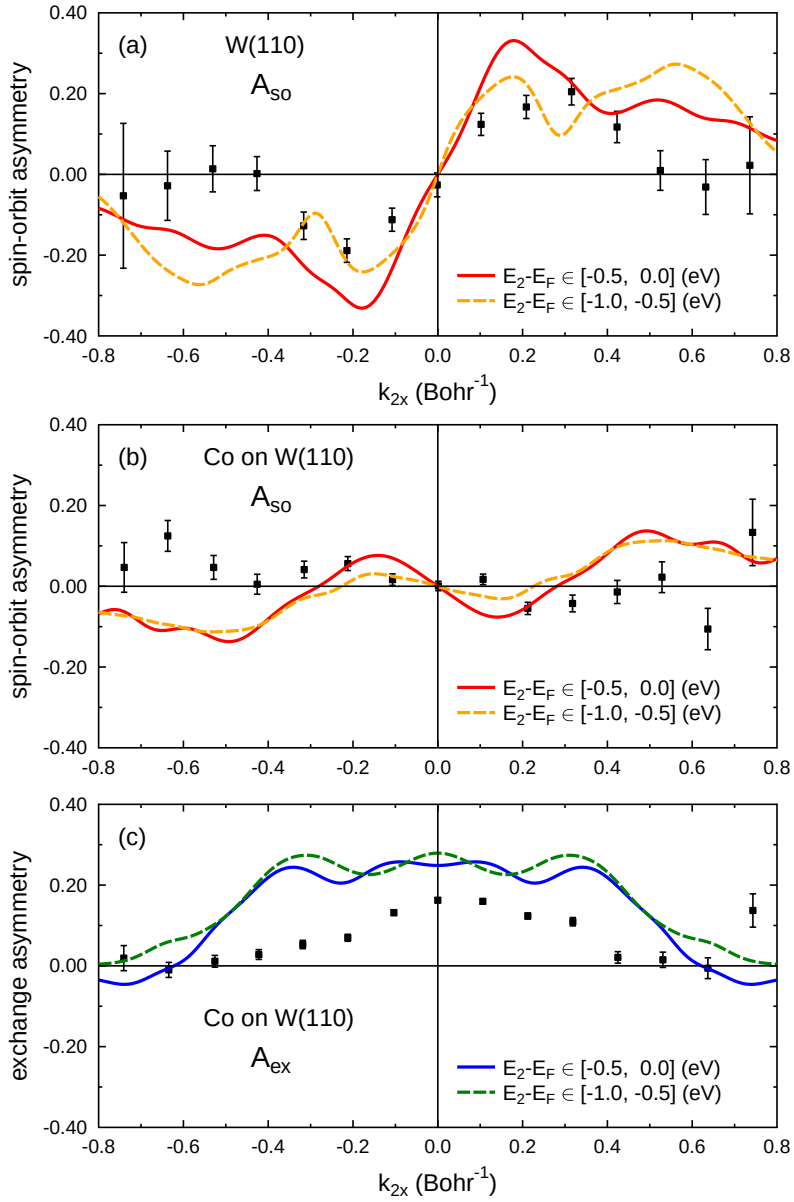

Fig. 7.23: Comparison of theoretical $(e, 2e)$ asymmetries (solid and dashed lines) with experimental ones [67] (dots with error bars) as functions of the valence electron surface-parallel momentum k_{2x}. The primary electron energy is 27 eV. The experimental valence electron energies range from $E_F - 0.5$ eV to E_F. Theoretical results are shown for this range (solid lines) and for the range from $E_F - 1.0$ eV to $E_F - 0.5$ eV (dashed lines). (a) $A_{\rm so}$ for clean W(110); (b) and (c): $A_{\rm so}$ and $A_{\rm ex}$ for Co on W(110); the theoretical curves were calculated for two pseudomorphic Co monolayers on W(110), whereas the experimental data were obtained for a noncommensurate hcp-like Co film of nominally three layers. The asymmetries shown in Ref. [67] are the raw ones as measured for a primary beam polarization of 66% [89]. For comparison with theory, we normalized them to 100% polarization, i.e., divided the raw ones by 0.66.

larger than what one would obtain from a semi-infinite Co crystal. For momentum values outside the range $[-0.4, 0.4]$, the agreement for A_{so} is less satisfactory. As a possible reason, we propose the following. The difference in the energies of the two emitted electrons, which is zero for $k_{2x} = 0$, increases with increasing k_{2x}. For larger k_{2x}, one of the electrons has a rather high energy and the other a rather low one. Since the state of the electron with the very low energy is more sensitive to variations of the surface barrier in theory and to contaminations of the surface in experiment, discrepancies between theory and experiment can arise more readily.

Chapter 8

Summary and outlook

Since spin-orbit coupling (SOC) plays an important role in low-energy electron-induced electron-electron emission [$(e, 2e)$] from ferromagnetic surface systems which involve a material with a large atomic number, an $(e, 2e)$ theory is required which includes SOC and magnetic exchange on an equal footing. Such theory has – in generalization of earlier $(e, 2e)$ formalisms – been developed on the basis of a Dirac equation, which contains, in addition to the usual electrostatic potential term, an effective magnetic field term. The four relevant one-electron states are layer-KKR-type solutions of this equation. The two outgoing electrons are represented by a two-electron state (final state), which is a generalized antisymmetric product of the two one-electron states involving a Coulomb correlation factor. The spin-dependent $(e, 2e)$ reaction cross section (intensity) is then expressed as the transition probability between an initial two-electron state, which is an antisymmetrized product of the incident and valence electron states, and this final two-electron state. With the effective magnetic field in the Dirac equation set to zero, our formalism is immediately applicable to $(e, 2e)$ from nonmagnetic systems. In order to handle positron-induced electron-positron emission [(p, ep)], the above final two-electron state has to be replaced by a simple product of an electron state, a positron state and a correlation factor due to an attractive screened Coulomb interaction.

The computational application of our pair emission theory requires as input the quasiparticle potential for the surface system under consideration. This potential is obtained in two steps. Firstly, the electronic structure of the ground state of the system is calculated ab initio in the framework of density functional theory, using the FLAWP method as implemented in the computer code FLEUR [39]. For the case of a positron, this code was augmented by a subroutine for the positron-electron correlation energy. In a second step, the real single-particle potential resulting from the ground state calculation is augmented by a complex self-energy correction to yield the quasiparticle potential.

This quasiparticle potential was also used to calculate spin- and layer-resolved valence electron densities of states (LDOS) (spectral functions), which are very valuable for the interpretation of the calculated pair emission spectra. Comparison of the LDOS with $(e, 2e)$ energy distributions demonstrates that a sizable underlying LDOS of the appropriate spatial symmetry type is a necessary condition for sizable $(e, 2e)$ features to occur. It is, however, not a sufficient condition, since matrix element effects, in particular interference of amplitudes arising from different layers, may lead to a very small $(e, 2e)$ intensity associated with regions of high LDOS.

The computer code, in which our formalism was implemented, was applied to obtain pair emission results for several prototypical cases.

A comparative study of $(e, 2e)$ and (p, ep) was carried out for the Cu(111) surface, a nonmagnetic system, for which spin-orbit coupling is weak for electrons and by an order of magnitude

weaker for positrons.

We found that the positron-electron Coulomb correlation is stronger than the electron-electron Coulomb correlation. This holds firstly for the pair correlation function between two plane-wave particles coupled by a screened or bare Coulomb interaction and secondly for the correlation part of the single-particle potential describing the interaction with the solid. As a consequence, the total inner potential (at low energies) for the positron is also negative despite the repulsive nature of the electrostatic Hartree potential part.

Equal-energy angular distributions for a fixed initial two-particle state are most suitable for studying Coulomb correlation effects. The latter tend to manifest themselves in (p, ep) as a central accumulation zone ("correlation hill"), as opposed to a central depletion zone ("correlation hole") in $(e, 2e)$. Comparison with results, which we obtained without Coulomb correlation in the emitted pair, shows, however, that the relative intensity and extension of this central zone can be strongly influenced by the above mentioned "matrix element effects". Caution is therefore required in viewing an observed central hill or hole as a correlation feature.

In conjunction with experimental work at the Max-Planck Institut für Mikrostrukturphysik in Halle, our $(e, 2e)$ theory was applied to the ferromagnetic Fe(001) surface, for which SOC is comparatively weak and its influence on $(e, 2e)$ turned out to be very small. The dependence of observed $(e, 2e)$ intensities on the primary electron spin is therefore essentially only due to the magnetic exchange interaction.

From our spin-, $k^{\parallel}$-, symmetry-, and layer-resolved LDOS we identified valence electron energy and parallel-momentum conditions, for which first one spin orientation dominates and second valence states exist of even and of odd symmetry with respect to a mirror plane perpendicular to the reaction plane. These two symmetries ensure, for equal energy sharing and emission in a mirror plane, that pair emission can occur for both primary spin orientations. For primary electrons with spin parallel to this dominant spin orientation of the valence electrons, $(e, 2e)$ spectra are subject to exchange and Coulomb correlation, whereas for primary electrons with opposite spin, i.e., antiparallel spins of the two electrons, there is only Coulomb correlation. In both cases, momentum distributions were found to exhibit a central depletion zone ("hole"), which is, however, significantly larger for parallel than for antiparallel spins. The exchange-correlation hole in momentum space is thus larger than the correlation hole.

Typical for $(e, 2e)$, we found a very high surface sensitivity. A comparison of momentum distributions, which were calculated for one, two and, three layers, with the distributions obtained for the semi-infinite crystal revealed that the latter arise almost completely from only three surface-parallel atomic layers. By comparing theoretical $(e, 2e)$ spectra for antiparallel spins with their experimental counterparts, an effective screening strength of the Coulomb interaction in the surface region could determined.

While in the cases of Cu(111) and Fe(001) spin-orbit coupling effects on $(e, 2e)$ are extremely small, they are sizable for large-Z materials like W. In view of recent experimental $(e, 2e)$ and photoemission studies, we chose the (110) surface of W as a typical case.

Our calculation of the electronic structure of W(110) confirmed the experimentally observed [85] spin polarization and almost linear dispersion of the two branches of a surface state with

energy inside a SOC-induced pseudo-gap of the surface-projected bulk band structure.

For a spin-polarized primary electron colliding with a spin-polarized surface state electron, the $(e, 2e)$ intensity as a function of the valence electron energy and momentum provides a spin-resolved mapping of the dispersion of the two oppositely polarized surface state branches.

Selecting a valence electron with fixed energy and momentum on the spin-up branch, we calculated the intensities resolved with respect to the spins of the primary and of the two emitted electrons as functions of the parallel momenta of the latter. For parallel spins of the emitted electrons, these momentum distributions exhibit, due to exchange and Coulomb correlation, a sizable central depletion zone (exchange-correlation hole). In the case of antiparallel spins, in which there is only Coulomb correlation, the depletion zone (correlation hole) is much smaller. This result is similar to what we found for Fe(001), for which the spin polarization of the selected valence state is due to ferromagnetism instead of SOC.

Spin-orbit coupling (SOC) plays an important role in low-energy $(e, 2e)$ from ferromagnetic surface systems which involve a large-Z material. After deriving, for cubic(110) surfaces, general symmetry properties of the fully spin-resolved intensities and asymmetries, we focussed on ferromagnetic ultrathin films of 1 and 2 ML Co on W(110). Fully spin-resolved $(e, 2e)$ intensities were presented as functions of the energy and surface-parallel momentum of the relevant valence electron. This facilitated an analysis of the $(e, 2e)$ spectra in terms of the simultaneously calculated spin- and layer-resolved valence electron densities of states.

In experimental reality, SOC acts in the three LEED-type states as well as in the valence state, and SOC effects in $(e, 2e)$ result from a combination of the SOC-induced properties of these individual states. Theory has the advantage of being able to selectively switch off SOC in the four individual one-electron states. By comparing the results of such "switch-off" calculations with those of an "all SOC" calculation, we could identify SOC in the valence state or in the LEED-type states as the chief origin of specific SOC-induced $(e, 2e)$ features.

In particular, we analyzed in this way the three asymmetries derived from the spin-dependent $(e, 2e)$ intensities. The SOC-induced asymmetry A_{so} as a function of the valence electron momentum turned out to be mainly determined by SOC in the LEED-type states. For A_{ex}, which requires magnetic exchange for its existence, we found that some features are hardly at all affected by SOC, while others change significantly only if SOC is present in all four states. Since our calculated A_{so} and A_{ex} spectra encouragingly agree with their experimental counterparts [67], our analysis is likely to apply to them as well. In contrast to A_{so} and to A_{ex}, the dichroic asymmetry A_u originates essentially from SOC in the valence states of Co on W(110). This recommends it as potentially useful for studying SOC in the occupied states of ultrathin magnetic films on large-Z nonmagnetic substrates.

Appendix A

Appendix

A.1 Expansion coefficients of the valence electron Green function

We recall Eq. (3.88) where the $\mathbf{k}^{\parallel}$-resolved valence electron Green function $G_2^{ij}(\mathbf{r}_i, \mathbf{r}'_j; E, \mathbf{k}^{\parallel})$ is written in the form (for $\mathbf{r}_i$ and $\mathbf{r}'_j$ in the representative unit cells of the i-th and j-th layer, respectively):

$$G_2^{ij}(\mathbf{r}_i, \mathbf{r}'_j; E, \mathbf{k}^{\parallel}) = \begin{cases} G_{j,a}(\mathbf{r}_j, \mathbf{r}'_j; E) + \sum\limits_{\substack{\kappa\mu \\ \kappa'\mu'}} J^{j,R}_{\kappa\mu}(\mathbf{r}_j) U^{jj}_{\kappa\mu,\kappa'\mu'}(E, \mathbf{k}^{\parallel}) \left(J^{j,L}_{\kappa'\mu'}(\mathbf{r}'_j) \right)^{\dagger} & \text{for } i = j \\ \sum\limits_{\substack{\kappa\mu \\ \kappa'\mu'}} J^{i,R}_{\kappa\mu}(\mathbf{r}_i) U^{ij}_{\kappa\mu,\kappa'\mu'}(E, \mathbf{k}^{\parallel}) \left(J^{j,L}_{\kappa'\mu'}(\mathbf{r}'_j) \right)^{\dagger} & \text{for } i \neq j \end{cases} \tag{A.1}$$

In this appendix, the expansion coefficients $U^{ij}_{\kappa\mu,\kappa'\mu'}$ in Eq. (A.1) for $i = j$ and $i \neq j$ are calculated. The arguments E and $\mathbf{k}^{\parallel}$ for the Green functions and the expansion coefficients are not written in the following derivations.

For the case $i = j$ we obtain

$$G_2^{jj}(\mathbf{r}_j, \mathbf{r}'_j) = G_{j,a}(\mathbf{r}_j, \mathbf{r}'_j) + \sum_{\substack{\kappa\mu \\ \kappa'\mu'}} J^{j,R}_{\kappa\mu}(\mathbf{r}_j) U^{jj}_{\kappa\mu,\kappa'\mu'} \left(J^{j,L}_{\kappa'\mu'}(\mathbf{r}'_j) \right)^{\dagger} \tag{A.2}$$

$$= G_0(\mathbf{r}_j, \mathbf{r}'_j) + \sum_{\substack{\kappa\mu \\ \kappa'\mu'}} j^{R}_{\kappa\mu}(\mathbf{r}_j) D^{jj}_{\kappa\mu,\kappa'\mu'} \left(j^{L}_{\kappa'\mu'}(\mathbf{r}'_j) \right)^{\dagger} \tag{A.3}$$

$$+ \int\limits_{v_{c,j}} \left\{ G_0(\mathbf{r}_j, \mathbf{r}''_j) + \sum_{\substack{\kappa\mu \\ \kappa'\mu'}} j^{R}_{\kappa\mu}(\mathbf{r}_j) D^{jj}_{\kappa\mu,\kappa'\mu'} \left(j^{L}_{\kappa'\mu'}(\mathbf{r}''_j) \right)^{\dagger} \right\} v_j(\mathbf{r}''_j)$$

$$\times \left\{ G_{a,j}(\mathbf{r}''_j, \mathbf{r}'_j) + \sum_{\substack{\tilde{\kappa}\tilde{\mu} \\ \tilde{\kappa}'\tilde{\mu}'}} J^{j,R}_{\tilde{\kappa}\tilde{\mu}}(\mathbf{r}''_j) U^{jj}_{\tilde{\kappa}\tilde{\mu},\tilde{\kappa}'\tilde{\mu}'} \left(J^{j,L}_{\tilde{\kappa}'\tilde{\mu}'}(\mathbf{r}'_j) \right)^{\dagger} \right\} d\mathbf{r}''_j$$

$$
\begin{aligned}
&= G_0(\mathbf{r}_j,\mathbf{r}'_j) + \sum_{\substack{\kappa\mu\\ \kappa'\mu'}} j^R_{\kappa\mu}(\mathbf{r}_j) D^{jj}_{\kappa\mu,\kappa'\mu'} \left(j^L_{\kappa'\mu'}(\mathbf{r}'_j)\right)^\dagger \qquad \text{(A.4)}\\
&\quad + \int\limits_{v_{c,j}} G_0(\mathbf{r}_j,\mathbf{r}''_j) v_j(\mathbf{r}''_j) G_{a,j}(\mathbf{r}''_j,\mathbf{r}'_j)\, d\mathbf{r}''_j\\
&\quad + \sum_{\substack{\tilde\kappa\tilde\mu\\ \tilde\kappa'\tilde\mu'}} \underbrace{\int\limits_{v_{c,j}} G_0(\mathbf{r}_j,\mathbf{r}''_j) v_j(\mathbf{r}''_j) J^{j,R}_{\tilde\kappa\tilde\mu}(\mathbf{r}''_j)\, d\mathbf{r}''_j}_{=J^{j,R}_{\tilde\kappa\tilde\mu}(\mathbf{r}_j) - j^R_{\tilde\kappa\tilde\mu}(\mathbf{r}_j)} U^{jj}_{\tilde\kappa\tilde\mu,\tilde\kappa'\tilde\mu'} \left(J^{j,L}_{\tilde\kappa'\tilde\mu'}(\mathbf{r}'_j)\right)^\dagger\\
&\quad + \sum_{\substack{\kappa\mu\\ \kappa'\mu'}} j^R_{\kappa\mu}(\mathbf{r}_j) D^{jj}_{\kappa\mu,\kappa'\mu'} \underbrace{\int\limits_{v_{c,j}} \left(j^L_{\kappa'\mu'}(\mathbf{r}''_j)\right)^\dagger v_j(\mathbf{r}''_j) G_{a,j}(\mathbf{r}''_j,\mathbf{r}'_j)\, d\mathbf{r}''_j}_{=\left(J^L_{\kappa'\mu'}(\mathbf{r}'_j)\right)^\dagger - \left(j^L_{\kappa'\mu'}(\mathbf{r}'_j)\right)^\dagger}\\
&\quad + \sum_{\substack{\kappa\mu\\ \kappa'\mu'}} \sum_{\substack{\tilde\kappa\tilde\mu\\ \tilde\kappa'\tilde\mu'}} j^R_{\kappa\mu}(\mathbf{r}_j) D^{jj}_{\kappa\mu,\kappa'\mu'} \underbrace{\int\limits_{v_{c,j}} \left(j^L_{\kappa'\mu'}(\mathbf{r}''_j)\right)^\dagger v_j(\mathbf{r}''_j) J^{j,R}_{\tilde\kappa\tilde\mu}(\mathbf{r}''_j)\, d\mathbf{r}''_j}_{=\frac{\mathrm{i}}{2k} t^{j,R}_{\kappa'\mu',\tilde\kappa\tilde\mu}} U^{jj}_{\tilde\kappa\tilde\mu,\tilde\kappa'\tilde\mu'} \left(J^{j,L}_{\tilde\kappa'\tilde\mu'}(\mathbf{r}'_j)\right)^\dagger\\
&= G_{j,a}(\mathbf{r}_j,\mathbf{r}'_j) + \sum_{\substack{\kappa\mu\\ \kappa'\mu'}} J^{j,R}_{\kappa\mu}(\mathbf{r}_j) U^{jj}_{\kappa\mu,\kappa'\mu'} \left(J^{j,L}_{\kappa'\mu'}(\mathbf{r}'_j)\right)^\dagger \qquad \text{(A.5)}\\
&\quad + \sum_{\substack{\kappa\mu\\ \kappa'\mu'}} j^R_{\kappa\mu}(\mathbf{r}_j) \left[-U^{jj}_{\kappa\mu,\kappa'\mu'} + D^{jj}_{\kappa\mu,\kappa'\mu'} + \frac{\mathrm{i}}{2k} \left(D^{jj} t^{j,R} U^{jj}\right)_{\kappa\mu,\kappa'\mu'}\right] \left(J^{j,L}_{\kappa'\mu'}(\mathbf{r}'_j)\right)^\dagger.
\end{aligned}
$$

Therefore $U^{jj} = D^{jj} + \frac{\mathrm{i}}{2k} D^{jj} t^{j,R} U^{jj}$ and hence $U^{jj} = (1 - \frac{\mathrm{i}}{2k} D^{jj} t^{j,R})^{-1} D^{jj}$.

For the case $i \neq j$ we obtain

$$G_2^{ij}(\mathbf{r}_i, \mathbf{r}'_j) = \sum_{\substack{\kappa\mu \\ \kappa'\mu'}} J^{i,R}_{\kappa\mu}(\mathbf{r}_i) U^{ij}_{\kappa\mu,\kappa'\mu'} \left(J^{j,L}_{\kappa'\mu'}(\mathbf{r}'_j) \right)^\dagger \tag{A.6}$$

$$= \sum_{\substack{\kappa\mu \\ \kappa'\mu'}} J^{i,R}_{\kappa\mu}(\mathbf{r}_i) D^{ij}_{\kappa\mu,\kappa'\mu'} \left(j^{L}_{\kappa'\mu'}(\mathbf{r}'_j) \right)^\dagger \tag{A.7}$$

$$+ \int\limits_{v_{c,j}} \left\{ \sum_{\substack{\kappa\mu \\ \kappa'\mu'}} J^{i,R}_{\kappa\mu}(\mathbf{r}_i) D^{ij}_{\kappa\mu,\kappa'\mu'} \left(j^{L}_{\kappa'\mu'}(\mathbf{r}''_j) \right)^\dagger \right\} v_j(\mathbf{r}''_j)$$

$$\times \left\{ G_{a,j}(\mathbf{r}''_j, \mathbf{r}'_j) + \sum_{\substack{\tilde{\kappa}\tilde{\mu} \\ \tilde{\kappa}'\tilde{\mu}'}} J^{j,R}_{\tilde{\kappa}\tilde{\mu}}(\mathbf{r}''_j) U^{jj}_{\tilde{\kappa}\tilde{\mu},\tilde{\kappa}'\tilde{\mu}'} \left(J^{j,L}_{\tilde{\kappa}'\tilde{\mu}'}(\mathbf{r}'_j) \right)^\dagger \right\} d\mathbf{r}''_j$$

$$= \sum_{\substack{\kappa\mu \\ \kappa'\mu'}} J^{i,R}_{\kappa\mu}(\mathbf{r}_i) D^{ij}_{\kappa\mu,\kappa'\mu'} \left(j^{L}_{\kappa'\mu'}(\mathbf{r}'_j) \right)^\dagger \tag{A.8}$$

$$+ \sum_{\substack{\kappa\mu \\ \kappa'\mu'}} J^{i,R}_{\kappa\mu}(\mathbf{r}_i) D^{ij}_{\kappa\mu,\kappa'\mu'} \underbrace{\int\limits_{v_{c,j}} \left(j^{L}_{\kappa'\mu'}(\mathbf{r}''_j) \right)^\dagger v_j(\mathbf{r}''_j) G_{a,j}(\mathbf{r}''_j, \mathbf{r}'_j)\, d\mathbf{r}''_j}_{= \left(J^{L}_{\kappa'\mu'}(\mathbf{r}'_j) \right)^\dagger - \left(j^{L}_{\kappa'\mu'}(\mathbf{r}'_j) \right)^\dagger}$$

$$+ \sum_{\substack{\kappa\mu \\ \kappa'\mu'}} \sum_{\substack{\tilde{\kappa}\tilde{\mu} \\ \tilde{\kappa}'\tilde{\mu}'}} J^{i,R}_{\kappa\mu}(\mathbf{r}_i) D^{ij}_{\kappa\mu,\kappa'\mu'} \underbrace{\int\limits_{v_{c,j}} \left(j^{L}_{\kappa'\mu'}(\mathbf{r}''_j) \right)^\dagger v_j(\mathbf{r}''_j) J^{j,R}_{\tilde{\kappa}\tilde{\mu}}(\mathbf{r}''_j)\, d\mathbf{r}''_j}_{= \frac{\mathrm{i}}{2k} t^{j,R}_{\kappa'\mu',\tilde{\kappa}\tilde{\mu}}} U^{jj}_{\tilde{\kappa}\tilde{\mu},\tilde{\kappa}'\tilde{\mu}'} \left(J^{j,L}_{\tilde{\kappa}'\tilde{\mu}'}(\mathbf{r}'_j) \right)^\dagger$$

$$= \sum_{\substack{\kappa\mu \\ \kappa'\mu'}} J^{i,R}_{\kappa\mu}(\mathbf{r}_i) \left[D^{ij}_{\kappa\mu,\kappa'\mu'} + \frac{\mathrm{i}}{2k} \left(D^{ij} t^{j,R} U^{jj} \right)_{\kappa\mu,\kappa'\mu'} \right] \left(J^{j,L}_{\kappa'\mu'}(\mathbf{r}'_j) \right)^\dagger . \tag{A.9}$$

Therefore we obtain (as a matrix equation):

$$U^{ij} = D^{ij} + \frac{\mathrm{i}}{2k} D^{ij} t^{j,R} U^{jj} \tag{A.10}$$

$$= D^{ij} \left(1 + \frac{\mathrm{i}}{2k} t^{j,R} U^{jj} \right) . \tag{A.11}$$

Bibliography

[1] J. Ullrich, R. Moshammer, A. Dorn, R. Dörner, L. P. H. Schmidt, and H. Schmidt-Böcking, Rep. Prog. Phys. **66**, 1463 (2003)

[2] L. Avaldi and A. Huetz, J. Phys. B: At. Mol. Opt. Phys. **38**, S861 (2005)

[3] A. Knapp, A. Kheifets, I. Bray, T. Weber, A. L. Landers, S. Schössler, T. Jahnke, J. Nickles, S. Kammer, O. Jagutzki, L. P. H. Schmidt, M. Schöffler, T. Osipov, M. H. Prior, H. Schmidt-Böcking, C. L. Cocke, and R. Dörner, J. Phys. B: At. Mol. Opt. Phys. **38**, 615 (2005)

[4] R. Feder and H. Gollisch, in *Solid-State Photoemission and Related Methods*, edited by W. Schattke and M. A. Van Hove (Wiley-VCH, Weinheim, 2003)

[5] J. Berakdar, *Concepts of Highly Excited Electronic Systems* (Wiley-VCH, Weinheim, 2003)

[6] *Correlation Spectroscopy of Surfaces, Thin Films, and Nanostructures*, edited by J. Berakdar and J. Kirschner (Wiley-VCH, Weinheim, 2004)

[7] F. O. Schumann, J. Kirschner, and J. Berakdar, Phys. Rev. Lett. **95**, 117601 (2005)

[8] J. Berakdar, *Electronic Correlation Mapping* (Wiley-VCH, Weinheim, 2006)

[9] F. O. Schumann, C. Winkler, J. Kirschner, F. Giebels, H. Gollisch, and R. Feder, Phys. Rev. Lett. **104**, 087602 (2010)

[10] F. Giebels, H. Gollisch, R. Feder, F. O. Schumann, C. Winkler, and J. Kirschner, Phys. Rev. B **84**, 165421 (2011)

[11] S. Samarin, O. M. Artamonov, V. N. Petrov, M. Kostylev, L. Pravica, A. Baraban, and J. F. Williams, Phys. Rev. B **84**, 184433 (2011)

[12] F. O. Schumann, R. S. Dhaka, G. A. van Riessen, Z. Wei, and J. Kirschner, Phys. Rev. B **84**, 125106 (2011)

[13] Z. Wei, F. O. Schumann, R. S. Dhaka, and J. Kirschner, Phys. Rev. B **85**, 195120 (2012)

[14] F. O. Schumann, L. Behnke, C. H. Li, and J. Kirschner, J. Phys.: Condens. Matter **25**, 094002 (2013)

[15] F. O. Schumann, C. Winkler, and J. Kirschner, Phys. Rev. B **88**, 085129 (2013)

[16] F. Giebels, H. Gollisch, and R. Feder, Phys. Rev. B **87**, 035124 (2013)

[17] H. Mirhosseini, F. Giebels, H. Gollisch, J. Henk, and R. Feder, New J. Phys. **15**, 095017 (2013)

[18] F. Giebels, H. Gollisch, and R. Feder, Phys. Rev. B **88**, 155422 (2013)

[19] M. Huth, C. T. Chiang, A. Trützschler, F. O. Schumann, J. Kirschner, and W. Widdra, Appl. Phys. Lett. **104**, 061602 (2014)

[20] J. Berakdar, Nucl. Instrum. Methods Phys. Res. B **171**, 204 (2000)

[21] G. A. van Riessen, F. O. Schumann, M. Birke, C. Winkler, and J. Kirschner, J. Phys.: Condens. Matter **20**, 442001 (2008)

[22] F. Giebels, H. Gollisch, and R. Feder, J. Phys.: Condens. Matter **21**, 355002 (2009)

[23] G. A. van Riessen, F. O. Schumann, M. Birke, C. Winkler, and J. Kirschner, Journal of Physics: Conference Series **194**, 012056 (2009)

[24] D. Meinert, *Relativistische Theorie der Elektronen-Koinzidenz-Spektroskopie für Festkörperoberflächen*, Dissertation, Gerhard-Mercator-Universität Duisburg (2000)

[25] R. Feder, H. Gollisch, D. Meinert, T. Scheunemann, O. M. Artamonov, S. N. Samarin, and J. Kirschner, Phys. Rev. B **58**, 16418 (1998)

[26] H. Gollisch, X. Yi, T. Scheunemann, and R. Feder, J. Phys.: Condens. Matter **11**, 9555 (1999)

[27] R. Feder, *Polarized Electrons in Surface Physics* (World Scientific, Singapore, 1985)

[28] S. V. Halilov, E. Tamura, D. Meinert, H. Gollisch, and R. Feder, J. Phys.: Condens. Matter **5**, 3859 (1993)

[29] E. Tamura, Phys. Rev. B **45**, 3271 (1992)

[30] B. Ackermann, *Relativistische Theorie der Photoemission und Streuung langsamer Elektronen von ferromagnetischen Oberflächen*, Dissertation, Universität Duisburg, GHS (1985)

[31] J. B. Pendry, *Low energy electron diffraction* (Academic Press, London and New York, 1974)

[32] D. P. Pappas, K. P. Kämper, B. P. Miller, H. Hopster, D. E. Fowler, C. R. Brundle, A. C. Luntz, and Z. X. Shen, Phys. Rev. Lett. **66**, 504 (1991)

[33] M. Getzlaff, J. Bansmann, and G. Schönhense, Solid State Commun. **87**, 467 (1993)

[34] F. Passek, M. Donath, and K. Ertl, J. Magn. Magn. Mater. **159**, 103 (1996)

[35] L. Chioncel, L. Vitos, I. A. Abrikosov, J. Kollár, M. I. Katsnelson, and A. I. Lichtenstein, Phys. Rev. B **67**, 235106 (2003)

[36] R. Hora and M. Scheffler, Phys. Rev. B **29**, 692 (1984)

[37] S. Takada, Progress of Theoretical Physics **36**, 224 (1966)

[38] H. Gollisch, N. v. Schwartzenberg, and R. Feder, Phys. Rev. B **74**, 075407 (2006)

[39] See www.flapw.de.

[40] S. H. Vosko, L. Wilk, and M. Nusair, Can. J. Phys. **58**, 1200 (1980)

[41] S. Hüfner, *Photoelectron Spectroscopy*, 3rd ed. (Springer, 2003)

[42] R. Courths, M. Lau, T. Scheunemann, H. Gollisch, and R. Feder, Phys. Rev. B **63**, 195110 (2001)

[43] O. V. Boev, M. J. Puska, and R. M. Nieminen, Phys. Rev. B **36**, 7786 (1987)

[44] N. G. Fazleev, J. L. Fry, and A. H. Weiss, Phys. Rev. B **57**, 12506 (1998)

[45] J. Arponen and E. Pajanne, Ann. Phys. **121**, 343 (1979)

[46] E. Boroński and R. M. Nieminen, Phys. Rev. B **34**, 3820 (1986)

[47] E. Boroński and H. Stachowiak, Phys. Rev. B **57**, 6215 (1998)

[48] S. N. Samarin, J. F. Williams, A. D. Sergeant, O. M. Artamonov, H. Gollisch, and R. Feder, Phys. Rev. B **76**, 125402 (2007)

[49] D. B. Lambrick and G. Siopsis, Surf. Sci. **120**, L491 (1982)

[50] J. Oliva, Phys. Rev. B **21**, 4909 (1980)

[51] P. Heimann, J. Hermanson, H. Miosga, and H. Neddermeyer, Phys. Rev. B **20**, 3059 (1979)

[52] A. H. Weiss, I. J. Rosenberg, K. F. Canter, C. B. Duke, and A. Paton, Phys. Rev. B **27**, 867 (1983)

[53] S. Samarin, O. M. Artamonov, A. D. Sergeant, J. Kirschner, A. Morozov, and J. F. Williams, Phys. Rev. B **70**, 073403 (2004)

[54] R. Feder, Solid State Commun. **34**, 541 (1980)

[55] I. S. Brandt, Z. Wei, F. O. Schumann, and J. Kirschner, Phys. Rev. Lett. **113**, 107601 (2014)

[56] U. Rücker, H. Gollisch, and R. Feder, Phys. Rev. B **72**, 214424 (2005)

[57] Z. Q. Wang, Y. S. Li, F. Jona, and P. M. Marcus, Solid State Commun. **61**, 623 (1987)

[58] R. Bertacco and F. Ciccacci, Phys. Rev. B **59**, 4207 (1999)

[59] S. Ohnishi, A. J. Freeman, and M. Weinert, Phys. Rev. B **28**, 6741 (1983)

[60] M. Eder, K. Terakura, and J. Hafner, Phys. Rev. B **64**, 115426 (2001)

[61] J. A. Stroscio, D. T. Pierce, A. Davies, R. J. Celotta, and M. Weinert, Phys. Rev. Lett. **75**, 2960 (1995)

[62] H. Gollisch and R. Feder, J. Phys.: Condens. Matter **16**, 2207 (2004)

[63] M. M. J. Bischoff, T. K. Yamada, C. M. Fang, R. A. de Groot, and H. van Kempen, Phys. Rev. B **68**, 045422 (2003)

[64] A. Morozov, J. Berakdar, S. N. Samarin, F. U. Hillebrecht, and J. Kirschner, Phys. Rev. B **65**, 104425 (2002)

[65] S. N. Samarin, J. Berakdar, O. Artamonov, and J. Kirschner, Phys. Rev. Lett. **85**, 1746 (2000)

[66] S. Samarin, O. M. Artamonov, A. D. Sergeant, and J. F. Williams, Phys. Rev. B **72**, 235419 (2005)

[67] S. Samarin, O. M. Artamonov, A. D. Sergeant, R. Stamps, and J. F. Williams, Phys. Rev. Lett. **97**, 096402 (2006)

[68] S. N. Samarin, O. M. Artamonov, A. D. Sergeant, and J. F. Williams, Surf. Sci. **601**, 4343 (2007)

[69] H. Knoppe and E. Bauer, Phys. Rev. B **48**, 1794 (1993)

[70] E. Bauer, J. Phys.: Condens. Matter **11**, 9365 (1999)

[71] M. Pratzer, H. J. Elmers, and M. Getzlaff, Phys. Rev. B **67**, 153405 (2003)

[72] H. L. Meyerheim, D. Sander, R. Popescu, P. Steadman, S. Ferrer, and J. Kirschner, Surf. Sci. **475**, 103 (2001)

[73] G. Teeter, J. Erskine, F. Shi, and M. A. V. Hove, Phys. Rev. B **60**, 1975 (1999)

[74] M. Arnold, G. Hupfauer, P. Bayer, L. Hammer, K. Heinz, B. Kohler, and M. Scheffler, Surf. Sci. **382**, 288 (1997)

[75] T. Scheunemann, R. Feder, J. Henk, E. Bauer, T. Duden, H. Pinkvos, H. Poppa, and K. Wurm, Solid State Commun. **104**, 787 (1997)

[76] E. Bauer, Rep. Prog. Phys. **57**, 895 (1994)

[77] K. Wurm, private communication (1997)

[78] T. Inui, Y. Tanabe, and Y. Onodera, *Group Theory and Its Applications in Physics*, Springer Series in Solid-State Sciences, Vol. 78 (Springer, Berlin Heidelberg, 1990)

[79] J. Feydt, A. Elbe, H. Engelhard, G. Meister, C. Jung, and A. Goldmann, Phys. Rev. B **58**, 14007 (1998)

[80] J. Sánchez-Barriga, J. Minár, J. Braun, A. Varykhalov, V. Boni, I. D. Marco, O. Rader, V. Bellini, F. Manghi, H. Ebert, M. I. Katsnelson, A. I. Lichtenstein, O. Eriksson, W. Eberhardt, H. A. Dürr, and J. Fink, Phys. Rev. B **82**, 104414 (2010)

[81] E. I. Rashba, Sov. Phys. Solid State **2**, 1109 (1960)

[82] J. Henk, M. Hoesch, J. Osterwalder, A. Ernst, and P. Bruno, J. Phys.: Condens. Matter **16**, 7581 (2004)

[83] R. Winkler, *Spin-Orbit Ccoupling Effects in Two-Dimensional Electron and Hole Systems* (Springer, Berlin Heidelberg, 2003)

[84] R. Feder and H. Gollisch, Solid State Commun. **119**, 625 (2001)

[85] K. Miyamoto, A. Kimura, K. Kuroda, T. Okuda, K. Shimada, H. Namatame, M. Taniguchi, and M. Donath, Phys. Rev. Lett. **108**, 066808 (2012)

[86] K. Miyamoto, A. Kimura, T. Okuda, K. Shimada, H. Iwasawa, H. Hayashi, H. Namatame, M. Taniguchi, and M. Donath, Phys. Rev. B **86**, 161411(R) (2012)

[87] A. Winkelmann, M. Ellguth, C. Tusche, A. A. Ünal, J. Henk, and J. Kirschner, Phys. Rev. B **86**, 085427 (2012)

[88] S. N. Samarin, O. M. Artamonov, H. Schwabe, and J. Kirschner, in *Coincidence Studies of Electron and Photon Impact Ionization*, edited by C. T. Whelan and H. R. J. Walters (Plenum Press, New York and London, 1997)

[89] S. Samarin, private communication

Acknowledgements

I am particularly grateful to Prof. Dr. Roland Feder for the opportunity to work on this exciting thesis project. He supported the work with many fruitful discussions and deep insights.

I am very grateful to Prof. Dr. Jürgen Kirschner for his help, encouragement, and the stimulating discussions at the Max-Planck Institute and at the memorable retreats. Additionally, I want to thank Prof. Dr. Jürgen Kirschner and the Max-Planck Society for providing financial support and computational resources for this thesis project.

A particular thank goes to Dr. Herbert Gollisch. His encouragement, consistent support, and help in many situations were invaluable in completing this thesis.

I want to thank Dr. Frank Schumann for his support and for many interesting discussions about experimental and theoretical aspects of the thesis topic and about physics in general.

I also want to thank Dr. Jürgen Henk for helpful discussions.

I am grateful to Dr. Carsten Winkler, Dr. Lucie Behnke, and Dr. Zheng Wei. They contributed very much to the friendly and productive atmosphere during the visits to Halle. Also many thanks to all other members and the staff of the Max-Planck Institute, who were always very helpful.

I also want to thank Prof. Dr. Stefan Blügel and Dr. Gustav Bihlmayer for providing the *ab initio* electronic structure program FLEUR.

I am grateful to Dr. Sevilay Akcöltekin, Shixun Cui, Dr. Miriam Klusmann, Reinhard Remfort, Jingyi Shi, Dr. Nicolas Wöhrl, and Julia Zech for the friendly atmosphere in the office.

Many thanks go to Carsten Klück and Erdal Akyildiz.

I am deeply indebted to my parents for their continuous support and patience.

Erklärung

Hiermit versichere ich, dass ich die vorliegende Arbeit ohne unzulässige Hilfe Dritter und ohne Benutzung anderer als der angegebenen Hilfsmittel angefertigt habe. Die aus fremden Quellen direkt oder indirekt übernommenen Gedanken sind als solche kenntlich gemacht. Die Arbeit wurde bisher weder im Inland noch im Ausland in gleicher oder ähnlicher From einer anderen Prüfungsbehörde vorgelegt.

Die Arbeit wurde unter wissenschaftlicher Betreuung durch Herrn Prof. Dr. Roland Feder an der Fakultät für Physik der Universität Duisburg-Essen angefertigt.

Duisburg, im November 2014 Franz-Josef Giebels